UNIVERSITÄT POTSDAM
Institut für Physik und Astronomie

IDENTIFICATION AND REDUCTION OF LOSSES IN PEROVSKITE SOLAR CELLS

Kumulative Dissertation zur Erlagung des akademischen Grades
doctor rerum naturalium (Dr. rer. nat.)
in der Wissenschaftsdisziplin Physik

eingereicht an der
Mathematisch-Naturwissenschaftlichen Fakultät
der Universität Potsdam von

CHRISTIAN MICHAEL WOLFF

Potsdam, Mai 2020

IDENTIFICATION AND REDUCTION OF LOSSES IN PEROVSKITE SOLAR CELLS

CHRISTIAN MICHAEL WOLFF

Publication-based Doctoral Thesis

Universität Potsdam
Mai 2020

Erstgutacher: Prof. Dr. Dieter Neher
Zweitgutacher: Prof. Dr. Natalie Banerji
Drittgutacher: Prof. Dr. Elizabeth von Hauff

https://doi.org/10.25932/publishup- 47930
https://nbn-resolving.org/urn:nbn:de:kobv:517-opus4- 479301

Physics isn't the most important thing. *Love* is.
— Richard P. Feynman

Dedicated to Sara, Paraschiva, Johann and Victor.

The digital version of this thesis is published online under: t.b.a.
In the digital version references within the text can be used as links to the bibliographies (separated per Chapter). For the convenience of the reader there are reverse links to the pages, the reference was mentioned in the main text, including multiple appearances.

ABSTRACT

Perovskite solar cells have become one of the most studied systems in the quest for new, cheap and efficient solar cell materials. Within a decade device efficiencies have risen to >25% in single-junction and >29% in tandem devices on top of silicon. This rapid improvement was in many ways fortunate, as *e. g.* the energy levels of commonly used halide perovskites are compatible with already existing materials from other photovoltaic technologies such as dye-sensitized or organic solar cells. Despite this rapid success, fundamental working principles must be understood to allow concerted further improvements. This thesis focuses on a comprehensive understanding of recombination processes in functioning devices.

First the impact the energy level alignment between the perovskite and the electron transport layer based on fullerenes is investigated. This controversial topic is comprehensively addressed and recombination is mitigated through reducing the energy difference between the perovskite conduction band minimum and the LUMO of the fullerene. Additionally, an insulating blocking layer is introduced, which is even more effective in reducing this recombination, without compromising carrier collection and thus efficiency. With the rapid efficiency development (certified efficiencies have broken through the 20% ceiling) and thousands of researchers working on perovskite-based optoelectronic devices, reliable protocols on how to reach these efficiencies are lacking. Having established robust methods for >20% devices, while keeping track of possible pitfalls, a detailed description of the fabrication of perovskite solar cells at the highest efficiency level (>20%) is provided. The fabrication of low-temperature p-i-n structured devices is described, commenting on important factors such as practical experience, processing atmosphere & temperature, material purity and solution age. Analogous to reliable fabrication methods, a method to identify recombination losses is needed to further improve efficiencies. Thus, absolute photoluminescence is identified as a direct way to quantify the Quasi-Fermi level splitting of the perovskite absorber (1.21eV) and interfacial recombination losses the transport layers impose, reducing the latter to ~1.1eV. Implementing very thin interlayers at both the p- and n-interface (PFN-P2 and LiF, respectively), these losses are suppressed, enabling a V_{OC} of up to 1.17eV. Optimizing the device dimensions and the bandgap, 20% devices with 1cm^2 active area are demonstrated. Another important consideration is the solar cells' stability if subjected to field-relevant stressors during operation. In particular these are heat, light, bias or a combination thereof. Perovskite layers – especially those incorporating organic cations – have been shown to degrade if subjected to these stressors. Keeping in mind that several interlayers have been successfully used to mitigate recombination losses, a family of perfluorinated self-assembled monolayers (X-PFC$_n$, where X denotes I/Br and n = 7-12) are introduced as interlayers at the n-interface. Indeed, they reduce interfacial recombination losses enabling device efficiencies up to 21.3%. Even more importantly they improve the stability of the devices. The solar cells with IPFC$_{10}$ are stable over 3000h stored in the ambient and withstand a harsh 250h of MPP at 85°C without appreciable efficiency losses. To advance further and improve device efficiencies, a sound understanding of the photophysics of a device is imperative. Many experimental observations in recent years have however drawn an inconclusive picture, often suffering from technical of physical impediments, disguising *e. g.* capacitive discharge as recombination dynamics. To circumvent these obstacles, fully operational, highly efficient perovskites solar cells are investigated by a combination of multiple optical and optoelectronic probes, allowing to draw a conclusive picture of the recombination dynamics in operation. Supported by drift-diffusion simulations, the device recombination dynamics can be fully described by a combination of first-, second- and third-order recombination and JV curves as well as luminescence efficiencies over multiple illumination intensities are well described within the model. On this basis steady state carrier densities, effective recombination constants, densities-of-states and effective masses are calculated, putting the devices at the brink of the radiative regime. Moreover, a comprehensive review of recombination in state-of-the-art devices is given, highlighting the importance of interfaces in nonradiative recombination. Different strategies to assess these are discussed, before emphasizing successful strategies to reduce interfacial recombination and pointing towards the necessary steps to further improve device efficiency and stability. Overall, the main findings represent an advancement in understanding loss mechanisms in highly efficient solar cells. Different reliable optoelectronic techniques are used and interfacial losses are found to be of grave importance for both efficiency and stability. Addressing the interfaces, several interlayers are introduced, which mitigate recombination losses and degradation.

CONTENTS

LIST OF FIGURES

LIST OF TABLES

ACRONYMS

HTL	hole transport layer
CTL	charge transport layer
ETL	electron transport layer
F_4TCNQ	2,3,5,6-petrafluoro-7,7,8,8-tetracyanoquinodimethane
DMF	dimethylformamide
DMSO	dimethyl sulfoxide
PTAA	poly(bis(4-phenyl)(2,4,6-trimethylphenyl)amine)
polyTPD	poly(N,N′-bis-4-butylphenyl-N,N′-bisphenyl)benzidine
PEDOT:PSS	poly(3,4-ethylenedioxythiophene)-poly(styrenesulfonate)
PCBM	phenyl-C_{61}-butyric acid methyl ester
spiro-OMETAD	2,2′,7,7-tetrakis(N,N-di-p-methoxyphenyl-amine)9,9′-spirofluorene
ICBA	indene-C_{60}-bisadduct
ICTA	indene-C_{60}-trisadduct
SEM	scanning electron microscopy
ITO	indium tin oxide
IPES	inverse photoelectron spectroscopy
UPS	ultraviolet photoelectron spectroscopy

PUBLICATIONS DISCUSSED AND DECLARATION OF CONTRIBUTIONS

---

1. Reduced Interface-Mediated Recombination for High Open-Circuit Voltages in $CH_3NH_3PbI_3$ Solar Cells

Christian M. Wolff, Fengshuo Zu, Andreas Paulke, Lorena Perdigón Toro, Norbert Koch and Dieter Neher

published in : *Adv. Mater.* ***2017**, 29 (28), 1700159*

C.M.W. planned the project together with D.N., drafted the manuscript and reviewer response, fabricated all cells and films with help from A.P. and L.P.T. and performed all optical and electrical measurements and analysis, including JV, MPP, EQE_{PV}, EQE_{EL}, TRPL, SEM and EDX. F.Z. performed photoemission spectroscopy measurements assisted by C.M.W.. D.N. & N.K. supervised the study, analyzed and interpreted all measurements, and contributed to manuscript drafting. All co-authors contributed to data analysis, interpretation, proof reading and addressing reviewer comments.

2. How to Make over 20% Efficient Perovskite Solar Cells in Regular (n-i-p) and Inverted (p-i-n) Architectures

Michael Saliba*, Juan-Pablo Correa-Baena*, Christian M. Wolff*, Martin Stolterfoht, Nga Phung, Steve Albrecht, Dieter Neher, Antonio Abate

published in : *Chem. Mater.* ***2018**, 30, 13, 4193-4201.*

* the first three authors contributed equally to this work

M.Sa., J.P. C.-B. and A.A. initiated the project and drafted the n-i-p part of the manuscript. N.P. assisted with photographs and interpretation. C.M.W. drafted the parts concerning p-i-n devices, analyzed the efficiency data from Potsdam, where all devices were fabricated by C.M.W. & M.S.. D.N. supervised the project with A.A. All co-authors contributed to interpretation, proof reading and addressing reviewer comments. The corresponding chapter focuses on my contribution to the description of inverted perovskite solar cells.

3. Visualization and Suppression of Interfacial Recombination for High-Efficiency Large-Area p-i-n Perovskite Solar Cells

Martin Stolterfoht*, Christian M. Wolff*, José A. Márquez, Shanshan Zhang. Charles J. Hages, Daniel Rothhardt, Steve Albrecht, Paul L. Burn, Paul Meredith, Thomas Unold & Dieter Neher

published in : *Nature Energy, (3), 847-854 (**2018**)*

M.S. planned the project together with C.M.W. and D.N.. MS drafted the manuscript and reviewer response, fabricated most cells and films with help of S.Z., D.R. and C.M.W. and performed electrical measurements. C.J.H. measured TRPL. C.M.W. provided main conceptual ideas regarding the identification and mitigation of the recombination losses (use of absolute PL, introducing both interlayers), contributed to device fabrication and TRPL measurements, and performed coupled optical and Shockley-Queisser modeling. J.A.M. performed all hyperspectral PL measurements and performed corresponding data analysis and interpretation. S.Z. helped with device optimization and fabrication. C.J.H. performed fluence- and wavelength-dependent TRPL measurements and analyzed data. T.U. performed numerical drift diffusion simulations with SCAPS1D and analyzed and interpreted the optical measurements. D.R. fabricated certified 1 cm^2 cells with M.S. & C.M.W.. as well as MAPI/FAPI cells and films. D.N. supervised the study, analyzed and interpreted all electrical and optical measurements, and contributed to manuscript drafting. All co-authors contributed to data analysis, interpretation, proof reading and addressing reviewer comments.

4. Perfluorinated Self-Assembled Monolayers Enhance the Stability and Efficiency of Inverted Perovskite Solar Cells

Christian M. Wolff, Laura Canil, Carolin Rehermann, Nguyen Ngoc Linh, Fengshuo Zu, Maryline Ralaiarisoa, Pietro Caprioglio, Lukas Fiedler, Martin Stolterfoht, Sergio Kogikoski Jr., Ilko Bald, Norbert Koch, Eva Unger, Thomas Dittrich, Antonio Abate and Dieter Neher

published in : *ACS Nano **2020**, 14, 2, 1445-1456*

C.M.W. and D.N. planned the project together with A.A.. C.M.W. drafted the manuscript and reviewer response, fabricated all cells and films and carried out $\mathrm{EQE}_{\mathrm{PV}}$, $\mathrm{EQE}_{\mathrm{EL}}$, TRPL, absolute PL, contact angle, JV, MPP, and FTIR measurements with help of M.S. and P.C. and L.F.. C.R. conducted XRD measurements and provided SPV measurements together with T.D.. L.C. helped with DSC measurements, interpretation and drafting. N.N.L. conducted DFT simulations. F.Z. and M.R. conducted photoemission spectroscopy under supervision of N.K.. S.K.Jr. and I.B. assisted with FTIR interpretation. E.L.U., N.K., T.D., A.A. and D.N. supervised the project. All co-authors contributed to data analysis, interpretation, proof reading and addressing reviewer comments.

5. Photophysics of High-Performance Perovskite Solar Cells

Christian M. Wolff, Sean Bourelle, Le Phuong, Jona Kupiers, Sascha Feldmann, Pietro Caprioglio, Jose Antonio Marquez-Prieto, Jonas Diekmann, Thomas Unold, Martin Stolterfoht, Safa Shoaee, Felix Deschler and Dieter Neher

in prepraration

C.M.W., D.N., and F.D. planned the project. C.M.W. drafted the manuscript and reviewer response, fabricated all cells and films and carried out $\mathrm{EQE}_{\mathrm{PV}}$, $\mathrm{EQE}_{\mathrm{EL}}$, SCAPS simulations, absolute PL, TAS, TDCF and JV measurements with help of S.B., J.K., S.F., M.S. and P.C.. L.P. conducted PIA studies under the supervision of S.S., J.A.M. carried out PL simulations under supervision of T.U.. J.D. conducted IonMoger simulations under supervision of M.S.. D.N. and F.D. supervised the project. All co-authors contributed to data analysis, interpretation, proof reading and addressing reviewer comments.

6.Nonradiative Recombination in Perovskite Solar Cells: The Role of Interfaces

Christian M. Wolff, Pietro Caprioglio, Martin Stolterfoht, and Dieter Neher

published in : *Adv. Mater.* ***2019****, 31, 1902762*

C.M.W. and M.S. drafted the manuscript and collected the relevant data and figures. P.C. assisted in proof reading and commenting. D.N. supervised the project and co-edited the manuscript.

Part I

BACKGROUND & FUNDAMENTALS

INTRODUCTION

ENERGY DEMAND AND CLIMATE CHANGE

Within the last two centuries the world has seen an unprecedented rise in population outcompeted only by an even faster rise in energy demand.[1–3] Fossil fuels are the main sources of energy and heat[4]. However, not only are current projections predicting "peak oil" - the maximum obtainable oil production - to be immanent or already passed,[5] but burning fossil fuels is the one of the main sources for rising atmospheric carbon dioxide - CO_2 - a highly potent green house gas.[6, 7] The Intergovernmental Panel on Climate Change (IPCC) reported since 1990 regularly of rising sea levels as a consequence of glacier melting due to rising global temperatures. Increasing numbers in extreme weather events such as droughts, flooding, tsunamis or tornadoes could despite years of debate[8] recently be causally linked to increasing temperatures and CO_2 emissions.[9–14] The immanent threat of raising global temperatures by more than 2°C above pre-industrial levels and the likely consequences for most economical[15, 16] and ecological systems calls for rapid action in transforming the energy production and consumption cycles. At the center of this transformation on the production side are renewable energies. Among these, hydropower (16%), wind (4%) and solar energy (3%) make up to 25% of the yearly energy production. In particular solar energy is a viable source, as the total yearly energy consumption (150TWh) is provided by the sun withing just two hours, if all incoming light was absorbed.[4]

SOLAR ENERGY FOR SUSTAINABLE ENERGY PRODUCTION

In practice, there are three main classes of solar energy conversion producing heat (photothermal), synthetic fuels (photocatalytic) or electricity (photovoltaic). Photothermal devices use the light to heat *e.g.* water directly for daily usage or heat a given material (*e.g.* high boiling point oil) that in turn drives steam generators to produce electricity. In photocatalytic cells, the energy provided by the sun is – very similar to photosynthesis – used to *catalyze* chemical reactions and thereby produce fuels such as alcohols or hydrogen, that can then be burned to generate heat and electricity. Photovoltaic devices bypass these intermediate steps and directly produce electrical power. These so-called solar cells have first been reported as early as the 1880s [17] with ~1% power conversion efficiency and have since sparked wide interest in research and commercial application. Today, solar cells based on silicon and gallium arsenide, have reached efficiencies up to 26.8% and 28.8%, respectively.[18] Commercially most established are silicon solar cells with a current market share of >95%.[19] This historical fact may seem surprising, given that silicon is a non-ideal candidate as the main material for a solar cell, due to comparably complicated production routes and an indirect bandgap which results in low absorption efficiencies, requiring thick absorber layers with high material cost. Therefore ongoing research has expanded to different semiconductors for the next generation of so-called *thin-film solar cells*. These materials include kesterites, chalcopyrites, chalcogenites, organic semiconductors, organic dyes and halide perovskites. Halide perovskites are of particular interest, as they pose a viable alternative or can serve as an add-on to silicon solar cells in so-called tandem solar cells. This is due to their direct bandgap, high absorption coefficient, spectral tunability and simplicity and cost-effectiveness in fabrication along with high photovoltaic efficiency.

PEROVSKITE SOLAR CELLS - A BRIEF NOTE ON DEVELOPMENT, STRENGTHS AND WEAKNESSES

Halide perovskite optoelectronic devices (predominantly tin-based) had been extensively studied in the late 1990s by *e. g.* Mitzi *et. al.* [20–23], but only in 2006 Kojima *et. al.* demonstrated the first lead halide based solar cell with an efficiency of 2.2% in a structure that most resembles that of an redox electrolyte-based dye-sensitized solar cell.[24] In short the then called *perovskite-dye* was deposited on a mesoporous scaffold of titania and capped by a liquid I^-/I_3^+ electrolyte (LiI & I_2). This electrolyte rendered the solar cells to be stable only for a few minutes. In their next publication in 2009, methylammonium lead bromide was replaced by methylammonium lead iodide, increasing the efficiency to 3.8%, but the low stability was inherited as a consequence of analogous device architecture.[25] The comparably rapid rise in efficiency led to more researchers investigating halide perovskites and in 2012 a major breakthrough was reported when Lee *et. al.* [26] replaced the electrolyte with the solid-state hole-selective material 2,2',7,7'-tetrakis-(N,N-di-p-methoxyphenyl-amine)-9,9'-spirobifluorene (spiro-MeOTAD) and thereby improved the efficiencies to ~10% and more importantly increased the stability by a manifold. Furthermore, by exchanging the titania scaffold with alumina, the ambipolar charge transport character of methylammonium lead iodide was discovered, opening the path for planar devices. Following these advances, a manifold of approaches including cation and anion mixtures[27], solvent engineering[28], additive management and transport layer development has – within less then a decade – led to devices that achieve independently certified power conversion efficiencies of 25.2%. Early on strong absorption[29], low electron-hole binding energies[30], long minority carrier lifetimes [31] and comparably high luminescence efficiencies [32] were reported, where the latter two entail slow nonradiative recombination, a rather atypical feature for low temperature solution-processed materials. The electronic structure of perovskites and in particular the fortunate position of energy levels have allowed to exploit transport materials that can be chosen from the rich toolsets of many other photovoltaic technologies such as dye-sensitized solar cells, organic solar cells or kesterite solar cells. Although high luminescence efficiencies of bare perovskite layers were reported, open-circuit voltages in devices barely exceeded 1V, indicating that additional losses must occur within the multilayer stack. Despite this, solar cell efficiencies have continuously risen and the remarkable advances have been closely followed by attempts to commercialize the technology. This pivoted some research towards the question, whether halide perovskite are stable enough for commercial application? A rule of thumb from the silicon industry says that typically the solar cells must maintain at least 80% of the initial efficiency after 25 years to become economical. This requirement can be met or reduced by either producing the devices at a lower cost, making them more efficient or more stable, which is still under debate due to the simple fact that the greatest part of research on these materials has been carried out only for ~10 years.

This thesis shows my contributions to the field in addressing the latter two objectives: **A.** improving the device efficiency by understanding the fundamental working principles and loss mechanisms – and mitigating them – and **B.** enhancing the device stability. The focus hereby lies in investigating losses that have their origin in the interfaces between the perovskite layer and the adjacent transport layers.

OUTLINE OF THE THESIS

After laying out the FUNDAMENTALS and describing the used METHODS, Chapter 3 discusses the impact the energy level alignment between the perovskite and the electron transport layer based on fullerenes has - primarily on the balance between generation and recombination and thus V_{OC}. This controversial topic is comprehensively addressed and recombination is mitigated through reducing the energy difference between the perovskite conduction band minimum and the LUMO of the fullerene. Alternatively, an insulating blocking layer is introduced, which is even more effective in reducing this recombination, without compromising carrier collection and thus efficiency. Less than ten years after the initial demonstration of a halide perovskite based solar cell, certified efficiencies have broken through the 20% ceiling, and thousands of researchers are working on perovskite-based optoelectronic devices, but reliable protocols on how to reach these efficiencies were lacking. Having established robust methods for >20% devices, while keeping track of possible pitfalls, Chapter 4 gives a detailed description of the fabrication of perovskite solar cells at the highest efficiency level (>20%). In particular, fabrication of low-temperature p-i-n structured devices is described, while commenting on important factors including processing atmosphere & temperature, material purity, solution age and practical experience. In Chapter 5 absolute photoluminescence is introduced as a direct way to quantify the Quasi-Fermi level splitting of the perovskite absorber (1.21eV) and interfacial recombination losses the transport layers impose, reducing the latter to ~1.1eV. By implementing interlayers at both the p- and n-interface (PFN-P2 and LiF, respectively) these losses are strongly reduced, enabling a V_{OC} of up to 1.17eV. Further optimizing the bandgap and the device dimensions, 20% devices with 1cm^2 active area are demonstrated. Beyond efficiency another important consideration is the solar cells' stability if subjected to stressors they might face in field operation. Among these are heat, light, bias or a combination thereof. Despite substantial progress in recent years, perovskite layers – especially those incorporating organic cations – have been shown to degrade if subjected to these stressors. In Chapter 6 a family of perfluorinated self-assembled monolayers (X-PFC$_n$, where X denotes I/Br and n = 7-12) are introduced as interlayers at the n-interface. They reduce interfacial recombination losses enabling device efficiencies up to 21.3% but even more importantly they improve the stability of the devices. The modified solar cells are stable over 3000h if stored in the ambient, but also withstand a harsh 250h of MPP at 85°C without appreciable degradation. In order to further improve device efficiencies, a sound understanding of the photophysics of a device is imperative. Many experimental observations in recent years have however drawn an inconclusive picture, often suffering from technical of physical impediments, disguising *e. g.* capacitive discharge as recombination dynamics. To circumvent these obstacles in Chapter 7 fully operational, highly efficient perovskites solar cells are investigated by a combination of multiple optical and optoelectronic probes, allowing to draw a conclusive picture of the recombination dynamics in operation. Supported by drift-diffusion simulations, the device recombination dynamics can be fully described by a combination of first-, second- and third-order recombination and JV curves, but also luminescence efficiencies over multiple illumination intensities are well described within the model. Chapter 8 gives an overview over the progress that has been made in understanding and preventing recombination losses that often have their origin in the interfaces. Different methods to probe recombination in perovskite solar cells are discussed, notwithstanding their pitfalls, before successful mitigation strategies are highlighted, outlining a way towards the radiative limit. Finally, this work is concluded by combining the collected experimental findings and putting it into a coherent picture of recombination losses and mitigation strategies, paving the way to further improvements in the near future.

FUNDAMENTALS

In this chapter the central principles of absorption and different types of recombination – in particular for semiconductors – are discussed. Starting from the principle of detailed balance, the electronic structure of semiconductors and basic considerations of generation and recombination of charge carriers are introduced. Next, thermodynamic limitations and additional loss processes in solar cells are treated before describing the properties of the family of semiconductors serving as the absorber in the solar cells with which the results in the following chapters are obtained - halide perovskites.

1.1 GENERATION AND RECOMBINATION OF CHARGE CARRIERS IN SEMICONDUCTORS

The interaction between light and matter is laid out in this part. In particular, detailed balance between absorption and emission is discussed, semiconductors are introduced and the essential concepts linking absorption and emission are outlined along the lines of [33].

Detailed Balance of Absorption and Emission

The principle of DETAILED BALANCE is fundamental in the description of *e. g.* ideal gases, where it was applied first by Maxwell and Boltzmann, and it essentially states that in the statistical description of an ideal gas all processes are time-invariant, so that albeit there is statistical fluctuation

$$\begin{aligned} k_{i\rightarrow j}P_i &= k_{j\rightarrow i}P_j \\ k_{i\rightarrow j}P_i &= k_{j\rightarrow i}e^{-(E_j-E_i)/k_BT}, \end{aligned} \tag{1}$$

where k are transition rates, P_x occupation probabilities and E_x the energetic levels of the corresponding states. This concept was translated to radiation by Kirchhoff, resulting in KIRCHHOFF'S LAW OF RADIATION, which states *"Ein Körper, der in einer Hülle sich befindet, deren Temperatur der seinigen gleich ist, ändert durch Wärmestrahlung nicht seine Temperatur, absorbirt also in einer gewissen Zeit eben so viel Strahlen als er aussendet. Schon vor langer Zeit hat man hieraus den Schluß gezogen, daß bei derselben Temperatur das Verhältniß zwischen dem Emissionsvermögen und dem Absorptionsvermögen für alle Körper das gleiche ist."*[1][34] – in a nutshell: in thermal equilibrium a black body's absorptivity is equal to its emissivity, $a(\hbar\omega) = e(\hbar\omega) = 1$ for all energies $\hbar\omega \in [0, \infty]$.[2] Kirchhoff[34], Wien[35] and Planck[36] developed a sound theory of the absorption and emission of thermal radiation by black bodies, rendering PLANCK'S RADIATION LAW for the spectral energy density per energy quanta ($d(\hbar\omega)$):

$$\rho_E = \frac{d}{d(\hbar\omega)}e_\gamma = \frac{(\hbar\omega)^3}{\pi^2\hbar^3c^3}\frac{1}{e^{\hbar\omega/k_BT}-1}\ . \tag{2}$$

This concept holds true even for NON-BLACK BODIES, where $1 \neq a(\hbar\omega) = 1 - r(\hbar\omega) - t(\hbar\omega)$, illustrated in Figure 1, where a black body and a non-black body are enclose in a cavity and separated by a filter, that allows only light of energy within $[\omega, \omega + d\omega]$ to pass and otherwise

---

[1] Translation: "A body, embedded in a cavity of equal temperature does not change its temperature by absorbing thermal radiation, meaning that – over a given time span– it absorbs as much radiation as it emits. It has been concluded a long time ago that for all bodies at the same temperature the ability to emit and absorb is the same."

[2] a= absorptivity, e=emissivity

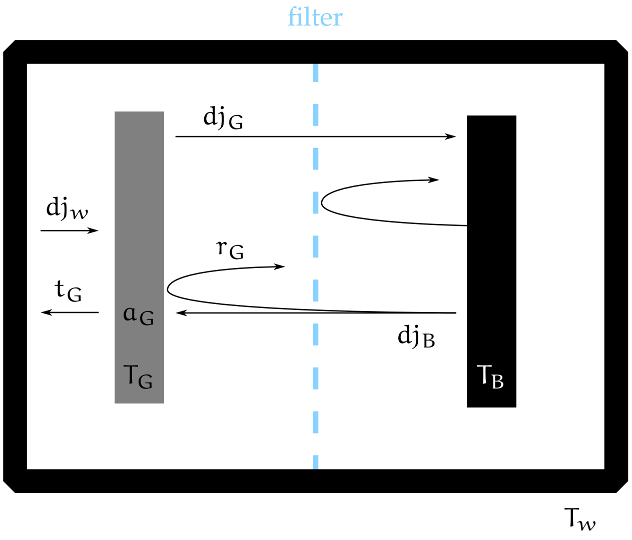

Figure 1: A black body and a non-black body (plates) enclosed in a cavity (likewise a black body) each with their respective temperature. The two plates are separated by a filter that allows only light of energy $[\omega, \omega + d\omega]$ to pass.

reflects. If the system is let to equilibrate, the temperatures equilibrate, so that $T_w = T_G = T_B = T$ and the energy fluxes per energy ($d\omega$) and solid angle ($d\Omega$) result to:

$$\begin{aligned}
dj_B &= dj_E^B B(T_B) = \frac{\hbar^3\omega^3}{4\pi^3\hbar^3c^2}\frac{1}{e^{\hbar\omega/k_BT}-1}d\Omega d\omega \\
r_G\,dj_B &= r_G\,dj_E^B B(T_B) \\
t_G\,dj_w &= t_G\,dj_E^B B(T_w) \\
dj_G &= \epsilon(\omega)dj_E^B B(T_B)\,,
\end{aligned} \tag{3}$$

where $\epsilon(\omega)$ denotes the emissivity of the non-black body.[37]. With $r_G(\omega) + t_G(\omega) + e_G(\omega) = 1$ it follows that $a_G(\omega) = e_G(\omega) \neq 1$, also for non-black bodies, so that Equation 2 is for real non-black bodies weighted by the absorptivity $a(\omega)$ and

$$dj_E = a(\omega)\frac{(\hbar\omega)^3}{\pi^2\hbar^3c^3}\frac{1}{e^{\hbar\omega/k_BT}-1}d\Omega d\hbar\omega\,. \tag{4}$$

Real materials are non-black bodies, however a good proxy for a black body is a metal plate, with a roughened surface[3], which absorbs and emits at (almost) any wavelength and after an electron is excited to a higher energetic state through absorption of a photon, rapidly relaxes to its initial states, by generating a manifold of phonons (heat) within $\sim 10^{-12}$s. For solar cells to work, this relaxation process must be slowed down, so that the excess energy electrons carry after photo excitation can be used externally. Semiconductors are such materials, where the relaxation is significantly decelerated, once the electrons/holes have relaxed within their *bands* to energetic states that are separated by a *gap* of inaccessible energies, originating from their electronic structure, discussed next.

---

[3] otherwise metals reflect most of the incoming light

Electronic Structure of Semiconductors

Semiconductors are a class of materials that in contrast to Insulators and metals (conductors) require additional external stimulus/energy (within the range of visible light), such as light or heat to transition between an insulating and conducting state. The fundamental origin of these three types of behavior lies in the electronic and structural order of the material in question. In this context, the quantum mechanical description of an atom in proximity to other atoms has to be considered. Atoms are comprising an atomic core, surrounded by electron(s). With the assumption that atomic cores only weakly interact with neighboring electrons due to significantly different weights (so-called Born-Oppenheimer approximation) the remaining interaction between atoms reduces to electron-electron coupling. Electrons are fermions and obey as such Fermi-Dirac statistics, which are a consequence of the spin-statistical theorem developed by Wolfgang Pauli in 1925/1940. The so-called Pauli exclusion principle entails that particles with half-integer spins (*i. e.* $s = \pm 1/2, 3/2, .. \hbar$) cannot be equal in all four quantum numbers (n, l, m, s - orbital, angular momentum, magnetic and spin), so that pairs of electrons from different atoms in proximity with overlapping wave-functions interact such that this principle is fulfilled. Exemplary, this can be understood for a simplified one-dimensional slab of a crystal made of atoms with cores at fixed distances (lattice constant, a) with their respective quasi-free electrons with energy $E = (\hbar k)^2/2m$, on an isoenergetic parabolic line in $\vec{k}$ space. Exemplary shown in Figure 2, overlapping energetic states emerge, but since Pauli's exclusion principle must be obeyed this *degeneracy* at the crossing points must be lifted and the accessible states in the $E - k$ diagram split into two levels that are separated by a forbidden energy band. Depending on the finite temperature of the system, electrons occupy these levels according to Fermi-Dirac statistics (shown on the right). If the so-called Fermi level (E_F) lies in this range of inaccessible energies, predominantly levels below ($E < E_F$) are occupied. This is an example of the emergence of a bandgap (E_G) in a semiconductor. Here, states in the lower part are occupied (red, typically called highest-occupied-molecular (HOMO) for molecules and valence band (-maximum) for crystalline solids), whereas additional energy (ΔE, at least E_G) is required for electrons to move across the bandgap to the lowest-unoccupied-molecular-orbital (LUMO) or the conduction band (mininum) or higher. The exact magnitude of the bandgap, form and symmetry of the accessible states – called density-of-states – is fundamentally impacted by the electronic structure of the atoms in the crystal and their arrangement. In reality, many of these more or less parabolic energy bands overlap and form more complicated forms and eventually entire bands of allowed and forbidden energetic states form. For example, the smallest (fundamental) bandgap may lay such that in addition to an energy difference there is also an momentum difference, (Δk, typically provided trough heat, *i. e.* phonons) necessary to transition from one state to another. Herein lies the difference between a direct and an indirect transition. In this context it is worth noting that the above mentioned parabolic form of both the initial and excited states (VB and CB)[4] can be used to derive the effective mass of the electrons/holes as $m^* = 1/\hbar^2\ (\partial^2 E/\partial \vec{k}^2)^{-1}$, often used to quantify how "free" the electrons/holes are in the specific material. Electrons and holes are fermions and as such it follows that they are distributed according to Fermi-Dirac statistics:

$$f(E) = \frac{1}{e^{(E-E_F)/k_B T} + 1} . \tag{5}$$

Within above mentioned parabolas, the electron and hole densities of states are

$$\begin{aligned} D_e(E_e) &= 4\pi \left(\frac{2m_e^*}{h^2}\right)^{\frac{3}{2}} \cdot (E_e - E_C)^{\frac{1}{2}} \\ D_h(E_h) &= 4\pi \left(\frac{2m_h^*}{h^2}\right)^{\frac{3}{2}} \cdot (E_V - E_h)^{\frac{1}{2}} . \end{aligned} \tag{6}$$

---

[4] valence-band and conduction-band

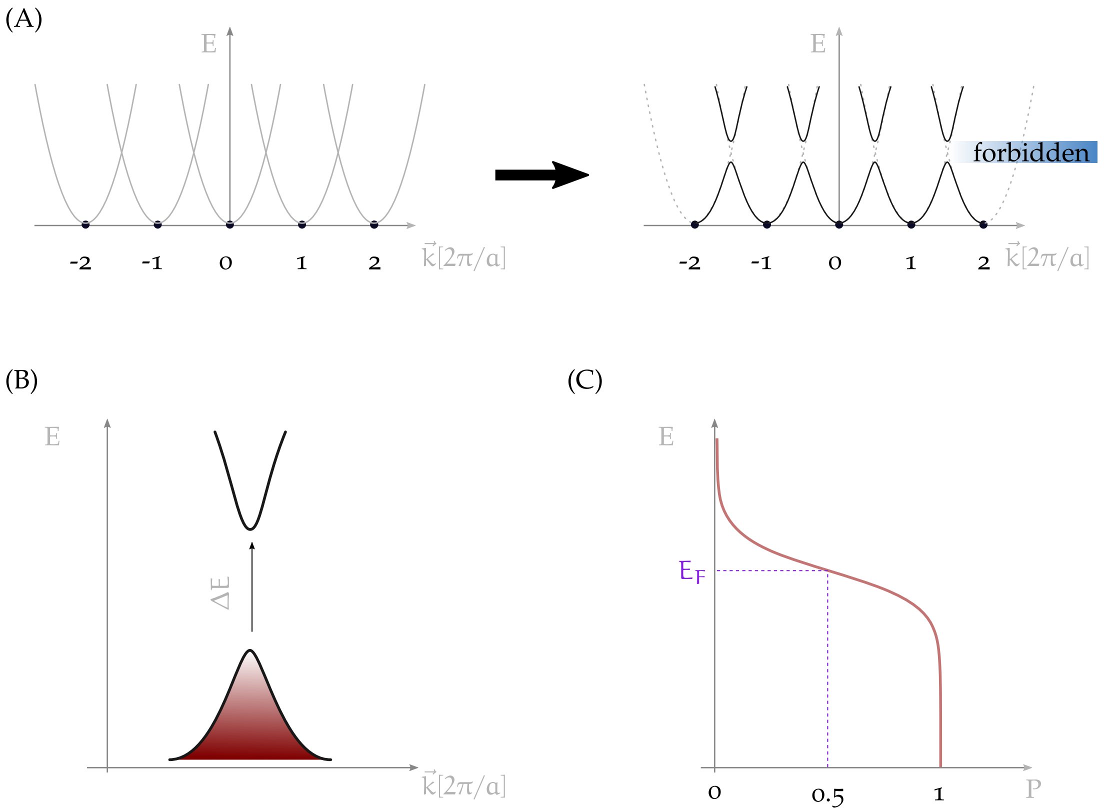

Figure 2: (A) A 1D lattice of nuclei with corresponding quasi-free electron parabolas in $E - k$ space. Due to Pauli's exclusion principle, the degeneracy at the intersects of the periodic parabolas must be lifted and a band of forbidden energies emerges (blue). (B) Simplified representation of a direct bandgap semiconductor in $E - k$ space and (C) an occupation probability distribution for electrons according to Fermi-Dirac statistics (red) ; E_F denotes the energy at which the probability is $P = 1/2$.

where the density of electrons and holes can then be calculated to

$$\begin{aligned} n_e &= \int_{E_C}^{\infty} f(E_e) D_{CB}(E_e)\ dE_e = \underbrace{2\left(\frac{2m_e^* k_B T}{h^2}\right)^{\frac{3}{2}}}_{N_C} e^{-(E_C-E_F)/k_B T} \\ n_h &= \int_{-\infty}^{E_V} [1-f(E_e)] D_V(E_e)\ dE_e = \underbrace{2\left(\frac{2m_h^* k_B T}{h^2}\right)^{\frac{3}{2}}}_{N_V} e^{-(E_F-E_V)/k_B T} \ , \end{aligned} \tag{7}$$

where the effective densities of states (N_C, N_V) are defined and the LAW OF MASS ACTION $(n_e^0 n_h^0 = N_C N_V e^{-(E_C-E_V)/k_B T} = n_i^2)$ with the intrinsic density n_i, that is independent of the Fermi level.

Quasi-Fermi Levels – Electrochemical Potential of Electrons and Holes

The concept of Quasi-Fermi levels can for example be obtained by considering the amount of work charge carriers in a semiconductor can provide externally:

$$\begin{aligned} dU &= \delta Q + \delta W \\ \delta W_{delivered} &= -\delta W = -dF = S\ dT + p\ dV - \mu dN \ . \end{aligned} \tag{8}$$

Assuming that the temperature and the volume of the semiconductor/carrier reservoir is constant $(dT = dV = 0)$, this reduces to $dF = \mu dN = \mu_e dN_e + \mu_h dN_h$, with the chemical potentials

$$\mu_{e/h} = \left(\frac{\partial F_{e/h}}{\partial N_{e/h}}\right)_{T,V=const.} \ . \tag{9}$$

that has to be corrected for the extra energy of a charge in an electrostatic potential rendering the electrochemical potentials $\bar{\mu}$

$$\begin{aligned} \bar{\mu}_e &= -\chi_e + \mu_e - e\ \rho \\ \bar{\mu}_h &= +\chi_h + \mu_e + e\ \rho \ . \end{aligned} \tag{10}$$

Electrons in the conduction band (with $E = E_C$) and holes in the valence band (with $E = E_V$) at comparably low concentrations can be considered to behave like an ideal gas (modified by the respective effective mass)

$$\mu_{e/h} = -k_B T \ln\left[2\left(\frac{2\pi m_{e/h} k_B T}{h^2}\right)^{3/2} \Big/ n_{e/h}\right] \ , \tag{11}$$

so that

$$\begin{aligned} \bar{\mu}_e &= E_C + k_B T \ln\left[\frac{n_e}{N_C}\right] = E_{F,e} \\ \bar{\mu}_h &= -E_V + k_B T \ln\left[\frac{n_h}{N_V}\right] = E_{F,h} \ . \end{aligned} \tag{12}$$

With this the free energy per electron hole pair can be obtained:

$$\begin{aligned} dF &= (\underbrace{\mu_e + \mu_h}_{\mu_{tot.}}) dN = (E_{F,e} - E_{F,h}) dN, \text{ so} \\ \mu_{tot.} &= \frac{dF}{dN} = E_{F,e} - E_{F,h} \ , \end{aligned} \tag{13}$$

which defines the Quasi-Fermi level splitting, the maximum obtainable (free) energy a semiconductor can deliver, when removing dN electrons and holes.

Absorption and Recombination in Semiconductors

Next, the outlined concepts of absorption and emission are adopted to semiconductors, where beyond incomplete absorption and differences in refractive indices, especially the bandgap requires reconsideration, rendering Würfel's generalized Planck law.

THERMAL AND NON-THERMAL RADIATION The solid angles of a semiconductor and the surrounding (*e.g.* air, vacuum) are linked via the refractive index $n_r^2 = \Omega_{air}/\Omega_{SC}$. If a semiconductor is left in the dark in thermal equilibrium with its surrounding the number of electrons and holes is statistically constant ($n_e^0 n_h^0 = n_i^2$) [5] and the generation (G_γ^0) and recombination (R_γ^0) rates are equal, *i.e.* $G_\gamma^0 = R_\gamma^0$, in order to obey the principle of detailed balance/ Kirchhoff's law of radiation. For absorption (emission) of photons $\gamma \rightarrow e^- + h^+$ ($e^- + h^+ \rightarrow \gamma$), both electrons and holes are required so that:

$$G_\gamma^0 = R_\gamma^0 = k_2 \cdot n_i^2 = 4\pi \int_0^\infty n_r^2(E) \cdot \alpha(E) \cdot \frac{2E^2}{h^3 c^2} \cdot \frac{1}{e^{E/k_B T} - 1} \, dE \, , \tag{14}$$

where the right hand side is the so-called VAN ROOSBROECK-SHOCKLEY relation[38]. If additional free charge carriers (n_e, n_h) with their respective Quasi-Fermi levels ($E_{F,e}, E_{F,h}$) are introduced *e.g.* through absorption of light from a light source or injection, additional spontaneous recombination events ($R_{sp,exc}$) due to this *additional* excitation happen and this recombination (one can write this in terms of generation by replacing R with G) is:

$$\begin{aligned} R_{sp,exc} &= R_0 \frac{n_e n_h}{n_e^0 n_h^0} - R_0 = k_2 \left(n_e n_h - \underbrace{n_e^0 n_h^0}_{=n_i^2}\right) \\ &= k_2 \cdot n_i^2 \cdot \left(e^{(E_{F,e} - E_{F,h})/k_B T} - 1\right) = k_2 \cdot n_i^2 \cdot \left(e^{\mu/k_B T} - 1\right) \, . \end{aligned} \tag{15}$$

From above equation the Quasi-Fermi level splitting (QFLS, μ) can be identified, which is the maximum work a semiconductor/solar cell can deliver externally per electron-hole pair, as outlined before. Würfel[39] was then able to demonstrate, that the concept of Equation 4 can be generalized to include absorption/emission for both thermal and non-thermal radiation for real non-black bodies (including semiconductors) rendering WÜRFEL'S GENERALIZED PLANCK LAW, expressed here in the form of an emitted photocurrent (spectral):

$$dj_\gamma(E) = a(E) \frac{\Omega_{em} E^2}{4\pi^2 \hbar^3 c^2} \left[e^{(E - \mu_\gamma)/k_B T} - 1\right]^{-1} dE \, , \tag{16}$$

where he concluded, that the difference in (electron/hole) Quasi-Fermi levels – as seen above – can be identified as the chemical potential of the absorbed/emitted photons in the case of semiconductors, while likewise covering the cases of grey/black bodies - thus general. Notably, Equation 16 directly links the maximum obtainable μ, to the amount of absorbed/emitted photons.

Nonradiative Recombination

In real solar cells the above mentioned types of radiative recombination (*i.e.* thermal and non-thermal), which go through the same "channels" are not the only ways through which excited electron-hole pairs can dissipate their energy, but there are additional types of recombination that can happen. In principle there are at least two more types: Auger- and Shockley-Read-Hall recombination.

---

[5] n_e^0 : electron density; n_h^0 : hole density; n_i : intrinsic carrier density

AUGER RECOMBINATION Auger Recombination can be understood as a form of electron-electron ionization, where *e. g.* one electron kicks an already excited electron to a higher energetic state (within the CB), while recombining nonradiatively with an hole. Since this requires carrier concentrations higher than typically attained under solar illumination[6], this process will not be treated in greater detail, except for pointing out that the process involves three particles - namely two electrons and one hole or vice versa two holes and one electron - and therefore the recombination proceeds proportional to the density of $n^2 \cdot p$ or $p^2 \cdot n$.[7]

SHOCKLEY-READ-HALL RECOMBINATION The third type of recombination is mediated by impurities that are electronically active and *trap* electrons or holes, depending on their energy relative to the conduction band minimum or valence band maximum. This recombination is commonly refereed to as *trap-assisted* or SHOCKLEY-READ-HALL RECOMBINATION after their discoverers. Interestingly this process happens likewise also in a dark sample and, as a consequence, there is likewise a dark trap-assisted generation, where phonons in the semiconductor excite a small portion of relaxed electrons into the traps and from there into the conduction band. This fraction ($G_{e/h,trap}$) is however typically very small in the dark. For electrons (n_e), holes (n_h) and traps (n_t, here *e. g.* traps are filled with electrons and then depleted when additionally a hole is trapped) the population changes according to the set of (dependent) coupled rate equations:

$$\begin{aligned}\partial_t n_e &= G_{abs.} - R_{rad.} - R_{e,trap} + G_{e,trap} \\ \partial_t n_h &= G_{abs.} - R_{rad.} - R_{h,trap} + G_{h,trap} \\ \partial_t n_t &= R_{e,trap} - R_{h,trap} - G_{e,trap} - G_{h,trap} \ ,\end{aligned} \tag{17}$$

as defined in Figure 3, where G denotes the generation rate from absorption of light ($G_{abs.}$) or re-emission of trapped electrons/holes from a trap back to the conduction/valence band ($G_{e/h,trap}$), $R_{rad.}$ radiative recombination and $R_{e/h,trap}$ trapping of electrons/holes. With the assumption that the semiconductor obeys charge neutrality (*i. e.* $q \cdot (n_t - n_e + n_h) = 0$)[37] another (third) linearly independent equation can be derived and the set of three variables (n_e, n_t, n_h) can be solved. Starting from a dark case in thermal equilibrium (*i. e.* $G_{abs.} = R_{rad.} = 0$, $\partial_x T = 0$) the populations do not change over time, so $\partial_t n_e = \partial_t n_h = \partial_t n_t = 0$. In the simplest form the trap recombination rate ($R_{e,trap}$) of electrons will depend on electrons being present ($\propto n_e$), them coming into the proximity of the trap ($\propto \sigma_e$, called capture cross section), the number of attempts ($\propto \nu_e$, expressed in form of a (thermal) velocity)) and how many of the total available traps (N_t) are free ($\propto (N_t - n_t)$). Likewise the dark electron generation requires the traps to be populated so ($G_{e,trap} \propto n_t$) and so:

$$\partial_t n_e = -\sigma_e \nu_e (N_t - n_t) n_e + \underbrace{\beta_e \cdot n_t}_{G_{e,trap}} = 0 \ . \tag{18}$$

Electrons (n_e) and trapped electrons (n_t) in thermal equilibrium are distributed according to Fermi-Dirac statistics, so $n_t = N_t \frac{1}{e^{(E_t - E_F)/k_B T} + 1}$ and $n_e = N_C \frac{1}{e^{(E_C - E_F)/k_B T} + 1} \approx N_C \cdot e^{-(E_C - E_F)/k_B T}$ and so :

$$n_t = N_t \frac{1}{\beta/(\sigma_e \nu_e n_e) + 1} = N_t \frac{1}{e^{(E_t - E_F)/k_B T} + 1} \tag{19}$$

from where it follows that $\beta_e = \sigma_e \nu_e N_C \cdot e^{-(E_C - E_t)/k_B T}$ and analogous $\beta_h = \sigma_h \nu_h N_V \cdot e^{-(E_t - E_V)/k_B T}$. For an uncontacted semiconductor in equilibrium between generation and recombination at low light intensities ($R_{rad.} \approx 0$) rearrangement of Equation 17 yields:

$$G = R_{total} = \frac{n_e n_h - n_i^2}{\frac{n_e + N_C\ e^{-(E_C - E_t)/k_B T}}{N_t \sigma_h \nu_h} + \frac{n_h + N_C\ e^{-(E_t - E_V)/k_B T}}{N_t \sigma_e \nu_e}} \ , \tag{20}$$

---

[6] Si solar cells however suffer from relatively strong Auger recombination, which limits their applicability in concentrator devices

[7] for homogeneous n&p a singular carrier density n can be used and the recombination is $\propto n^3$

where one can define individual SHOCKLEY-READ-HALL lifetimes for electrons and holes ($\tau_{SRH,x} = (N_t\ \sigma_x\ v_x)^{-1}$). The simplest case of mid-gap traps ($E_t = 1/2(E_C - E_V)$), symmetrical densities of states ($N_C = N_V$) and excitation ($n_e = n_h = n \gg n_i$), as well as capture cross sections and thermal velocities ($\sigma_e = \sigma_h, v_e = v_h$) renders a much simpler expression:

$$G = R = n/\tau_{SRH} = k_{SRH}\ n \tag{21}$$

from where it is convenient to define a rate constant $k_{SRH} = (\tau_{SRH})^{-1}$.

SURFACE RECOMBINATION A special type of Shockley-Read-Hall recombination proceeds at the surfaces of a semiconductors. Due to the finite dimensions of any real device the semiconducting material must have a surface, where *e.g.* dangling bonds exist. These are by definition crystal imperfections and most often charged, attracting electrons or holes. As such, they act as recombination sites, similar to the bulk imperfections mentioned above, but - since their chemical nature may be very different - with an own capture cross section (σ_S) and a different *surface* density (N_S, the unit is 1/area as compared to 1/volume) and thus a surface recombination velocity (S) can be defined, rendering a surface recombination rate:

$$R_{surface} = \underbrace{\sigma_S\ N_S\ v_e}_{S}\ n\ , \tag{22}$$

which is expressed in units of inverse area and time, *e.g.* $(cm^2 s)^{-1}$. For this recombination to proceed carriers must first diffuse to the surface, so that the thickness (d) and the diffusivity (D) of the material will play an additional role in defining the surface recombination rate

$$k_{surface} = \left[\frac{4d^2}{\pi^2 D} + \frac{d}{S}\right]^{-1}\ , \tag{23}$$

where the first term accounts for the time it takes to diffuse to the surface and the second for the actual recombination.
Together, bulk (SRH) and surface recombination form the total first order recombination, expressed by the first order recombination coefficient (rate) k_1:

$$k_1 = \frac{1}{\tau_{SRH}} + \left[\frac{4d^2}{\pi^2 D} + \frac{d}{S}\right]^{-1}\ , \tag{24}$$

which enters the overall rate Equation 26 below.

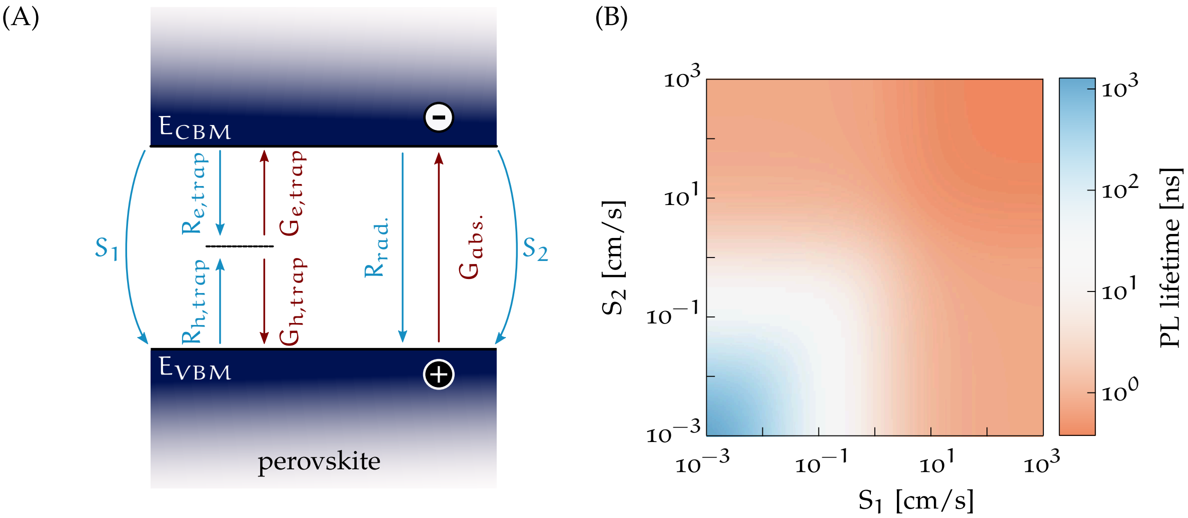

Figure 3: (A) Energy band diagram of a semiconductor (*e.g.* perovskite) with indicated generation (red) and recombination (blue) processes. (B) Expected carrier lifetime for balanced diffusivity ($D = 2.5\text{cm}^2/\text{s}$) a thickness ($d = 450\text{nm}$) and a bulk SRH lifetime of 1000ns as a function of surface recombination velocities ($R_{surf.} \neq S$) at two surfaces (S_1, S_2 *e.g.* left & right).

Overall Recombination Dynamics

On the basis of the aforementioned recombination processes a generic set of coupled rate equations for a 1D slab of semiconductor, including all generation and recombination processes can be obtained:

$$\begin{aligned}
\partial_t n_e(x) &= G_{abs.}(x) + G_{e,trap}(x) - R_{rad.}(x) - R_{e,trap}(x) - R_{e,Auger}(x) + D_e \frac{\partial^2 n_e(x)}{\partial x^2} \\
\partial_t n_h(x) &= G_{abs.}(x) + G_{h,trap}(x) - R_{rad.}(x) - R_{h,trap}(x) - R_{h,Auger}(x) + D_h \frac{\partial^2 n_h(x)}{\partial x^2} \\
\partial_t n_t(x) &= R_{e,trap}(x) - R_{h,trap}(x) - G_{e,trap}(x) - G_{h,trap}(x)\ .
\end{aligned} \tag{25}$$

For the sake of completeness inhomogeneous carrier profiles ($n_i(x)$) and as a consequence thereof diffusion $\left(D \frac{\partial^2 n_i(x)}{\partial x^2}\right)$ is also introduced. Yet again charge neutrality is a prerequisite to solve these equations, but with a few simple assumptions this set of equations can be drastically reduced to a singular rate equation. As such, we need to assume that electrons and holes have similar diffusion constants ($D_h = D_e$), traps recombination is dominated by a mid-gap states (on average only weakly populated, *i.e.* $N_t \gg n_t(t) = \text{constant}$), and surface recombination (*i.e.* all trap assisted/ surface recombination is convoluted into one single k_1) is symmetrical. Likewise for sufficiently homogeneous excitation or after a short time, homogeneous profiles are obtained $\left(G(x) := G, \frac{\partial^2 n_i(x)}{\partial x^2} = 0\right)$. With these assumptions a simplistic singular empiric rate equation can be derived as simple superposition of all individual recombination and generation processes:

$$\frac{d}{dt} n = G \underbrace{- k_1\, n - k_2\, n^2 - k_3\, n^3}_{-R}\ , \tag{26}$$

where the partial derivative can be replaced by a total derivative because n does no longer depend on the position x. At first this seems like a big set of assumptions that needs to be justified and the general approach outlined above is certainly less error-prone. However, determining all the individual properties and consequently rate coefficients is experimentally often challenging or even not possible, nor necessary. For example, the material system studied in this thesis (*i.e.* halide perovskites) allows to make these assumptions, as will be outlined in Section 1.4. In equilibrium, where $dn/dt = 0$ and consequently $G = R$, the fraction any of these processes contribute to the total recombination process can be calculated. For example the efficiency of radiative recombination in comparison to the total recombination is quantified with the photoluminescence quantum yield – PLQY:

$$\mathrm{PLQY} = \frac{k_2 \cdot n^2}{k_1 \cdot n + k_2 \cdot n^2 + k_3 \cdot n^3} = \frac{\phi_{PL}}{\phi_{abs.}} \; . \tag{27}$$

On the basis of Würfel's generalized Planck law, (Equation 16), a neat equation that allows to calculate the Quasi-Fermi level splitting from the measurement of the number of emitted versus absorbed photons can be derived:

$$\mu = k_B T \cdot \ln \left[\underbrace{\frac{n_{photon,em.}}{n_{photon,abs.}}}_{=\mathrm{PLQY}} \frac{J_G}{J_{dark,rad.}} \right] = k_B T \cdot \left(\ln\left[\mathrm{PLQY}\right] + \underbrace{\ln \left[\frac{J_G}{J_{dark,rad.}} \right]}_{\mu_{rad.}/k_B T} \right) \; , \tag{28}$$

where a high PLQY naturally emerges as a figure-of-merit when trying to maximize μ and the second term on the right-hand-side of the equation denotes the maximum obtainable QFLS in the limit of PLQY=1, thus called RADIATIVE LIMIT - $\mu_{rad.}$, which will be derived next.

1.2 THERMODYNAMIC LIMITATIONS OF ENERGY CONVERSION

Solar energy conversion devices under illumination can convert only a fraction of the incoming energy, these losses and consequently fundamental limitations are outlined along [40, 41]. Sources for losses are manifold but can be categorized in thermalization of absorbed photons with $E > E_G$, entropic losses due to the sun's small solid angle *vs.* the device's emission angle, incomplete absorption, Carnot(-like) losses due to the temperature difference between the sun and the device, and finally emissive losses - a small fraction of light is lost, because in order to fulfill detailed balance, even for non-black bodies any absorber must likewise emit photons[39–43]. These losses depend on the nature of the absorber versus temperature of the sun and corresponding illumination spectrum. On earth, with illumination by our sun, when considering an AM 1.5G spectrum one can calculate each of these loss terms on the basis of generalized Planck's law (assuming first $a(\hbar\omega) = 1$ above a threshold of $\hbar\omega_G := E_G$) with a (particle) current J per solid angle Ω and energy quanta dE

$$J(E, T, \mu, \Omega) = \frac{1}{q} \underbrace{\frac{2\Omega}{h^3 c^2} \frac{E^2}{e^{(E-\mu)/k_B T} - 1}}_{\phi_{BB,T}(E,\mu)} \approx \frac{1}{q} \frac{2\Omega}{h^3 c^2} \cdot E^2 \cdot e^{-(E-\mu)/k_B T} \; . \tag{29}$$

Here, q is the elementary charge, h Planck's constant, E photon energy, μ the chemical potential, k_B is the Boltzmann constant and T the temperature of the given black body with an emission flux $\phi_{BB,T}(E, \mu)$. The approximation in the right part of the equation is called Boltzmann approximation and a simplification (*i.e.* $e^x - 1 \approx e^x$), accurate for $E - \mu \gg k_B T$. Hence, for two black bodies that exchange particles with energy - *e.g.* photons - the net currents according to detailed balance of absorbed an emitted photons sums up to

$$J_{tot} = \int_{E_G}^{\infty} J(E, T_S, 0, \Omega_{absorbed}) \, dE - \int_{E_G}^{\infty} J(E, T_A, \mu, \Omega_{emitted}) \, dE \; . \tag{30}$$

Considering that power is the product of current and potential (for now we assume the inner and outer chemical potential is equal: $\mu = qV$, this will be discussed in Figure 1.3) an conversion efficiency (η) can be calculated:

$$\eta = \frac{JV}{P_{in}} \tag{31}$$

with

$$P_{in} = \int_0^{\infty} E\,\frac{1}{q}\,J(E, T_S, 0, \Omega_{absorbed})\,dE \tag{32}$$

being the power provided by the sun. When looking for the maximum conversion efficiency versus photon energy, we deduce two partial differential equations:

$$\left(\frac{\partial\eta}{\partial E_G}\right)_{\mu=const.} = 0 \tag{33}$$

$$\left(\frac{\partial\eta}{\partial\mu}\right)_{E_G=const.} = 0\,. \tag{34}$$

With the Boltzmann approximation the integrals in Equation 30 are analytically solvable and Equation 33 renders a relation for the maximum power (point) potential

$$q\mu_{MPP} = E_G \underbrace{\left(1 - \frac{T_A}{T_S}\right)}_{\text{Carnot-like loss}} - T_A \underbrace{k_B \ln\left(\frac{\Omega_{emitted}}{\Omega_{absorbed}}\right)}_{=\Delta S,\text{ entropic loss}}\,. \tag{35}$$

Here, two loss factors can be seen, a Carnot-like[8] loss due to a temperature difference between radiation field and solar cell and an entropic loss, due to different solid angles of emission and absorption. Likewise, by setting Equation 30 equal to zero one can derive *qua definition* the open-circuit voltage/potential (V_{OC}/μ_{OC}) as:

$$qV_{OC} = \underbrace{E_G\left(1 - \frac{T_A}{T_S}\right) - k_B\,T_A \ln\left(\frac{\Omega_{emitted}}{\Omega_{absorbed}}\right)}_{\mu_{MPP}} + T_A \underbrace{k_B \ln\left(\frac{\xi(E_G, T_S)}{\xi(E_G, T_A)}\right)}_{\Delta S,\text{ entropic gain}}\,, \tag{36}$$

where

$$\xi(E_G, T_i) = \frac{2k_B T_i}{h^3 c^2}\left(E_G^2 + 2k_B T_i E_G + 2k_B^2 T_i^2\right)\,. \tag{37}$$

The additional term when going from μ_{MPP} to μ_{OC} can be understood as an entropic "gain" in free energy, stemming from 1. the finite temperature difference between the sun and the absorber and 2. under the condition of open circuit there is a loss in information/direction, since net no carriers leave the semiconductor. In turn, the excited carrier population will actually cool and heat the lattice net transferring entropy into the latter to overall obey the second law of thermodynamics. Analogously, the maximum obtainable current (J_{max}) and the maximum power (point) current (J_{MPP}) can be calculated as:

$$J_{max} = \int_{E_G}^{\infty} J(E, T_S, 0, \Omega_{absorbed})\,dE \tag{38}$$

and

$$J_{MPP} = \int_{E_G}^{\infty} J(E, T_S, 0, \Omega_{absorbed})\,dE - \int_{E_G}^{\infty} J(E, T_A, \mu_{MPP}, \Omega_{emitted})\,dE\,. \tag{39}$$

At this point the concept of fill-factor (FF) may be introduced that represents a figure-of-merit, as it quantifies the fraction of actually usable power versus internally generated power.

$$FF = \frac{J_{MPP}\,\mu_{MPP}}{J_{max}\,\mu_{OC}} \tag{40}$$

With these equations at hand, one can calculate the efficiency and corresponding losses as a function of bandgap and - essentially cutting a vertical line at the optimal bandgap - of a perfect solar cell at

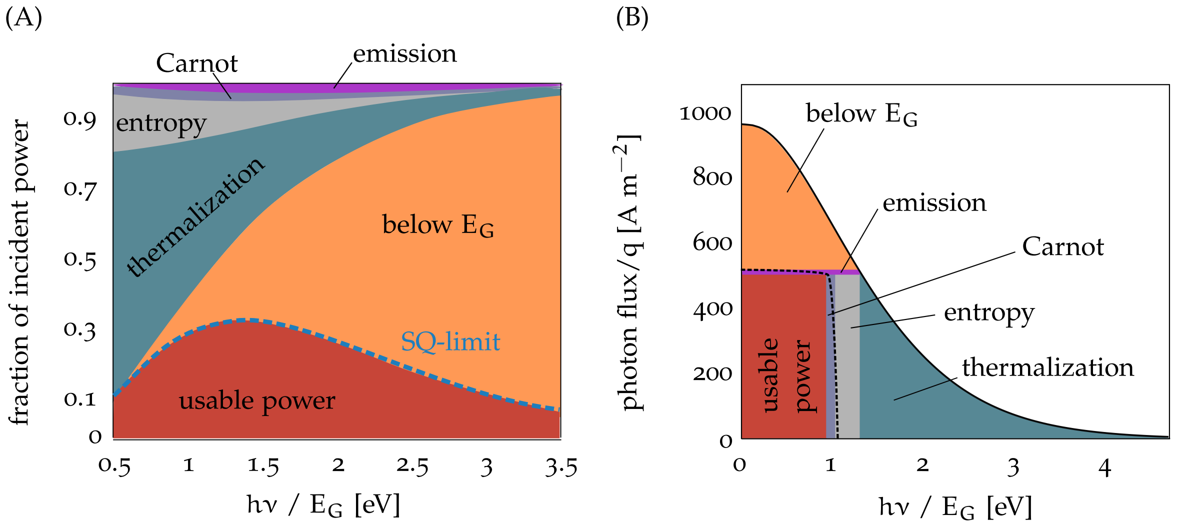

Figure 4: (A) Fraction of incident power, split into usable power as well as losses due to below E_G excitation, thermalization, entropy losses, black body (-like) losses and radiative losses. In comparison the calculated SQ-limit. (B) Dissection of these losses for the optimal bandgap solar cell. Calculated along [40].

e.g. 300°K illuminated by the sun (simplification: black body at T_S = 5700°K) as shown in Figure 4. In an alternative, slightly simpler approach William Shockley and Hans Queisser reported/established a bandgap dependent limitation of efficiency, now commonly referred to as Shockley-Queisser limit (SQ-limit) on the basis of three fundamental assumptions: 1. detailed balance is fulfilled, 2. absorption above the bandgap has unity efficiency and generates one electron-hole pair per photon, and 3. photogenerated carriers have unity collection efficiency. Assumption 1 entails that the even in the dark, any black body is in thermal equilibrium with its surrounding and that all generated carriers recombine and re-emit their energy. In current representation this can be written as $J_{total} = 0 = J_{gen} - J_{rec}$ analogous to Equation 30. Here, the radiation by the solar cell is that of a non-black body (also referred to as grey body) with an emitted areal photon flux $\phi_{BB,T}$, according to the generalized Planck's law and hence the recombination current in the dark (J_0) is

$$J_0 = q \cdot \int_{E_G}^{\infty} \phi_{BB,T}(E)\ dE\ . \tag{41}$$

Würfel expanded this approach by adding an non-equilibrium term accounting for an applied bias, rendering:

$$J_{rec}(V) = J_0 \cdot e^{qV/k_B T} \tag{42}$$

at low voltages. The total current absorbed by an optimal solar cell at a given bandgap is in accord with Equation 38 and assumption 2 & 3:

$$J_G = J_{SC} = \int_{E_G}^{\infty} J(E, T_S, 0, \Omega_{absorbed})\ dE \tag{43}$$

where this current is of opposing direction as the current is emitted by the solar cell, rendering a total current of

$$J(V) = J_0 \cdot \left(e^{qV/k_B T} - 1\right) - J_G \tag{44}$$

---

[8] it is not a "clean" Carnot loss, as a semiconductor is not a "clean" Carnot machine, unless one would illuminate monochromatically with exactly E_G[41]

the so-called Shockley-diode equation. Numerically computing the maximum obtainable power ($J(V, E_G) \cdot V$) for any given bandgap compared to incoming (solar) power renders the infamous SQ-limit, as can be seen in Figure 4. Again we can derive a (different) representation for the open-circuit voltage (V_{OC}), where the total current is set to zero.

$$V_{OC} = \frac{k_B\,T}{q} \ln\left(\frac{J_G}{J_0} + 1\right) . \tag{45}$$

Both derivations of maximum attainable efficiency are in close agreement, since they rely on the same fundamental assumptions. Likewise, the different mathematical expressions for VOC/μ_{OC} (Equation 36 and Equation 45) each have advantages. *E.g.* Equation 45 allows to identify that V_{OC} is (almost) proportional to temperature and logarithmically dependent on the generated current, whereas Equation 36 nicely displays, how concentrator solar cells (reduction of $\Omega_{absorbed}$) work and that optical EMISSION management (increase of $\Omega_{emitted}$) can improve the efficiency of a solar cell. Irrespective of the representation, even at the optimum E_G of 1.34eV a perfect device can only convert a third (33.6%) of the incoming energy into electrical power and the best certified efficiencies for single-junction solar cells are 29.1% for GaAs at a bandgap of 1.37eV, considered to be at the *practical* limit[9]. Solar cells based on other semiconductor (combinations) such as Si, CdTe, CZTS (kesterites), $CuIn_xGa_{1-x}Se_2$ (CIGS/Se), organic semiconductors or halide perovskites operate at lower efficiencies (compared to the SQ-limit at their respective bandgap). In the following, different loss mechanisms are discussed.

1.3 DESCRIPTION OF POWER LOSSES IN SOLAR CELLS

In the forgoing section thermodynamic limitations of ideal solar cells were discussed. Unfortunately, real solar cells suffer from additional power losses such as unwanted recombination, imperfect absorption, finite refractive indices or electrical transport limitations, either of which reduce the actual power output. In the framework of the Shockley equation (44) additional terms have been introduced to account for imperfections of real solar cells. For example the diode equation was extended to include series and shunt resistance, to convey carrier transport limitations (R_{series}) and internal short circuits parallel to the actual diode (R_{shunt}), as well as introducing an ideality factor (n) and additional (nonradiative) currents $J_{0,nr}$ to account for unwanted recombination.

$$J(V) = \underbrace{(J_{0,r} + J_{0,nr})}_{J_0} \cdot \left(e^{\frac{V+J\,R_{series}}{n\,k_B\,T}} - 1\right) + \frac{V + J\,R_{series}}{R_{shunt}} - J_G . \tag{46}$$

In Figure 5 the impact of introducing R_{series} and R_{shunt} for variable values (as indicated) is visualized on the basis of a perfect semiconductor with a bandgap of 1.62eV. The R_{series} impacts primarily the FF as an additional resistance in the device will entail that a fraction of the V_{MPP} is dropped across this additional resistor, while at V_{OC} no net current flows, thus additional resistance has no impact. In fact, external ultrahigh resistors are commonly used to determine V_{OC} precisely in the first place. The short circuit current (J_{SC}) is reduced by a factor $\left(1 - \frac{R_{series}}{R_{shunt}}\right)$. A low R_{shunt} signifies that there is a parallel Ohmic connection between the device's electrodes - called shunt - through which a portion of the carriers recombines in parallel to the actual diode and loose their energy only through resistive heating of the R_{shunt} - occasionally this is used to burn through existing shunts in *e.g.* LEDs. R_{shunt} firmly changes the overall form of a typical JV curve by removing the rectifying behavior of the diode, which initially reduces the inherent resistance (thus increases the slope at voltages $V \leqslant V_{MPP}$) implying a reduction of J_{MPP} and even the short circuit current (J_{SC}) as noted above by a factor $\left(1 - \frac{R_{series}}{R_{shunt}}\right)$. In extreme cases a significant amount of the

---

[9] The term is a bit ambiguous, I would interpret it as : the benefit from further improvements is probably not worth the investment, especially w.r.t. industrial applications

current will flow through the shunts, which then likewise reduces the ability to accumulate charges and build up a voltage (precisely V_{OC}), even if there is no net current.

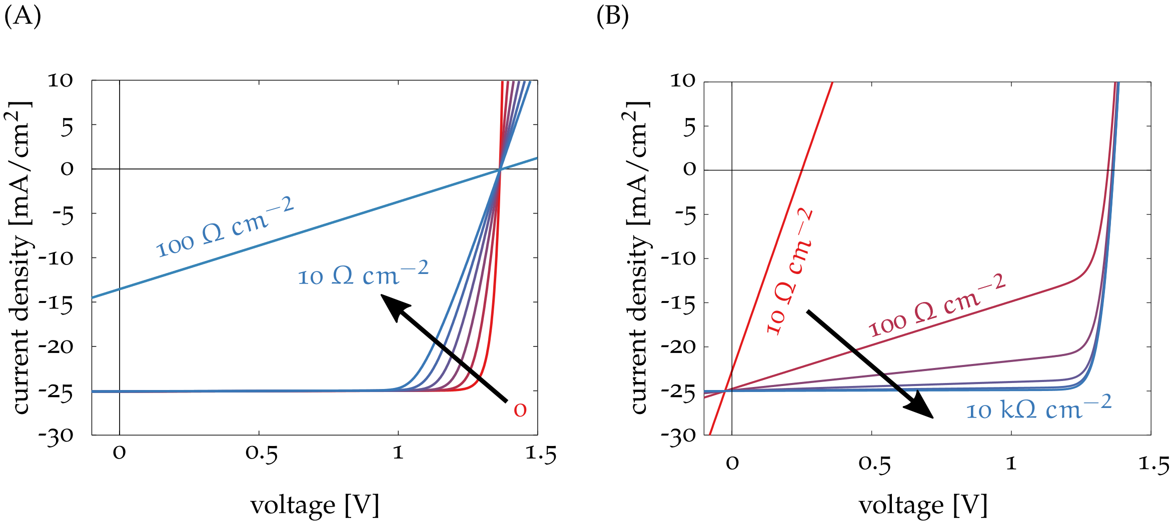

Figure 5: (A) Impact of series resistance (R_{series}) and (B) shunt resistance (R_{shunt}) on simulated JV curves.

In an attempt to model JV characteristics obtained from measurements of real solar cells, an additional factor was introduced, which allows to vary the steepness of the exponential term in the diode equation and thereby quantify how IDEAL the respective device is, thus the name IDEALITY FACTOR - n. Empirically, solar cells with an ideality factor > 1 exhibit additional recombination - *e.g.* due to crystal imperfections - entailing a much higher dark recombination current. In a purely mathematical description, a higher ideality factor (while maintaining J_0 fixed) would be preferable[10], but is in reality probably impossible. As discussed before, J_0 – in particular $J_{0,rad.}$ – is a consequence of the solar cell emitting light at a given temperature T at all wavelengths it can likewise absorb. As temperatures change (*e.g.* winter versus summer) the solar cell in thermal contact with its surrounding will therefore cool down or heat up. Figure 6 displays the effect, the temperature of the solar cell and the ideality factor have on its JV curve and consequently power output, both primarily impacting the V_{OC} through a higher dark recombination current. In reality, the FF may likewise be strongly depending on temperature, since carrier mobilities are typically temperature-dependent material properties. An example would be the thermally activated transport in organic semiconductors increasing the mobility at higher temperatures versus higher electron-phonon scattering reducing mobilities in inorganic semiconductors with band-like transport.

---

[10] The FF actually increases from a purely mathematical point-of-view, since the recombination current would increase more slowly

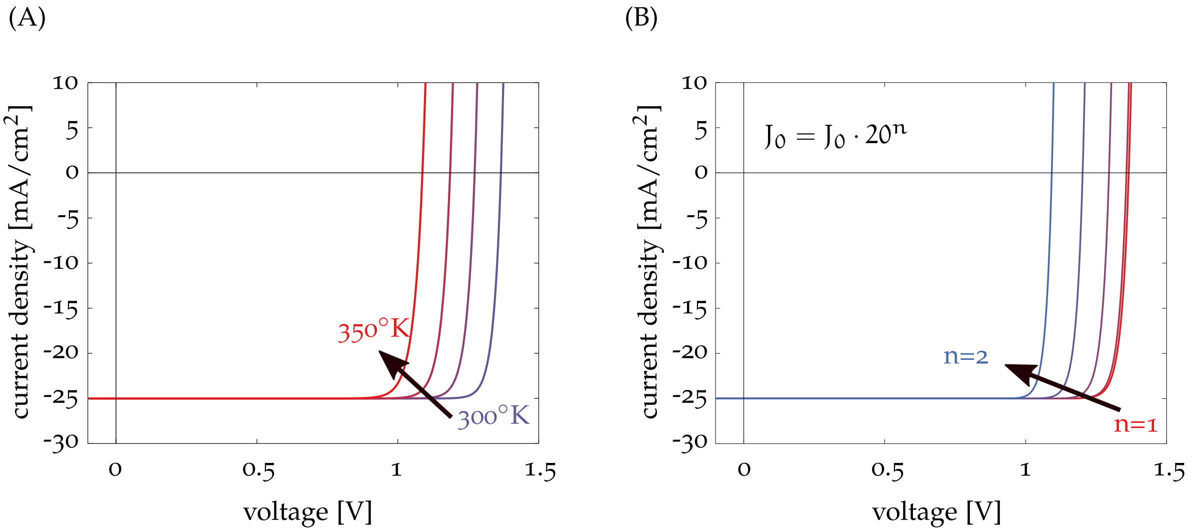

Figure 6: (A) Impact of solar cell temperature (T_A) and (B) ideality factor (n) on simulated JV curves. In panel (B) n artificial non-linearity 20^n as indicated was introduced at random, which is supposed to reflects that devices with an ideality factor different from 1 exhibit substantially higher J_0 due to additional recombination.

Reciprocity in Solar Cells

In analogy to Equation 27 for the luminescence efficiency upon photo excitation - thus PLQY - carriers can also be injected into a solar cell/ light-emitting-diode (LED) and a natural definition of *electroluminescence* (EL) and a corresponding quantum yield thereof can be defined in terms of currents as

$$\mathrm{ELQY}(V) = \mathrm{EQE}_{\mathrm{EL}}(V) = \frac{J_{\mathrm{em.}}(V)}{J_{\mathrm{inj.}}(V)} = \frac{J_{\mathrm{em.}}(V)}{J_{\mathrm{em.}}(V) + J_{\mathrm{nr.}}(V)} \,, \tag{47}$$

where we assume that the emission stems from excess carriers with a potential $\mu = qV$ and analogous to Equation 42

$$J_{\mathrm{em.}}(V) = J_{\mathrm{em.},0}\left(e^{qV/k_B T} - 1\right) \,. \tag{48}$$

Rau[43] translated the theory of detailed balance into the realms of solar cell properties rendering the optoelectronic RAU RECIPROCITY RELATION, (RRR):

$$J_{\mathrm{em.},0} = q\,\phi_{\mathrm{emission},0} = q \int \mathrm{EQE}_{\mathrm{PV}}(E)\,\phi_{\mathrm{BB}}(E)\,dE \,. \tag{49}$$

Combining this with equations 47 and 48 at a specific voltage (*e.g.* the open-circuit voltage - V_{OC}, with

$$J_{SC} = q \int \mathrm{EQE}_{\mathrm{PV}}(E)\,\phi_{\mathrm{Sun}}(E)\,dE \,, \tag{50}$$

allows

$$V_{OC} = \frac{k_B T}{q} \cdot \ln\left[\mathrm{EQE}_{\mathrm{EL}} \frac{J_{SC}}{J_{\mathrm{em.},0}}\right] = \frac{k_B T}{q} \cdot \left(\underbrace{\ln(J_{SC}/J_{\mathrm{em.},0})}_{V_{OC}^{\mathrm{rad.}}/kT/q} + \underbrace{\ln(\mathrm{EQE}_{\mathrm{EL}})}_{\Delta V_{OC}/kT/q}\right) \,, \tag{51}$$

which is the analogy to Equation 28, detailing the balance between absorption and emission as a means to quantify the maximum obtainable potential energy (here a voltage) and losses due to nonradiative recombination. This relation relies on the premise that excess/injected carriers at the electrodes ($\Delta n_{e/h}(0/d)$) and the carriers within the device ($(n_{e/h}(\vec{x})$) are in equilibrium and connected to one another through a function

$$f(\vec{x}) = \frac{\Delta n_{e/h}(\vec{x})/n^0_{e/h}(\vec{x})}{\Delta n_{e/h}(0/d)/n^0_{e/h}(0/d)}\,, \tag{52}$$

and that this holds simultaneously for *both* collection ($f_c(\vec{x})$) (of absorbed) and injected ($f_i(\vec{x})$) carriers - the so-called Donolato theorem. For efficient solar cells the latter holds true, especially if the layer thickness ≈ diffusion lengths of carriers, but in some LEDs, layers adjacent to the emission layers are chosen such that injection and extraction are not balanced through a single function $f(\vec{x})$, but typically $f_c(\vec{x}) < f_i(\vec{x})$. Similarly, there are systems with low and/or imbalanced electron/hole mobilities, where collection is hampered and RRR may not be applicable. Altogether, radiative efficiency for both electroluminescence (Equation 47) and photoluminescence (Equation 27) or more generally external radiative efficiency (ERE) are key when aiming for a low voltage deficit (ΔV_{OC}) and thus high open-circuit voltage, as can be seen in Figure 7 for record solar cells based on different materials.

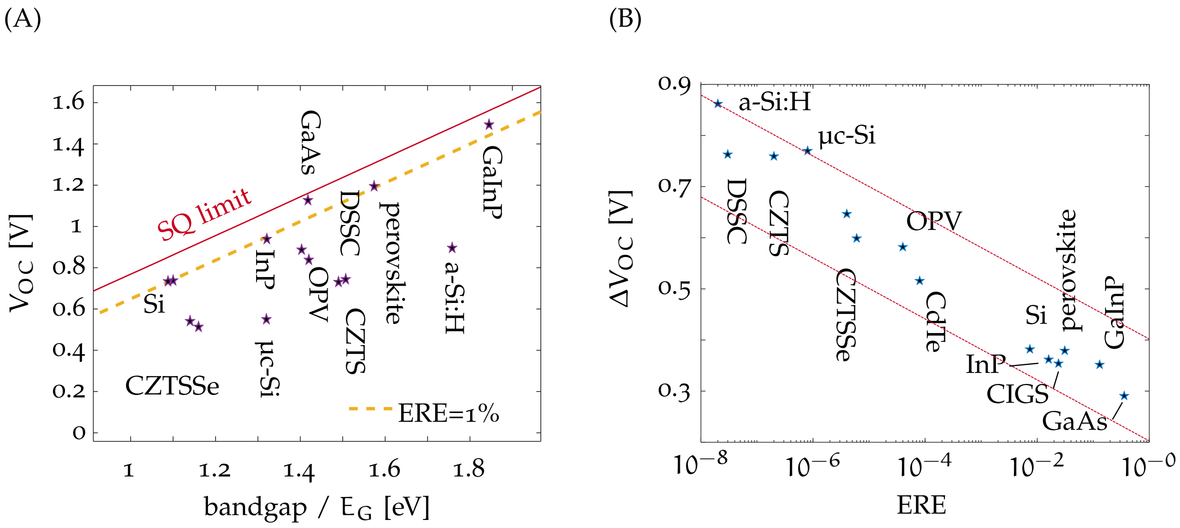

Figure 7: (A). V_{OC} of different record solar cell materials with varying bandgap (stars) as well as the SQ-limit (red) and the SQ limit with an external radiative efficiency of 1% (yellow). (B) Voltage deficit versus the bandgap as a function of radiative efficiency for different record devices. The red lines are guides to the eye parallel to $k_B T/q \ln(\mathrm{ERE})$. Reproduced from [44].

1.4 HALIDE PEROVSKITES

Perovskites with the generic chemical formula ABX_3 are a class of materials based on the crystal structure of calcium titanate ($CaTiO_3$), which was discovered 1839 by Gustav Rose and named after Lew Alexejewitsch Perowski. A broad range of materials with an even broader range of physical properties can be found in nature or synthesized. Examples include $SrTiO_3$ (simultaneous electron and ion conductor), $CaCO_3$ (birefringence) or $YBa_xCu_{1-x}O_3$ (depending on the Ba/Cu ratio insulating or high-T superconductor). Man-made perovskites with halides on the X-site and organic cations methylammonium ($CH_3NH_3^+$) on the A-site were first discovered in the late 1970's by Dieter Weber[45, 46], who already described their semiconducting (Pb-based) to semi-metallic (Sn-based) behavior. Here, typically A is a monovalent cation, B a divalent metal and X a monovalent anion. Following the initial discovery, halide perovskites were studied in depth by Mitzi and coworkers[20, 23, 47, 48]. The majority of today's most widely used deposition techniques such as solution-based deposition, two-step deposition (including dip conversion) or thermal evaporation were already then explored to produce both three-dimensional and layered two-dimensional halide perovskites which were employed as active layers for optoelectronic devices such as field-effect transistors. Despite these encouraging results, the instability - especially w.r.t. moisture - retarded further progress. Only after the first demonstration of solar cells in 2009 by Myasaka and coworkers and finally after the transition to solid-state transport layers a whole new research field developed. Today organic/inorganic perovskite are among the most studied material systems in optoelectronics. The majority of studied systems are based on the generic structure ABX_3, where typically employed constituents are A = Rb^+, Cs^+, FA^+ (formamidinium), MA^+ (methylammonium)...; B = Ge^{2+}, Sn^{2+} and Pb^{2+} as well as X = I^-, Br^-, Cl^-. The compositional space spanned by these constituents is enormous and only mildly limited due to *e.g.* restricted space within a crystal lattice, which can be described by the Goldschmidt tolerance factor

$$t = \frac{r_A + r_X}{\sqrt{2} \cdot (r_B + r_X)} , \tag{53}$$

where r_i is the ionic radius of the respective ions on A,B and X-sites. Empirically, stable three-dimensional perovskites were obtained for $t \in [0.8, 1]$, however recent findings suggest that a modified tolerance factor may be favorable in predicting stable compositions for both halide and oxide perovskites[49]. Beyond this, mixed 2D/3D perovskites that form different phases (*e.g.* Ruddlesden-Popper phase) have been more recently likewise been explored either as interfacial modifiers adjacent to 3D perovskites or even as independent subjects. The main difference lies in the chemical structure of the A-site cations (or a fraction thereof), where the rich toolbox of chemical synthetic methods allows for a myriad of structural and functional modifications. For example the bandgap of perovskites can be more or less continuously tuned from the UV (Cl-based), to the green (Br-based) to the red/NIR (I-based), simply by mixing the corresponding salts[11] (*e.g.* MACl, MABr, MAI and corresponding PbX_2 salts). With this also the nature of electron-hole binding shifts from bound Frenkel-excitons (Cl-perovskites) to free-carrier (Wannier-Mott excitons with binding energies $< k_B T$ that easily split). These examples now only indicated the versatility when addressing the X-site anion. Similarly the A- and B-site can be modified rendering even more possibilities, including quantum-confinement in quasi-2D perovskites. Generic to all perovskites is the central crystallographic structure based on the PNMA space group forming an orthorhombic/ pseudo-cubic crystal system. The latter is depicted in Figure 8 in two commonly used presentations with multiple corner sharing (BX_6) octahedra that surround the A-site cations or the classical unit cell, where one octahedron is embedded in a A-site sub-lattice[12].

---

[11] The mixtures may however demix, as described by [50]

[12] The aforementioned 2D perovskites still contain the BX_6 octahedra, albeit the exact crystal structure may be very different otherwise

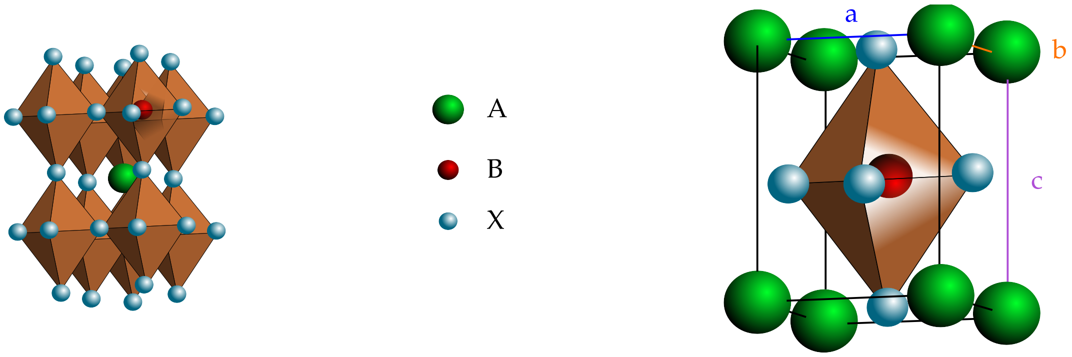

Figure 8: Two perovskite lattice representations, showing the corner sharing octahedra BX_6 encaging the A-site cation (green) on the left and the classic unit cell representation with one octrahedron surrounded by eight A-site cations on the right. Note that the shown structure represents the most general orthorhombic structure, where the lattice constants (a, b, c) all have different lengths $(a \neq b \neq c \neq a)$.

Properties of Halide Perovskites

The large class of halide perovskites has attracted much attention over the last decade as indicated in the INTRODUCTION. This was triggered by several key discoveries, which will be swiftly outlined here in the context of optoelectronic properties desirable for the active layer in solar cells or LEDs. On the basis of previously outlined considerations for what is required of a semiconducting material in order to construct a good solar cell a list of (hard and soft) requirements can be compiled. These include a *suitable direct bandgap* with *high absorption coefficients* or relative to this a *long diffusion length*, *low "active" defect density*, *strong luminescence* and *suitable energy levels* compatible with selective contact materials and/or metals. Many of these properties are causally linked and will be discussed here. Facts relevant for commercial application furthermore include intrinsic and extrinsic stability (over a given time period) against external stresses (heat, light, bias, environment), cheap/easy production & recycling and ideally low toxicity. Typically solar cells do not combine all of these factors and along these properties solar cell technologies are divided into different generations. *E. g.* 1st generation devices are typically wafer-based inorganic semiconductors that require high energy and cost in the production, but have high efficiency, long lifetimes and high stability. The 2nd generation on the other hand is prototypically based on cheap, easily deposited materials but often exhibit low efficiency and limited stability. These are historical observations, but in principle easily fabricated high quality layers based on abundant materials are not impossible and much research has been conducted to investigated a broad range of material systems including CZTS (kesterites), $CuIn_xGa_{1-x}Se_2$ (CIGS/Se), organic semiconductors or halide perovskites. [13] On the basis of the prototypical methylammonium lead halide ($CH_3NH_3PbI_3$) several of these desired properties were discovered. For example, although for several years a debate was carried out, now there is ample proof that the strong absorption (due to strong coupling between Pb-Pb) and high luminescence[51] are a consequence of the direct bandgap nature[52]. The way in which halide perovskites are typically synthesized, namely solution-based at low temperatures, with low long-range structural order (*e. g.* "grains" are only ~100-1000nm in size) without large electronic disorder seems to be in stark contrast to experience with other semiconductors. Despite this, minority carrier lifetimes [14] above 1µs and balanced electron and diffusion lengths above 1µm were found. Explanations for these comparably long lifetimes include the soft and polar nature of halide perovskites - enabling "polaron protection", with comparably heavy atoms with low frequency phonon modes. Translated

---

[13] The term 3rd generation is ambiguous, commonly it is discussed that these devices will beat the Shockley-Queisser limit with ideas such as multi-exciton-generation, singlet fission, hot carrier solar cells...

[14] earlier referred to as SRH lifetime

into energy space, this means only low energy phonons are available for electron-phonon scattering ($E_{phon.} \approx 10-20meV$), so that 100-200 scattering events need to take place to loose the energy of an excited electron. This is kinetically unfavorable, even if the material exhibits comparably high impurity densities with energy levels relatively deep within the bandgap. Kirchartz *et. al.* [53] describe this in the framework of the Huang-Rhys factor, which is in essence a measure of how strong the coupling between the electronic and vibronic system is. Considering nonradiative recombination as a multiphonon decay process, the Huang-Rhys factor considers lattice deformation due to light, the effective mass of the constituent materials and different phonon energies. This picture goes beyond Shockley-Read-Hall recombination – which considers only singular defect energies – but the two concepts are difficult to merge into one sound description[54]. Additionally, DFT-based calculations predicted that most defect levels due to atomic vacancies or (*e. g.* oxygen-) interstitials are shallow compared to the respective bands (*e. g.* $E_{IO^-} - E_{VB} = 0.1eV$) or even lie within these, entailing that trapping is unfavorable. This effect was then coined as an intrinsic *defect tolerance*[15] and predictions were supported by *e. g.* DLTS[55]. Further explanations include that the comparably soft nature of the material and rapidly moving organic cations enable structural and electronic flexibility[56, 57], even at or across grain boundaries[58]. All together, albeit the exact origin is most likely a combination of the mentioned phenomena, the resulting properties are: a direct bandgap with high absorption coefficients ($10^4 - 10^5 cm^{-1}$ in the visible range), decent and balanced mobilities ($\mu_{e/h} \approx 20\frac{cm^2}{V \cdot s}$), slow nonradiative recombination ($\tau \approx 1\mu s$) entailing sufficient diffusion lengths ($L = \sqrt{D\tau} > 1\mu m$)[31] to absorb >90% of above bandgap photons, without compromising carrier collection. Strong emission (due to a sharp absorption onset) complemented by slow nonradiative recombination results in high luminescence efficiency and thus low voltage losses (Equation 51). At the core of all this research lie the mechanisms governing the recombination dynamics. Most of the properties where typically measured on perovskite single layers without transport layers attached, for example, Wehrenpfennig *et. al.* [59] determined mobilites of ~33 $\frac{cm^2}{V \cdot s}$ using THz pump-probe and reported a diffusion length of 3µm for both electrons and holes at carrier densities <10^{17} cm^{-3} and minority carrier lifetimes of several hundred ns. Using transient microwave conductivity measurements Ponseca *et. al.* [60] and Bi *et. al.* [61] even reported up to 15µs in single crystals and low trap densities ~$10^{15} cm^{-3}$. A comprehensive study was carried out be Richter *et. al.* [62], who performed a combination of transient absorption and photoluminescence and deduced kinetic variables in a first-, second- and third-order recombination model, which was verified by correctly reproducing absolute photoluminescence under multiple excitation conditions. Measurements on multilayer stacks and modeling of the transients obtained from THz pump probe spectroscopy revealed sub-picosecond extraction of holes to Spiro-OMeTAD but comparably slow transfer of electrons to PCBM(~ns)[63]. Temperature-dependent photoluminescence measurements by Wright *et. al.* [64] revealed that electron phonon coupling in neat perovskite absorbers proceeds via Fröhlich scattering with longitudinal optical phonons with energy ~10meV and Fröhlich coupling constants of ~40meV.

Measurements on devices revealed a rather inconsistent picture of the recombination dynamics in operating cells. For example, TPV/TPC[16] measurements by Wheeler *et. al.* [65] or Kiermasch *et. al.* [66, 67] led to reported carrier lifetimes of several µs, while the open-circuit voltages of the measured devices barely exceeded 1V. Ideality factor measurements often resulted in ideality factors of ~1.5[68], which is commonly interpreted as a competition between bimolecular and monomolecular recombination[69]. Other common solar cell characterization techniques such as impedance spectroscopy [70–73] were employed, but the results concerning recombination dynamics

---

[15] I would argue that this is misleading. The position of electronic defects is a property closely linked to the atoms and the bands they form. The fact that defects are electronically not particularly active is fortunate, but the material is not tolerant in the sense that structural or chemical stability is not affected, quite the contrary. Many semiconductors suffering from high defect densities consequently suffer from chemical instability, so optoelectronic quality is (albeit weakly) linked to structural stability. This red flag is missing for perovskites.

[16] transient photovoltage (TPV); transient photocurrent (TPC,CE)

are often obstructed by effects related to ionic movement. A debated topic remains the importance of energy level alignment in solar cell stacks. Multiple contradicting studies have either shown the impact of energy level alignment[74] on the open-circuit voltage or in contrast the independence on the latter[75, 76]. Having pointed out favorable optoelectronic properties of halide perovskite semiconductors, their shortcomings cannot be unmentioned. The high ionicity and comparably low binding between the atoms renders the materials prone to dissolution by polar solvents. As such, in particular perovskites with organic cations (MA/FA) are prone to irreversible degradation due to water[77], where in principle a few water molecules can - through a cyclical light induced reaction - decompose multiple methylammonium cations irreversibly. The aforementioned *defect tolerance* is potentially a wolf in sheep's clothing, since the maintained optoelectronic quality may initially masks the fact that there are substantial amounts of vacancies/impurities in the material. Yet again the high ionicity (*i. e.* comparably strong local charge of atoms) together with relatively high ion mobilites ($\mu_{ion} = 10^{-12} - 10^{-7} cm^2/Vs$) then comes into play, especially under prolonged operation (heat/bias) where accumulation of ions at interfaces with potentially reactive metals[17] may induce irreversible degradation. These instabilities, led to the search of alternatives to the archetypical methylammonium-based perovskites, to circumvent the intrinsic volatility of methylammonium[78]. Therefore Cesium (Cs) and Formamidium (FA)-based layers were investigated[79, 80] exhibiting enhanced thermal stability. Unfortunately, both FA and Cs have ionic radii slightly too large (FA, $t = 1.01$) or slightly too small (Cs, $t = 0.8$) to form stable perovskite phases at room-temperature when iodine is used as anion (see tolerance factor). Thus, mixtures of formamidinium and cesium on the A-site[81, 82], as well as, I/Br on the X-site emerged, rendering more stable perovskites with higher reproduciblility and efficiency. This approach was taken further, culminating in triple-[83], quadruple-[84, 85] and even quintuple-cation (KRbCsMAFA)[86], double anion (I/Br) compositions[87]. While initially the role of potassium and rubidium was highly debated, it is now established that they do not incorporate into the lattice[88], but enhance the optoelectronic property of the perovskite through passivation.[89] Additionally, the mixtures of compatible (w.r.t. optoelectronic properties) constituents adds the bonus of enhanced structural stability due to a higher crystal mixing entropy[90]. Together with encapsulation schemes relevant for industrial applications[91, 92], stable solar cells without losses after 10.000h (=1yr)[93] continuous illumination have been reported. Having pointed out instability as an issue and strategies that lead to impressive results another aspect to be considered is that halide perovskite contain lead and/or tin, leading to questionable safety in the context of toxicity, especially when considering large-scale deployment. Assessments on the toxicity of Pb- and Sn-based perovskites[94–96] clearly demonstrates that adequate measurements will have to be taken to ensure minimal leakage of Pb/Sn constituents into the environment and different approaches have been lately demonstrated with promising results[96, 97].

---

[17] a common product with Ag is AgI_3, which forms comparably easily

BIBLIOGRAPHY

[1] John Cleland. “World Population Growth; Past, Present and Future.” In: *Environmental and Resource Economics* 55.4 (Aug. 2013), pp. 543–554 (cit. on p. 5).

[2] Francisco José Gomes da Silva and Ronny Miguel Gouveia. “Global Population Growth and Industrial Impact on the Environment.” In: *Cleaner Production*. Cham: Springer International Publishing, 2020, pp. 33–75 (cit. on p. 5).

[3] Manuela Tvaronavičienė et al. “Global energy consumption peculiarities and energy sources.” In: *Energy Transformation Towards Sustainability*. Elsevier, Jan. 2020, pp. 1–49 (cit. on p. 5).

[4] *World Energy Outlook 2019 – Analysis - IEA* (cit. on p. 5).

[5] R. A. Kerr. “Peak Oil Production May Already Be Here.” In: *Science* 331.6024 (Mar. 2011), pp. 1510–1511 (cit. on p. 5).

[6] B. Ekwurzel et al. “The rise in global atmospheric CO2, surface temperature, and sea level from emissions traced to major carbon producers.” In: *Climatic Change* 144.4 (Oct. 2017), pp. 579–590 (cit. on p. 5).

[7] Andrew A. Lacis et al. “Atmospheric CO2: Principal control knob governing earth’s temperature.” In: *Science* 330.6002 (Oct. 2010), pp. 356–359 (cit. on p. 5).

[8] Myles Allen. “Liability for climate change.” In: *Nature* 421.6926 (Feb. 2003), pp. 891–892 (cit. on p. 5).

[9] Thomas C. Peterson, Peter A. Stott, and Stephanie Herring. “Explaining Extreme Events of 2011 from a Climate Perspective.” In: *Bulletin of the American Meteorological Society* 93.7 (July 2012), pp. 1041–1067 (cit. on p. 5).

[10] Thomas L. Delworth and Fanrong Zeng. “Regional rainfall decline in Australia attributed to anthropogenic greenhouse gases and ozone levels.” In: *Nature Geoscience* 7.8 (2014), pp. 583–587 (cit. on p. 5).

[11] Friederike E. L. Otto. “Attribution of extreme weather.” In: *Nature Geoscience* 8.8 (Aug. 2015), pp. 581–582 (cit. on p. 5).

[12] Kevin E. Trenberth, John T. Fasullo, and Theodore G. Shepherd. “Attribution of climate extreme events.” In: *Nature Climate Change* 5.8 (Aug. 2015), pp. 725–730 (cit. on p. 5).

[13] Peter A. Stott et al. “Attribution of extreme weather and climate-related events.” In: *Wiley Interdisciplinary Reviews: Climate Change* 7.1 (Jan. 2016), pp. 23–41 (cit. on p. 5).

[14] Friederike E. L. Otto et al. “The attribution question.” In: *Nature Climate Change* 6.9 (Sept. 2016), pp. 813–816 (cit. on p. 5).

[15] Paul C. Stern, Benjamin K. Sovacool, and Thomas Dietz. *Towards a science of climate and energy choices*. May 2016 (cit. on p. 5).

[16] A. T. D. Perera et al. “Quantifying the impacts of climate change and extreme climate events on energy systems.” In: *Nature Energy* 5.2 (Feb. 2020), pp. 150–159 (cit. on p. 5).

[17] C.E. Fritts. “On the fritts selenium cells and batteries.” In: *Journal of the Franklin Institute* 119.3 (Mar. 1885), pp. 221–232 (cit. on p. 5).

[18] NREL. *Best Research-Cell Efficiencies*. 2019 (cit. on pp. 5, 110).

[19] *Fraunhofer ISE PV Report 2019* (cit. on p. 5).

[20] David B. Mitzi, Kangning Liang, and Shumin Wang. “Synthesis and Characterization of [NH 2 C(I)NH 2] 2 ASnI 5 with A = Iodoformamidinium or Formamidinium: The Chemistry of Cyanamide and Tin(II) Iodide in Concentrated Aqueous Hydriodic Acid Solutions.” In: *Inorganic Chemistry* 37.2 (1998), pp. 321–327 (cit. on pp. 6, 23).

[21] Shumin Wang et al. “Synthesis and Characterization of [NH2C(I)=NH2]3MI5 (M = Sn, Pb): Stereochemical Activity in Divalent Tin and Lead Halides Containing Single (1 10) Perovskite Sheets.” In: *Journal of the American Chemical Society* 117.I (1995), pp. 5297–5302 (cit. on p. 6).

[22] David B. Mitzi. “Thin-Film Deposition of Organic-Inorganic Hybrid Materials.” In: *Chemistry of Materials* 13.10 (Oct. 2001), pp. 3283–3298 (cit. on p. 6).

[23] David B. Mitzi. “Templating and structural engineering in organic–inorganic perovskites.” In: *Journal of the Chemical Society, Dalton Transactions* 1 (2001), pp. 1–12 (cit. on pp. 6, 23).

[24] *Novel Photoelectrochemical Cell with Mesoscopic Electrodes Sensitized by Lead-Halide Compounds (2) - IOPscience* (cit. on p. 6).

[25] Akihiro Kojima et al. “Organometal Halide Perovskites as Visible-Light Sensitizers for Photovoltaic Cells.” In: *Journal of the American Chemical Society* 131.17 (May 2009), pp. 6050–6051 (cit. on p. 6).

[26] Michael M. Lee et al. “Efficient Hybrid Solar Cells Based on Meso-Superstructured Organometal Halide Perovskites.” In: *Science* 338.October (Nov. 2012), pp. 643–647 (cit. on p. 6).

[27] Michael Saliba. “Polyelemental, Multicomponent Perovskite Semiconductor Libraries through Combinatorial Screening.” In: *Advanced Energy Materials* 9.25 (July 2019), p. 1803754 (cit. on pp. 6, 119).

[28] Nam Joong Jeon et al. “Solvent engineering for high-performance inorganic–organic hybrid perovskite solar cells.” In: *Nature Materials* 13.July (July 2014), pp. 897–903 (cit. on pp. 6, 44, 45, 60).

[29] Stefaan De Wolf et al. “Organometallic Halide Perovskites: Sharp Optical Absorption Edge and Its Relation to Photovoltaic Performance.” In: *The Journal of Physical Chemistry Letters* 5.6 (Mar. 2014), pp. 1035–1039 (cit. on p. 6).

[30] Atsuhiko Miyata et al. “Direct measurement of the exciton binding energy and effective masses for charge carriers in organic–inorganic tri-halide perovskites.” In: *Nature Physics* 11.June (2015) (cit. on p. 6).

[31] Samuel D Stranks et al. “Electron-Hole Diffusion Lengths Exceeding 1 Micrometer in an Organometal Trihalide Perovskite Absorber.” In: 342.October (2013), pp. 341–345 (cit. on pp. 6, 26, 49, 97).

[32] Samuel D. Stranks et al. “Recombination Kinetics in Organic-Inorganic Perovskites: Excitons, Free Charge, and Subgap States.” In: *Physical Review Applied* 034007 (2014), pp. 1–8 (cit. on pp. 6, 113).

[33] Peter Würfel. “Semiconductors.” In: *Physics of Solar Cells*. Weinheim, Germany: Wiley-VCH Verlag GmbH, 2005, pp. 37–84 (cit. on p. 8).

[34] G. Kirchhoff. “Ueber das Verhältniss zwischen dem Emissionsvermögen und dem Absorptionsvermögen der Körper für Wärme und Licht.” In: *Annalen der Physik und Chemie* 185.2 (1860), pp. 275–301 (cit. on p. 8).

[35] Willy Wien. “Ueber die Energievertheilung im Emissionsspectrum eines schwarzen Körpers.” In: *Annalen der Physik und Chemie* 294.8 (Jan. 1896), pp. 662–669 (cit. on p. 8).

[36] Max Planck. *Theorie der Wärmestrahlung*. Leipzig: Barth, 1906 (cit. on p. 8).

[37] Peter Würfel. *Physics of Solar Cells - From Principles to New Concepts*. Wiley-VCH, 2005, p. 186 (cit. on pp. 9, 14, 112, 126).

[38] W. van Roosbroeck and W. Shockley. “Photon-Radiative Recombination of Electrons and Holes in Germanium.” In: *Physical Review* 94.6 (June 1954), pp. 1558–1560 (cit. on pp. 13, 100).

[39] P Wurfel. “The chemical potential of radiation.” In: *Journal of Physics C: Solid State Physics* 15.18 (1982), pp. 3967–3985 (cit. on pp. 13, 17, 72, 116).

[40] Louise C. Hirst and Nicholas J. Ekins-Daukes. “Fundamental losses in solar cells.” In: *Progress in Photovoltaics: Research and Applications* 19.3 (May 2011), pp. 286–293 (cit. on pp. 17, 19).

[41] Uwe Rau, Ulrich W. Paetzold, and Thomas Kirchartz. “Thermodynamics of light management in photovoltaic devices.” In: *Physical Review B - Condensed Matter and Materials Physics* 90.3 (July 2014), p. 035211 (cit. on pp. 17, 19).

[42] Robert T. Ross. “Some Thermodynamics of Photochemical Systems.” In: *The Journal of Chemical Physics* 46.12 (June 1967), pp. 4590–4593 (cit. on p. 17).

[43] Uwe Rau. “Reciprocity relation between photovoltaic quantum efficiency and electroluminescent emission of solar cells.” In: *Physical Review B* 76.8 (Aug. 2007), p. 085303 (cit. on pp. 17, 22, 50, 86, 117).

[44] Martin A. Green and Anita W. Y. Ho-Baillie. “Pushing to the Limit: Radiative Efficiencies of Recent Mainstream and Emerging Solar Cells.” In: *ACS Energy Letters* 4.7 (July 2019), pp. 1639–1644 (cit. on pp. 23, 97, 119).

[45] Dieter Weber. *CH3NH3SnBrxI3 x (x = 0-3), ein Sn(II)-System mit kubischer Perowskitstruktur CHsNHsSnBraJa-z = 0-3), a Sn(II)-System with Cubic Perovskite Structure*. Tech. rep. 1978, pp. 862–865 (cit. on p. 23).

[46] Dieter Weber. “CH3NH3PbX3, ein Pb(II)-System mit kubischer Perowskitstruktur / CH3NH3PbX3, a Pb(II)-System with Cubic Perovskite Structure.” In: *Zeitschrift für Naturforschung B* 33.12 (Dec. 1978), pp. 1443–1445 (cit. on p. 23).

[47] D. B. Mitzi et al. “Conducting tin halides with a layered organic-based perovskite structure.” In: *Nature* 369.6480 (June 1994), pp. 467–469 (cit. on p. 23).

[48] D. B. Mitzi et al. “Conducting layered organic-inorganic halides containing <110>-oriented perovskite sheets.” In: *Science* 267.5203 (Mar. 1995), pp. 1473–1476 (cit. on p. 23).

[49] Christopher J. Bartel et al. “New tolerance factor to predict the stability of perovskite oxides and halides.” In: *Science Advances* 5.2 (Feb. 2019), eaav0693 (cit. on p. 24).

[50] Eric T. Hoke et al. “Reversible photo-induced trap formation in mixed-halide hybrid perovskites for photovoltaics.” In: *Chem. Sci.* 6.1 (2015), pp. 613–617 (cit. on p. 24).

[51] Ian L. Braly et al. “Hybrid perovskite films approaching the radiative limit with over 90% photoluminescence quantum efficiency.” In: *Nature Photonics* 12.6 (June 2018), pp. 355–361 (cit. on pp. 25, 110, 111, 129, 130).

[52] Christopher L. Davies et al. “Bimolecular recombination in methylammonium lead triiodide perovskite is an inverse absorption process.” In: *Nature Communications* 9.1 (Dec. 2018), p. 293 (cit. on pp. 25, 100).

[53] Thomas Kirchartz et al. “Impact of Small Phonon Energies on the Charge-Carrier Lifetimes in Metal-Halide Perovskites.” In: *Journal of Physical Chemistry Letters* 9.5 (Mar. 2018), pp. 939–946 (cit. on pp. 26, 124).

[54] Basita Das et al. “What is a deep defect? Combining Shockley-Read-Hall statistics with multiphonon recombination theory.” In: *Physical Review Materials* 4.2 (Feb. 2020), p. 024602 (cit. on p. 26).

[55] Sung Heo et al. “Deep level trapped defect analysis in CH3NH3PbI3 perovskite solar cells by deep level transient spectroscopy.” In: *Energy and Environmental Science* 10.5 (May 2017), pp. 1128–1133 (cit. on p. 26).

[56] Kiyoshi Miyata et al. “Large polarons in lead halide perovskites.” In: *Science Advances* 3.8 (Aug. 2017), e1701217 (cit. on p. 26).

[57] Haiming Zhu et al. “Screening in crystalline liquids protects energetic carriers in hybrid perovskites.” In: *Science* 353.6306 (Sept. 2016), pp. 1409–1413 (cit. on p. 26).

[58] Makhsud I. Saidaminov et al. “Multi-cation perovskites prevent carrier reflection from grain surfaces.” In: *Nature Materials* (Feb. 2020), pp. 1–7 (cit. on p. 26).

[59] Christian Wehrenfennig et al. “Charge-carrier dynamics in vapour-deposited films of the organolead halide perovskite CH3NH3PbI3-xClx.” In: *Energy & Environmental Science* 7.7 (2014), p. 2269 (cit. on p. 26).

[60] Carlito S Ponseca et al. “Organometal halide perovskite solar cell materials rationalized: ultrafast charge generation, high and microsecond-long balanced mobilities, and slow recombination.” In: *Journal of the American Chemical Society* 136.14 (Apr. 2014), pp. 5189–92 (cit. on p. 26).

[61] Yu Bi et al. “Charge Carrier Lifetimes Exceeding 15 µs in Methylammonium Lead Iodide Single Crystals.” In: *Journal of Physical Chemistry Letters* 7.5 (Mar. 2016), pp. 923–928 (cit. on p. 26).

[62] Johannes M. Richter et al. “Enhancing photoluminescence yields in lead halide perovskites by photon recycling and light out-coupling.” In: *Nature Communications* 7 (Dec. 2016), p. 13941 (cit. on pp. 26, 71, 72, 86, 97, 132).

[63] Carlito S. Ponseca et al. “Mechanism of Charge Transfer and Recombination Dynamics in Organo Metal Halide Perovskites and Organic Electrodes, PCBM, and Spiro-OMeTAD: Role of Dark Carriers.” In: *Journal of the American Chemical Society* 137.51 (Dec. 2015), pp. 16043–16048 (cit. on pp. 26, 52).

[64] Adam D. Wright et al. “Electron–phonon coupling in hybrid lead halide perovskites.” In: *Nature Communications* 7 (May 2016), p. 11755 (cit. on pp. 26, 86).

[65] Scot Wheeler et al. “Transient Optoelectronic Analysis of the Impact of Material Energetics and Recombination Kinetics on the Open-Circuit Voltage of Hybrid Perovskite Solar Cells.” In: *The Journal of Physical Chemistry C* 121.25 (June 2017), pp. 13496–13506 (cit. on pp. 26, 97, 102, 114, 115).

[66] David Kiermasch et al. “Improved charge carrier lifetime in planar perovskite solar cells by bromine doping.” In: *Scientific Reports* 6.1 (Dec. 2016), p. 39333 (cit. on pp. 26, 85, 97, 102, 111, 114).

[67] David Kiermasch et al. “Revisiting lifetimes from transient electrical characterization of thin film solar cells; a capacitive concern evaluated for silicon, organic and perovskite devices.” In: *Energy & Environmental Science* 11.3 (Mar. 2018), pp. 629–640 (cit. on pp. 26, 86, 97, 101, 115).

[68] Gert-Jan a. H. Wetzelaer et al. “Trap-Assisted Non-Radiative Recombination in Organic-Inorganic Perovskite Solar Cells.” In: *Advanced Materials* 27.11 (2015), pp. 1837–1841 (cit. on pp. 26, 112).

[69] Wolfgang Tress. “Perovskite Solar Cells on the Way to Their Radiative Efficiency Limit - Insights into a Success Story of High Open-Circuit Voltage and Low Recombination.” In: *Advanced Energy Materials* 7.14 (July 2017), p. 1602358 (cit. on pp. 26, 67, 70, 86, 110, 112, 119, 123).

[70] Antonio Guerrero et al. “Properties of Contact and Bulk Impedances in Hybrid Lead Halide Perovskite Solar Cells Including Inductive Loop Elements.” In: *Journal of Physical Chemistry C* 120.15 (2016), pp. 8023–8032 (cit. on pp. 26, 114).

[71] Adam Pockett et al. “Characterization of Planar Lead Halide Perovskite Solar Cells by Impedance Spectroscopy, Open-Circuit Photovoltage Decay, and Intensity-Modulated Photovoltage/Photocurrent Spectroscopy.” In: *J. Phys. Chem. C* 119 (2015), p. 3 (cit. on p. 26).

[72] Amalie Dualeh et al. “Impedance spectroscopic analysis of lead iodide perovskite-sensitized solid-state solar cells.” In: *ACS Nano* 8.1 (2014), pp. 362–373 (cit. on p. 26).

[73] Isaac Zarazúa et al. “Operating Mechanisms of Mesoscopic Perovskite Solar Cells through Impedance Spectroscopy and J-V Modeling.” In: *The Journal of Physical Chemistry Letters* 8.24 (Dec. 2017), pp. 6073–6079 (cit. on p. 26).

[74] Lauren E. Polander et al. “Hole-transport material variation in fully vacuum deposited perovskite solar cells.” In: *APL Materials* 2.8 (Aug. 2014), p. 081503 (cit. on pp. 27, 44, 127).

[75] Rebecca A. Belisle et al. “Minimal Effect of the Hole-Transport Material Ionization Potential on the Open-Circuit Voltage of Perovskite Solar Cells.” In: *ACS Energy Letters* 1.3 (Sept. 2016), pp. 556–560 (cit. on pp. 27, 44, 128).

[76] Miao Hu et al. “Distinct exciton dissociation behavior of organolead trihalide perovskite and excitonic semiconductors studied in the same system.” In: *Small* 11.18 (May 2015), pp. 2164–2169 (cit. on pp. 27, 45, 138).

[77] Bert Conings et al. “Intrinsic Thermal Instability of Methylammonium Lead Trihalide Perovskite.” In: *Advanced Energy Materials* 5.15 (Aug. 2015), pp. 1–8 (cit. on p. 27).

[78] Bert Conings et al. “The impact of precursor water content on solution-processed organometal halide perovskite films and solar cells.” In: *J. Mater. Chem. A* 00 (2015), pp. 1–6 (cit. on p. 27).

[79] Giles E. Eperon et al. “Formamidinium lead trihalide: a broadly tunable perovskite for efficient planar heterojunction solar cells.” In: *Energy & Environmental Science* 7.3 (Mar. 2014), p. 982 (cit. on p. 27).

[80] Jin-Wook Lee et al. “High-Efficiency Perovskite Solar Cells Based on the Black Polymorph of HC(NH2)2PbI3.” In: *Advanced Materials* 26.29 (2014), pp. 4991–4998 (cit. on p. 27).

[81] Zhen Li et al. “Stabilizing Perovskite Structures by Tuning Tolerance Factor: Formation of Formamidinium and Cesium Lead Iodide Solid-State Alloys.” In: *Chemistry of Materials* 28.1 (Jan. 2016), pp. 284–292 (cit. on p. 27).

[82] Jin-Wook Lee et al. “Formamidinium and Cesium Hybridization for Photo- and Moisture-Stable Perovskite Solar Cell.” In: *Advanced Energy Materials* 5.20 (Oct. 2015), p. 1501310 (cit. on p. 27).

[83] Michael Saliba et al. “Cesium-containing triple cation perovskite solar cells: improved stability, reproducibility and high efficiency.” In: *Energy Environ. Sci.* 9.6 (June 2016), pp. 1989–1997 (cit. on pp. 27, 111).

[84] Michael Saliba et al. “Incorporation of rubidium cations into perovskite solar cells improves photovoltaic performance.” In: *Science* 354.6309 (Oct. 2016), pp. 206–209 (cit. on pp. 27, 67, 70, 81).

[85] Mojtaba Abdi-Jalebi et al. “Maximizing and stabilizing luminescence from halide perovskites with potassium passivation.” In: *Nature* 555.7697 (Mar. 2018), pp. 497–501 (cit. on pp. 27, 111, 116, 129, 131).

[86] Bingbing Cao et al. “Flexible quintuple cation perovskite solar cells with high efficiency.” In: *Journal of Materials Chemistry A* 7.9 (Feb. 2019), pp. 4960–4970 (cit. on p. 27).

[87] Nam Joong Jeon et al. “Compositional engineering of perovskite materials for high-performance solar cells.” In: *Nature* 517.7535 (Jan. 2015), pp. 476–480 (cit. on pp. 27, 44).

[88] Dominik J. Kubicki et al. “Phase Segregation in Cs-, Rb- and K-Doped Mixed-Cation (MA)x(FA)1-xPbI3 Hybrid Perovskites from Solid-State NMR.” In: *Journal of the American Chemical Society* 139.40 (Oct. 2017), pp. 14173–14180 (cit. on p. 27).

[89] Juan Pablo Correa-Baena et al. "Homogenized halides and alkali cation segregation in alloyed organic-inorganic perovskites." In: *Science* 363.6427 (Feb. 2019), pp. 627–631 (cit. on p. 27).

[90] Chenyi Yi et al. "Entropic stabilization of mixed A-cation ABX 3 metal halide perovskites for high performance perovskite solar cells." In: *Energy Environ. Sci.* 9.2 (Feb. 2016), pp. 656–662 (cit. on p. 27).

[91] Rongrong Cheacharoen et al. "Encapsulating perovskite solar cells to withstand damp heat and thermal cycling." In: *Sustainable Energy and Fuels* 2.11 (Oct. 2018), pp. 2398–2406 (cit. on p. 27).

[92] Rongrong Cheacharoen et al. "Design and understanding of encapsulated perovskite solar cells to withstand temperature cycling." In: *Energy & Environmental Science* 11.1 (2018), pp. 144–150 (cit. on p. 27).

[93] G. Grancini et al. "One-Year stable perovskite solar cells by 2D/3D interface engineering." In: *Nature Communications* 8.1 (June 2017), p. 15684 (cit. on pp. 27, 67, 81, 125).

[94] Aslihan Babayigit et al. "Assessing the toxicity of Pb-and Sn-based perovskite solar cells in model organism Danio rerio." In: *Scientific Reports* 6.1 (Jan. 2016), pp. 1–11 (cit. on p. 27).

[95] Aslihan Babayigit et al. "Toxicity of organometal halide perovskite solar cells." In: *Nature Materials* 15.3 (Mar. 2016), pp. 247–251 (cit. on p. 27).

[96] Junming Li et al. "Biological impact of lead from halide perovskites reveals the risk of introducing a safe threshold." In: *Nature Communications* 11.1 (Dec. 2020), p. 310 (cit. on p. 27).

[97] Xun Li et al. "On-device lead sequestration for perovskite solar cells." In: *Nature* (Feb. 2020), pp. 1–4 (cit. on p. 27).

2

METHODS

The experimental setups and methods used to collect the data outlined in the results are presented. In particular electrical, optical and optoelectronic setups are described.

2.1 SAMPLE PREPARATION

The samples and devices used for the investigations in this thesis were fabricated at the University of Potsdam, Germany, in the laboratories of Prof. Dr. Dieter Neher. In general two fabrication methods are employed: solution processing (predominantly spin-coating) and vacuum processing (thermal evaporation). Chapter 4 is dedicated to a detailed description of preparation steps and corresponding materials and possible pitfalls during preparation. The general layout is shown in Figure 9, where the thicknesses and the typical fabrication from solution or thermal evaporation is likewise indicated.

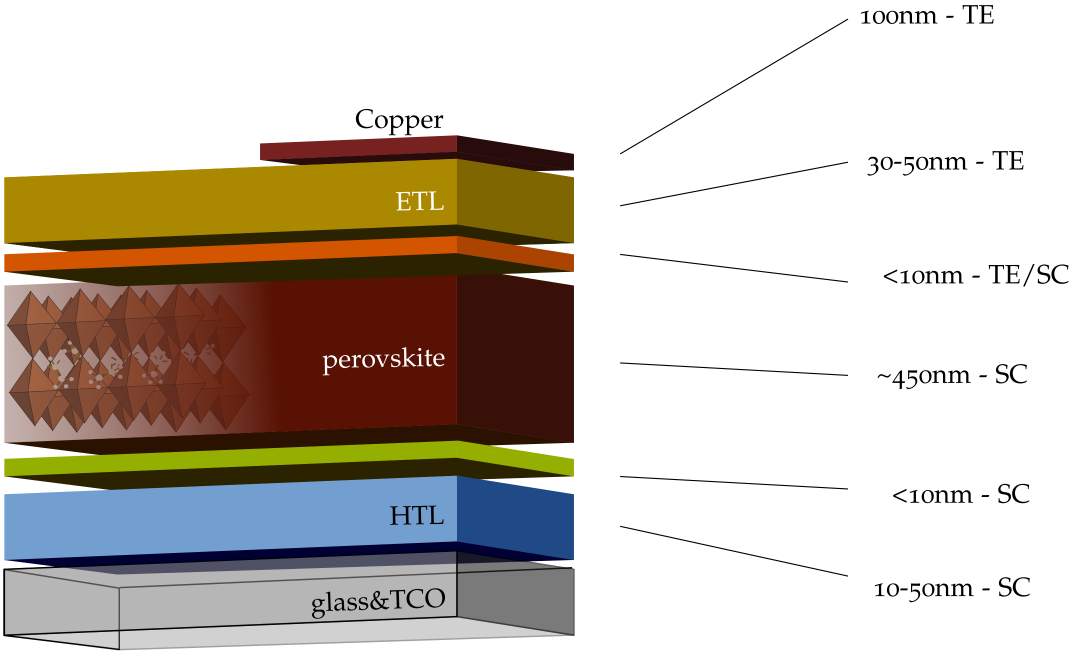

Figure 9: Solar Cell Stack Schematics. The device stack is schematically shown with the thicknesses indicated on the right, together with the fabrication from thermal evaporation (TE) or spin-coating (SC). The green and orange layers are optional interlayers discussed in the respective chapters.

2.2 OPTICAL CHARACTERIZATION

External Photoluminescence Quantum Efficiency - EQE_{PL} / PLQY

The external quantum efficiency of photoluminescence or photoluminescence quantum yield is directly linked to QFLS of a semiconductor through Equation 27. Therefore it is a powerful technique to determine the maximum achievable V_{OC} of a solar cell. The basic principle is a simple matter of counting absorbed and emitted photons, however, experimentally the implementation is often difficult, leading to erroneous results. For example, to collect all emitted photons commonly an integrating sphere (Ulbricht sphere, NewPort 819C) is employed. The setup used herein is depicted in Figure 10. Light from a laser diode is coupled into a fiber and directed into an integrating sphere, where the sample is illuminated. The emission from the sample is homogenized and reflected multiple times until it is coupled out into another fiber directed towards a (sensitive) spectrometer (Andor SR393i-B spectrometer equipped with a silicon detector DU420A-BR-DD (iDus)). Comparing emission to excitation (with and without the sample present) and careful calibration enables to measure PLQYs down to 10^{-8}. As an add-on an automated OD filter wheel and a reference diode were installed. These additions allow to measure the PLQY fully automated as function of intensity over > four orders of magnitude in excitation intensity.

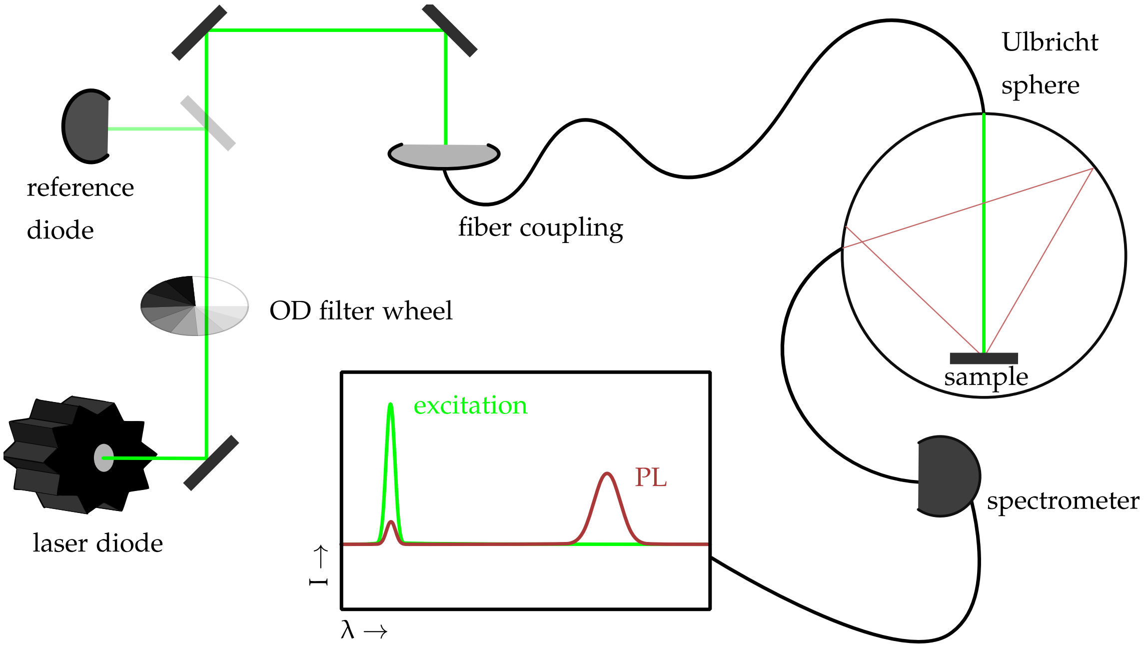

Figure 10: PLQY setup. The laser light is coupled into a fiber directed into an Ulbricht sphere, where the sample is illuminated. The emission is collected through another fiber, coupling the light into a spectrometer. Additionally an OD filter wheel and a reference diode enable intensity-dependent measurements.

In the actual measurement, due to the specific spectral sensitivity of the spectrometer and the comparably low PLQYs typically measured (<1%), two additional measurements are necessary, *i. e.* with long-pass filters cutting out the excitation. These filters themselves show weak fluorescence (most likely through color-centers in the glass), which the spectra have to be corrected for.

2.3 DEVICE CHARACTERIZATION

Voltage-Current Characterization - JV

A common characteristic of a solar cell or any diode is its' JV curve, displaying the current (J) that flows through the device under an applied voltage (V), either with or without illumination. With the maximum of the product ($P = J \cdot V$) the produced power can be derived and comparing to the incoming power the PCE can roughly be determined. Furthermore, it is easy to read off the J_{SC}, the FF and the V_{OC} of the device. The setup is schematically shown in Figure 11. The setup used in this thesis has four additional features: 1. it is flipped upside down in order to illuminate the sample through a window with the sample holder 2. inside a N_2-filled glovebox. 3. The sample holder with the Peltier element has a so called pixel switcher attached, which enables measuring different spots (pixels) on the sample individually and 4. a reference photodiode measures the light intensity to correct for the slowly degrading light source. This light source is an Oriel class AAA Xenon lamp, that closely mimics the solar spectrum (AM1.5G) where the mismatch between intended and measured spectrum is small (expressed as a spectral mismatch factor $M = 0.9985$). The source meter employed is a Keithley 2400 controlled through a home-built LabView program enabling to vary scan speed, resolution, scan direction and settling time. All other components are home-built.

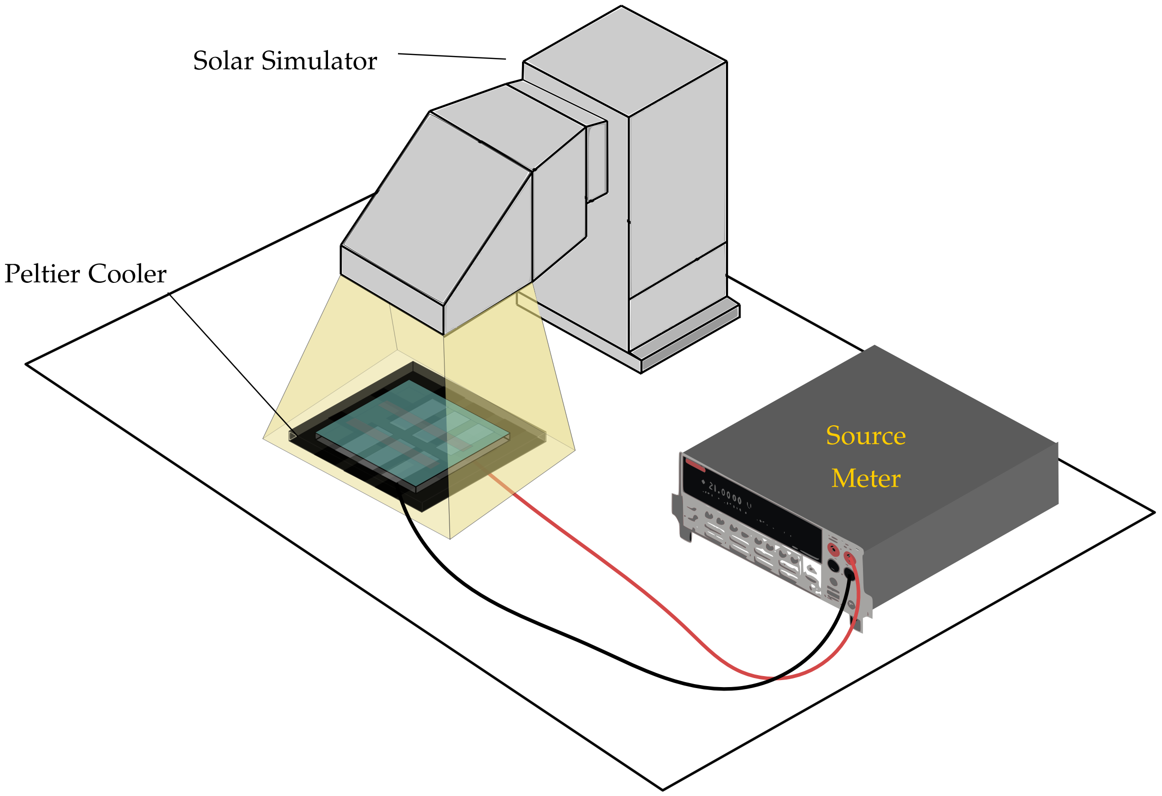

Figure 11: Solar Simulator. The device (green) is placed under illumination from an arc lamp (solar simulator) on a Peltier element, that stabilizes the temperature of the device, whereas the source meter sets a voltage and measures the corresponding current. The solar cell and the Peltier element are scaled for better visualization.

Maximum-Power-Point Tracking

While JV scans allow to quickly measure the three photovoltaic figures-of-merit (V_{OC}, J_{SC} & FF) there is no information whether the device can deliver a certain output power over longer times. To test this there are generally two options: 1. stabilized-power-output measurements (SPO) or maximum-power-point-tracking (MPP). SPO is a more realistic real world operation where a cell in a module is subjected to an average power-point-voltage of the module, but has the disadvantage, that *e.g.* transient improvements (*e.g.* burn-in effects), especially w.r.t. to FF cannot be detected. Therefore for individual cells MPP is a valuable option. MPP measurements shown in this thesis are based on a perturb-and-observe algorithm, where after a predefined time-interval (dynamically changing relative to the changes) the currently applied voltage is perturbed (typically ± 10 mV) and out of the three consecutive measurements the voltage with maximum delivered power is kept until the next cycle. Simultaneously applied voltage (V_{MPP}) and current (J_{MPP}) is monitored. The setup I developed for long-term illumination utilizes a small array of white-light LEDs with only mediocre stability. To compensate for fluctuations and slight degradation of the LEDs, the current of a reference photo-diode is also monitored to finally correct for this effect. The source meter employed is a Keithley 2400 controlled through a home-built LabView program with variable Δt and ΔV. All other components are home-built.

ACCREDITED LAB ROUTINES During real operation, there is no applied bias voltage, but the solar cell delivers work to a consumer with a certain resistance (R), consequently this is the method accredited labs use for stabilized certification, where an external resistor ($\mu\Omega - G\Omega$) is applied and then the current is left to settle. Thereby any condition between (almost) short-circuit($\mu\Omega$) and (almost) open-circuit ($G\Omega$) can be realized and the device does actually have to work against a consumer, sometimes resulting is slightly lower FFs compared to JV-scans.

External Photovoltaic Quantum Efficiency - EQE_{PV}/IPCE

A key requirement of any good solar cell is that light with energy above the bandgap is absorbed and photogenerated carriers can be extracted. To measure the INCIDENT-PHOTON-TO-CURRENT-EFFICIENCY (IPCE), alternatively called EQE_{PV}, light from a broadband light source (Philips Projection lamp Type 7724, 12 V, 100 W) is chopped and selected through a monochromator (Oriel Cornerstone 74100) and directed onto the sample through a fiber. In doing so, measurements in a N_2-filled glovebox can be carried out. The modulated signal is lock-in amplified (EG&G Princeton Applied Research Model 5302) across a 50 or 1000 Ω resistor so that sensitive measurements down to 10^{-6} are possible. The setup is schematically shown in Figure 12.

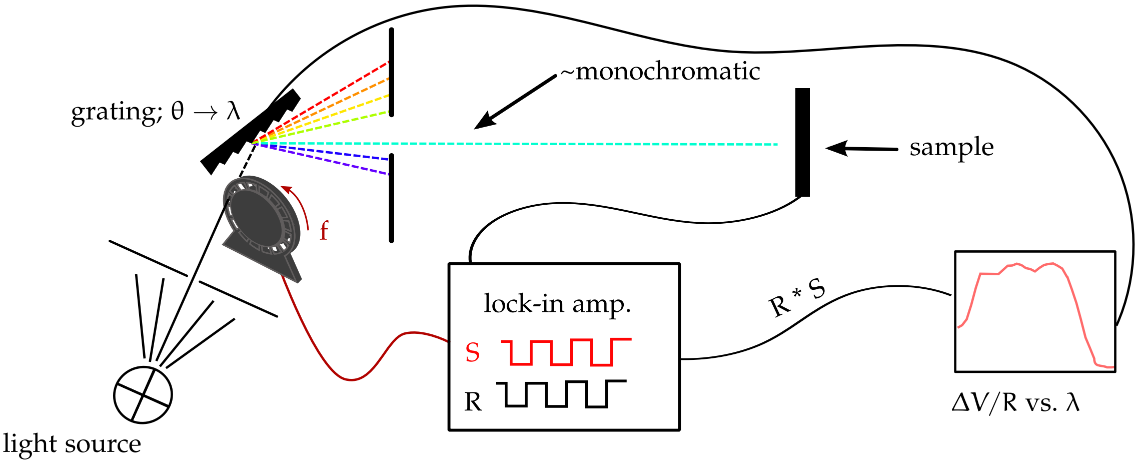

Figure 12: IPCE Setup. Broadband white-light is optically chopped and spectrally separated through a double grating monochromator. The chopped "monochromatic" light is directed onto the sample and the produced current is lock-in amplified a resistor rendering the spectral response. By comparison to a calibrated reference diode the IPCE is calculated with resolution down to 10^{-6}.

External Electroluminescence Quantum Efficiency - EQE_{EL}

Luminescence from a semiconductor can be excited through various ways, one of which is luminescence upon injection of electrical current, thus called ELECTROLUMINESCENCE. As pointed out by Rau, the quantum efficiency of electroluminescence is a key figure-of-merit for a good solar cell with high V_{OC} (see *e.g.* Equation 51). The method employed is based on two consecutive measurements. The solar cell is mounted in a home-built sample holder and bias is applied through a Keithley 2400

SourceMeter unit. First the relative emission spectrum is acquired using a calibrated spectrometer (Andor SR393i-B spectrometer equipped with a silicon detector DU420A-BR-DD (iDus)). Second, a calibrated UV-enhanced Si photodetector (Newport) is placed in front of the solar cell collecting the emitted photons. By convoluting a normalized emission spectrum with the accredited EQE of the photodetector and comparing it to the absolute flux provided by the solar cell a scaling factor ν is calculated. Comparing the injected current with the photo-current detected by the photodetector (re-scaled by ν, measured by a Keithley 485 pA meter) renders the EQE_{EL}. All components are controlled through a home-built LabView program Dr. S. Roland and I programmed. The method is schematically depicted in Figure 13.

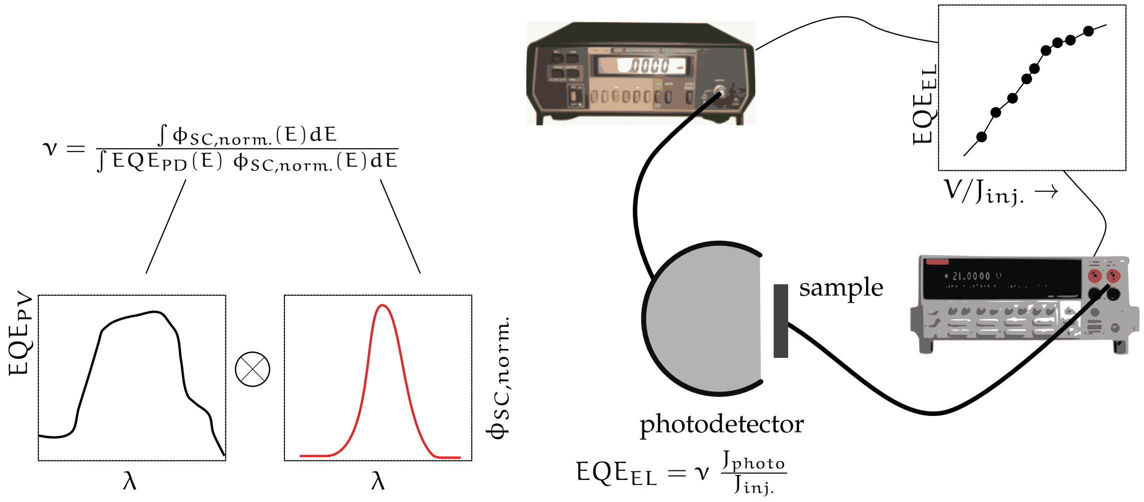

Figure 13: A solar cell is driven into forward bias by a Keithley 2400 and the photocurrent measured on a pA meter is recorded and multiplied by a scaling factor ν measured fronm a seperate measurement

Note, it is essential to carefully place the photodetector close to the measured pixel, to collect all emitted photons. In principle a correction on the basis of multiple distances according to can be done. The error for a 6mm^2 - if carefully placed - was however <10% and therefore neglected.

2.4 TIME-RESOLVED CHARACTERIZATION

Time-Resolved Photoluminescence

TIME-RESOLVED PHOTOLUMINESCENCE (TRPL) is a valuable characterization technique to track the dynamics of photoluminescence and thereby the product of carrier densities. To do so, a pulsed laser diode (LDH470, PicoQuant, $\lambda = 470\mathrm{nm}$) triggered by a function generator produces sub-ns pulses with pulse fluences (nJ/cm^2-µJ/cm^2) depending on the spot-size at repetition rates between 500kHz and 40MHz. The photons emitted from the sample are culminated using a concave mirror onto a double grating, which spatially separates different spectral bands with ~6nm bandwidth. The photons are directed onto a 16-channel photomultiplier array (PML-16-C, Becker & Hickl), where TIME-CORRELATED-SINGLE-PHOTON-COUNTING (TCSPC) is used in a single photon counter chip (SPC830, Becker & Hickl) to acquire histograms of incident photons as a function of time. Combining spectral (= spatial) and temporal resolution allows to acquire 2D plots as shown in Figure 14. A long-pass filter (>600nm) is used to remove the excitation pulses.

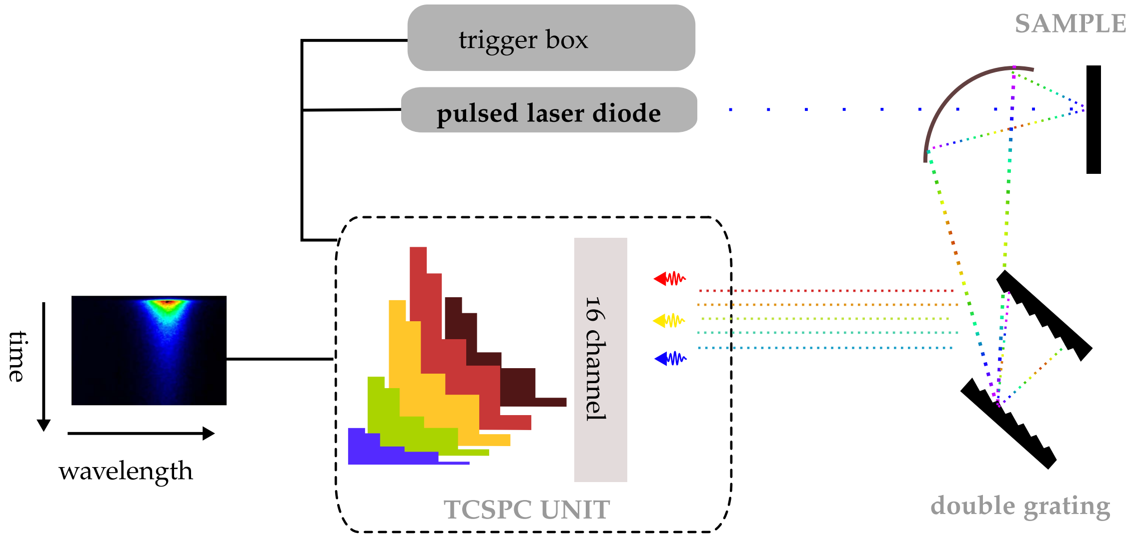

Figure 14: TCSPC setup. The sample is excited with a laser pulse (blue) with variable fluence (nJ/cm^2-µJ/cm^2) and the emitted light is spectrally separated by a double grating and directed onto a 16-channel photomultiplier array in a TCSPC unit, where each channel produces photon incident histograms through single-photon-counting. The final measurement are coarse spectra $\Delta\lambda \approx 10\mathrm{nm}$ with comparably good time-resolution ($\Delta t < 0.4\mathrm{ns}$).

Transient Absorption Spectroscopy

Photogenerated charge carriers can recombine through a manifold of pathways, only one of which is radiation. PL can therefore not deliver a complete picture of the total carrier dynamics. An alternative technique is Transient Absorption Spectroscopy (TAS), which monitors the dynamical change in absorption due to photo-excitation. This method is a pump-probe technique, where two laser pulses consecutively hit the sample in overlaying spots: first carriers are excited with a pump pulse and after a defined delay a much weaker (broad-band) second pulse probes the excited area. By repeating this measurement with different delay times, and comparing it to the non-excited transmission, a relative change in signal can be measured, where depending on the setup geometry both transmission and reflection can be measured. The collected signal is a differential change expressed as $\Delta X/X$, where X is R or T, respectively. With a broad-band probe pulse a monochromator and an array of photodetectors thereby transient spectra can be recorded. The setup used for this work is schematically shown in Figure 15. The setup is built around a Ti:Sa laser (Coherent Libra), which itself consists of a pump laser (Coherent Evolution), a seed laser (Coherent Vitesse) a stretcher-compressor unit and a regenerative amplifier unit with a Z-scheme cavity. In short, the fs laser pulses are first stretched (to reduce the intensity and avoid damage to the laser medium during amplification) and then directed into the amplifier where the pump laser has driven the Ti:Sa into the inversion regime. The fs pulses travel through the cavity and are amplified with each passage up to a total factor of ~10^6. Single pulses of the continuously running pulse train are then deflected out of the cavity by a pair of Pockel cells. The now amplified pulses are finally compressed again. This system delivers ~800nm pulses with up to 4mJ at a duration of 50fs and a repetition rate of 1kHz. This laser light is used to feed one (in principle two) non-collinear optical amplifier (NOPA, Coherent OperA solo). Through non-linear optics (*i. e.* white-light generation, sum/difference-frequency generation/amplification) a broad range(200-2700nm) of wavelengths with high energy pulses can be produced. For the experiments in this thesis, 530nm and 1400nm are chosen, respectively. The 1400nm pulses are thereafter used to generate broadband white-light pulses in a YAG crystal ranging from 500nm to 1600nm, ideally suited for lead halide perovskites with absorption edges <850nm. The 530nm pulses are selected as pump pulses. To vary the delay between pump and probe pulses a motorized optical stage (OWIS limes, controlled by a nanotec SM135) with a mounted retro-reflector (UBBR-2.5) is moved, allowing for a delay-window up to 9ns. To probe even longer delay times, the pump pulses are alternatively delivered from an electronically triggered laser (innolas AOT). This laser delivers <ns pulses at 1064nm, which are frequency-doubled to 532nm giving up to 200µJ/cm^2 pulses. This is also the reason why above 530nm where chosen as pump laser wavelength to complement this laser. To monitor the transient spectra the probe pulses are directed into a VIS-NIR spectrometer (optical components by Carl-Zeiss Jena, electronics by Entwicklungsbüro Stresing) and optical stage/triggering, spectrometer readout and data processing are done in a LabView program I devised.

RECENT MODIFICATIONS The initial design of the setup was done by Dr. Jona Kupiers, but due to several violations of specification compliance – in particular w.r.t. the spectrometers – the setup had to be redesigned. To optimize the sensitivity and speed of the setup a first a high speed spectrometer pair (UV-Vis & Vis-NIR) with new gratings had to be implemented. Finally a second pair of spectrometers was introduced to compensate for correlated pulse-to-pulse white light fluctuations and the gratings were replaced by pairs of dispersion-"free" prisms.The interested reader is directed to [98]. The overall development, redesign and programming occupied a considerable amount of time, but was then key in acquiring the data shown in Chapter 7.

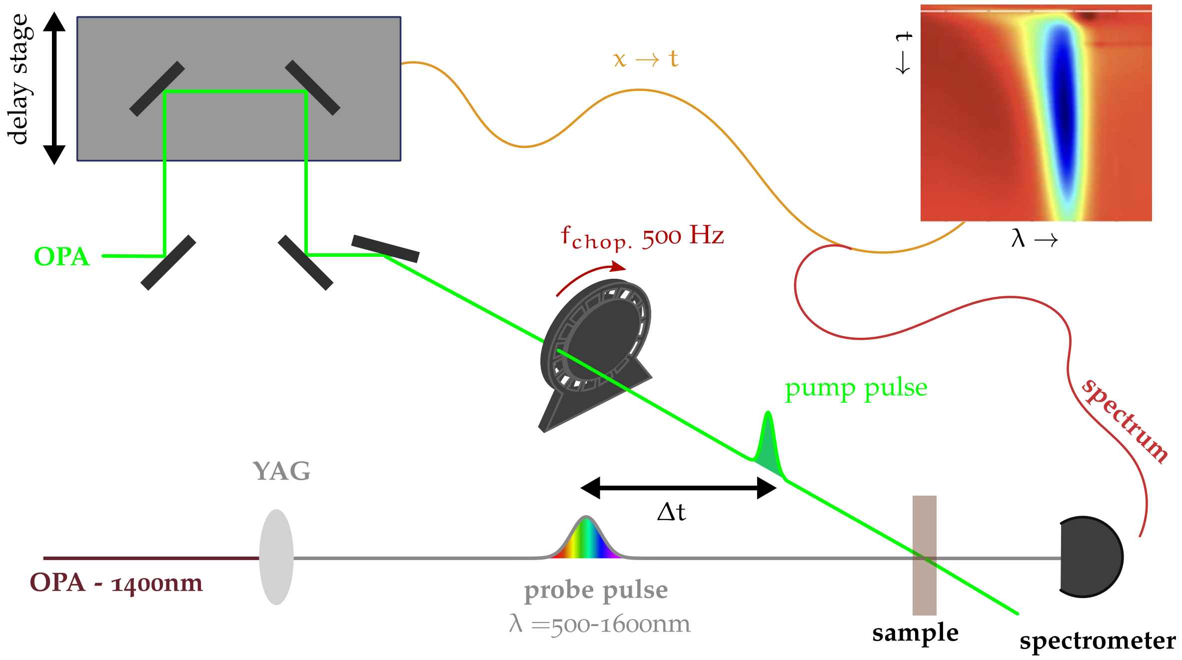

Figure 15: TAS setup. Probe light is generated in an OPA and delayed by *e.g.* a delay stage, before being chopped to modulate between on and off. In parallel a white-light probe continuum is generated, which is used to probe the photo response. The setup in Potsdam now operates with a delayed probe, which was found to be more robust.

Time-Delayed-Collection-Field

The aforementioned all-optical transient measurements predominantly probe the bulk of the active solar cells material with strong changes in optical absorption. Charge carriers in multi-layer solar cells - such as the herein employed p-i-n structure - are additionally extracted to the charge transport layers, where the individual polarons typically have very weak optical signal. Therefore an opto-electronic measurement that extracts all carriers - including the ones sitting on the transport layers - is a valuable complement. TIME-DELAYED-COLLECTION-FIELD (TDCF) is such a technique, that enables sensitive measurements on fully operational solar cells. In this measurement the solar cell is first kept at a defined voltage (V_{pre}). A laser pulse then excites charge carriers. After a defined delay time the voltage across the device is flipped to a comparably strong negative voltage and the remaining charge carriers are extracted. By varying the delay time between excitation and extraction the total amount of charge carriers in the device as a function of time is determined. To probe under realistic conditions the sample can furthermore be illuminated by a cw-laser establishing steady state working conditions. To then probe *e. g.* recombination at *e. g.* open-circuit conditions, ideally V_{pre} is set to match V_{OC}. The additional laser-pulse induced carriers change the electric fields across the device slightly (*i. e.* $V_{pre} < V_{OC}$), so that a fraction of carriers flow out of the device. These charges are hereafter called Q_{pre}, whereas the charges collected after the voltage change are called Q_{coll}. By comparing two consecutive measurements (with and without pulsed excitation) the effect of injected carriers (due to V_{pre}) is compensated. Schematically the measurement is depicted in Figure 16. The short laser pulses (Innolas AOT, <1ns) are used to trigger a fast photodiode (EOT, ET-2030TTL) before being optically delayed and homogenized in a long optical fiber (LEONI, 85m). This is necessary to compensate for the electronic delay of the function generator (Agilent 81150A) and the voltage amplifier (built by J. Kupiers & A. Pucher). The extracted carriers are monitored with a on an oscilloscope (Yokogawa DL9140) across a 50 Ω resistor.

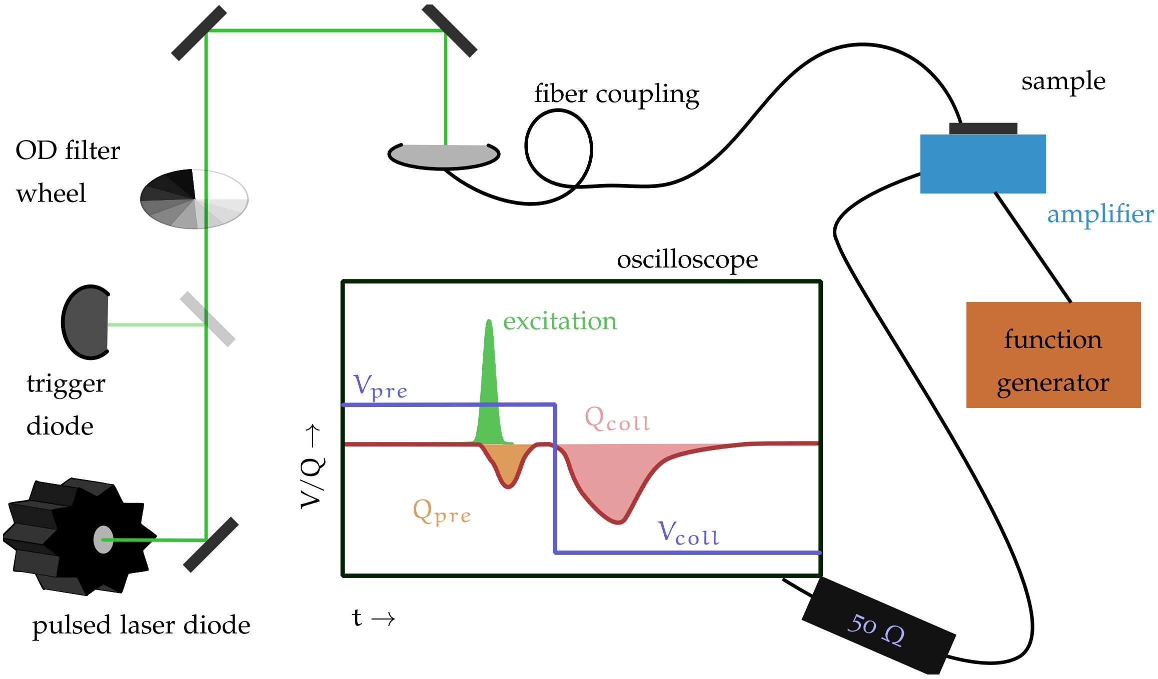

Figure 16: TDCF setup. The sample is held at a certain voltage V_{pre} and is then excited with a (green) laser pulse, which likewise triggers the system/amplifier. After a chosen delay to voltage is changed to V_{coll}. All charge and discharge transients are monitored on a scope across a 50 Ohm resistor.

Part II

RESULTS

3

REDUCED INTERFACE-MEDIATED RECOMBINATION FOR HIGH OPEN-CIRCUIT VOLTAGES IN $CH_3NH_3PBI_3$ SOLAR CELLS

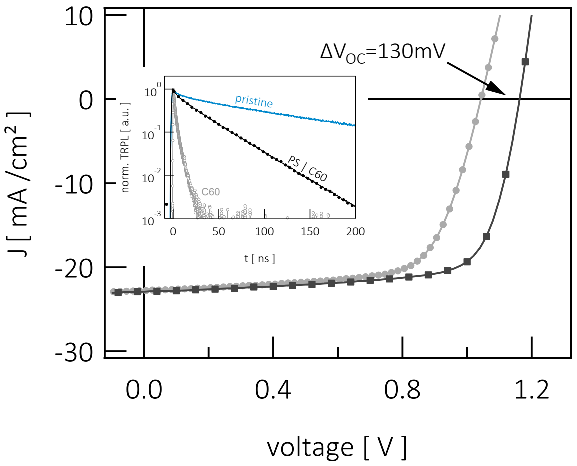

Motivated by the contradicting results in literature w.r.t. the role of energy level alignment of the transport layers, this work is focusing on delivering a comprehensive study on the impact energy level alignment has on the recombination dynamics in perovskite solar cells, identifying the electron-transport layer interfaces as limitation.

This chapter is a preprint of:

Reduced Interface-Mediated Recombination for High Open-Circuit Voltages in $CH_3NH_3PbI_3$ Solar Cells

Christian M. Wolff, Fengshuo Zu, Andreas Paulke, Lorena Perdigón Toro, Norbert Koch and Dieter Neher

published in : *Adv. Mater. 2017, 29 (28), 1700159.*

3.1 ABSTRACT

Perovskite solar cells with all-organic transport layers exhibit efficiencies rivaling their counterparts that employ inorganic transport layers, while avoiding high-temperature processing. Herein, it is investigated how the choice of the fullerene derivative employed in the electron-transporting layer of inverted perovskite cells affects the open-circuit voltage (V_{OC}). It is shown that nonradiative recombination mediated by the electron-transporting layer is the limiting factor for the V_{OC} in the cells. By inserting an ultrathin layer of an insulating polymer between the active $CH_3NH_3PbI_3$ perovskite and the fullerene, an external radiative efficiency of up to 0.3%, a V_{OC} as high as 1.16 V, and a power conversion efficiency of 19.4% are realized. The results show that the reduction of nonradiative recombination due to charge-blocking at the perovskite/organic interface is more important than proper level alignment in the search for ideal selective contacts toward high V_{OC} and efficiency.

3.2 INTRODUCTION

Perovskite solar cells have emerged at an unprecedented pace with certified efficiencies of more than 22% after only seven years of intense research. This fast development can be attributed to the excellent optoelectronic properties of the absorber material combined with the variety of available preparation routes spanning from various solution approaches[28, 100–102] to vacuum deposition[103, 104] and vapor treatment techniques[105–107]. The organometallic 3D perovskite species $CH_3NH_3PbI_3$ (MAPI) can be considered the working horse of this technology where the absorber material (i) is sandwiched between two selective electron (n) and hole (p) transport layers-formed by either organic[104, 108] or inorganic materials, or a combination of both.[101, 109] A huge variety of transport layers have been explored in perovskite solar cells, with the highest efficiencies reported for selective layers consisting of the electron-transporting materials (ETLs) TiO_2[110], SnO_2[111, 112], ZnO[113, 114], or fullerene derivatives such as PCBM[104, 115]. Likewise, a broad range of hole-transport materials (HTLs) have been tested - most common ones are spiro-OMETAD.[116], PEDOT:PSS[117], PTAA[87], polyTPD[104] or NiO[118].Independent of the particular arrangement of the cell in n-i-p or p-i-n configuration the devices achieved high efficiencies above 15% for almost any combination of the aforementioned materials, with open-circuit voltages (V_{OC}) of close to or above 1 V. Typically, high V_{OC} values are realized with high-quality perovskite layers, exhibiting small densities of grain boundaries and impurities, which might act as trapping and recombination centers. In addition, proper energetic alignment at the interfaces between the perovskite and the transport layers was proposed to be important in achieving high V_{OC}.[119, 120] For example, Polander *et. al.* studied vacuum-deposited MAPI-based perovskite solar cells in a n-i-p architecture, where the ionization energy (IE) of the undoped HTL was varied from 5.0 to 5.6 eV.[74] The V_{OC} (sample average) increased systematically by 150 meV with an increase of the ionization energy from 5.0 to 5.3 eV. On the other hand, Belisle *et. al.* investigated a similar device architecture, revealing only a marginal effect of the IE of the HTL on the V_{OC}, explained through remote-doping of the HTLs through the large carrier concentration close to the electrode.[75] It was proposed that ion migration in the perovskite redistributes the electrostatic potential such that the quasi-Fermi level positions inside the active material are less dependent on the electronic structure of the HTL. Yan *et. al.* studied p-i-n architectures based on MAPI, with four different polymers prepared by electrochemical polymerization serving as the HTL.[121] Increasing the IE by 0.3 V led to an improvement of the V_{OC} by more than 0.2 eV, which from impedance spectroscopy was assigned to reduced carrier recombination. Following the same line of arguments, the rather poor performance of PEDOT:PSS as a HTL in p-i-n perovskite solar cells has been attributed to inefficient electron-blocking and significant nonradiative recombination.[122, 123] On the cathode side, few studies have considered the relation between the lowest unoccupied molecular orbital (LUMO) position of the ETL and V_{OC}. Wang *et. al.* and later Wu *et. al.* reported an up to 0.2 V higher V_{OC} in perovskite p-i-n structure after replacing the commonly used PCBM by the higher adduct fullerene ICBA.[124, 125] The improvement was attributed to the higher LUMO level position of the ICBA, resulting in better energy alignment with the perovskite conduction-band minimum (CBM). Notably, work by Shao *et. al.* suggested a significant impact of the structural order of the PCBM ETL on V_{OC}, varied through the annealing protocol.[126] The high V_{OC} in the case of a solvent-annealed PCBM layer was explained by a narrower density of state distribution, with less tailing into the perovskite bandgap. Interestingly, transient photovoltage measurements (TPV) revealed very similar decay dynamics in both samples, implying an only minor effect of the ETL energetics and drastically too high carrier densities ($\approx 10^{17}\,\mathrm{cm}^{-3}$), rendering these measurements unreliable.

3.3 DEVICES AND PHOTOVOLTAIC CHARACTERIZATION

Here, we perform a comprehensive study of the energetics and the V_{OC} losses in MAPI-based p-i-n devices with different fullerenes. We show that PCBM but also C_{60} are not ideal candidates when targeting high V_{OC}, despite proper energy alignment. We attribute this to rapid electron extraction and subsequent interface-mediated nonradiative recombination. Increasing the fullerene LUMO level, when going from C_{60} to indene-C_{60}-trisadduct (ICTA) causes a significant reduction of these losses, but a more prominent improvement is seen when adding an ultrathin insulating polystyrene (PS) interlayer between MAPI and C_{60}. With radiative efficiencies further up to 0.3%, the devices exhibit a high V_{OC} of 1.16 V and a power conversion efficiency (PCE) of up to 19.4%. Hybrid perovskite solar cells were fabricated in an inverted p-i-n structure with the hole-transporting polymer PTAA, doped with 2,3,5,6-petrafluoro-7,7,8,8-tetracyanoquinodimethane (F_4TCNQ), forming the HTL, MAPI as the active material, and the four fullerene combinations,*i. e.* , C_{60}, PCBM | C_{60}, ICTA | C_{60}, and PS | C_{60}, as ETL (see Figure 17d for the chemical structures of all organic compounds). These fullerenes are widely used in the perovskite as well as in bulk-heterojunction organic photovoltaics as electron acceptors.[76, 127, 128] Density functional theory calculations and experimental studies suggest that the LUMO level of these fullerene derivatives increases by as much as 500 meV when going from C_{60} to PCBM to ICBA to ICTA.[129–131] Also, motivated by the work of Wang *et. al.* [132] samples with an ultrathin layer of the insulating polymer PS, added between MAPI and C_{60}, were tested. Perovskite solar cells in the p-i-n architecture were prepared on prestructured indium tin oxide (ITO). A detailed description of the fabrication is given in Chapter 4. In short, the doped PTAA (30 nm layer thickness), the active perovskite, the soluble fullerene derivatives (50-60 nm) and the PS (<5 nm) were deposited by spin coating, while the C_{60} layer (20 nm) was evaporated along with the top contact consisting of 8 nm bathocuproine (BCP) and 80-100 nm copper (Cu). Figure 17a shows schematically the use and position of these materials in the devices and Figure 17b displays a cross-section of a sample, showing the compact perovskite layer with large single grains in vertical direction. The perovskite solution consisted of 1 mmol PbI_2, 1 mmol methyl ammonium iodide (MAI), 0.85 mmol dimethyl sulfoxide (DMSO), and 0.15 mmol thiourea (TU) in 636 µL anhydrous N,N-dimethylformamide (DMF). Following modified but established recipes,[133, 134] the deposition of the MAPI layer involved a 500 µL diethyl ether washing 10 s after the start of spin-coating. The use of two Lewis-bases, DMSO[28, 134, 135] and TU[134] enabled us to prepare compact, high-quality layers of about 550-600 nm thickness (DMSO/TU optimization is shown in Figure 22). The top-view SEM image in Figure 17c of a sample on a fully covered glass | ITO | PTAA substrate demonstrates high quality of the so-formed perovskite layer with a thickness of~500nm. The SEM images show very uniform and flat layers up to the 100 µm scale, though the films still exhibit structures on the order of several hundreds of nanometers, which we consider a more realistic estimate for the grain size given further data, discussed below.

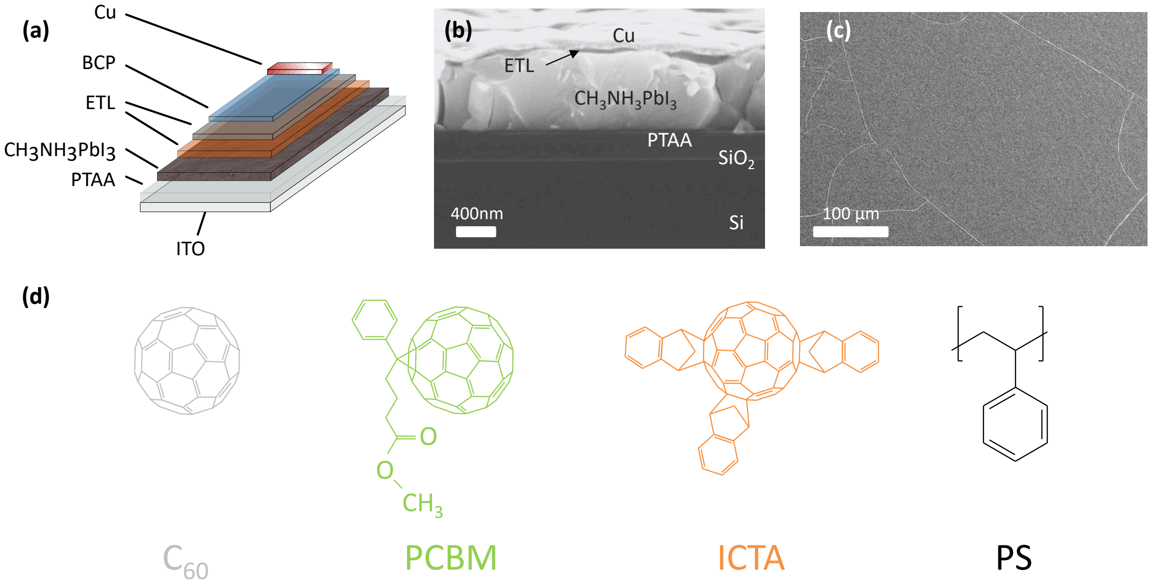

Figure 17: a) Schematics of the layer stack in a full device, b) example cross-sectional SEM image of the full device stack (including a PS interlayer) on Si | SiO2, and c) a top-view SEM of the as-deposited perovskite layer on glass | PTAA. d) Chemicals used in this study for the electron-transport layer. Adapted with permission.[99] Copyright 2017, John Wiley and Sons.

We evaluated the quality of these smooth films by recording their luminescent lifetime. Typically films derived from PbI_2-MAI suffer from comparably short lifetimes and thus cannot compete with their analogs made from different lead precursors such as $Pb(CH_3COO)_2$ or $PbCl_2$.[136] Additives, such as Lewis-bases, hydrohalic acids,[136] or metal ions[137] have been shown to improve the crystallization and reduce the defect density (*e. g.* , I_2 sites) or microstrain and thus produce compact and electronically purer films. As shown below, our pristine perovskite films exhibit long fluorescent lifetimes, with more than 100 ns for the long-lived tail, meaning that trapping and trap-assisted recombination must be slow (Figure 20c). Figure 18a shows the current density versus voltage (J-V) scans of the four champion solar cells recorded in reverse scan direction at 60 mV s^{-1} (1.3 V to -0.2 V). The integrated photovoltaic external quantum efficiency (EQE_{PV}) spectra in Figure 18b match well the short-circuit current density (J_{SC}) values obtained from J-V scans, indicating the absence of higher order recombination losses at short-circuit and AM1.5G illumination conditions. Inverted (p-i-n) perovskite solar cells are less prone to hysteresis as observed before.[133, 134] Exemplary direction and scan-rate dependent J-V curves in Figure S4 (SI) show little to no deviations. Likewise, the stabilized power output over ≈2 min (Figure S3, SI) closely matches the PCEs obtained from J-V scans. Table 1 summarizes the photovoltaic parameters PCE, fill factor (FF), J_{SC}, V_{OC} averaged over 2-3 independent batches of cells (resulting in 12-18 devices per structure) for the different ETL (evaporated C_{60}, PCBM | C_{60}, ICTA | C_{60}, and PS | C_{60}).

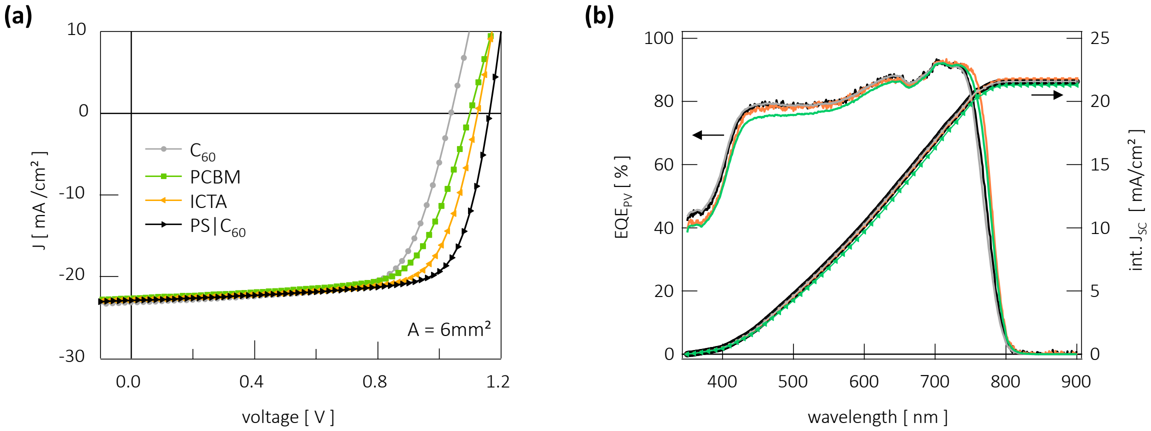

Figure 18: a) JV-curves of the champion devices under simulated AM1.5G light (noncorrected for small deviations in the illumination intensity (98 ± 4 mW cm^{-2})) measured with ≈60 mV s^{-1} from forward bias to negative bias. b) The linear EQE (full lines) including the integrated J_{SC} (lines with markers). Adapted with permission.[99] Copyright 2017, John Wiley and Sons.

	V_{OC} [V]	J_{SC} [mA/cm^2]	FF [%]	PCE[%]
C_{60}	1.01 ± 0.02 [1.03]	21.2 ± 0.4 [21.7]	73.0 ± 0.8 [73.8]	15.4 ± 0.9 [16.49]
PCBM	1.03 ± 0.03 [1.05]	22.0 ± 0.4 [22.6]	70.2 ± 0.9 [71.2]	15.9 ± 1.8 [16.89]
ICTA	1.08 ± 0.01 [1.10]	21.3 ± 0.5 [22.1]	72.5 ± 0.7 [74.2]	17.04 ± 1.2 [18.04]
PS I C_{60}	1.13 ± 0.02 [1.16]	21.8 ± 0.7 [22.3]	74.5 ± 0.9 [75.2]	18.61 ± 0.5 [19.42]

Table 1: Photovoltaic Performance with different Fullerenes: Average photovoltaic parameters and standard-deviations of the presented batches obtained from JV scans at a scan speed of 60 mV/s. The numbers in the brackets represent the numbers for the best-performing device per type. ^{a} : The J_{SC} was corrected to 100 mW/cm^2, since the illumination intensity varied slightly between measurements (98 ± 4 mW/cm^2, error ≈ 4%).

Without the PS interlayer, devices with ICTA, which has the lowest electron affinity, *i.e.* , the highest lying LUMO among the fullerenes tested here, exhibit the highest V_{OC} while C_{60}, with the lowest lying LUMO, leads to the lowest V_{OC}. Devices with PCBM, of intermediate electron affinity, complete the series. These data suggest a direct correlation between the energetics of the electron-transporting material and the achievable V_{OC}, as noted before. However, the highest V_{OC} among all of our cells is realized upon inserting an ultrathin tunneling layer (PS) between the perovskite and C_{60}, despite the high electron affinity of this fullerene. A slight improvement of the V_{OC} (0.03 V) using PS has been previously reported compared to a reference device employing PCBM by Wang *et. al.* ,37 explaining this by improved charge separation. In our study, the use of PS raises the V_{OC} by as much as 130 mV (on average 120 mV), compared to the C_{60} reference device, while retaining high FF > 70%. Notably, this V_{OC} enhancement is consistent over a broad range of illumination intensities (Figure S3, SI), meaning that it is not related to simple charge accumulation effects but must have its reason in the overall improved generation-recombination balance.

3.4 ENERGY LEVEL ALIGNMENT

The alignment of the fullerenes' LUMO and highest occupied molecular orbital (HOMO) levels relative to the band edges of the perovskite was analyzed by inverse photoelectron spectroscopy (IPES) and ultraviolet photoelectron spectroscopy (UPS) on samples closely resembling devices (perovskite | ETL stacks on fully covered glass | ITO | PTAA substrates). The spectra shown in Figure 19a,b reveal a somewhat unexpected result. Apart from the C_{60}-only samples (*i. e.* , C_{60} and PS | C_{60}), all fullerene derivatives have their LUMO level onsets (as determined from the linear extrapolation of the dominant IPES signal in the linear plot) above the perovskite conducting band minimum. This is in accordance with the level alignment in MAPI-fullerene stacks reported earlier, though there is a wide spread in literature values.[138–143] However, the IPES spectra also show that the density of unoccupied states in the fullerene layers tails down to the perovskites' conduction-band edge, meaning that barrier-free injection of electrons across the hybrid interface should still be possible. This is in concert with the finding that all of our cells exhibit high FFs, irrespective of the fullerene LUMO position. Furthermore, the energy offset between the perovskites' valance-band minimum and the onset of occupied states in the fullerene is small (≈200 meV), again with a notable component of the fullerene density of states (DOS) reaching into the bandgap (see logarithmic representation in Figure S6, SI). The only exception is PS | C_{60}, where we measure an offset >300 meV, which we attribute to electronic decoupling of the perovskite and C_{60} by the inert PS. There is a very similar secondary electron cut-off of the PS | C_{60} sample compared to the pristine MAPI layer, suggesting vacuum level alignment. Neither the work function nor the valence band/HOMO spectra determined (by UPS) before and after the extensive (approximately hours) IPES measurements changed significantly, indicative of negligible sample damage under our experimental conditions. This ascertains the validity of the IPES measurements.

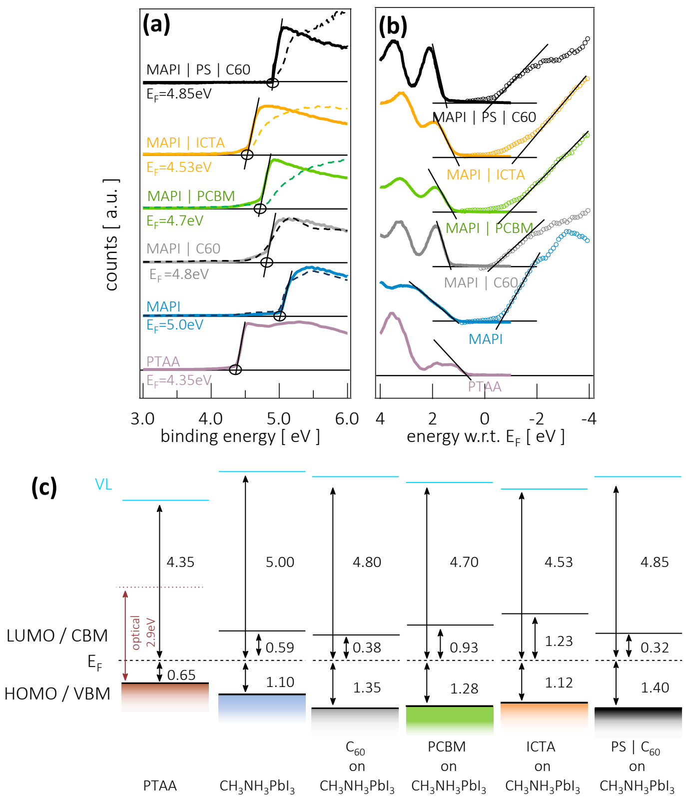

Figure 19: a,b) Secondary electron cut-off (full line before and dashed line after IPES) (a) and IPES spectra of all layers in the stack in device-like samples (ITO | PTAA | MAPI | ETL) (b). c) Schematic energy-level diagram of the different layers relative to E_F. The solution-processed ETLs were ≈50 nm thick. Adapted with permission.[99] Copyright 2017, John Wiley and Sons.

3.5 VOLTAGE LOSS ANALYSIS

We used TRPL to monitor the fate of photogenerated carriers through their time dependence of radiative recombination. Figure 20c shows representative TRPL traces of films with the respective transport layers without electrodes. The signal of the pristine perovskite layer on glass exhibits an initial fast drop of the PL intensity followed by an almost monoexponential decay (marked by a red dashed line in Figure 20c) with a lifetime of >100 ns. Capping the perovskite top surface with C_{60} or PCBM causes a vast reduction of the PL lifetime.[31] Based on the energetic structure in Figure 18 and data in the literature, this acceleration of the PL decay kinetics is assigned to fast electron transfer to the fullerene layer. The other fullerene derivatives quench the fluorescence likewise, however not as strongly as C_{60} and behave consistently with the energy offset for electron transfer; higher lying LUMO levels result in longer PL lifetimes. Quenching of the PL is efficient even with ICTA, which exhibits the highest lying LUMO among the studied fullerenes. Inserting the PS interlayer between MAPI and C_{60} increases the PL lifetime to a larger extent than increasing the LUMO energy. Films with this layer decay to background level on substantially longer timescales (≈250 ns) than the signal of all fullerene-containing samples without the blocking layer (≈30 ns), though still faster than the pristine film (PS has no effect, not shown).

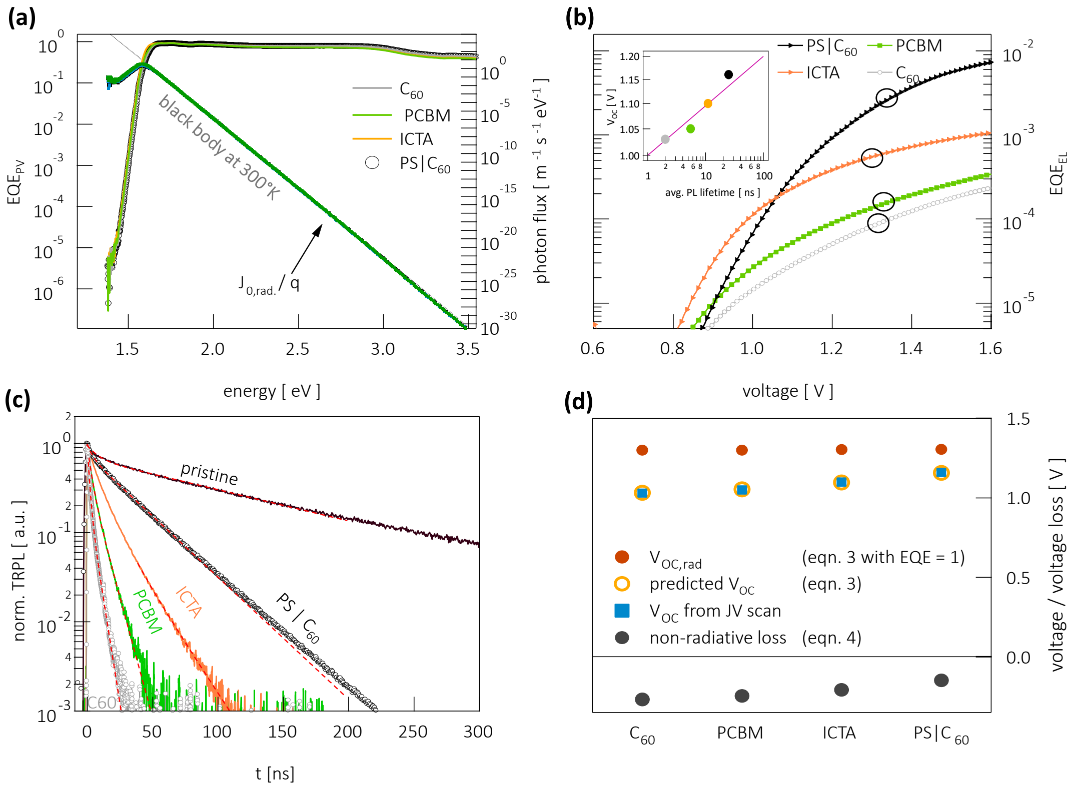

Figure 20: EQE$_{PV}$ and $J_{0,rad.}/q = \phi_{emission}$ spectra of the different systems. b) EQE$_{EL}$ as a function of applied forward bias. The circles indicate the values at injection current densities equivalent to J_{SC} under 1 sun illumination. The inset shows the EQE$_{EL}$ versus average fluorescent lifetime with a line as a linear reference. c) Fluorescence decays of MAPI films in device-like architecture with and without (denoted as pristine) the adjacent ETLs with biexponential fits (red dashed lines). d) The open-circuit voltages obtained from JV-scans (blue squares) as well as the calculated values (orange open circles) with the corresponding open-circuit voltages in their radiative limit (red circles) and nonradiative losses (gray full circles). Adapted with permission.[99] Copyright 2017, John Wiley and Sons.

Electroluminescence was performed to measure the external radiative efficiencies (expressed as the EQE$_{EL}$). According to detailed balance[144] and Rau's reciprocity relation[43], an ideal solar cell is likewise an ideal light-emitting device. Normalized EL spectra of the different devices are shown in Figure S8 (SI). Within the spectral range recorded, all samples exhibit the same emission spectrum, which is assigned to the radiative recombination of injected charge in the perovskite layer. Changing the ETL has no effect on the spectral shape, meaning that no additional *radiative* recombination channels (*e.g.* across-interfaces) are introduced.The intensity however vastly changes. For injection currents equivalent to J_{SC} at AM1.5G illumination, lifting the LUMO level position by going from C$_{60}$ to ICTA increases the EQE$_{EL}$ by nearly one order of magnitude, from $7 \cdot 10^{-5}$ to $5 \cdot 10^{-4}$. Adding the PS interlayer causes a further push of the EQE$_{EL}$ to $3 \cdot 10^{-3}$, which is the highest efficiency of all the devices. This means that nonradiative recombination of injected charge becomes progressively suppressed upon lifting the LUMO level, and it is further reduced upon addition of the PS layer. In accord with RRR V_{OC} can be reconstructed[145] or predicted[146] from the measurement of the EQE$_{PV}$ and EQE$_{EL}$. Convoluting the EQE$_{PV}$ with the solar spectrum renders J_{SC}, whereas convolution with blackbody spectrum at 300°K yields $J_{0,rad.}$ with Equation 49 and 38:

$$J_{em.,0} = J_{0,rad.} = q\phi_{emission,0} = q\int EQE_{PV}\phi_{BB}(E)\,dE$$

and

$$J_{SC} = q\int EQE_{PV}(E)\phi_{Sun}(E)\,dE\,.$$

The V_{OC} can then be calculated with Equation 51:

$$V_{OC} = \frac{k_B T}{q}\cdot \ln\left[EQE_{EL}\frac{J_{SC}}{J_{em.,0}}\right]\,.$$

It is noteworthy that all EQE_{EL} versus voltage curves exhibit a pronounced dependence on the injection current (Figure S2,SI). This is a well-known effect, attributed to trap-assisted recombination at low carrier densities. Therefore, in Equation 51, values for EQE_{EL} were taken at $J_{inj.} = J_{SC}$. These values are marked with rings in Figure 20b. In addition, we plot in Figure 20a the EQE_{PV} spectra of all device architectures, together with the black body spectrum at 300°K. Within the spectral range considered (and the resolution of the employed EQE measurement setup), all samples exhibit the same shape and magnitude. In agreement with these conclusions from the great similarity of the EL spectra, this finding implies that the choice of fullerene does not open new pathways for the photogeneration (and radiative recombination) of charges. Accordingly, $J_{0,rad.}$ calculated from these spectra with Equation 49 varies only little among the samples, uncorrelated to the LUMO level. Finally, Figure 20d compares the calculated V_{OC} values with those obtained from the JV scans and the nonradiative V_{OC} loss according to Equation 51:

$$\Delta V_{OC,\text{nonrad.}} = \frac{k_B T}{q}\cdot \ln(EQE_{EL})\,.$$

The above results show a direct correlation between the V_{OC} of the hybrid device and the external electroluminescence efficiency, but also with the lifetime of photoluminescence from the active perovskite material. First the strict relation between V_{OC} and EQE_{EL} is addressed. According to above equations, any increase in V_{OC} must have its origin in a larger J_{SC}, a smaller $J_{0,rad.}$, a higher EQE_{EL}, or a combination of these effects. The choice of the fullerene, deposition method, or whether or not an extra thin polymer layer is inserted, have a negligible effect on the shape and magnitude of the EQE_{PV}, which means the intrinsic optical and optoelectronic properties of the active perovskite, particular its ability to generate and transport charges, are virtually the same for all studied cells. Therefore, one can rule out a significant penetration of the fullerenes into the perovskite bulk. This is in accordance with the observation of a dense and high-quality perovskite layer, rendering fullerene penetration deep into the active material quite unlikely. Consistently the shape of the emission spectrum (in EL and PL) is not affected by use of different fullerenes (or the addition of the thin PS layer). Therefore the increase in V_{OC} cannot be attributed to variations in J_{SC} or $J_{0,rad.}$, but is entirely due to an increase in the EQE_{EL}. This increase in turn originates from suppression of nonradiative pathways related to the perovskite/organic interface. The second important observation is the strict correlation between V_{OC} and the PL lifetime (see inset in Figure 20b). The PL measurements are performed in the absence of an electric field – on complete layer stacks but without the electrodes – therefore carrier motion across the layer is only due to diffusion, especially under low excitation condition. Organometallic perovskites are special in combining a long bulk carrier lifetime,[147] high charge-carrier mobility, and diffusion coefficients with large extinction coefficients.[148] With reported mobilities of ≈10 cm^2/Vs, charges in MAPI will diffuse through the active layer within a few nanoseconds and approach interfaces multiple times. Therefore, the overall prolongation of the PL lifetime when either raising the fullerene LUMO level or adding a PS blocking layer is a consequence of a reduced rate of electron extraction and/or accelerated reinjection at the perovskite/organic interface. Consequently, carriers photogenerated at V_{OC} will frequently approach the perovskite/ETL interface during their lifetime and eventually become transferred. The strong correlation between PL lifetime and V_{OC} implies that extracted electrons are not stored on the ETL under these illumination conditions, but that they undergo and possibly foster nonradiative recombination, most likely at the interface with long-lived holes situated on the perovskite. This picture is in accordance with recent results from transient absorption spectroscopy, time-resolved microwave conductivity (TRMC) and transient photocurrent measurements and a combined measurement/simulation approach by Krogmeier *et. al.* [63, 149–151] Also, given the weak extraction barrier for holes observed from UPS, holes may likewise be injected from the perovskite to the fullerene. Due to the low dielectric constant and a high density of high energy vibronic transistions in organic semiconductors fast recombination - either raditive or nonradiative - will proceed rapidly[1]. The main consequence of raising the LUMO position therefor is then to slow down extraction of electrons to the organic layer or to accelerate reinjection increasing the probability that photogenerated electrons contribute to radiative recombination on the active perovskite instead of nonradiative recombination at the interface. The fact that insertion of the PS interlayer increases the PL lifetime is direct evidence for an additional slow-down of electron extraction, resulting in a further suppression of nonradiative recombination. Contrary to an often cited figure-of-merit within the perovskite community,*PL quenching* is in fact detrimental to V_{OC} if the extracted charges participate in nonradiative recombination. In full devices, the photoluminescence should be quenched only at short-circuit, whereas at open-circuit and at the maximum power point strong luminescence is desirable for high efficiency. Inserting a thin PS layer has enables prolonged PL lifetimes and stronger radiative recombination while still enabling efficient extraction under steady state illumination conditions, as seen by the high FF in devices. The results of our study also highlight a key feature of perovskite solar cells: These cells are strongly emissive with EQE_{EL} on the order of 0.01-0.3%, meaning that open-circuit voltages are roughly 150 meV within reach of their radiative limit. These considerations underline the impressive progress this technology made within a short time span, putting it already close to the extensively engineered GaAs or CdTe solar cells in terms of their low loss in potential, despite their solution processability and low fabrication cost. To get an estimate of the minimum achievable voltage loss, we calculated $J_{0,rad.}$ by assuming a step-like absorption onset, yielding $J_{0,rad.,min} \approx 10^{-20}$ A m^{-2} for an optical bandgap of 1.6 eV and 100% absorption. Assuming further that all photons absorbed contribute to the photocurrent, the absolute radiative V_{OC} limit is about 1.33 V (this implies an insurmountable radiative voltage loss of 0.27 V at 300°K). Our devices show a fourfold to tenfold higher $J_{0,rad.}$, corresponding to an additional radiative loss of about 40-60 meV, and a radiative limit up to 1.29 V, due to an imperfect absorption onset (the Urbach energy, E_U, of our devices is ≈13.8-14.2 meV, Figure S1, SI). These values are remarkably close to the values calculated by Staub *et. al.* [152] who measured a very similar absorber, but additionally considered parasitic absorption of adjacent layers, photon-recycling within the active layer and nonideal in/outcoupling efficiencies in a solar cell stack similar to ours (ITO | PEDOT | Perovskite | PCBM | ZnO). Overall, the nonradiative losses in our devices still impose the greater penalty (>100 meV nonradiative versus 40-60 meV radiative), in accord with the highest reported V_{OC} values for perovskite solar cells with comparable bandgaps. During the preparation and review of this paper, several authors reported similar radiative efficiencies and correspondingly high V_{OC}'s by employing novel charge-transporting materials or by proper interface design. Xue *et. al.* introduced didydromethano/indene fullerene [C_{60} (CH_2)(Ind)] as an alternative ETL, where the replacement of PCBM by C_{60} (CH_2)(Ind) increased the V_{OC} in MAPI-based devices from 1.05 to 1.13 V.[153] Based on an observed increase in lifetimes in TRPL and TPV experiments, the authors concluded effective suppression of trap-assisted charge recombination to be the main origin of the improved device performance. Cho *et. al.* employed composition engineering to form a thin higher-bandgap perovskite interlayer between $(FAPbI_3)_{0.85}(MAPbBr_3)_{0.15}$ and the HTL.[154] As a consequence of electron blocking and reduced

---

[1] above it was indicated that in comparing PL (without transport layers) and EL no new spectral features appeared, therefore radiative recombination induced by the ETL can be excluded

interfacial recombination, these devices had a V_{OC} of 1.16 eV. These reports highlight the importance of reduction of interfacial recombination because of the herein shown reasons.

CONCLUSION In summary, we thoroughly investigated the role of the ETL on the open-circuit voltage of perovskite solar cells using the standard MAPI. We show that C_{60} and its soluble analogs PCBM and ICTA – despite allowing for decent efficiencies and reasonably high V_{OC} – are not ideal candidates to form the ETLs. We attribute this to significant electron-extraction to the electron-transporting material followed by interface-mediated nonradiative recombination with holes on either the perovskite or the fullerene, the latter process being enabled by the small energy offset between the perovskite valence-band maximum (VBM) and the HOMO onset of the fullerenes. This interpretation is full accord with results from very recent TRMC data by Hutter *et. al.* [150] showing high electron- but also hole-extraction velocities from MAPI to C_{60} and PCBM, which then are possessively reduced when employing higher adduct fullerenes such as ICBA. According to our study, inserting a thin interlayer of PS between MAPI and C_{60} is more efficient in reducing electron-extraction and interfacial recombination at V_{OC} than raising the LUMO level position by employing higher adduct fullerenes, highlighting the importance of interfacial dynamics. As a result, we succeeded in preparing devices with radiative efficiencies of up to 0.3%, leading to V_{OC}'s as high as 1.16 V and PCEs of up to 19.4%. Our results show that reduction of nonradiative recombination mediated by the charge-transport layers, due to improved charge-blocking, outcompetes energetic alignment in the search for ideal selective contacts for high V_{OC} devices.

[98] M. Bradler and E. Riedle. “Temporal and spectral correlations in bulk continua and improved use in transient spectroscopy.” In: *Journal of the Optical Society of America B* 31.7 (July 2014), p. 1465 (cit. on p. 40).

[99] Christian M. Wolff et al. “Reduced Interface-Mediated Recombination for High Open-Circuit Voltages in CH3NH3PbI3Solar Cells.” In: *Advanced Materials* 29.28 (2017) (cit. on pp. 43, 46–48, 50, 82, 85, 98, 111, 122, 123, 127, 129, 131, 138).

[100] Michael M. Lee et al. “Efficient Hybrid Solar Cells Based on Meso-Superstructured Organometal Halide Perovskites.” In: 338.November (2012), pp. 643–647 (cit. on pp. 44, 67).

[101] Jin Hyuck Heo et al. “Efficient inorganic–organic hybrid heterojunction solar cells containing perovskite compound and polymeric hole conductors.” In: *Nature Photonics* 7.6 (May 2013), pp. 486–491 (cit. on p. 44).

[102] Zhengguo Xiao et al. “Solvent Annealing of Perovskite-Induced Crystal Growth for Photovoltaic-Device Efficiency Enhancement.” In: *Advanced Materials* 26.37 (Oct. 2014), pp. 6503–6509 (cit. on pp. 44, 62).

[103] Chong Liu et al. “A fully integrated nanosystem of semiconductor nanowires for direct solar water splitting.” In: *Nano Letters* 13.6 (June 2013), pp. 2989–92 (cit. on p. 44).

[104] Olga Malinkiewicz et al. “Metal-Oxide-Free Methylammonium Lead Iodide Perovskite-Based Solar Cells: the Influence of Organic Charge Transport Layers.” In: *Advanced Energy Materials* 4.15 (Oct. 2014), p. 1400345 (cit. on p. 44).

[105] Qi Chen et al. “Planar heterojunction perovskite solar cells via vapor-assisted solution process.” In: *Journal of the American Chemical Society* 136.Scheme 1 (2013), pp. 3–6 (cit. on p. 44).

[106] Huanping Zhou, Qi Chen, and Yang Yang. “Vapor-assisted solution process for perovskite materials and solar cells.” In: *MRS Bulletin* 40.08 (Aug. 2015), pp. 667–673 (cit. on p. 44).

[107] Carolin M. Sutter-Fella et al. “High Photoluminescence Quantum Yield in Band Gap Tunable Bromide Containing Mixed Halide Perovskites.” In: *Nano Letters* 16.1 (2016), pp. 800–806 (cit. on p. 44).

[108] Pablo Docampo et al. “Efficient organometal trihalide perovskite planar-heterojunction solar cells on flexible polymer substrates.” In: *Nature communications* 4 (2013), p. 2761 (cit. on p. 44).

[109] Julian Burschka et al. “Sequential deposition as a route to high-performance perovskite-sensitized solar cells.” In: *Nature* 499.7458 (2013), pp. 316–9 (cit. on p. 44).

[110] Akihiro Kojima et al. “Organometal halide perovskites as visible-light sensitizers for photovoltaic cells.” In: *Journal of the American Chemical Society* 131.17 (2009), pp. 6050–6051 (cit. on pp. 44, 67).

[111] Zonglong Zhu et al. “Mesoporous SnO 2 single crystals as an effective electron collector for perovskite solar cells.” In: *Physical Chemistry Chemical Physics* 17.28 (2015), pp. 18265–18268 (cit. on p. 44).

[112] Juan Pablo Correa Baena et al. “Highly efficient planar perovskite solar cells through band alignment engineering.” In: *Energy & Environmental Science* 8.10 (2015), pp. 2928–2934 (cit. on p. 44).

[113] Dianyi Liu and Timothy L. Kelly. "Perovskite solar cells with a planar heterojunction structure prepared using room-temperature solution processing techniques." In: *Nature Photonics* 8.2 (2013), pp. 133–138 (cit. on p. 44).

[114] Christopher Manspeaker et al. "Reliable Annealing of CH3NH3PbI3 Films Deposited on ZnO." In: *Journal of Physical Chemistry C* 120.12 (2016), pp. 6377–6382 (cit. on p. 44).

[115] Pablo Docampo et al. "Efficient organometal trihalide perovskite planar-heterojunction solar cells on flexible polymer substrates." In: *Nature Communications* 4 (Nov. 2013) (cit. on p. 44).

[116] Jun Hong Noh et al. "Nanostructured TiO2/CH3NH3PbI3 heterojunction solar cells employing spiro-OMeTAD/Co-complex as hole-transporting material." In: *Journal of Materials Chemistry A* 1.38 (2013), p. 11842 (cit. on p. 44).

[117] Cheng Bi et al. "Understanding the formation and evolution of interdiffusion grown organolead halide perovskite thin films by thermal annealing." In: *J. Mater. Chem. A* 2.43 (2014), pp. 18508–18514 (cit. on p. 44).

[118] Jingbi You et al. "Improved air stability of perovskite solar cells via solution-processed metal oxide transport layers." In: *Nature Nanotechnology* 11.1 (Oct. 2015), pp. 75–81 (cit. on p. 44).

[119] Seungchan Ryu et al. "Voltage output of efficient perovskite solar cells with high open-circuit voltage and fill factor." In: *Energy & Environmental Science* 7.8 (June 2014), p. 2614 (cit. on p. 44).

[120] Sadia Ameen et al. "Perovskite Solar Cells: Influence of Hole Transporting Materials on Power Conversion Efficiency." In: *ChemSusChem* 9.1 (Jan. 2016), pp. 10–27 (cit. on p. 44).

[121] Weibo Yan et al. "Increasing open circuit voltage by adjusting work function of hole-transporting materials in perovskite solar cells." In: *Nano Research* 9.6 (June 2016), pp. 1600–1608 (cit. on p. 44).

[122] Yi Hou et al. "Overcoming the Interface Losses in Planar Heterojunction Perovskite-Based Solar Cells." In: *Advanced Materials* 28.25 (July 2016), pp. 5112–5120 (cit. on pp. 44, 121).

[123] Kristofer Tvingstedt et al. "Removing Leakage and Surface Recombination in Planar Perovskite Solar Cells." In: *ACS Energy Letters* 2.2 (Jan. 2017), pp. 424–430 (cit. on pp. 44, 67, 85, 112).

[124] Qi Wang et al. "Large fill-factor bilayer iodine perovskite solar cells fabricated by a low-temperature solution-process." In: *Energy Environ. Sci.* 7.7 (2014), pp. 2359–2365 (cit. on p. 45).

[125] Chun-Guey Wu, Chien-Hung Chiang, and Sheng Hsiung Chang. "A perovskite cell with a record-high-V oc of 1.61 V based on solvent annealed CH 3 NH 3 PbBr 3 /ICBA active layer." In: *Nanoscale* 8.7 (2016), pp. 4077–4085 (cit. on pp. 45, 127).

[126] Yuchuan Shao, Yongbo Yuan, and Jinsong Huang. "Correlation of energy disorder and open-circuit voltage in hybrid perovskite solar cells." In: *Nature Energy* 1.1 (Jan. 2016), p. 15001 (cit. on p. 45).

[127] Jun-Yuan Jeng et al. "CH 3 NH 3 PbI 3 Perovskite/Fullerene Planar-Heterojunction Hybrid Solar Cells." In: *Advanced Materials* 25.27 (July 2013), pp. 3727–3732 (cit. on p. 45).

[128] Lidón Gil-Escrig et al. "Fullerene imposed high open-circuit voltage in efficient perovskite based solar cells." In: *J. Mater. Chem. A* 4.10 (2016), pp. 3667–3672 (cit. on p. 45).

[129] Hyunbum Kang et al. "Controlling Number of Indene Solubilizing Groups in Multiadduct Fullerenes for Tuning Optoelectronic Properties and Open-Circuit Voltage in Organic Solar Cells." In: *ACS Applied Materials & Interfaces* 4.1 (Jan. 2012), pp. 110–116 (cit. on p. 45).

[130] Shaohua Huang et al. "Beyond PCBM: methoxylated 1,4-bisbenzyl[60]fullerene adducts for efficient organic solar cells." In: *J. Mater. Chem. A* 4.2 (2016), pp. 416–424 (cit. on p. 45).

[131] Steve Albrecht et al. “On the Efficiency of Charge Transfer State Splitting in Polymer:Fullerene Solar Cells.” In: *Advanced Materials* 26.16 (Apr. 2014), pp. 2533–2539 (cit. on p. 45).

[132] Qi Wang et al. “Thin Insulating Tunneling Contacts for Efficient and Water-Resistant Perovskite Solar Cells.” In: *Advanced Materials* 28.31 (Aug. 2016), pp. 6734–6739 (cit. on pp. 45, 82).

[133] Namyoung Ahn et al. “Thermodynamic Regulation of CH3NH3PbI3 Crystal Growth and Its Effect on Photovoltaic Performance of Perovskite Solar Cell.” In: *J. Mater. Chem. A* (2015) (cit. on pp. 45, 46).

[134] Jin Wook Lee, Hui Seon Kim, and Nam Gyu Park. “Lewis Acid-Base Adduct Approach for High Efficiency Perovskite Solar Cells.” In: *Accounts of Chemical Research* 49.2 (2016), pp. 311–319 (cit. on pp. 45, 46).

[135] W. S. Yang et al. “High-performance photovoltaic perovskite layers fabricated through intramolecular exchange.” In: *Science* May (2015), pp. 1–8 (cit. on pp. 45, 77).

[136] Wei Zhang et al. “Ultrasmooth organic–inorganic perovskite thin-film formation and crystallization for efficient planar heterojunction solar cells.” In: *Nature Communications* 6 (Jan. 2015), p. 6142 (cit. on pp. 46, 67).

[137] Jacob Tse-Wei Wang et al. “Efficient perovskite solar cells by metal ion doping.” In: *Energy Environ. Sci.* 9.9 (2016), pp. 2892–2901 (cit. on p. 46).

[138] Yuchuan Shao et al. “Origin and elimination of photocurrent hysteresis by fullerene passivation in CH3NH3PbI3 planar heterojunction solar cells.” In: *Nat Commun* 5 (Dec. 2014) (cit. on p. 48).

[139] Selina Olthof. “Research Update: The electronic structure of hybrid perovskite layers and their energetic alignment in devices.” In: *APL Materials* 4.9 (Sept. 2016), p. 091502 (cit. on p. 48).

[140] Jennifer Emara et al. “Impact of Film Stoichiometry on the Ionization Energy and Electronic Structure of CH 3 NH 3 PbI 3 Perovskites.” In: *Advanced Materials* 28.3 (Jan. 2016), pp. 553–559 (cit. on p. 48).

[141] Philip Schulz et al. “Electronic Level Alignment in Inverted Organometal Perovskite Solar Cells.” In: *Advanced Materials Interfaces* 2.7 (May 2015), p. 1400532 (cit. on p. 48).

[142] Ming-fai Lo et al. “Electronic Structures and Photoconversion Mechanism in Perovskite/-Fullerene Heterojunctions.” In: *Advanced Functional Materials* 25.8 (Feb. 2015), pp. 1213–1218 (cit. on p. 48).

[143] Chenggong Wang et al. “Electronic structure evolution of fullerene on CH3NH3PbI3.” In: *Applied Physics Letters* 106.11 (2015) (cit. on p. 48).

[144] William Shockley and Hans J. Queisser. “Detailed Balance Limit of Efficiency of p-n Junction Solar Cells.” In: *Journal of Applied Physics* 32.3 (Mar. 1961), pp. 510–519 (cit. on pp. 50, 72).

[145] Kristofer Tvingstedt et al. “Radiative efficiency of lead iodide based perovskite solar cells.” In: *Scientific Reports* 4 (Aug. 2014), p. 6071 (cit. on pp. 50, 72, 85, 86, 121).

[146] Wolfgang Tress et al. “Predicting the Open-Circuit Voltage of CH 3 NH 3 PbI 3 Perovskite Solar Cells Using Electroluminescence and Photovoltaic Quantum Efficiency Spectra: the Role of Radiative and Non-Radiative Recombination.” In: *Advanced Energy Materials* 5.3 (Feb. 2015), p. 1400812 (cit. on pp. 50, 72, 121).

[147] Yasuhiro Yamada et al. “Dynamic Optical Properties of CH ₃ NH ₃ PbI ₃ Single Crystals As Revealed by One- and Two-Photon Excited Photoluminescence Measurements.” In: *Journal of the American Chemical Society* 137.33 (Aug. 2015), pp. 10456–10459 (cit. on p. 51).

[148] Laura M. Herz. “Charge-Carrier Dynamics in Organic-Inorganic Metal Halide Perovskites.” In: *Annual Review of Physical Chemistry* 67.1 (May 2016), pp. 65–89 (cit. on pp. 51, 71).

[149] Tomas Leijtens et al. “Carrier trapping and recombination: the role of defect physics in enhancing the open circuit voltage of metal halide perovskite solar cells.” In: *Energy Environ. Sci.* 9.11 (2016), pp. 3472–3481 (cit. on pp. 52, 110, 125).

[150] Eline M. Hutter et al. “Charge Transfer from Methylammonium Lead Iodide Perovskite to Organic Transport Materials: Efficiencies, Transfer Rates, and Interfacial Recombination.” In: *Advanced Energy Materials* (Feb. 2017), p. 1602349 (cit. on pp. 52, 53, 111, 123–125).

[151] Benedikt Krogmeier et al. “Quantitative Analysis of the Transient Photoluminescence of CH 3 NH 3 PbI 3 /PC 61 BM Heterojunctions by Numerical Simulations.” In: *Sustainable Energy & Fuels* 00 (2018), pp. 1–8 (cit. on pp. 52, 123, 124).

[152] Florian Staub et al. “Beyond Bulk Lifetimes: Insights into Lead Halide Perovskite Films from Time-Resolved Photoluminescence.” In: *Physical Review Applied* 6.4 (Oct. 2016), p. 044017 (cit. on pp. 52, 71, 72, 86, 97, 123).

[153] Qifan Xue et al. “Dual Interfacial Modifications Enable High Performance Semitransparent Perovskite Solar Cells with Large Open Circuit Voltage and Fill Factor.” In: *Advanced Energy Materials* (Dec. 2016), p. 1602333 (cit. on p. 52).

[154] Kyung Taek Cho et al. “Highly efficient perovskite solar cells with a compositionally engineered perovskite/hole transporting material interface.” In: *Energy Environ. Sci.* 10.2 (2017), pp. 621–627 (cit. on pp. 52, 129, 131).

4

HOW TO MAKE >20% PEROVSKITE SOLAR CELLS IN INVERTED ARCHITECTURE

This chapter is focusing on delivering a detailed description of the methods used to make highly efficient inverted (p-i-n) perovskite solar cells. The ambiguity in reported methods and the lack of detail make reproducibility particularly difficult. Motivated by this, we sought to enable more researchers to adopt reliable protocols and help identifying/avoiding pitfalls, we already encountered.

This chapter is an adapted preprint of:

How to Make over 20% Efficient Perovskite Solar Cells in Regular (n-i-p) and Inverted (p-i-n) Architectures

Michael Saliba*, Juan-Pablo Correa-Baena*, Christian M. Wolff*, Martin Stolterfoht, Nga Phung, Steve Albrecht, Dieter Neher, Antonio Abate

published in : *Chem. Mater. 2018, 30, 13, 4193-4201*

* the first three authors contributed equally to this work

4.1 BROADER CONTEXT

Among the many semiconductors employed in solar cells, few systems have – despite decades of research – reached very high efficiencies. Within only ten years after the initial demonstration, halide perovskite-based solar cell reached certified efficiencies of 25.2% and have thereby broken through the 20% ceiling. Although thousands of researchers are working on perovskite-based optoelectronic devices, reliable protocols on how to reach these efficiencies are scarce – at best. Having kept track of pitfalls and errors we developed robust methods for >20% devices – these are discussed herein. Although efficiencies are approaching the thermodynamic limitations, incomplete knowledge of fundamental working and degradation mechanisms restricts further progress that were often driven on the basis of trial-and-error. Likewise, deeper understanding arising from detailed description of fabrication is therefore crucial to improve device performances and long-term stability further. The rising complexity of perovskite compositions, including multiple cations, anions, and metals, renders reliable results rather difficult, especially when aiming at reproducing previous effects. Albeit fundamental research can be gained also from mediocre or bad-performing devices, the most meaningful insights stem from research that is conducted on high performing and reproducible devices that are frequently very different in nature from their less efficient counterparts, *e.g.* through varying defect chemistry. As a result of incomplete reports on device fabrication methodologies, a significant gap has emerged between groups that can achieve high-efficiency solar cells and groups that investigate fundamental properties of materials and devices. This naturally slows down progress and often even manifests in seemingly contradictory results. In this chapter, protocols that yield reproducible >20% devices in one of the main architectures – p-i-n structure – is presented. Regularly encountered problems, and the strategies to circumvent them, are discussed including observations on the basis of methods reported in literature.

4.2 SOLUTION PREPARATION

The preparation of the perovskite precursor solutions seems apparently simple, however, fractional variations in stochiometry[155], solution aging[156–158] and with this the formation of side-products from hydrolysis of solvents[159] form coordinating metal acid complexes [160–162] within perovskite precursors that impact performance and stability. Intentional additive engineering has been broadly studied, however, often methods start from different material purity levels. For example, commonly employed methylammonium iodide is synthesized by reacting metylamine with hydroiodic acid.[163] Hydroiodic acid can typically be purchased in two variations: non-stabilized – where I_2 rapidly forms as a byproduct – or stabilized with hypophosphorous acid. This stabilization agent, can – depending on the purification – remain as an "impurity" within the synthesized methylammonium iodide powder and active control of non-zero levels of this acid has actually allowed improving perovskite thin-film quality[164, 165]. Similarly, recent examples working on the fully inorganic perovskite $CsPbI_3$ have demonstrated, that simple solution heating of dimethylformamide (DMF) induces the formation of dimethylammonium iodide (DMAI),[166] which improved efficiency and stability of these devices.[1] Therefore, both preparation and storing conditions of the perovskite precursor solution are very delicate and likely affect the reproducibility, efficiency and stability of the devices. To reduced these impacts the first step is a controlled preparation environment, *i.e.* a nitrogen-filled glovebox with low water and oxygen content <10ppm. Solvents and salts should be comparably fresh and of high purity and recently calibrated balances and pipets are essential. Table 3 gives an overview of all employed materials and an exemplary recipe for a standard 83/17 triple-cation mix can be found in Table 4.

---

[1] whether one should call an *inorganic* perovskite – with *organic* molecules incorporated – *inorganic* is free to the choice of the reader

Substrate Cleaning

Pre-patterened ITO substrates (15 Ohm/sqr Lumtec or Automatic Research) are thoroughly cleaned using the following procedure in the list on page 148. The substrates should be processed further immediately after the cleaning. Letting the surface equilibrate may hamper with the wetting process of subsequent layers.

Hole-Transport-Layer Deposition

After cleaning the substrates are quickly transferred to a nitrogen-filled glovebox and after optical inspection and removal of possible dust/lint with a nitrogen gun the HTL is deposited by spin-coating 70 µL of the as-prepared solution of PTAA at 6000 rpm with minimal acceleration time for 30 s. Thereafter the substrates are annealed for 10 min. on a 100 °C hotplate and then cooled down for another 5 min. before further processing. To deposit the wetting-agent PFN-P2, 40µL of the as prepared solution are deposited, while the substrate is spinning at 6000 rpm. No annealing is necessary.

Perovskite Deposition

Halide perovskites are – thus far known – not found in nature, but man-made materials. The most widely studied among them is arguably methylammonium lead iodide – $CH_3NH_3PbI_3$, a direct semiconductor with 1.59eV bandgap and – as mentioned in the introduction of this thesis – several advantageous properties for optoelectronics. Initial solar cell fabrication runs based on the basis of so-called two-step deposition and led to first published results [167] were quickly replaced by new the so-called one-step deposition route with anti-solvent dripping – also refereed to as solvent-engineering[28]. The general idea is to initially complex the lead salts in the precursor solution with a Lewis-base (*e.g.* DMSO), which moderates – due to its comparably strong binding – the crystallization process. To facilitate this, excess solvent is washed away dynamically during the spin-coating process by applying a solvent, that mixes well with the actual perovskite solvent (DMF), but not the complexed perovskite salts themselves. Thereby crystallization is initiated already while spin-coating, because the thin liquid film is driven into super-saturation (the greatest part of the solvent is washed away), and the perovskite crystal precipitates top-to-bottom.

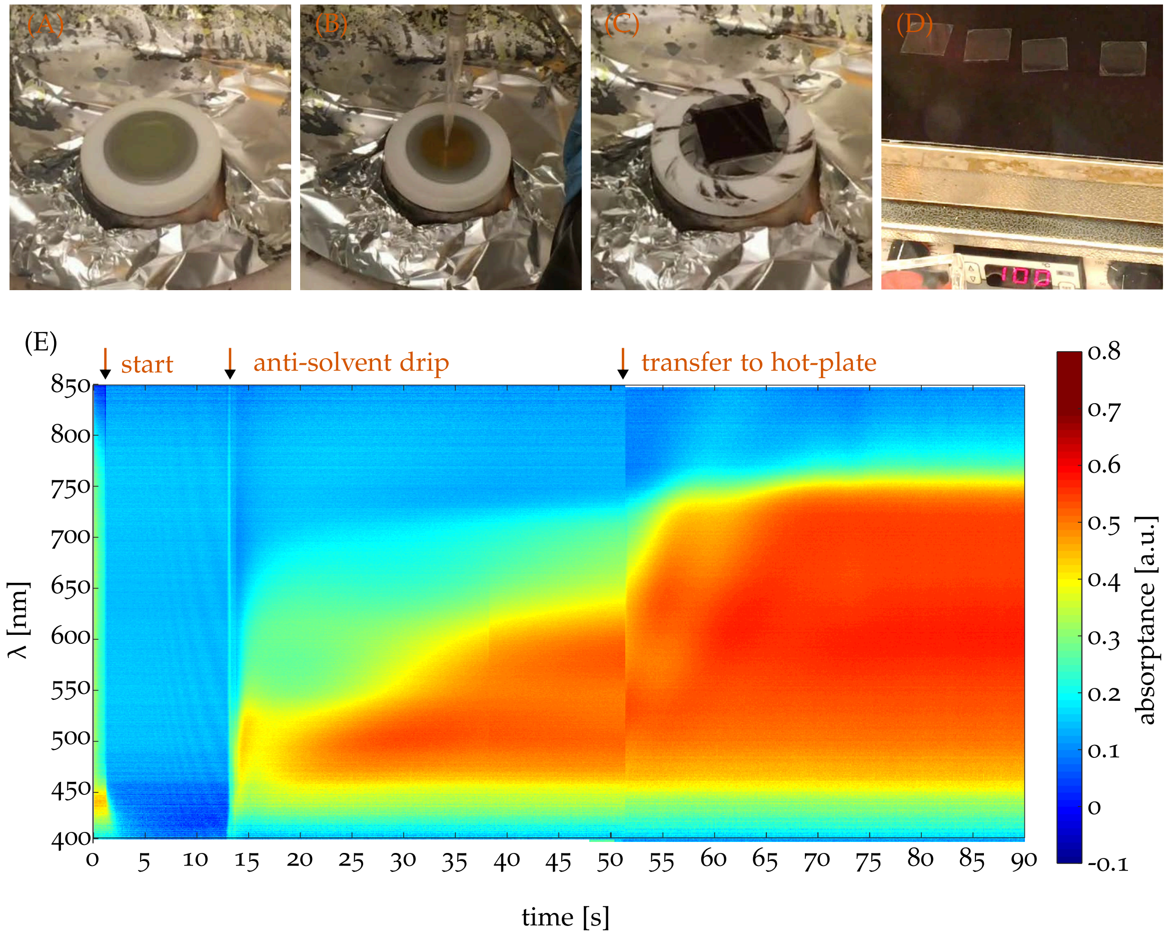

Figure 21: Perovskite Formation. (A) shows a photograph right after the start of the spin-coating, (B) during anti-solvent dripping, (C) after spin-coating and (D) on the hot-plate. In panel (E) the absorptance as a function of time during these processes is shown and the different steps are indicated by the orange arrows. Recorded at HZB, Berlin with assistance by C. Rehermann

Exemplary this is shown in Figure 21. In the top panel screenshots from a video of the deposition process are taken [168] at the relevant stages (start of spin-coating, anti-solvent application, after spin-coating, during annealing.) 150µL of a triple-cation perovskite are dispensed and spincoated at 4000rpm (~3000rpm/s acceleration) for 35s. Clearly visible is that the film initially starts from a light yellow color that changes to reddish-brown upon anti-solvent dripping and then to dark brown, when heat is applied. Additionally, *in-situ* absorption measurements shown in the lower panel show this the rather subjective observation also empirically. After the start of the spinning the liquid film thins (interference fringes at around 10 s), whereas strong absorption emerges at ~13s, when the anti-solvent is applied. The initial bandgap at around 700 nm then slowly shifts towards the "actual" bandgap at 780 nm and after transfer to the hotplate the main crystallization finishes within a few more seconds. Remnant solvent, heat and Lewis-base induce then dynamic thickness-fluctuations that subjectively change the color of the film a bit and can be seen by the broad and slowly disappearing interference fringes at times > 55 s around 800nm. Typically, 150 µL of perovskite precursor solution are centrally dropped on the substrate and accelerated to 4000 rpm within 2 s. After 10 s, 300 µL of ethyl acetate (EA) is dispensed on the sample and after another 25 s the sample is quickly transferred to a hotplate at 100 °C and annealed for 1 h.

Electron-Contact & Metal Deposition

C_{60} and 2,9-dimethyl-4,7-diphenyl-1,10-phenanthroline (BCP) are deposited via thermal evaporation in an ultrahigh vacuum. During the evaporation, the pressure is held constant at about 5×10^{-7} mbar. First, 30 nm C_{60} and then 8 nm BCP are evaporated at 0.1 Å/s on the complete perovskite film without masking, before finally a total of 80 to 100 nm of copper (Cu) is evaporated at 0.2-0.8 Å/s out of a molybdenum boat using a shadow mask to define the electrodes.

Pitfalls - Things to avoid

Due to experimental lab-to-lab variations, complete adaption of the shown methods may not always be possible. Still, several observed pitfalls w.r.t. device performance must be avoided.

SOLUTION PREPARATION Apart from obvious mistakes stemming from ill-calibrated balances or pipets a common source of error are vials and stir-bars. Both should be cleaned thoroughly with clean solvents. While high purity solvents seem naturally the right choice, caution must be taken. For example, ethanol at a purity of ~96% is preferable to higher purity grades, because the latter typically require metallic catalysts in the purification step, introducing minor metal amounts, not found in the distillation purified 96%, which contains primarily water as impurity. Likewise, stir-bars are potential sources of impurities, if not cleaned properly. To remove metal residues, *e. g. aqua regia* may be used, or stir-bars are removed and by using a vibrating vortex shaker.

SOLUTION DISSOLUTION AND MIXING Care must be taken to fully dissolve the precursors. Due to the formation of colloids the term *precursor solution* may be imprecise, but common. These colloids evolve over time and are in part responsible for the age-dependent film quality. From practical experience overnight dissolution (> 10 h) is sufficient to render clear solutions. Filtering with 0.2 µm PTFE filters with mild pressure (again a matter of experience) gives an indication of the colloid size, otherwise quantifiable with *e. g.* dynamic light scattering. Milky solutions are indicative of errors in the preparation and should be discarded.

PEROVSKITE DEPOSITION A successful perovskite deposition is shown in Figure 21, but errors may occur, if the glovebox temperature is too high (> 28 °C). Likewise the presence of substantial amounts of DMF/DMSO vapor may change the crystallization drastically[102]. To overcome this, the glovebox is typically purged with nitrogen during deposition and the spin-coater is regularly (every 2-3 samples) dried with a nitrogen gun and a designated hair drier.

TRANSFER AND EVAPORATION The glass | ITO | PTAA | perovskite substrates are transferred into an evaporation chamber without exposing them to air, which may induce unwanted oxidations or attract dust. The whole evaporation including Cu, BCP and C_{60} is typically completed under vacuum $p<10^{-6}$ mbar without breaking the vacuum in between steps. This requires a change of masks (open mask to shadow mask) under vacuum before evaporating the Cu. Breaking the vacuum between BCP and Cu irregularly results in lower efficiencies (only ≈10-15% PCE for reference cells), although the exact reason behind this is unclear. On the other hand, breaking the vacuum after the C_{60} layer did not result in efficiency losses. During the evaporation of the organic molecules, the deposition rates, or more precisely the heating temperatures should not exceed 400°C and 150° for C_{60} and BCP, respectively. C_{60} may dimerize at high temperatures, rendering impurities that may induce traps and BCP may form large clusters, which are insulating themselves, but leave plenty of area for metal/ C_{60} contact. For high metal deposition rates (>1 Å/s) Cu layers that are seemingly less shiny/reflective are produced, which yield poorer performing solar cells, possibly by fostering BCP clustering and partial oxidation of Cu.

4.3 SOLAR CELL PERFORMANCE TRACKING

Over the course of several years, more than 100 solar cell batches were prepared. The description of all variations goes beyond the scope of this thesis, but generic to all is that typically one parameter was optimized at a time. Exemplary, one major breakthrough optimization leading to the devices in Chapter 3 is shown in Figure 22, where two Lewis-bases (thiourea(TU) and DMSO) and their relative molar ratio is optimized.

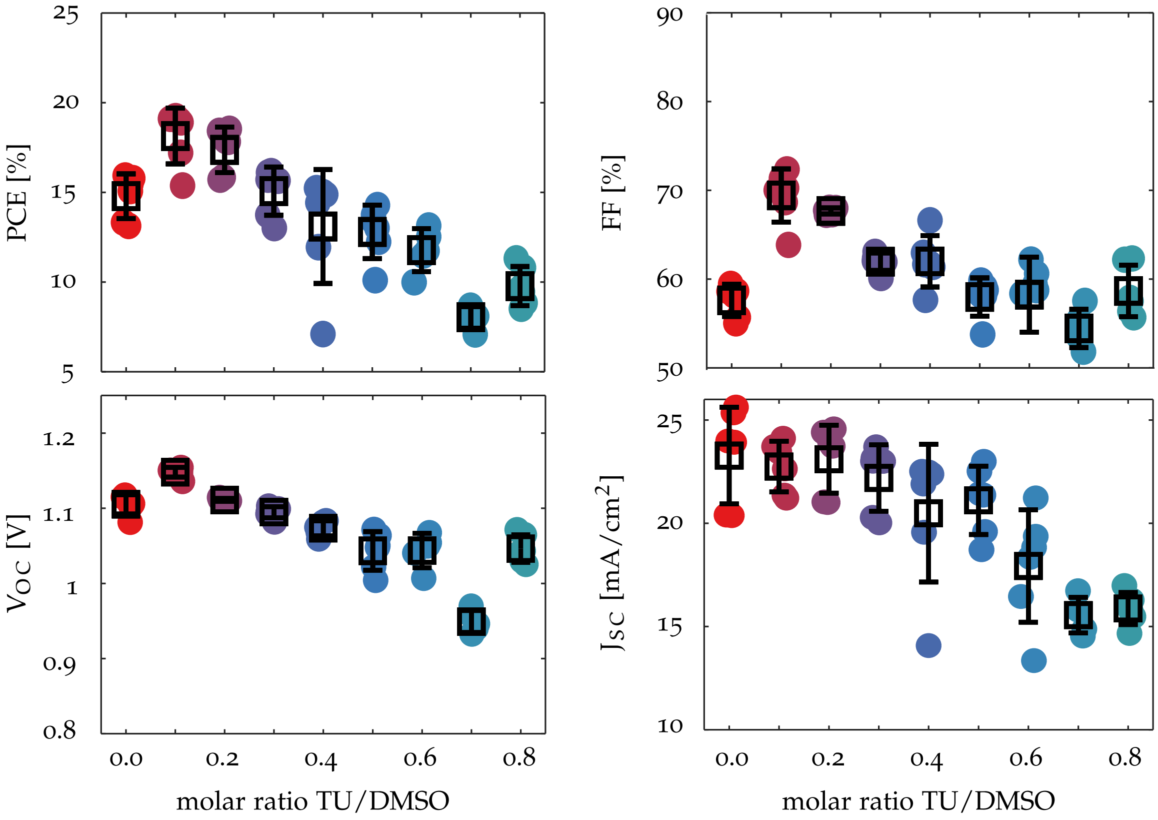

Figure 22: Exemplary Optimization Run. The four main figures-of-merit PCE, FF, V_{OC} and J_{SC} are plotted. The perovskite (MAPI) solar cells in this run – fabricated in mid-2016 – the molar ratio of TU/DMSO, was varied. All devices have the structure ITO | PTAA | perovskite | PS | C_{60} | BCP | Al. The J_{SC} and therefore PCE values are slightly overestimated, due to the use of 1mm^2 pixels measured without masking.

On the basis of these results, different electron-transport layers were tested, as discussed in Chapter 3. Other projects that I initiated include variation of SrI_2 as additive that led to [169] or variable doping of PTAA with the family of strong acceptors F_xTCNQ leading to [170]. These examples exclude further advances that were enabled by addressing the top surface of the perovskite, shown in Chapter 5 and Chapter 6. Overall, tracking of solar cell efficiencies over a longer timescale is essential in detecting issues with either of the above-mentioned chemicals, the glovebox atmosphere or other parameters. Figure 23 displays the power conversion efficiency of all devices prepared in the course of over four years which led to achieving 20% PCE. The learning curve to develop the described protocol is long and requires teamwork to produce such a large number of devices (all samples displayed were fabricated by M. Stolterfoht and myself, but several runs were performed, where L. Perdigon Toro, Y. Amir or P. Caprioglio assisted). Even with a robust protocol, underperforming batches still occurred. Most of the time this could be linked to obvious errors made during the preparation (*e.g.* incomplete substrate coverage), to chemical/solvent contamination, to degradation or failed experiments (*e.g.* new interlayers/additives that worsened performance). It is therefore useful to keep track of the PCE trend over longer time to monitor the quality of the protocol to continuously improve it.

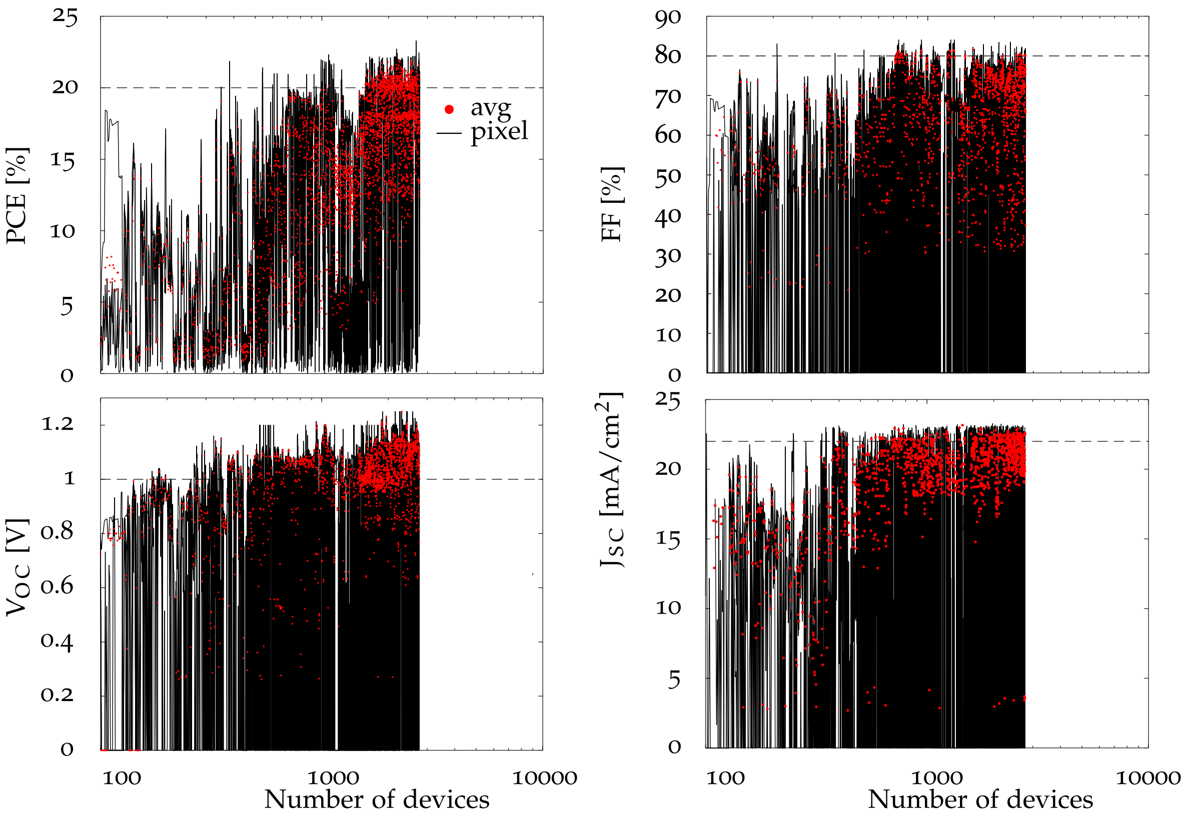

Figure 23: Long-Term Statistics. The four main figures-of-merit PCE, FF, V_{OC} and J_{SC} are plotted as a function of prepared devices over the course of >4 years demonstrating the clear trajectory of efficiency and especially V_{OC}. Under-performing pixels regularly still occur (black lines), but substrate averages (red dots) confirm long-term improvement and enhanced reproducibility.

CONCLUSION In this chapter, a detailed protocol for the preparation of perovskite solar cells for the common inverted (p-i-n) configuration is given. The protocol reliably renders devices with over 20% efficiency. The most common issues encountered are discussed and potential source of errors that need to be considered during device preparation are pointed out. Control of the environmental parameters during the deposition of the perovskite layer is found to be crucial. Especially, the presence of DMSO/DMF solvent vapors and high glovebox temperatures are observed to influence the quality of the perovskite films negatively and thus the final device performance. Overheating of the samples during the evaporation of the metal contacts is a frequent cause of poorly performing devices, as is the use of solutions older than 1 week. High purity of fresh solvents and chemicals is fundamental to achieving the highest efficiencies and practical experience is highly important to realize the highest efficiency devices reproducible, albeit underperforming batches may still occur along the learning curve. Based on these observations, future-protocols need to be made even more robust and detailed descriptions are of great importance. This will be greatly beneficial for the future development of perovskite solar cells but also for perovskite research in general.

[155] Paul Fassl et al. "Fractional deviations in precursor stoichiometry dictate the properties, performance and stability of perovskite photovoltaic devices." In: *Energy & Environmental Science* 11.12 (Dec. 2018), pp. 3380–3391 (cit. on pp. 59, 119).

[156] Passarut Boonmongkolras et al. "Understanding effects of precursor solution aging in triple cation lead perovskite." In: *RSC Advances* 8.38 (June 2018), pp. 21551–21557 (cit. on p. 59).

[157] Benjia Dou et al. "Degradation of Highly Alloyed Metal Halide Perovskite Precursor Inks: Mechanism and Storage Solutions." In: *ACS Energy Letters* 3.4 (Apr. 2018), pp. 979–985 (cit. on p. 59).

[158] Hanul Min et al. "Stabilization of Precursor Solution and Perovskite Layer by Addition of Sulfur." In: *Advanced Energy Materials* 9.17 (May 2019), p. 1803476 (cit. on p. 59).

[159] Thomas Cottineau et al. "Hydrolysis and complexation of N, N -dimethylformamide in new nanostructurated titanium oxide hybrid organic-inorganic sols and gel." In: *Journal of Physical Chemistry C* 115.25 (June 2011), pp. 12269–12274 (cit. on p. 59).

[160] Pabitra K. Nayak et al. "Mechanism for rapid growth of organic-inorganic halide perovskite crystals." In: *Nature Communications* 7.1 (Nov. 2016), pp. 1–8 (cit. on p. 59).

[161] David P. McMeekin et al. "Crystallization Kinetics and Morphology Control of Formamidinium–Cesium Mixed-Cation Lead Mixed-Halide Perovskite via Tunability of the Colloidal Precursor Solution." In: *Advanced Materials* 29.29 (Aug. 2017), p. 1607039 (cit. on p. 59).

[162] Nakita K. Noel et al. "Unveiling the Influence of pH on the Crystallization of Hybrid Perovskites, Delivering Low Voltage Loss Photovoltaics." In: *Joule* 1.2 (Oct. 2017), pp. 328–343 (cit. on p. 59).

[163] Qi Wang et al. "Large fill-factor bilayer iodine perovskite solar cells fabricated by a low-temperature solution-process." In: *Energy & Environmental Science* 7.7 (2014), p. 2359 (cit. on p. 59).

[164] Wei Zhang et al. "Enhanced optoelectronic quality of perovskite thin films with hypophosphorous acid for planar heterojunction solar cells." In: *Nature Communications* 6.1 (Nov. 2015), pp. 1–9 (cit. on p. 59).

[165] Juliane Borchert et al. "Impurity Tracking Enables Enhanced Control and Reproducibility of Hybrid Perovskite Vapor Deposition." In: *ACS Applied Materials and Interfaces* 11.32 (Aug. 2019), pp. 28851–28857 (cit. on p. 59).

[166] Yong Wang et al. "Thermodynamically stabilized b-CsPbI3–based perovskite solar cells with efficiencies >18%." In: *Science* 365.6453 (Aug. 2019), pp. 591–595 (cit. on p. 59).

[167] Andreas Paulke et al. "Charge carrier recombination dynamics in perovskite and polymer solar cells." In: *Applied Physics Letters* 108.11 (Mar. 2016), p. 113505 (cit. on pp. 60, 97, 116).

[168] Michael Saliba et al. "How to Make over 20% Efficient Perovskite Solar Cells in Regular (n-i-p) and Inverted (p-i-n) Architectures." In: *Chemistry of Materials* 30.13 (July 2018), pp. 4193–4201 (cit. on pp. 61, 98).

[169] Pietro Caprioglio et al. "High open circuit voltages in pin-type perovskite solar cells through strontium addition." In: *Sustainable Energy & Fuels* 3.2 (Oct. 2019), pp. 550–563 (cit. on pp. 63, 85, 130).

[170] Lorena Perdigón-Toro. "Doping design for hole transporting polymers in perovskite solar cells." M.Sc. Universität Potsdam, 2017 (cit. on p. 63).

5

VISUALIZATION AND SUPPRESSION OF INTERFACIAL RECOMBINATION LOSSES

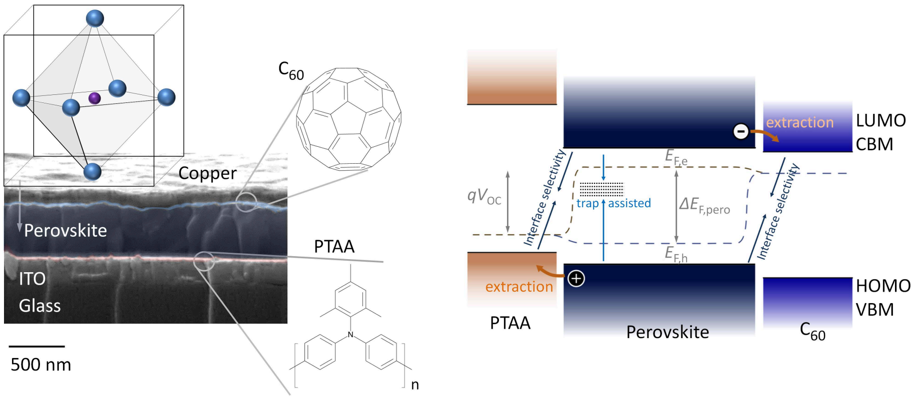

This part was motivated by the search for a reliable tool to identify where in the devices recombination losses occur. After several less successful approaches, Dr. José Márquez presented some data on a new setup he had developed, which paved the way for this study. Interfacial recombination was pinpointed as limiting the open-circuit voltages, asking for mitigation strategies, which was achieved by implementing interlayers at both p- and n-interfaces.

This chapter is a preprint of:

Visualization and suppression of interfacial recombination for high-efficiency large-area p-i-n perovskite solar cells

Martin Stolterfoht*, Christian M. Wolff*, José A. Márquez, Shanshan Zhang, Charles J. Hages, Daniel Rothhardt, Steve Albrecht, Paul L. Burn, Paul Meredith, Thomas Unold & Dieter Neher

published in : *Nature Energy vol. 3, pages 847-854 (2018)*

* the first two authors contributed equally to this work

Reproduced with permission.[171] Copyright 2018, Springer Nature

5.1 ABSTRACT

The performance of perovskite solar cells is predominantly limited by nonradiative recombination, either through trap-assisted recombination in the absorber layer or via minority carrier recombination at the perovskite/transport layer interfaces. Here, we use transient and absolute photoluminescence imaging to visualize all nonradiative recombination pathways in planar p-i-n- type perovskite solar cells with undoped organic charge transport layers. We find significant quasi-Fermi-level splitting losses (135 meV) in the perovskite bulk, whereas interfacial recombination results in an additional free energy loss of 80 meV at each individual interface, which limits the open-circuit voltage (V_{OC}) of the complete cell to ~1.12 V. Inserting ultrathin interlayers between the perovskite and transport layers leads to a substantial reduction of these interfacial losses at both the p and n contacts. Using this knowledge and approach, we demonstrate reproducible dopant-free 1 cm^2 perovskite solar cells surpassing 20% efficiency (19.83% certified) with stabilized power output, a high V_{OC} (1.17 V) and record fill factor (>81%).

5.2 INTRODUCTION

The solution processability and potential for simple manufacturing from earth-abundant materials drives research into perovskite solar cells in the search for cheap, printable photovoltaic devices. The discovery that perovskites effectively sensitize titanium dioxide (TiO_2) in dye-sensitized solar cells in 2009[110], and the demonstration of the first thin-film solid-state perovskite solar cells in 2012[100, 172] has spurred tremendous research efforts concerning the understanding and optimization of perovskite-based optoelectronic devices. Though power conversion efficiencies (PCEs) of perovskite solar cells[173] are rapidly approaching industrially engineered silicon and inorganic thin-film solar cells[174], several key issues remain that need to be understood and overcome. These include fundamental questions regarding recombination losses[69], long-term stability[93] and difficulties in scaling to large electrode areas[175]. Today it is well known that to unlock the full thermodynamic potential of perovskite solar cells it is imperative to suppress all nonradiative recombination losses, which manifest as increased dark currents and ideality factors greater than one, limiting both the cells' open-circuit voltage (V_{OC}) and fill factor[69, 176]. One of the most challenging tasks in this regard is being able to pinpoint the origin of these losses in a complete device under operational conditions. In general, recombination losses may occur either in the perovskite bulk[69, 136, 173] or close to the interface of an adjacent transport layer as a result of a higher density of trap states at the surface[177, 178]. Likewise, recombination may also occur across interfaces[123, 177, 179] between charges in the transport layer and minority carriers in the perovskite, or in the transport layers themselves[177]. The situation becomes more challenging for cells with a comparatively large area (for example, 1 cm^2), where additional losses come from inhomogeneities of the active perovskite absorber as well as at the interfaces to the transport layers, with transport resistances also becoming an issue[175]. Knowing the origin of the nonradiative recombination losses would greatly facilitate targeted improvements in device performance[179]. This is particularly relevant for planar perovskite devices in the p-i-n configuration, which still lag behind the most efficient n-i-p cells [84, 173, 177, 180–182] due to their lower open-circuit voltage and higher nonradiative recombination losses (for example, 1.15 V for record p-i-n cells [177] compared to more than 1.23 V for n-i-p cells[84, 179]). Nevertheless, p-i-n-type cells are very attractive for single-junction solar cells as they require only ultrathin undoped charge transport layers (for example, 8 nm poly[bis(4-phenyl) (2,4,6-trimethylphenyl)amine] (PTAA), 30 nm C_{60})[176] without the need for extensive chemical doping [176] and annealing at temperatures above 100 °C. This renders their fabrication compatible with roll-to-roll deposition on flexible plastic substrates. Moreover, a p-i-n perovskite device architecture is required for Si/perovskite tandem applications in combination with well-established solar cell technologies based on p-type silicon[183, 184]. Thus, a detailed investigation of nonradiative recombination losses and which interface represents the bottleneck for cell efficiency is urgently needed. We use a combination of steady-state and time-resolved photoluminescence (PL and TRPL) measurements to pinpoint the origin of nonradiative recombination losses in pin-type perosvkite solar cells. In particular, we determine the recombination kinetics and quasi-Fermi-level splitting (QFLS) in sample stacks consisting of the perovskite absorber-only, and perovskite/charge transport layer heterojunctions on length scales relevant to our solar cells (1 cm^2). We identify the main limitation to higher performance to be minority carrier recombination at the heterojunction with the organic charge transport layers. These losses are found to be surprisingly similar at the electron- and hole-selective interfaces. We therefore optimized the hole-selective interface through the use of a conjugated polyelectrolyte, which almost entirely suppressed interfacial recombination while simultaneously improving the wetting of the perovskite solution on the hole transport layer surface, delivering reproducible 1 cm^2 devices. With the knowledge that the V_{OC} of the final device is now largely defined by the QFLS of the inferior perovskite/C_{60} heterojunction we introduced an ultrathin layer of LiF (0.6-1 nm) between the absorber and the electron transport layer. This allowed us to reduce the interfacial recombination loss at the electron-selective interface by 35 meV. Suppressing the nonradiative recombination at both interfaces directly resulted in critical V_{OC} and fill factor improvements in complete devices, allowing 1 cm^2 cells with ~20% efficiency, stabilized maximum power output and high reproducibility. This is currently the highest certified efficiency for a published 1 cm^2 perovskite solar cell structure. Last, numerical simulations highlight the importance of interface optimizations versus bulk optimizations for further perovskite solar cell developments.

5.3 DEVICES ARCHITECTURE TO MITIGATE SCALING LOSSES

Our work builds on recent advancements in the understanding and improvement of p-i-n devices[177, 182, 185]. The chemical structures of PTAA, perovskite and C_{60} as used in our standard cells with architecture [(indium tin oxide, ITO (150 nm)/PTAA (8 nm)/perovskite (400-500 nm)/C_{60} (30 nm)/bathocuproine, BCP (8 nm)/Cu (100 nm)] are shown in Figure 24a. For the active layer material, we chose the previously reported 'triple cation perovskite' mixture with the composition $(CsPbI_3)_{0.05}[(FAPbI_3)_{0.89}(MAPbBr_3)_{0.11}]_{0.95}$, as it delivers among the best photovoltaic performance. We note that though we focus on triple cation cells we have also generalized the results to methylammonium lead iodide $MAPbI_3$ and caesium formamidinium lead iodide $Cs_{0.05}FA_{0.95}PbI_3$ absorber layers, as discussed at the end of the manuscript. Figure 24b displays a schematic energy level diagram based on the results from ultraviolet and inverse photoemission spectroscopy, and proposes possible recombination mechanisms. One of the most important considerations for scaling the device area is the electrode architecture, due to the relatively high sheet resistance of the transparent conducting electrode (TCE). It is thus essential to minimize the distance carriers have to traverse through the comparatively high resistance electrode (that is, ITO versus copper). Figure 2a shows the current-voltage characteristics of optimized 1 cm^2 cells with electrode widths of 8 mm and 4 mm,which demonstrate that the fill factor can be increased from 69% to 77.9% simply by reducing the width of the active area. This is also in agreement with numerical solutions of the Shockley equation for different electrode aspect ratios, as illustrated in Fig. 2b, which confirm a roughly 2% absolute efficiency gain through the fill factor (Supplementary Fig. 1, SI). This approach is in principle scalable, as the rectangular cells can be connected using laser patterning[186] while the electrode width may be slightly increased using a lower-resistance ITO substrate (for instance, $10\Omega/sq$).

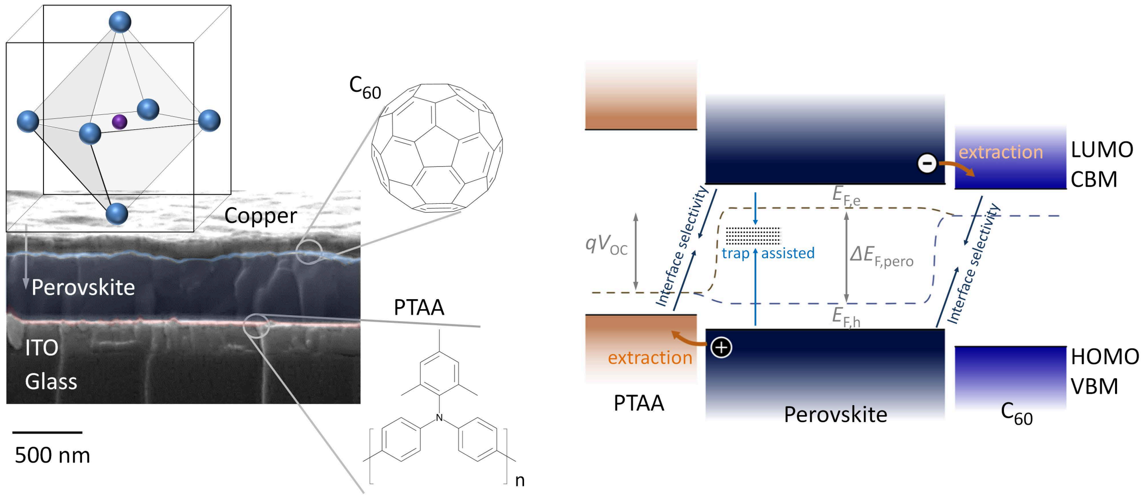

Figure 24: Schematic device architecture and energetics. (left) Cross-section of a full device comprising, from bottom to top: the glass and transparent conducting electrode (ITO), the hole-selective polymeric layer of PTAA, the perovskite absorber layer, the electron selective C_{60} layer and the metallic top electrode (copper). Chemical structures are shown for PTAA, C_{60} and a schematic perovskite crystal structure. The violet sphere represents Pb^{2+}, and the blue sphere represents I^{-}. (right) Schematic energy level diagram and pathways of nonradiative recombination via traps in the perovskite bulk or at the interfaces as a minority carrier loss. Also shown is the extraction of majority carriers to the transport layers, the quasi-Fermi levels of electrons $(E_{F,e})$ and holes (EF, h), the resulting quasi-Fermi-level splitting $(\Delta E_{F,pero})$ in the perovskite, and the recombination-limited V_{OC}. VBM, valence band maximum; CBM, conduction band minimum; HOMO, highest occupied molecular orbital; LUMO, lowest unoccupied molecular orbital. Reproduced with permission.[171] Copyright 2018, Springer Nature

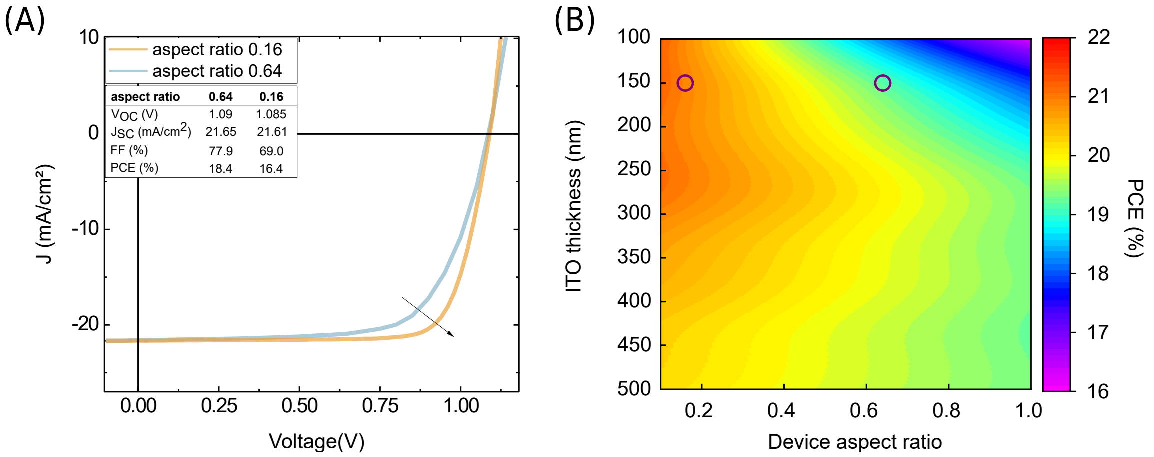

Figure 25: Optimization of electrode design. (A) Experimental JV curves of 1 cm^2 cells comprising a PTAA/perovskite/C_{60} stack with different electrode aspect ratios. Reducing the active area width from 8 mm (aspect ratio 0.64) to 4 mm (aspect ratio 0.16) while keeping the active area the same improved the fill factor by approximately 9%, as indicated by the arrow. (B) Simulated solar cell efficiencies using a combination of optical simulations of the obtainable short-circuit current, and the Shockley equation with a finite ITO series resistance depending on its thickness and the device aspect ratio. An internal cell resistance of 1.5 Ω cm^2 (for a 1 cm^2 cell) and an ideality factor of 1.5 were assumed, as previously determined. The two circled points correspond to the two devices from a. Reproduced with permission.[171] Copyright 2018, Springer Nature

5.4 NONRADIATIVE RECOMBINATION LOSSES

Among the most widely used and trusted techniques in the commu- nity to study the fate of photogenerated charges in perovskite solar cells is TRPL. At sufficiently low fluences a mono-exponential decay is usually observed, indicative of an underlying nonradiative trap-induced recombination that gradually reduces the density of emitting species, and hence the PL signal. The fluence dependence of the TRPL signals is illustrated in Supplementary Fig. 2 (SI). Figure 26 shows the result of such an experiment on a neat perovskite film, which displays a long PL lifetime of approximately half a microsecond, comparable to previously reported perovskite films on TiO_2.[84] Significantly longer lifetimes have been reported, for example, a lifetime of 8 µs was realized through surface passivation of the perovskite with tri-n-octylphosphine.[187] As demonstrated, the achievable V_{OC} in case of dominant Shockley-Read-Hall recombination can be predicted from the carrier lifetime with Equation 21. A TRPL (SRH) lifetime of 500 ns as deduced from the exponential PL decay of the neat perovskite layer should limit the open-circuit voltage to approximately 1.23 V at room temperature. Given that the measured V_{OC} of the device is significantly lower suggests that addition of the CTLs induces substantial nonradiative recombination losses. Figure 26 demonstrates the large impact the addition of charge transporting layers has on the TRPL decay, consistent with previous studies.[180] Interestingly, all samples comprising one or two transport layers exhibited a similar and fast bi-exponential decay. As pointed out previously, this may be either due to the rapid extraction of charges on (sub) ns timescales (quenching), or increased nonradiative recombination losses - two processes that are inherently difficult to disentangle from the TRPL signal only. Notably, large reductions in PL lifetimes are seen independent of whether the PTAA is added between the glass and the active material or coated on top of the perovskite film (on glass), indicating that differences in perovskite morphology related to the nature of the underlying substrate are of minor importance in determining the PL lifetime (see Supplementary Fig. 3, SI). Interestingly, all samples comprising one or two transport layers exhibited a similar and fast bi-exponential decay. As pointed out previously[69, 188], this may be due either to the rapid extraction of charges on (sub)nanosecond timescales (quenching) or increased nonradiative recombination losses—two processes that are inherently difficult to disentangle from the TRPL signal alone. However, unless one transport layer completely depletes the perovskite bulk of one carrier type, the impact of nonradiative interface recombination will be visible in the signal. As the bulk recombination happens at rather long timescales (lifetime ~500 ns), it can be concluded that the TRPL signals, on the films with transport layers present, are subjected to additional nonradiative interface recombination. Following this line of argument, the fast initial decay is attributed to the loss of carriers at the interfaces due to charge extraction and the second decay to interface recombination. Following this line of reasoning, we attribute the fast initial decay to the loss of carriers at the interfaces due to charge extraction to the transport layers and/or to interface recombination, and the second decay (for which the mono-exponential lifetimes are provided in Figure 26) to interface recombination. In accordance with this, the initial decay becomes less pronounced and smeared out when increasing the excitation wavelength, *i. e.* when light penetrates deeper into the perovskite layer (see Supplementary Figure 2, SI). The rather similar decays after the initial drop in the samples with either PTAA or C_{60} indicate that the two perovskite/organic heterojunctions are equally limiting the V_{OC} due to additional nonradiative recombination losses at the interfaces. After carriers reach a quasi-equilibrium distribution, the lifetime (τ_{total}) can be described by an equilibrium between decay time (τ_{SRH}), the diffusion to the surface$\left(\frac{4d^2}{\pi^2 D}\right)$ and interface loss velocity (S_1) with Equation 23, that is $\tau_{total} = \frac{1}{\tau_{SRH}} + \left[\frac{4d^2}{\pi^2 D} + \frac{d}{S}\right]^{-1}$, where d is the perovskite thickness and D the diffusion constant. [62, 152] Using the bulk lifetime of 700 ns, a mobility of 30 $cm^2V^{-1}s^{-1}$ (ref. [148]), d = 400 nm, and the measured τ_{total} value of 20-30 ns would result in an interface loss velocity of S_1 ~1000 cm/s at the interface between the charge transport layer and the perovskite. However, other processes may potentially influence the TRPL signal as well, such as a decelerating charge extraction, light soaking effects,[189] photon-recycling,[62, 189] or a graded generation profile. Thus, whilst TRPL is a useful guide to recombination losses, it doesn't provide definitive mechanistic insight.

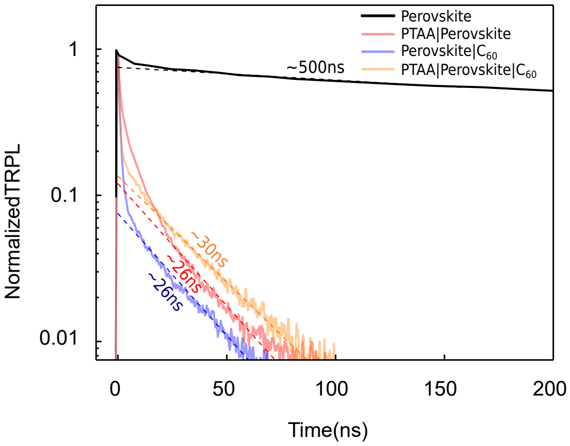

Figure 26: Impact of transport layers on kinetics of charge recombination.TRPL decay of a neat perovskite film indicating the dominance of trap-assisted recombination in the bulk or at the surface. Thecorresponding mono-exponential lifetime is around 500 ns. The TRPL signals of perovskite/transport layer heterojunctions show a bi-exponential decay, indicating rapid charge extraction and interfacial recombination on different timescales. The samples were illuminated at 470 nm (~30 nJ/cm^2) through the organic layer, and through C_{60} in the case of the p-i-n stack. Reproduced with permission.[171] Copyright 2018, Springer Nature

5.5 PHOTOLUMINESCENCE AND QUASI-FERMI LEVEL SPLITTING

A much more direct way to quantify to quantify nonradiative recombination losses at the perovskite/organic interfaces is steady-state PL. As indicated in Equation 27, the absolute PL intensity (I_{PL}) is a direct measure of the QFLS (μ).[39, 190–194] Here, we use hyperspectral absolute photoluminescence imaging is used to create depth averaged maps of the QFLS on the neat perovskite films in comparison to multilayer samples comprising one or both types of transport layers. This approach has been recently used by El-Hajje *et. al.* [190] to spatially resolve the opto-electronic quality of evaporated methylammonium lead iodide junctions, and to study the hole blocking of different electron transport layers. Moreover, absolute PL has been recently applied to disentangle interfacial and bulk recombination losses in n-i-p cells by Sarritzu *et. al.* [192], though the QFLS was not compared to the device voltage, and thus open-circuit voltage losses were not directly quantified. As discussed in Chapter 1 there are different approaches to calculate the QFLS from absolute PL spectra, which are all based on Würfel's generalized Planck law that describes the non-thermal radiation of a semiconductor according to:

$$\phi_{PL}(E) = \frac{1}{\pi^2 h^3 c^2} \frac{a(E)\, E^2}{e^{(E-\mu)/k_B T} - 1} \,.$$

Under the assumption that for emission energies above the PL maximum, a(E) is close to unity, this expression can be simplified to

$$\ln\left[\frac{\phi_{PL}(E)}{a(E)\ \phi_{inc}(E)}\right] = -\frac{E-\mu}{k_B T}$$

This allows to deduce μ simply from fitting the high energy slope of the PL emission. By applying said equation to every spectrum associated with each pixel (10 µm in diameter) of the hyperspectral images, μ distribution maps can be created. Figure 27 shows depth averaged QFLS maps (1 cm^2) of the neat triple cation perovskite film, with either PTAA, C_{60} or both transport layers being present. The perovskite absorber exhibits a homogeneous profile with a QFLS of approximately 1.21 eV. While this value is remarkably close to the V_{OC} obtained from the TRPL lifetime, it is substantially below the radiative V_{OC} of approximately 1.34 eV. The latter is estimated from Equation 45 with a $J_{0,rad.}$~10^{-20} A/m^2 and a J_{SC}~220A/m^2. (see Supplementary Figure 4, SI) This approach for calculating the radiative V_{OC} limit has been extensively applied to perovskite solar cells, as shown in refs [145, 146, 195] and dates back to Shockley and Queisser[144]. We also note that the emitted PL can be influenced by photon recycling[62, 152]. However, this does not affect our conclusions, because it is the external PL quantum yield that determines the QFLS and maximum achievable device V_{OC} (ref. [196]). Figure 27 also shows that the QFLS of the perovskite/C_{60} film is significantly reduced to approximately 1.136 eV ± 10 mV, while the PTAA/perovskite film exhibits a QFLS of 1.125 eV ± 10 mV. It is important to note that, compared to the neat absorber material with a PLQY of ~0.5 %, addition of PTAA or C_{60} results in a large reduction of average photoluminescence efficiency (*e. g.* 0.017% for a perovskite/C_{60} film) which means a large increase in the nonradiative loss current. Despite the different nature of these two interfaces, the nonradiative recombination losses at both interfaces are similar and lower the QFLS by ~80 meV compared to the neat absorber. For this p-i-n stack (glass/PTAA/perovskite/C_{60}) a QFLS of approximately 1.121V ± 10 mV is obtained, which matches the average V_{OC} in complete cells under comparable illumination intensities. This value lies only slightly below the QFLS of samples with only one transport layer present, indicating that the nonradiative recombination losses at each individual interface are both reducing the $I_{PL}(E)$, yet the QFLS only through the logarithm in Equation 45.The samples exhibit good reproducibility and homogeneity of the QFLS maps on the neat perovskite film and all films with C_{60}. Although Figure 27 shows that bulk recombination in the perovskite absorber already imposes a large limitation on the V_{OC}, the weakest component of the (p-i-n) stack dominates the nonradiative loss currents and sets the upper limit for the device V_{OC}. In order to further clarify the importance of interfacial optimizations in relation to bulk optimizations depending on the selectivity of the interlayers, numerical simulations of the open-circuit voltage of a p-i-n device stack are carried out, varying the interfacial recombination velocities and the bulk lifetime using a drift-diffusion simulator (SCAPS, Supplementary Figure 6, SI). Applying the measured interface-recombination velocity prior to optimization (*i. e.* ~2000 cm/s) at a bulk lifetime (500 ns) as input parameters, the simulation accurately describes the V_{OC} of the reference cells. The simulations clearly show that even if the perovskite bulk lifetime was improved multiple times (»500 ns), no V_{OC} improvements are possible when the interface recombination velocities stay at 2000 cm/s. Thus, the V_{OC} of the devices is entirely limited by the interfaces, and any improvement of the bulk would be essentially lost due to rapid interfacial recombination. Thus, it is essential to systematically improve both interfaces discussed in the following.

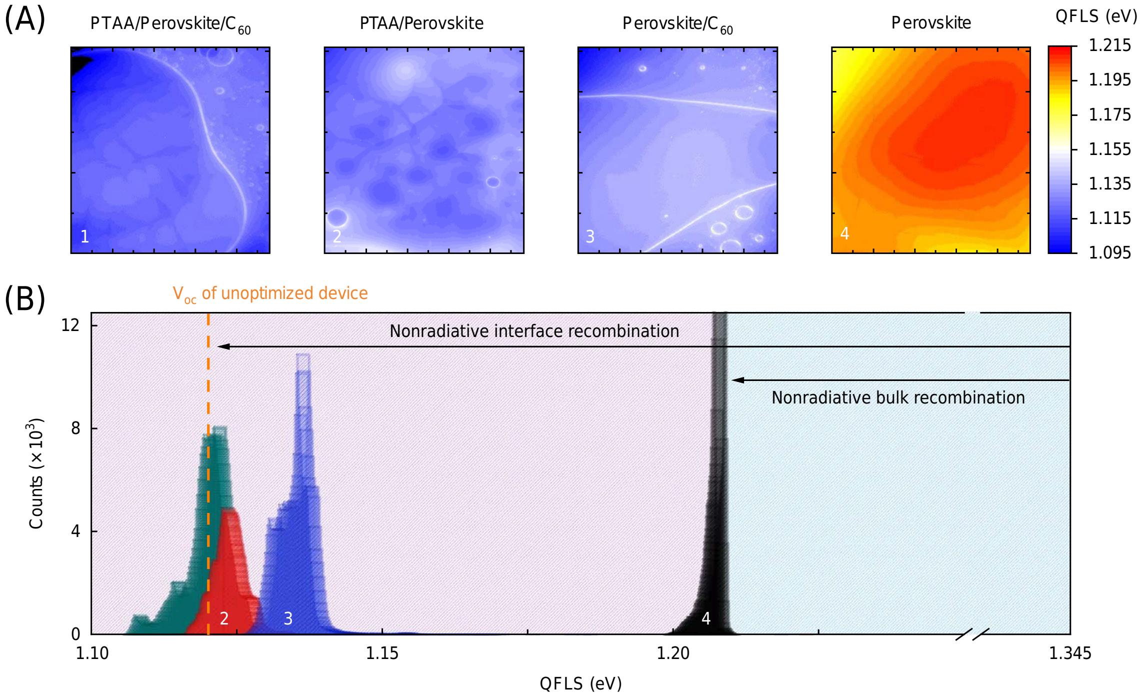

Figure 27: Visualization of nonradiative interfacial recombination through absolute photoluminescence imaging. Quasi-Fermi level splitting maps(1 cm^2) (A) and corresponding energy histograms (B) on perovskite-only, perovskite/C_{60}, PTAA/perovskite and PTAA/perovskite/C_{60} films on glass. The neat perovskite absorber allows a QFLS (and thus potential V_{OC}) of approximately 1.208 eV (at 300 K), consistent with the transient photoluminescence decay, but significantly below the QFLS in the radiative limit (1.345 eV), as indicated by the arrow. Addition of only one transport layer (either PTAA or C_{60}) induces additional nonradiative recombination pathways, which lower the QFLS to approximately 1.125-1.135 eV. The p-i-n junction with both transport layers adjacent to the perovskite absorber still has an average QFLS of approximately 1.121 eV. The arrow shows that interfacial recombination dominates the nonradiative recombination losses in the stack. Films were excited at 450 nm with 1 Sun equivalent intensity and the histograms were recorded on 5 mm x 5 mm squares in the middle of the films without edge effects (PL quenching) due to the *e. g.* encapsulation glue. Reproduced with permission.[171] Copyright 2018, Springer Nature

5.6 SUPPRESSION OF INTERFACIAL RECOMBINATION

The approach proposed by Lee *et. al.* [197] allows to improve the wettability of perovskite precursor solutions and thereby layers on hydrophobic CTLs. The interface compatibilizer PFN-P2 - a conjugated polyelectrolyte (CPE) is used to functionalize the PTAA layer. This greatly enhances the fabrication yield of the fabricated cells without frequent pinhole formation without.To reveal possible changes of the layer morphology as a function of the underlying substrate, we performed top and cross-sectional scanning electron microscopy (SEM) measurements of perovskite films deposited on glass, glass/ITO/PTAA and glass/ITO/PTAA/PFN-P2. The images shown in Supplementary Fig. 7 (SI) demonstrate perovskite grains ranging from tens of nanometres to micrometres in size and indicate, at least qualitatively, only small changes of the perovskite bulk morphology across these substrates. Importantly,interjecting PFN-P2 causes a substantial reduction of the recombination at the HTL contact as shown in Figure 28 resulting in an average QFLS close to the value for the neat perovskite (~1.21 eV) while simultaneously improving the homogeneity of the absolute PL image due to the superior wetting. In accordance with the higher QFLS, a significantly slower TRPL decay on samples including PFN-P2 is observed. Motivated by this success, the remaining limitation due to the perovskite/ETL interface is addressed.Different strategies have been reported to block holes at the n-interface, such as polystyrene[177] or choline chloride[177] for pin cells or Ga_2O_3 for n-i-p cells[179]. These approaches were slightly unreliable for this perovskite composition and for these triple cation p-i-n-perovskite solar cells the most significant effect on the QFLS and device efficiency is achieved, when inserting an ultrathin layer (0.6 nm - 1 nm) of LiF between the perovskite and C_{60}, causing a reduction of the nonradiative interfacial recombination loss by 35 meV. Again, the increase in QFLS is directly correlated with a slower mono-exponential TRPL decay (lifetimes increase from 26 ns to 180 ns for a perovskite/C_{60} and perovskite/LiF/C_{60} film on glass, respectively.)

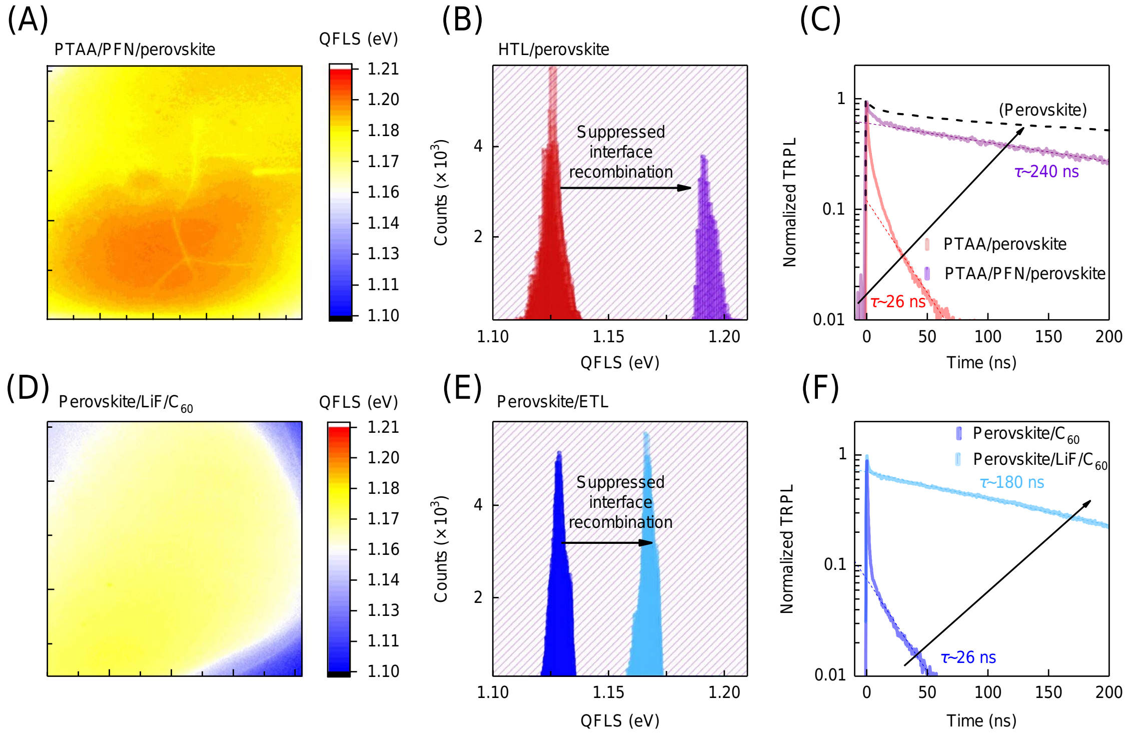

Figure 28: Suppression of interfacial recombination through interlayers. QFLS map (1 x 1 cm) (A) and QFLS histogram (B) of a PTAA/PFN-P2/perovskite film on glass, demonstrating a comparatively high average QFLS of approximately 1.19 eV. This represents a significant enhancement of approximately 65 meV compared to the QFLS of the PTAA/perovskite film and approaches the QFLS potential of the neat perovskite within 20 mV. QFLS map (1 x 1 cm^2) (D) and QFLS histogram (E) of a perovskite/LiF/C_{60} film on glass, demonstrating the reduced interfacial recombination loss at the n-contact. Importantly, the average QFLS of the perovskite/LiF/C_{60} stack (1.169 eV) and the p-i-n device stack (1.173 eV) are both almost identical to the V_{OC} of our optimized cells (1.16-1.17 V). The histograms were recorded on a 5 mm × 5 mm square in the middle of the films, without edge effects (PL quenching) due to the encapsulation glue. TRPL transients highlighting the significant prolongation of the carrier lifetime when either PFN-P2 (C) or LiF (F) is added as interlayer. Reproduced with permission.[171] Copyright 2018, Springer Nature

5.7 PHOTOVOLTAIC PERFORMANCE

Introducing both interlayers considerably improve the cell efficiency (from average 18% to 20%) through an increase in V_{OC} and FF (see Supplementary Figure 8, SI). Importantly, the average V_{OC} of cells with both interlayers present is 1.16 V which compares well with the average QFLS of the perovskite/LiF/C_{60} stack and the complete device stack (~1.17 eV). Measuring the V_{OC} as a function of light intensity on cells with and without both interlayers reveals a similar ideality factor but a smaller dark recombination current density for the interlayer-containing device, indicating that these additional layers do affect the rate but not the overall nature of the recombination process (Supplementary Figure 9, SI) From the device manufacturing perspective, introducing PFN-P2 greatly improves the homogeneity of the perovskite films which allows to manufacture 1cm^2 cells without pinhole formation encountered without the interlayer. Typically, without PFN-P2, only one out of three 1cm^2 cells resulted in efficiencies above 18%, while this PCE could be safely achieved for more than 90% of cells if PFN-P2 was included. Cells with PFN-P2 (but without LiF) reached efficiencies up to 19.6% (J_{SC} = 21.85mA cm^{-2}, V_{OC} = 1.143 V, FF = 78.6%, see Supplementary Figure 10, SI) when measured with an aperture mask (1.018 cm^2) at 25oC. The short-circuit current matched the integrated EQE and solar spectrum product ($21.5 mAcm^{-2}$) within an error of less than 2% (see Supplementary Figure 11, SI). This cell was certified by an independent accredited institute (Institute for Solar Energy, Fraunhofer Freiburg), which gave a stabilized PCE of 19.22% Supplementary Figure 12, SI) with a negligible mismatch to our J-V measurement in terms of current. Moreover, encapsulated cells were stable for at least 100 h under maximum power point (MPP) tracking conditions in air and constant illumination from a white light-emitting diode (LED) with 1 Sun equivalent light intensity, with only a small loss in efficiency (0.6% absolute) (Supplementary Fig. 13, SI). We also note that using $10\Omega/sq$ ITO substrates instead of our standard 15 Ω/sq ITO substrates allowed us to achieve fill factors above 81%; values which, to our knowledge, are 3% higher than the highest reported fill factors for 1 cm^2 size cells (Supplementary Fig. 14, SI). As expected from the QFLS analysis, the V_{OC} of these cells is significantly increased through introduction of the LiF interlayer (1.17 V), pushing the PCE up to a value of 20.0% with virtually no hysteresis and stable power output as shown in Figure 29.

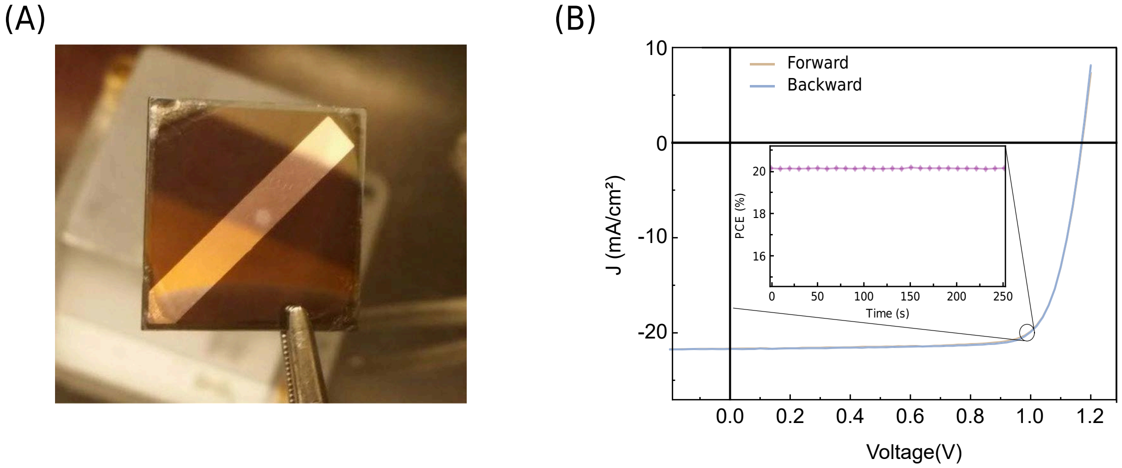

Figure 29: 20% efficient p-i-n-type perovskite cells with 1 cm^2 active area. (A) Photograph of a fabricated 1 cm^2 cell with a rectangular active electrode area. (B) 1 cm^2 perovskite cells reaching 20% PCE were achieved using a combination of PFN-P2 and LiF interlayers (J_{SC} = 21.7 mA cm^2, fill factor = 78.6%, V_{OC} = 1.17 V) as measured with an aperture mask (1.018 cm^2) at 25oC. The inset shows the stabilized power output at 20.1%. Reproduced with permission. [171] Copyright 2018, Springer Nature

However, compared to the highest certified $1cm^2$ cells with a PCE of 20.9%[198] (J_{SC} of 24.9mA cm^{-2}, geometry and structure unpublished) a remaining limitation is the relatively low short-circuit current. Thus, in order to lower the bandgap of the perovskite layer, the ratio of $FAPbI_3$ to $MAPbBr_3$ is optimized. Using a ratio of 89:11 allows a significant improvement in short-circuit current (0.5-1mA cm^{-2}) with surprisingly minimal loss in V_{OC} and efficiencies up to 21.6% for small 6 mm^2-size cells (J_{SC} = 23.2mA cm^{-2}, V_{OC} = 1.156V, FF = 80.4%). The 1 cm^2 devices, Figure 29 (also Supplementary Fig. 15a, SI) shows the hero device with both interlayers included (PFN-P2 and LiF) fabricated from a $(CsPbI_3)_{0.05}[(FAPbI_3)_{0.89}(MAPbBr_3)_{0.11}]_{0.95}$ perovskite with an efficiency of 20.3%. This cell was certified by Fraunhofer-ISE resulting in a *stabilized* PCE of 19.83%, which is currently the highest efficiency fora $1cm^2$ perovskite cell with published geometry and structure (Supplementary Figs. 16 and 17,SI).We also highlight the important fact that the efficiency of our cells is stabilized, in contrast to most previous perovskite solar cell certifications, which are denoted as “not stabilized”.[198] Last, we note that our concept to identify and suppress interfacial recombination can be successfully generalized to other perovskite compositions, including the standard methylammonium lead iodide absorber (MAPI), where we reached efficiencies slightly above 20%; as well as Cs-containing formamidinium lead iodide perovskite cells $(Cs_{0.05}FA_{0.95})PbI_3$

with close to 20% PCE (Supplementary Fig. 18, SI). The latter system is particularly interesting as pure FAPbI3 exhibits a bandgap of 1.47 eV, which is closer to the optimum bandgap in the Shockley-Queisser model. However, reports of FAPbI3 cells are rare and the efficiencies of such devices lag significantly behind the mixed perovskite systems[135, 199, 200]. Measurement of the absolute PL from the individual perovskite/charge transport layer junctions proves once again substantial reduction of interfacial recombination by the addition of PFN-P2 and LiF at the p- and n-interfaces, respectively (Supplementary Table 2, SI). Notably, this allowed the devices to reach record efficiencies for MA/Br-free FAPbI3 perovskite solar cells, which further underlines the potential of our recombination analysis and interfacial engineering approach (Supplementary Fig. 18, SI).

CONCLUSION In conclusion, hyperspectral photoluminescence imaging allows to identify the origin of nonradiative recombination loss channels by mapping the QFLS of the relevant perovskite/-transport layer combinations. Significant nonradiative recombination losses in the neat perovskite layer reduce the potential V_{OC} by approximately 135 mV compared to the radiative limit of this type of perovskite (1.345 V). However, interface recombination at each individual hybrid interface (PTAA/perovskite and perovskite/C_{60}) dominates the nonradiative loss current in the stack and results in a significant further reduction of the QFLS to 1.13 eV. In line with this interpretation, considerable improvement of the device performance can be achieved by applying PFN-P2 and LiF as interfacial layers, which suppress the recombination losses by 65 meV and 35 meV at the p-and-n-interface, respectively. The reduced recombination and increased QFLS splitting resulted in significant V_{OC} and FF gains, which in combination with an optimized composition of the perovskite layer led to a PCE above 20% for 1 cm^2 sized cells with a certified PCE of 19.83% and stabilized power output. This demonstrates how interfacial recombination losses can be unambiguously identified and suppressed, paving the way to reach the thermodynamic limit for perovskite solar cells through further minimization of interface and trap-assisted recombination in the absorber layer.

[171] Martin Stolterfoht et al. “Visualization and suppression of interfacial recombination for high-efficiency large-area pin perovskite solar cells.” In: *Nature Energy* 3.10 (Oct. 2018), pp. 847–854 (cit. on pp. 66, 69–71, 73, 75, 76, 82, 85, 98, 119, 138).

[172] Hui-Seon Kim et al. “Lead Iodide Perovskite Sensitized All-Solid-State Submicron Thin Film Mesoscopic Solar Cell with Efficiency Exceeding 9%.” In: *Scientific Reports* 2 (2012), pp. 1–7 (cit. on p. 67).

[173] Ye Yang et al. “Top and bottom surfaces limit carrier lifetime in lead iodide perovskite films.” In: *Nature Energy* 2.2 (Jan. 2017), p. 16207 (cit. on pp. 67, 110, 123).

[174] Kunta Yoshikawa et al. “Silicon heterojunction solar cell with interdigitated back contacts for a photoconversion efficiency over 26%.” In: *Nature Energy* 2.5 (Mar. 2017), pp. 1–8 (cit. on pp. 67, 110).

[175] Qianqian Lin et al. “Considerations for Upscaling of Organohalide Perovskite Solar Cells.” In: *Advanced Optical Materials* 5.2 (Jan. 2017), p. 1600819 (cit. on p. 67).

[176] Martin Stolterfoht et al. “Approaching the fill factor Shockley-Queisser limit in stable, dopant-free triple cation perovskite solar cells.” In: *Energy Environ. Sci.* 10.6 (2017), pp. 1530–1539 (cit. on pp. 67, 82, 110, 112, 122, 139).

[177] Xiaopeng Zheng et al. “Defect passivation in hybrid perovskite solar cells using quaternary ammonium halide anions and cations.” In: *Nature Energy* 2.7 (June 2017), p. 17102 (cit. on pp. 67, 68, 74, 82, 110, 129).

[178] Tejas S. Sherkar et al. “Recombination in Perovskite Solar Cells: Significance of Grain Boundaries, Interface Traps, and Defect Ions.” In: *ACS Energy Letters* 2.5 (2017), pp. 1214–1222 (cit. on pp. 67, 110, 113).

[179] Juan-Pablo Correa-Baena et al. “Identifying and suppressing interfacial recombination to achieve high open-circuit voltage in perovskite solar cells.” In: *Energy Environ. Sci.* 10.5 (May 2017), pp. 1207–1212 (cit. on pp. 67, 74, 81, 85, 129).

[180] Hairen Tan et al. “Efficient and stable solution-processed planar perovskite solar cells via contact passivation.” In: *Science* 355.6326 (Feb. 2017), pp. 722–726 (cit. on pp. 67, 70).

[181] Yi Hou et al. “A generic interface to reduce the efficiency-stability-cost gap of perovskite solar cells.” In: *Science* 358.6367 (Nov. 2017), pp. 1192–1197 (cit. on p. 67).

[182] Cristina Momblona et al. “Efficient vacuum deposited p-i-n and n-i-p perovskite solar cells employing doped charge transport layers.” In: *Energy Environ. Sci.* 9.11 (2016), pp. 3456–3463 (cit. on pp. 67, 68, 130).

[183] Kevin A. Bush et al. “23.6%-efficient monolithic perovskite/silicon tandem solar cells with improved stability.” In: *Nature Energy* 2.4 (Feb. 2017), p. 17009 (cit. on pp. 67, 82, 110).

[184] Steve Albrecht et al. “Monolithic perovskite/silicon-heterojunction tandem solar cells processed at low temperature.” In: *Energy Environ. Sci.* 9.1 (2016), pp. 81–88 (cit. on p. 67).

[185] Nandi Wu et al. “Identifying the Cause of Voltage and Fill Factor Losses in Perovskite Solar Cells by Using Luminescence Measurements.” In: *Energy Technology* 5.10 (Oct. 2017), pp. 1827–1835 (cit. on pp. 68, 116, 117, 121, 126).

[186] Alessandro Lorenzo Palma et al. “Laser-Patterning Engineering for Perovskite Solar Modules With 95% Aperture Ratio.” In: *IEEE Journal of Photovoltaics* 7.6 (Nov. 2017), pp. 1674–1680 (cit. on p. 68).

[187] Dane W. DeQuilettes et al. “Photoluminescence Lifetimes Exceeding 8 μs and Quantum Yields Exceeding 30% in Hybrid Perovskite Thin Films by Ligand Passivation.” In: *ACS Energy Letters* 1.2 (Aug. 2016), pp. 438–444 (cit. on p. 70).

[188] Richard K. Ahrenkiel. “Minority-Carrier Lifetime in III–V Semiconductors.” In: *Semiconductors and Semimetals* 39.C (Jan. 1993), pp. 39–150 (cit. on p. 70).

[189] Dane W. DeQuilettes et al. “Photo-induced halide redistribution in organic–inorganic perovskite films.” In: *Nature Communications* 7.May (May 2016), p. 11683 (cit. on pp. 71, 116).

[190] Gilbert El-Hajje et al. “Quantification of spatial inhomogeneity in perovskite solar cells by hyperspectral luminescence imaging.” In: 7 (2016) (cit. on pp. 72, 116, 118).

[191] Ian L. Braly and Hugh W. Hillhouse. “Optoelectronic Quality and Stability of Hybrid Perovskites from MAPbI3 to MAPbI2Br Using Composition Spread Libraries.” In: *Journal of Physical Chemistry C* 120.2 (2016), pp. 893–902 (cit. on pp. 72, 116, 118).

[192] Valerio Sarritzu et al. “Optical determination of Shockley-Read-Hall and interface recombination currents in hybrid perovskites.” In: *Scientific Reports* 7 (2017) (cit. on pp. 72, 116–118).

[193] Steve Johnston et al. “Correlations of Cu(In, Ga)Se 2 imaging with device performance, defects, and microstructural properties.” In: *Journal of Vacuum Science & Technology A: Vacuum, Surfaces, and Films* 30.4 (July 2012), p. 04D111 (cit. on p. 72).

[194] G. H. Bauer, L. Gütay, and R. Kniese. “Structural properties and quality of the photoexcited state in Cu(In 1-xGax)Se2 solar cell absorbers with lateral submicron resolution.” In: *Thin Solid Films*. Vol. 480-481. Elsevier, June 2005, pp. 259–263 (cit. on p. 72).

[195] Thomas Kirchartz and Uwe Rau. “Detailed balance and reciprocity in solar cells.” In: *physica status solidi (a)* 205.12 (Dec. 2008), pp. 2737–2751 (cit. on p. 72).

[196] Thomas Kirchartz, Florian Staub, and Uwe Rau. “Impact of Photon Recycling on the Open-Circuit Voltage of Metal Halide Perovskite Solar Cells.” In: *ACS Energy Letters* 1.4 (Oct. 2016), pp. 731–739 (cit. on p. 72).

[197] Jinho Lee et al. “Achieving Large-Area Planar Perovskite Solar Cells by Introducing an Interfacial Compatibilizer.” In: *Advanced Materials* 29.22 (June 2017), p. 1606363 (cit. on p. 74).

[198] Martin A. Green et al. “Solar cell efficiency tables (Version 55).” In: *Progress in Photovoltaics: Research and Applications* 27.1 (Jan. 2020), pp. 3–12 (cit. on pp. 76, 81, 104, 110, 119).

[199] Tanghao Liu et al. “High-Performance Formamidinium-Based Perovskite Solar Cells via Microstructure-Mediated δ-to-α Phase Transformation.” In: *Chemistry of Materials* 29.7 (Apr. 2017), pp. 3246–3250 (cit. on p. 77).

[200] Yue Yu et al. “Improving the Performance of Formamidinium and Cesium Lead Triiodide Perovskite Solar Cells using Lead Thiocyanate Additives.” In: *ChemSusChem* 9.23 (Dec. 2016), pp. 3288–3297 (cit. on p. 77).

6

PERFLUORINATED SELF-ASSEMBLED MONOLAYERS ENHANCE THE STABILITY AND EFFICIENCY OF INVERTED PEROVSKITE SOLAR CELLS

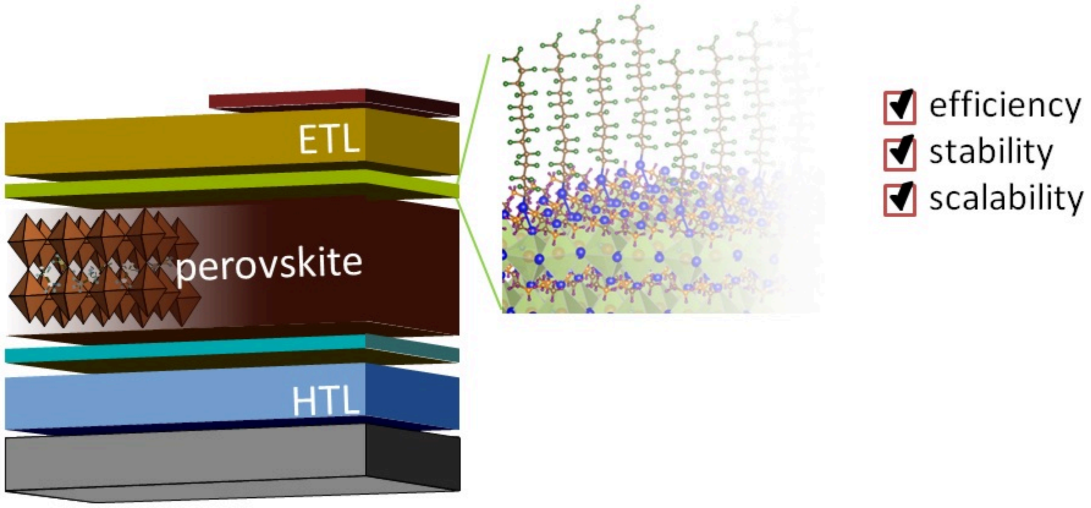

Beyond efficiency another prerequisite before any commercialization is stable performance of devices over decades. In a discussion following a talk on one of the HyPerCells retreats, Prof. Dr. Dieter Neher, Prof. Dr. Antonio Abate and I discussed the possibility to use halogen-bound molecular layers to improve the device stability based on previous work by A.A., which resulted in this work and is a step beyond reducing interfacial recombination losses enhancing also stability.

This chapter is a preprint of:

Perfluorinated Self-Assembled Monolayers Enhance the Stability and Efficiency of Inverted Perovskite Solar Cells

Christian M. Wolff, Laura Canil, Carolin Rehermann, Nguyen Ngoc Linh, Fengshuo Zu, Maryline Ralaiarisoa, Pietro Caprioglio, Lukas Fiedler, Martin Stolterfoht, Sergio Kogikoski Jr., Ilko Bald, Norbert Koch, Eva Unger, Thomas Dittrich, Antonio Abate and Dieter Neher

published in : *ACS Nano 2020, 14, 2, 1445-1456*

6.1 ABSTRACT

Perovskite solar cells are among the most exciting photovoltaic systems as they combine low recombination losses, ease of fabrication, and high spectral tunability. The Achilles heel of this technology is the device stability due to the ionic nature of the perovskite crystal, rendering it highly hygroscopic, and the extensive diffusion of ions especially at increased temperatures. Herein, we demonstrate the application of a simple solution-processed perfluorinated self-assembled monolayer (p-SAM) that not only enhances the solar cell efficiency, but also improves the stability of the perovskite absorber and, in turn, the solar cell under increased temperature or humid conditions. The p-i-n-type perovskite devices employing these SAMs exhibited power conversion efficiencies surpassing 21%. Notably, the best performing devices are stable under standardized maximum power point operation at 85 °C in inert atmosphere (ISOS-L-2) for more than 250 h and exhibit superior humidity resilience, maintaining ~95% device performance even if stored in humid air in ambient conditions over months (~3000 h, ISOS-D-1). Our work, therefore, demonstrates a strategy towards efficient and stable perovskite solar cells with easily deposited functional interlayers.

6.2 INTRODUCTION

Recent years have witnessed a huge improvement in the efficiency and stability of solar cells based on metal halide perovskites. Systematic improvements of the perovskite composition and morphology, combined with the development of new charge-transporting materials, led to certified power conversion efficiencies (PCEs) of up to 25.2%.[198] In parallel, various strategies have been developed to improve the stability of the perovskite itself and the entire device, and good to excellent stabilities in light, air, or electrical load stress tests have been demonstrated.[202, 203] Many of these approaches, however, required rather complicated and thus expensive encapsulation schemes, such as deposition of inorganic layers by ALD (atomic layer deposition) or sputtering.[204, 205] A few early attempts include the use of long alkyl chain halide molecules for surface modifications, other moisture-repelling molecules,[206] or the cross-linking agent ABPA.[207] Likewise, Lewis base passivation protocols[208, 209] have been shown to improve the performance and stability, and recently, composites incorporating 2D perovskites were shown to exhibit substantially improved resilience to environmental stress.[93, 210, 211] Notably, most of the recent achievements toward high efficiencies and/or stability employed n-i-p architecture, where the active perovskite is coated on a (commonly used) n-type transparent metal oxide and the cell is completed with a fairly thick (and often doped) p-type organic semiconductor. To the best of our knowledge, the most stable (encapsulated) n-i-p devices were reported by Grancini *et. al.* [93] (initial PCE: 12%, sealed and measured in ambient, 10.000 h at J_{SC} at 55 °C without loss), by Christians *et. al.* [203] (initial PCE: 12.2%, measured in ambient (10-20% RH) for >1000 h close to maximum power point (MPP) at 30 °C, retaining >88% efficiency), by Saliba *et. al.* [84] (initial PCE: 17%, MPP-tracking in nitrogen for 500 h at 85 °C, retaining 95% efficiency), and by Jeon *et. al.* [212] (initial PCE: 20.8%, encapsulated and measured in ambient at 25 °C for 300 h, retaining 92% efficiency). On the other hand, p-i-n cells are particularly attractive due to their very simple device architecture, often comprising very thin charge-transporting layers with the active perovskite occupying over 90% of the cell volume. These cells often use undoped organic charge transport layers and are processed at temperatures below 100 °C. Chemical doping of transport layers has been identified as one major source for device degradation.[179] Probably most importantly, p-i-n is the preferred architecture for tandem applications on top of silicon solar cells, which currently exhibit a market share of over 90% of all industrial solar cells. Therefore, and perhaps not surprisingly, all recently published records of monolithic Si/perovskite tandem cells employed a p-i-n-type cell as the top cell.[213–215] Unfortunately, the efficiency and stability of p-i-n-type cells lag behind those of the more commonly employed n-i-p architectures. In this context, it has been acknowledged that nonradiative recombination of photogenerated charges at the interface between the perovskite and the electron-transporting layer (ETL) is a major loss channel, especially in p-i-n devices.[216] Various strategies including compositional engineering[217] or addition of interlayers[99, 132, 171] have been demonstrated to decrease these losses, resulting in reproducible efficiencies of up to 20.9% for small devices and 19.8% on 1 cm^2 pixels. On the other hand, very few publications report long-term stabilities of p-i-n-type cells under relevant storage or illumination conditions. For example, Zheng *et. al.* showed moderate stability of an unencapsulated cell under ambient MPP tracking for 25 h with high efficiencies,[177] and we previously reported 168 h stability on a non-encapsulated cell with a PCE of 16% under MPP tracking at 25 °C in inert gas.[176] A successful approach to improve the stability of p-i-n-type perovskite solar cells is to protect the active perovskite by combining an ALD-deposited transparent metal oxide layer in combination with sputtered top contacts or AZO-NPs, and these devices showed exceptional lifetimes (*e. g.* , a T_{80} of 100 h during MPP at 100 °C in ambient atmosphere for <16% PCE devices[218, 219] or 1000 h in ambient MPP with an initial PCE of 13% [183]). Other approaches to increase the stabilities of such cells include silane molecules,[220] the use of quaternary ammonium halides to passivate the perovskite or multiple ALD layers.[221] With the above-mentioned exceptions, p-i-n devices are usually not subjected to simultaneous thermal light bias stress, and no highly efficient (>20%) devices have been shown to rival the stability of the n-i-p structured devices. In this report, we introduce a simple yet effective functionalization of a triple cation lead halide perovskite with a self-assembled monolayer (SAM) made of simple perfluorinated aliphatic carbon chains terminated with an iodine- or bromine-anchoring group. The p-i-n cells comprising these layers exhibit efficiencies above 21% while being processed at temperatures no higher than 100 °C. The layer significantly improves the resilience of the whole solar cell to heat, light, and moisture. If operated at the maximum power point, the cells maintain 99% of their initial efficiency even after 250 h of continuous illumination at 85 °C (ISOS-L-2 conditions). This is remarkable given that the chosen p-i-n structure does not require chemical dopants nor any encapsulation.[222–224]

6.3 DEVICE PERFORMANCE

Figure 30 displays our standard p-i-n solar cell architecture with the structure $\mathrm{ITO} \,|\, \mathrm{HTL} \,|\, \mathrm{CsI_{0.05}[FA_{0.85}MA_{0.15}Pb(I_{0.85}Br_{0.15})_3]_{0.95}} \,|\, \mathrm{SAM} \,|\, \mathrm{C_{60}} \,|\, \mathrm{BCP} \,|\, \mathrm{Cu}$. Such cells exhibit power conversion efficiencies of roughly 19% with an average open-circuit voltage of <1.1 V, 77% fill factor (FF), and a short-circuit current density (J_{SC}) of 22.3 $mAcm^{-2}$. The introduction of the p-SAMs directly influences all photovoltaic parameters, depending on the nature of the anchoring group (iodine or bromine) and the length of the perfluorinated carboxylic tail (Figure 31A). We deposit the SAMs by submerging the annealed perovskite for ~20 min in a dilute solution of the respective molecules (10 mM), which we found to be the optimum concentration in initial tests, especially with regard to FF (Figure S2, SI). Notably, the iodine-terminated molecules improve the photovoltaic performance, predominately through the improvement of V_{OC} to an average above 1.15 V, whereas other metrics remain practically unchanged. The current density of 22.5 $mAcm^{-2}$ is confirmed by the integrated EQE_{PV} spectrum in Figure S1, SI. Employing a Br-terminated SAM increases the V_{OC} above 1.10 V but causes a continuous decrease of the FF with the increasing length of the perfluorinated tail, resulting in an overall reduction of the PCE. Given the fact that the nature of the binding moiety affects mainly the FF, we speculate that the decrease in efficiency upon inserting the Br-terminated SAM is related to the efficiency of charge extraction. This point will be addressed later. The optimal performance in this series is obtained with $IPFC_{10}$—perfluorodecyl iodide—with which we achieve a V_{OC} of 1.18 V at a thermodynamic limit of 1.32 V. This is among the highest open-circuit voltage reported for p-i-n-type perovskite solar cells—beaten only by a very recent approach using a secondary perovskite phase at the perovskite/ETL interface[217] or with very specific processing conditions and unstable transient performance (*i. e.* , strong light soaking required). [225] The corresponding nonradiative loss in potential is only ~150 mV, which is among the lowest losses for the given band gap of the absorber—irrespective of the architecture.

As a result, inserting IPFC$_{10}$ causes an average improvement of the PCE by absolute 1.5%, with a record efficiency of 21.3% (average 20.5%). We note that the devices do not exhibit pronounced hysteric effects, irrespective of scan speed or direction, and the obtained efficiencies coincide with the stabilized MPP output (Figure 31B,C and Figure S3, SI).

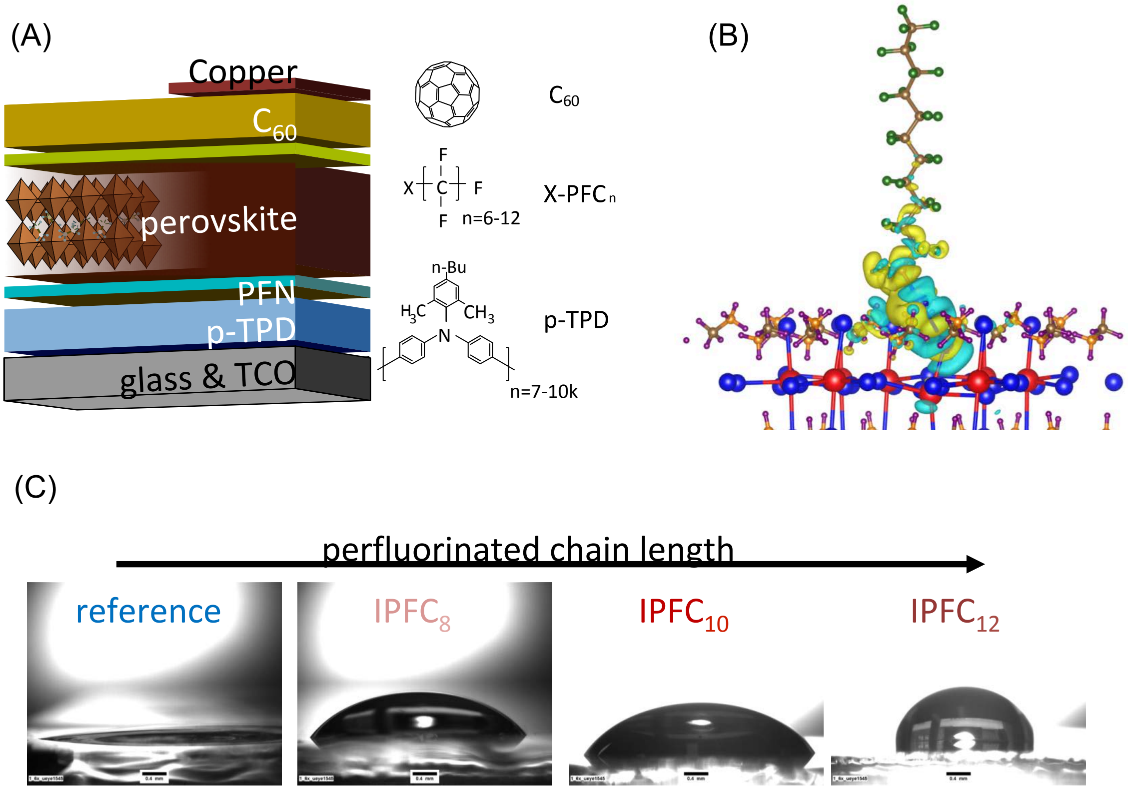

Figure 30: (A)Schematics of the p-i-n-type device architecture showing the position of the individual layers, as well as the chemical structure of the molecules used for the SAM preparation and the transport layers. (B) Density functional theory (DFT) simulations of the coupling between an IPFC$_{12}$ molecule and a perovskite (I-terminated) surface together with the positive (yellow) and negative (turquoise) charge redistribution responsible for the halogen-type bonding. (C) Contact angle measurements of 2-propanol on perovskite | IPFC$_n$-SAM-samples with different n= 0, 8, 10, 12. Reproduced with permission. [201] Copyright 2020, American Chemistry Society.

6.4 SAM BOND FORMATION AND LAYER CHARACTERISTICS

It has been proposed that halogenated organic compounds bind to undercoordinated halide anions at the perovskite surface by the formation of noncovalent halogen bonds.[226] The binding and SAM properties of linear I-terminated perfluorocarbons on different model interfaces have been studied recently.[227] For IPFC$_{12}$ on silicon nitride, density functional theory (DFT) revealed noncovalent halogen bond formation, where approximately 0.5 electrons were transferred from the nucleophilic nitrogen surface atom to the electrophilic iodine atom, going along with large binding energy of 128 kJ/mol. Halogen bond formation was confirmed by ssNMR on the self-assembled monolayer adsorbed to SiNx nanoparticles. The study of a SAM on a flat SiN$_x$ with X-ray reflectometry and contact angle measurements revealed the formation of a dense molecular with a critical surface energy of only 2.6 Nm. DFT calculations were performed to explore the potential interaction of our SAM molecules to the perovskite surface. Because we were interested specifically in the nature and strength of a possible binding of the SAM molecules to the halide anions, we restricted our simulations to the case that molecules adsorb on an I-terminated (111) perovskite surface (calculation details are given in the Supplementary Note 1, SI). In Scheme S1, we show the side views of $IPFC_{12}$ molecules assembled on a perovskite surface. Although these are simplifications—for example, the perovskite surface may expose different facets [228]– this DFT model is useful to elucidate the electron distribution at the hybrid interface and with that the strength and nature of a formed I-I bond. Similar to the case of $IPFC_{12}$ on silicon, silicon nitride, or silicon oxide surface, the interaction between $IPFC_{12}$ and the perovskite surface is primarily electrostatic in nature, although second-order contributions such as polarization, dispersion, and charge transfer are present.[227] Figure 30b shows the iso-surface plot of the induced charge density, defined as $\Delta n(r) = n_{tot} - [n_{mol} + n_{surf}]$, that is, the difference between the charge density of the adsorption system and the sum of the isolated $IPFC_{12}$ molecule and the perovskite surface. The Löwdin atomic charge analysis[229] of such a molecule-substrate system reveals that up to 0.3 electrons are transferred from the nucleophilic iodine surface to the electrophilic iodine atom of the molecule with respect to its neutral valence charge. The computed binding energy is 183 kJ/mol, higher than the binding energy between $IPFC_{12}$ on the silicon nitride surface (128 kJ/mol).[227, 230–233] To confirm the existence of a SAM on our perovskite samples, we carried out photoemission (X-ray photoemission spectroscopy, Figure S4, SI) and Fourier transform infrared (FTIR) spectroscopy (Figure S5, SI) studies on neat and SAM-modified perovskite samples. The F 1s core-level XPS spectra reveal the presence of fluorinated species on the surface of the perovskite concurrent with a shift in work function as obtained from Kelvin probe measurements (both Figure S4, SI). Unfortunately, we were not able to deduce specific information on the type of binding from these XPS spectra. It is known that X-ray illumination and substrate-induced photochemical reactions may remove iodine from the molecules. FTIR spectra (shown in Figure S5, SI) consolidate the presence of the molecules on top of the perovskite, as indicated by the appearance of additional modes at 1150-1300 cm^{-1}, absent in the unmodified perovskite. Interestingly, we observed a small blue shift of the prominent molecular bands of the SAM (Figure S5C, SI) at ~1200 and 1150 cm^{-1} when deposited on the perovskite. This may indicate a larger degree of disorder in the surface-bound molecular layer compared to the pristine $IPFC_{12}$. One reason for this may be the strong binding of the I-terminated molecule to the perovskite, as suggested by the above DFT calculations. Strong surface binding is known to inhibit the formation of dense molecular packing by reducing the mobility of the molecules along the surface. In fact, comparing the strength of the $I_{3d\ 5/2}$ signal of the pristine perovskite and samples modified with a $IPFC_{10}$ revealed an average thickness of the I-terminated SAM of only 2.6 Å. This value may be considered as a lower limit due to the instability of the I binding under X-ray exposure. Notably, the estimated average thickness of the Br-terminated SAM (in this case $Br\text{-}PFC_9$) is larger (~4.7 Å). Also, the comparison of the FTIR spectra of the surface-bound molecules and the dense molecular film revealed identical peak positions, indicative of a higher molecular order in the Br-terminated SAM. This may be due to a smaller strength of the formed halogen bond,[234, 235] rendering the Br-terminated molecules more mobile. The formation of a denser and thicker SAM from the Br-terminated perfluorocarbons may be the reason for the significant lowering of the FF with increasing molecular length and concentration as noted above.[236, 237] Proof for a dense coverage of the perovskite surface with perfluorinated carbon chains (even in the case of I termination) comes from the measurements of contact angle. Figure 30C shows photographs of contact angle measurements with 2-propanol (IPA) on the perovskite with and without the iodated SAMs. The sample without any treatment shows a contact angle of <5°, which steadily increases when employing SAMs with longer tails, reaching 88° in the case of $IPFC_{12}$.

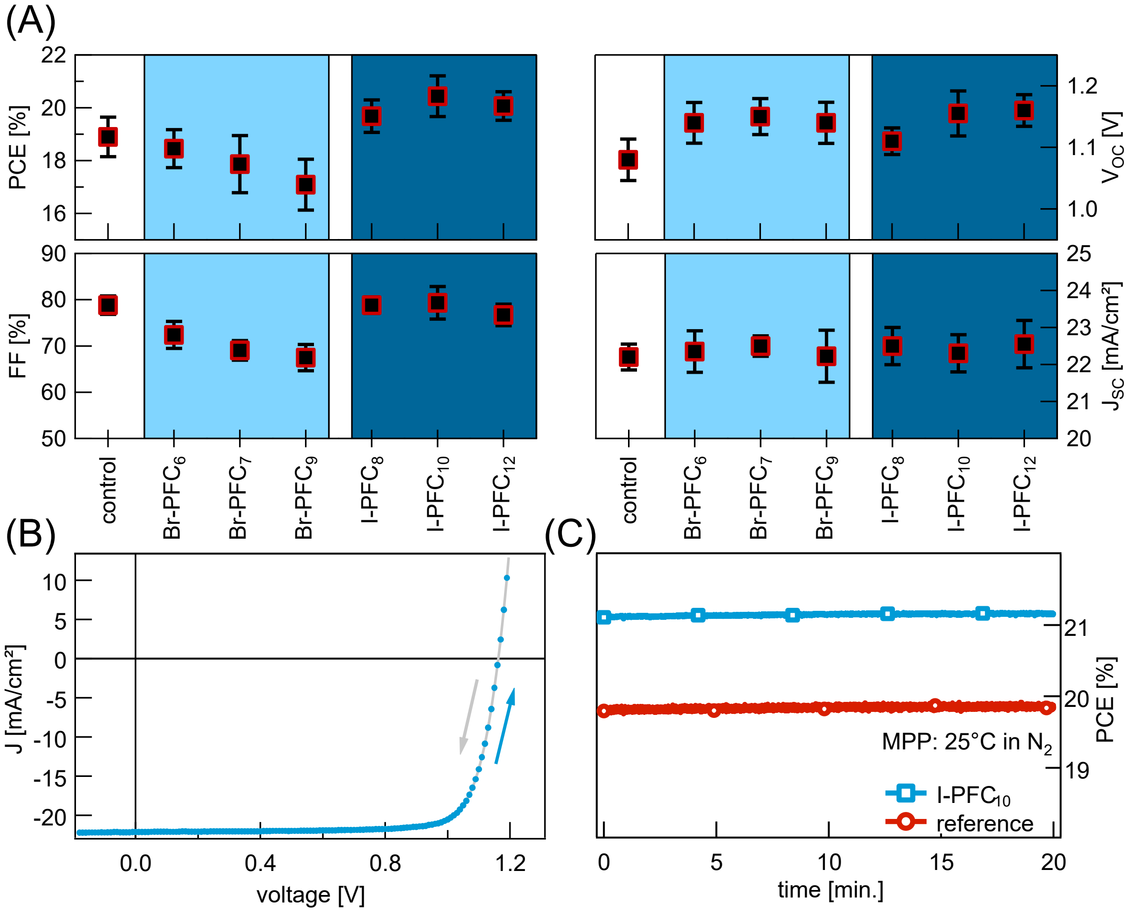

Figure 31: (A) Average statistics of the photovoltaic parameters PCE, V_{OC}, FF, and J_{SC} over several batches including the standard deviation of each parameter. (B) JV curve of the best performing device with an IPFC10 SAM in forward and backward scan direction (100 mV/s), yielding a PCE of 21.3%. (C) Representative maximum power point tracking over the course of 20 min of one of the highest performing IPFC$_{10}$ and reference devices. Reproduced with permission. [201] Copyright 2020, American Chemistry Society.

6.5 LOSS IN POTENTIAL AND IMPROVEMENT OF THE V_{OC}

The significant increase of the V_{OC} upon insertion of the SAMs requires special attention. It has previously been shown that any improvement in V_{OC} is related to an increase in band gap or a reduction of recombination, either in the perovskite bulk, at the perovskites' surface or at the interface with an adjacent layer.[66, 99, 123, 145, 179, 238] In previous publications, we identified interfacial recombination as the primary source for a decreased photovoltage of p-i-n-type perovskite solar cells.[99, 171] Mitigating these losses often comes at the expense of FF.[99, 169, 239, 240] However, the exact origin of the V_{OC} improvements will depend largely on the system of interest, and it is yet not clear whether additives or interlayers improve V_{OC} by reducing recombination in the bulk (and grain boundaries) or at the interfaces with the adjacent transport layers.[241] It has been proposed that the binding of organohalides to a perovskite surface decreases the density of surface traps.[226] To investigate whether our SAMs improve the V_{OC} predominantly via trap passivation or through the suppression of interfacial recombination, we determined the quasi-Fermi-level splitting (QFLS) in the perovskite through the measurement of the absolute PL on the neat perovskite, multilayer stacks, or full devices with Equation 27:

$$\mu = k_B T \cdot \ln \left[\text{PLQY} \frac{J_G}{J_{0,rad}} \right]$$

Here, PLQY is the external quantum efficiency of photoluminescence, and J_G/q and $J_{0,rad}/q$ are the photon flux of solar and blackbody radiation, respectively, which is absorbed/emitted by the active layer. This equation is only correct in absence of excitonic effects, meaning that every absorbed photon generates a free electron-hole pair and that all PL stems from direct free carrier recombination. As the QFLS in the absorber limits the V_{OC} of the solar cell, information on the QLFS and how it is affected by the SAM and the addition of the charge-transporting layers is of crucial importance to understand the V_{OC} improvement. For the pure absorber or the absorber in contact with additional layers under the condition of no electrical contact, any charges generated in the device must recombine within this stack. In the ideal case, all absorbed photons are simply re-emitted—called photoluminescence. In addition to photon emission, the electrons and holes can also lose their energy through nonradiative recombination,[64] resulting in the dissipation of heat, which would decrease PLQY, reducing the QFLS.[242] Thus, measuring the rate of emitted photons versus generated carriers is a measure of how energy is lost through these unwanted processes. We performed several pulsed and steady-state measurements to unambiguously show the processes that limit the solar cells' V_{OC} at varying carrier densities. In Figure 32a, we show the EQE_{PV} spectra of the perovskite solar cells measured under short-circuit conditions. All devices exhibit a very similar spectral shape with a band gap of 1.61 eV (half-maximum) and Urbach energies of ~15 meV. The deduced generation ($J_G = J_{SC} = q \int \phi_{sun} EQE_{PV} dE$) and radiative dark recombination current at 300 K ($J_{0,rad.} = q \int \phi_{BB} EQE_{PV} dE$) are ~22 mA cm^{-2} (see Figure S1, SI) and ~10^{-21} mA cm^{-2}, respectively. Here, we also assume that all photogenerated charge carriers reach the electrodes under short-circuit conditions, which is a reasonable assumption given that perovskite solar cells with comparable band gap show flat internal quantum efficiency spectra with close to 100% efficiency. This results in a radiative limit of 1.32 eV for the obtainable QFLS and thus V_{OC} (details on the calculations are in Supplementary Note 2,).[43, 69, 145, 152] As the devices' V_{OC} values are substantially lower than that, the devices obviously suffer from substantial additional nonradiative recombination currents. In order to decouple the losses, we measured the luminescent efficiency of samples that are made from the individual layers (always with perovskite) of the solar cell stack or of the whole solar cells. Figure 32B and Figure S3(SI) show the obtained PL spectra at 1 sun equivalent illumination conditions. The pristine perovskite has an external PLQY of just below 1%, which allows for a maximum QFLS of 1.23 eV (see Supplementary Note 2, SI). Adding the SAMs to the neat perovskite film has no effect on the PL emission properties (Figure S6, SI), irrespective of the nature of the anchoring group used herein. Therefore, we can rule out surface passivation of device-relevant traps as the main source for the significant improvement of the device performance. On the other hand, the perovskite in direct contact with C_{60} only emits 1 photon for every ~10^5 incoming photons (Figure 32B). Upon introduction of the perfluorinated SAMs, this reduction is mitigated by almost 2 orders of magnitude, rendering PLQYs of up to ~0.5% This implies that the nonradiative losses at this interface are decreased by up to $\approx$ 120 meV, comparable to the average improvement in the device V_{OC} of ~90 mV (105 mV in the best case). These experiments were complemented by the investigation of the carrier dynamics after photogeneration by performing time-resolved photoluminescence (tr-PL) measurements at low excitation intensities. This allows deducing mean carrier lifetimes free of capacitive effects,[67] which in turn yield the average carrier densities under steady-state illumination in the limit of predominant first-order recombination from which V_{OC} can be estimated (see Supplementary Note 2, SI).[69] The pure perovskite has PL decay times (1/e) of ~600-800 ns. Plugging this into eqs S5 and S6 results in a QFLS of up to 1.23 eV, consistent with the previous PLQY measurements. We note again that this is to be expected only if the transient PL decay is dominated by a first-order recombination loss, for example, recombination via traps in the bulk or by interfacial recombination, while free carrier recombination is insignificant.[62] Importantly, as shown in Figure 32b, the functionalization of the perovskite with the SAMs (but without the presence of C_{60}) did not change the monoexponential tr-PL lifetime, again ruling out trap passivation as the source of the improvement in V_{OC}, which is also evident from the absolute PL measurements on pristine versus modified perovskite as noted above. In contrast, depositing C_{60} on the perovskite decreases the lifetime. Although it has been suggested that fullerenes passivate traps in the perovskite or rather at the grain boundaries,[243, 244] we observe a drastic reduction of carrier lifetime, which is consistent with the large decrease in QFLS as noted above. The carrier lifetime can however be partially recuperated by interjecting SAMs. The lifetimes increase from ~25 ns (C_{60} only) up to ~150 ns, which allow us to calculate obtainable QFLS values of 1.080 and 1.173 eV, respectively, in excellent agreement to the measured V_{OC}. Finally, we combined measurements of the EQE_{PV} and of the external quantum efficiency of electroluminescence, EQE_{EL}, on full devices to deduce values of V_{OC} with Rau's reciprocity relation. In contrast to the methods described above, Rau's reciprocity explicitly considers the exchange of charge carriers between the perovskite absorber and the contacts. It has been pointed out before that errors between the predicted and measured V_{OC} may arise from insufficient collection and/or injection of electrical charges.[245]Figure 32D summarizes the results from all three techniques on multiple samples. We supported these findings by measuring the surface photovoltage (SPV) on half-cells comprising ITO | HTL | perovskite alone or capped with C_{60}, the SAMs, or SAMs and C_{60}. The spectrally dependent voltage buildup (photovoltage) of the devices (Figure S7C, SI) without C_{60} exhibits no appreciable difference between pristine or modified perovskites, indicating that the electronic structure of the perovskite at the surface is not changed. Yet, with the C_{60} present (Figure S7B, SI), the situation differs, as the samples are now able to better separate charges (*i. e.* , generate voltage due to electron accumulation in the C_{60} layer). We find that this voltage increases in the following order: perovskite < perovskite | C_{60} < perovskite | SAM | C_{60}, corroborating that the incorporation of the SAM improves charge separation at the n-interface, and that the effect due to the SAM is only seen if C_{60} is also present. Therefore, the main difference between the studied cells is nonradiative recombination at the perovskite/C_{60} interface, which is decreased progressively with increasing length of the SAMs. We are able to draw the following conclusions: (1) All four techniques (PLQY, EQE_{EL}, tr-PL, and SPV) are mutually in excellent agreement. (2) The QFLS in the perovskite layer determines the V_{OC} in the devices. Therefore, all changes in V_{OC} (from the addition of the charge-transporting layers and the SAM) originate from differences in the QFLS of the absorber and must, therefore, be related to the charge recombination dynamics. Notably, the perovskite layers on glass or on the HTL both allow a $V_{OC} > 1.2$ V, which also means that nonradiative recombination at the interface between the perovskite and the HTL (poly-TPD) is comparably slow. (3) The perovskite/C_{60} interface is the bottleneck for a high photovoltage output, as it decreases the obtainable V_{OC} (QFLS) to a maximum of 1.08 V (eV) on average (1.1 V max). (4) Given that the deposition of the SAMs on the neat perovskite layer does not affect the luminescent properties or the magnitude of the SPV signal, we can rule out passivation of the perovskite surface as the main reason for the shown improvement. We can, therefore, assign the improved QFLS and lifetime of the cells to suppressed across-interface recombination. Lastly, we note that a recent similar[246] approach reports on a red shift of the perovskite absorption onset by annealing the samples after the deposition of a similar molecule in vastly higher concentrations, whereas we observe essentially no change in the band gap energy or tail slope (see Figure S8, SI).

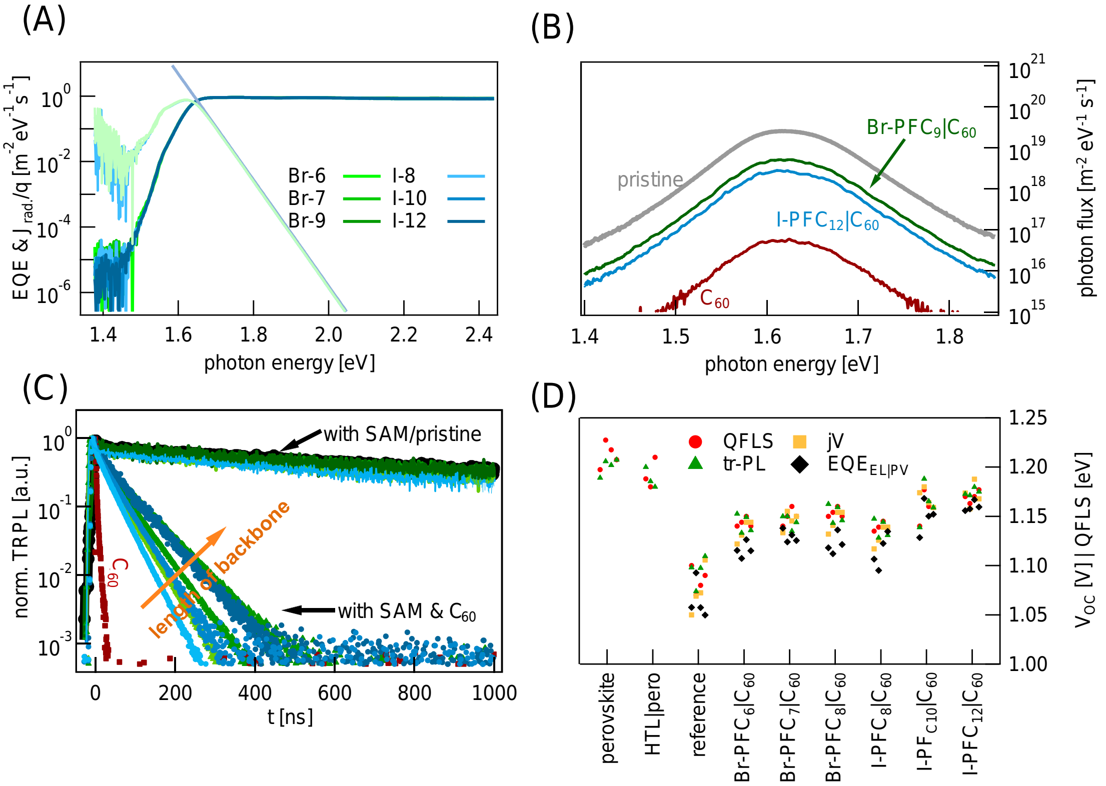

Figure 32: (A) EQE_{PV} and $J_{0,rad.}/q$ for of the solar cells with the different interlayers. (B) PL photon flux under a 1 sun equivalent 445 nm illumination of the neat perovskite reference, the perovskite covered with C_{60}, and with the two longest molecule chain SAMs between. (C) Normalized tr-PL decays of perovskite (black dots) with the different SAMs (green and blue lines), compared to the corresponding devices with an additional C_{60} layer, with (green and blue dots) or without (dark red dots) the SAMs. All measurements were performed with excitation at 470 nm and 40 nJ/cm^2. (D) Deduced QFLS or qV_{OC} as determined from the absolute PL (red), tr-PL (green), JV scan (yellow), or the electroluminescence efficiency (black) for several samples each.Reproduced with permission. [201] Copyright 2020, American Chemistry Society.

6.6 DEVICE STABILITY

Many of the state-of-the-art perovskite solar cells—irrespective of p-i-n or n-i-p architecture—show excellent performance. At the same time, the number of reports concerning enhanced stability has increased following this rapid increase in efficiency.[202, 203] The general belief is that the perovskite is the weakest link in the multilayer devices. In particular, the organic cations—foremost methylammonium—are blamed as the culprit due to their volatile nature. Various approaches have been employed to decrease or mitigate these losses through (partial) cation exchange with bigger molecules such as formamidinium or guanidinium, encapsulation, blocking layer deposition, or passivation.[218, 219, 247–249] Whereas most approaches concern either rigid hard encapsulation through ALD layers or additive engineering, fewer have adopted ways to improve the interfaces as a simple postprocess. We sought to test the impact on stability for the best performing devices in our SAM series. We anticipated that the binding between the p-SAMs and the perovskite and the strong entanglement of the perfluorinated tail of the molecules decreases the permeability for small molecules and ions at the perovskite | C_{60} interface in either direction. As ingress of water and evolution of MA^+ are considered the Achilles heel of perovskite solar cells, preventing the latter two seems to be the natural approach. As a proof of principle, we also provide photographs of perovskite layers with a water droplet, revealing a drastic suppression of perovskite decomposition upon SAM deposition. Whereas in the case of the untreated perovskite a yellow spot is visible shortly after dropping the water, indicating the irreversible formation of PbI_2, this irreversible decomposition is drastically slowed in the case of $IPFC_{12}$ (both in Figure S9, SI), where this decomposition takes minutes to occur. This effect is likewise visible when comparing the absorption spectra of a similar perovskite (slightly higher Br/I ratio) as a function of storage time in ambient conditions. In the case of a sample without functionalization, the perovskite decomposes as evident from the increase in the PbI_2 absorption signal (Figure S10, SI). We rationalize this slowdown of decomposition by measuring X-ray diffractograms of perovskite films with and without $IPFC_{10}$ or Br-PFC9 after exposure to humid air (~50% RH) overnight (Figure S10D, SI). We find that the interlayers effectively retard the ingress of water, evident from the absence of perovskite hydrate phases,[250] which give rise to characteristic diffraction features at ~11° in contrast to the unmodified perovskite (Figure S10D, SI). This slowdown will, in turn, retard water-induced degradation. Finally, we measured full solar cells over the course of 4 months (~3000 h) both "encapsulated" in an inert atmosphere and under ambient conditions without encapsulation, with weak light exposure (*i. e.* , shelf storage). Figure 33A shows that when stored in the inert atmosphere, both reference and modified devices are essentially stable, whereas when they are stored in the ambient environment, the devices without SAMs lose up to 30% of their initial (already lower) efficiency. In contrast, the devices with a modified interface retain 95% of their initial efficiency under ISOS-D-1 conditions. We conclude that surface modification effectively decreases the ingress of moisture, which we consider to be the main reason for the device degradation. The alternative to diffusion into or within the cell is the diffusion of organic cations out of the cell; in particular, MA^+ may be lost due to this process, which potentially induces an irreversible degradation. As diffusion is a thermally activated motion, we tested the thermal stability of the individual volatile components in the perovskite. To this end, we performed differential scanning calorimetry (DSC) measurements on MAI, $IPFC_{10}$, and a combined powder (MAI + $IPFC_{10}$), as seen in Figure 33B. The melting point of pure $IPFC_{10}$ is visible at ~70 °C, whereas MAI shows a peak at ~150 °C which is associated with a phase transition of MAI from the solid crystalline phase to a premelting state called ionic plastic phase, as reported in the literature.[251, 252] In contrast, the mixed powder completely lacks the spike at 70 °C and shows the same thermal transition of MAI but is shifted by ~15 °C to higher temperatures, indicating the stabilizing effect of $IPFC_{10}$ on MAI. These observations led to the hypothesis that the $IPFC_{10}$-modified solar cells will be more thermally stable than the reference counterparts. We tested this hypothesis by measuring some of the most efficient devices at various relevant temperatures (Figure 33C), where we were able to extract thermal efficiency loss coefficients of -0.106 and -0.122%/°C for the $IPFC_{10}$ and the reference device, respectively, indicating a small improvement in the modified cells. We note that these numbers are comparable to those in previous reports,[253] although a bit lower. Finally, we subjected these cells to an intensive coupled heat-light load stress test by measuring the power output of the devices held at MPP at 85 °C with an equivalent of ~1 sun illumination in a nitrogen atmosphere (Figure 33D), consistent with the ISOS-L-2 protocol. Much of the recent reports show normalized efficiencies, especially when performing aging tests. Although we believe that in many cases this may help to visualize the improvement, we want to stress that performing standardized stress tests on the highest performing devices is essential and often omitted. Also, we did not encapsulate the devices on purpose to show the full potential of the SAMs.[254] Initially, the cells are at room temperature and then heated within a few minutes to 85 °C, causing a rapid initial decrease of ~6% due to a higher thermal recombination current (Jrad) of the device at 85 °C compared to 25 °C, which in turn decreases V_{OC} and V_{MPP} and thus PCE. After this, the best reference device still degraded rapidly to <5% within ~30 h. In stark contrast, the modified device recovered from the initial decrease within a few hours and stabilized at 16%. This device maintained this efficiency over the next 250 h without any additional loss, without the need for elaborate encapsulation strategies.[218, 219, 255] The high stability is very encouraging given the simplicity of the approach and that the perovskite is only capped by another 40 nm of small organic molecules (C_{60} and

BCP) and a metal cathode. We also observe a mild improvement in V_{MPP} over time (Figure S11A, SI), which we believe is due to a light-induced modification/relaxation of the perovskite,[256–258] enhancing the PLQY, which we could likewise observe for the mixed-halide/mixed-cation perovskite in a reference experiment (Figure S11B, SI).

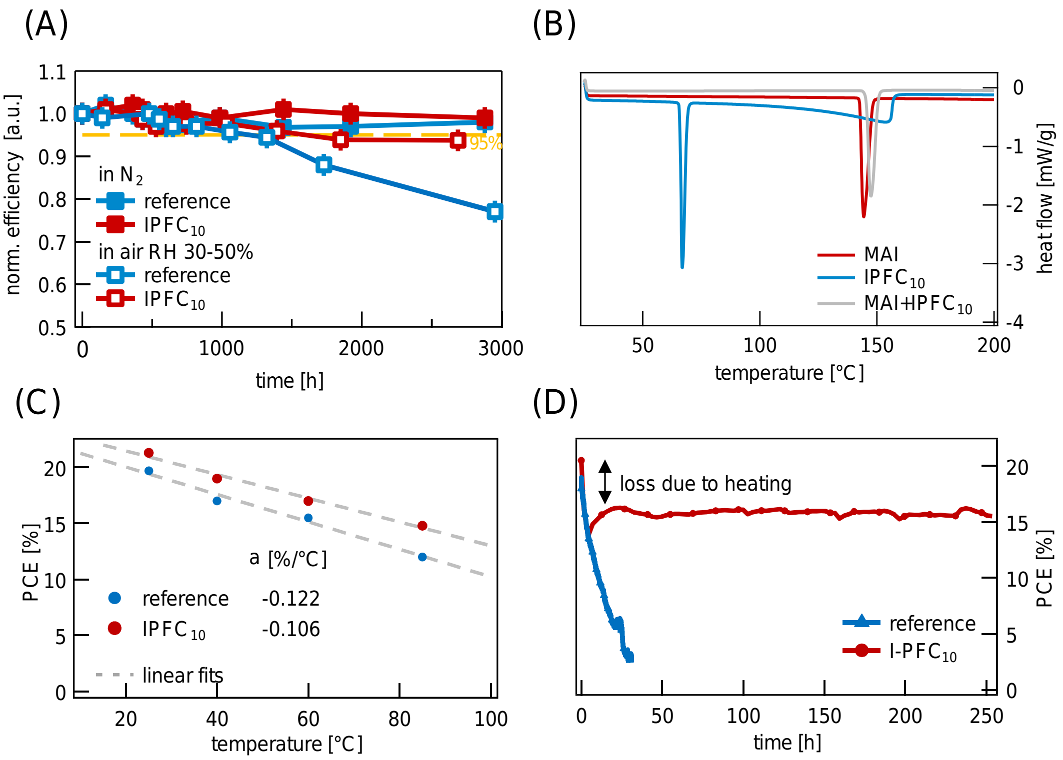

Figure 33: (A) Stability of perovskite solar cells stored in nitrogen or ambient air over the course of 4 months. (B) DSC measurements on MAI, I-PFC10, and a mixture of the latter that show the interaction of the I-terminated group to iodine in MAI enhancing the latter's thermal stability. (C) Temperature-dependent PCE with linear fitting renders efficiency loss coefficients of ~0.1%/°C. (D) Maximum power point tracking at increased temperature (85°C) in a nitrogen-filled glovebox for the reference (red) and modified device (blue). Both devices show a quick initial decrease due to the increase in temperature. Reproduced with permission. [201] Copyright 2020, American Chemistry Society.

CONCLUSION In summary, we present a facile method to modify the perovskite absorber in highly efficient p-i-n-type solar cells through the use of perfluorinated halogenated self-assembled molecules. Functionalization of the perovskite surface with I-terminated linear fluorocarbons comes with a significant increase of the open-circuit voltage up to 1.18 V, while leaving the other photovoltaic parameters unchanged. Such SAM-functionalized perovskite devices exhibited power conversion efficiencies surpassing 21%. XPS, ultraviolet photoelectron spectroscopy, and FTIR suggest that the SAMs interact with the perovskite surface mainly through mild electrostatic interactions. Using absolute PL, tr-PL electroluminescence, and SPV measurements, we show that the deposition of the SAM has no effect on the recombination properties of the perovskite itself, ruling out trap passivation as the main reason for the performance increase. Instead, we show that the functionalization of the perovskite top surface with the fluorocarbon molecules improves charge separation and suppresses nonradiative recombination at the perovskite/C_{60} interface. Due to the sufficiently strong adhesion to the surface and its fluorinated water-repelling backbone, cells comprising the SAM molecules withstand harsh stress tests such as 250 h MPP tracking at increased temperatures (85 °C) or long-term exposure to ambient air without appreciable efficiency loss under standardized harsh testing conditions (ISOS-D-1 and ISOS-L-2). This work demonstrates advancement in the quest to improve the stability and efficiency of perovskite solar cells toward industrial standards using a simple solution-based approach, without the need for elaborate and complicated processing schemes, compatible with conformal growth methods, even on rough or textured surfaces.[213, 214, 259–261] Combining these dual benefits of stability and decreased interfacial recombination with surface passivation layers will be the next step toward highly efficient and more stable devices, pushing this technology to the verge of commercialization.

[201] Christian M. Wolff et al. "Perfluorinated Self-Assembled Monolayers Enhance the Stability and Efficiency of Inverted Perovskite Solar Cells." In: *ACS Nano* 14.2 (Feb. 2020), pp. 1445–1456 (cit. on pp. 80, 83, 85, 88, 90).

[202] Caleb C. Boyd et al. "Understanding Degradation Mechanisms and Improving Stability of Perovskite Photovoltaics." In: *Chemical Reviews* 119.5 (Mar. 2019), pp. 3418–3451 (cit. on pp. 81, 88).

[203] Jeffrey A. Christians et al. "Stability in Perovskite Photovoltaics: A Paradigm for Newfangled Technologies." In: *ACS Energy Letters* 3.9 (Sept. 2018), pp. 2136–2143 (cit. on pp. 81, 88).

[204] J. Zhao et al. "Self-Encapsulating Thermostable and Air-Resilient Semitransparent Perovskite Solar Cells." In: *Advanced Energy Materials* 7.14 (July 2017), p. 1602599 (cit. on p. 81).

[205] Dibyashree Koushik et al. "High-efficiency humidity-stable planar perovskite solar cells based on atomic layer architecture." In: *Energy Environ. Sci.* 10.1 (Jan. 2017), pp. 91–100 (cit. on p. 81).

[206] Shuang Yang et al. "Functionalization of perovskite thin films with moisture-tolerant molecules." In: *Nature Energy* 1.2 (Jan. 2016), p. 15016 (cit. on p. 81).

[207] Xiong Li et al. "Improved performance and stability of perovskite solar cells by crystal crosslinking with alkylphosphonic acid ω-ammonium chlorides." In: *Nature Chemistry* 7.9 (Aug. 2015), pp. 703–711 (cit. on p. 81).

[208] Nakita K. Noel et al. "Enhanced Photoluminescence and Solar Cell Performance via Lewis Base Passivation of Organic–Inorganic Lead Halide Perovskites." In: *ACS Nano* 8.10 (Oct. 2014), pp. 9815–9821 (cit. on p. 81).

[209] Sagar Motilal Jain et al. "Frustrated Lewis pair-mediated recrystallization of CH 3 NH 3 PbI 3 for improved optoelectronic quality and high voltage planar perovskite solar cells." In: *Energy Environ. Sci.* 9.12 (Nov. 2016), pp. 3770–3782 (cit. on p. 81).

[210] Hsinhan Tsai et al. "High-efficiency two-dimensional Ruddlesden–Popper perovskite solar cells." In: *Nature* 536.7616 (Aug. 2016), pp. 312–316 (cit. on p. 81).

[211] Zhiping Wang et al. "Efficient ambient-air-stable solar cells with 2D–3D heterostructured butylammonium-caesium-formamidinium lead halide perovskites." In: *Nature Energy* 2.9 (Aug. 2017), p. 17135 (cit. on p. 81).

[212] Nam Joong Jeon et al. "A fluorene-terminated hole-transporting material for highly efficient and stable perovskite solar cells." In: *Nature Energy* 3.8 (Aug. 2018), pp. 682–689 (cit. on pp. 81, 127, 128).

[213] Marko Jošt et al. "Textured interfaces in monolithic perovskite/silicon tandem solar cells: advanced light management for improved efficiency and energy yield." In: *Energy & Environmental Science* 11.12 (Dec. 2018), pp. 3511–3523 (cit. on pp. 81, 91).

[214] Florent Sahli et al. "Fully textured monolithic perovskite/silicon tandem solar cells with 25.2% power conversion efficiency." In: *Nature Materials* 17.9 (Sept. 2018), pp. 820–826 (cit. on pp. 81, 91, 110).

[215] Luana Mazzarella et al. "Infrared Light Management Using a Nanocrystalline Silicon Oxide Interlayer in Monolithic Perovskite/Silicon Heterojunction Tandem Solar Cells with Efficiency above 25%." In: *Advanced Energy Materials* (Feb. 2019), p. 1803241 (cit. on p. 81).

[216] Christian M. Wolff et al. “Nonradiative Recombination in Perovskite Solar Cells: The Role of Interfaces.” In: *Advanced Materials* (Oct. 2019), p. 1902762 (cit. on pp. 82, 109, 138).

[217] Junsheng Luo et al. “Toward high-efficiency, hysteresis-less, stable perovskite solar cells: unusual doping of a hole-transporting material using a fluorine-containing hydrophobic Lewis acid.” In: *Energy & Environmental Science* 11.8 (Aug. 2018), pp. 2035–2045 (cit. on p. 82).

[218] Kevin A. Bush et al. “Thermal and Environmental Stability of Semi-Transparent Perovskite Solar Cells for Tandems Enabled by a Solution-Processed Nanoparticle Buffer Layer and Sputtered ITO Electrode.” In: *Advanced Materials* 28.20 (May 2016), pp. 3937–3943 (cit. on pp. 82, 88, 89).

[219] K.O. Brinkmann et al. “Suppressed decomposition of organometal halide perovskites by impermeable electron-extraction layers in inverted solar cells.” In: *Nature Communications* 8 (Jan. 2017), p. 13938 (cit. on pp. 82, 88, 89).

[220] Yang Bai et al. “Enhancing stability and efficiency of perovskite solar cells with crosslinkable silane-functionalized and doped fullerene.” In: *Nature Communications* 7.1 (Nov. 2016), p. 12806 (cit. on p. 82).

[221] Seongrok Seo et al. “Perovskite Solar Cells with Inorganic Electron- and Hole-Transport Layers Exhibiting Long-Term (~500 h) Stability at 85 °C under Continuous 1 Sun Illumination in Ambient Air.” In: *Advanced Materials* 30.29 (July 2018), p. 1801010 (cit. on p. 82).

[222] Laura Calió et al. “Hole-Transport Materials for Perovskite Solar Cells.” In: *Angewandte Chemie International Edition* 55.47 (Nov. 2016), pp. 14522–14545 (cit. on p. 82).

[223] Taisuke Matsui et al. “Additive-Free Transparent Triarylamine-Based Polymeric Hole-Transport Materials for Stable Perovskite Solar Cells.” In: *ChemSusChem* 9.18 (Sept. 2016), pp. 2567–2571 (cit. on p. 82).

[224] Fei Guo et al. “A generic concept to overcome bandgap limitations for designing highly efficient multi-junction photovoltaic cells.” In: *Nature Communications* 6 (2015), p. 7730 (cit. on p. 82).

[225] Zhifa Liu et al. “Open-Circuit Voltages Exceeding 1.26 V in Planar Methylammonium Lead Iodide Perovskite Solar Cells.” In: *ACS Energy Letters* (Dec. 2018), pp. 110–117 (cit. on pp. 82, 119, 130, 132, 138).

[226] Antonio Abate et al. “Supramolecular Halogen Bond Passivation of Organic–Inorganic Halide Perovskite Solar Cells.” In: *Nano Letters* 14.6 (June 2014), pp. 3247–3254 (cit. on pp. 83, 85).

[227] Antonio Abate et al. “Halogen-bond driven self-assembly of perfluorocarbon monolayers on silicon nitride.” In: *Journal of Materials Chemistry A* 7.42 (2019), pp. 24445–24453 (cit. on pp. 83, 84).

[228] Sibel Y. Leblebici et al. “Facet-dependent photovoltaic efficiency variations in single grains of hybrid halide perovskite.” In: *Nature Energy* 1.8 (Aug. 2016), p. 16093 (cit. on p. 84).

[229] Per-Olov Löwdin. “On the Non-Orthogonality Problem Connected with the Use of Atomic Wave Functions in the Theory of Molecules and Crystals.” In: *The Journal of Chemical Physics* 18.3 (Mar. 1950), pp. 365–375 (cit. on p. 84).

[230] Hendrik J. Monkhorst and James D. Pack. “Special points for Brillouin-zone integrations.” In: *Physical Review B* 13.12 (June 1976), pp. 5188–5192 (cit. on p. 84).

[231] John P. Perdew, Kieron Burke, and Matthias Ernzerhof. “Generalized Gradient Approximation Made Simple.” In: *Physical Review Letters* 77.18 (Oct. 1996), pp. 3865–3868 (cit. on p. 84).

[232] Paolo Giannozzi et al. “QUANTUM ESPRESSO: a modular and open-source software project for quantum simulations of materials.” In: *Journal of Physics: Condensed Matter* 21.39 (Sept. 2009), p. 395502 (cit. on p. 84).

[233] Riccardo Sabatini, Tommaso Gorni, and Stefano de Gironcoli. "Nonlocal van der Waals density functional made simple and efficient." In: *Physical Review B* 87.4 (Jan. 2013), p. 041108 (cit. on p. 84).

[234] Timothy Clark et al. "Halogen bonding: The σ-hole: Proceedings of "Modeling interactions in biomolecules II", Prague, September 5th-9th, 2005." In: *Journal of Molecular Modeling* 13.2 (Feb. 2007), pp. 291–296 (cit. on p. 84).

[235] Gabriella Cavallo et al. "The Halogen Bond." In: *Chemical Reviews* 116.4 (Feb. 2016), pp. 2478–2601 (cit. on p. 84).

[236] D. Schondelmaier et al. "Orientation and self-assembly of hydrophobic fluoroalkylsilanes." In: *Langmuir* 18.16 (Aug. 2002), pp. 6242–6245 (cit. on p. 84).

[237] Keyun Shou et al. "Ultralow surface energy self-assembled monolayers of iodo-perfluorinated alkanes on silica driven by halogen bonding." In: *Nanoscale* 11.5 (Feb. 2019), pp. 2401–2411 (cit. on p. 84).

[238] Dongqin Bi et al. "Efficient luminescent solar cells based on tailored mixed-cation perovskites." In: *Science Advances* 2.1 (2016) (cit. on p. 85).

[239] Boyuan Cai et al. "4-fold photocurrent enhancement in ultrathin nanoplasmonic perovskite solar cells." In: *Optics Express* 23.24 (Nov. 2015), A1700 (cit. on p. 85).

[240] Jun Peng et al. "A Universal Double-Side Passivation for High Open-Circuit Voltage in Perovskite Solar Cells: Role of Carbonyl Groups in Poly(methyl methacrylate)." In: *Advanced Energy Materials* 8.30 (Oct. 2018), p. 1801208 (cit. on pp. 85, 129, 131).

[241] Martin Stolterfoht et al. "The impact of energy alignment and interfacial recombination on the internal and external open-circuit voltage of perovskite solar cells." In: *Energy and Environmental Science* 12.9 (Oct. 2019), pp. 2778–2788 (cit. on pp. 85, 111, 116, 119–122, 126, 127).

[242] Samuel D. Stranks. "Nonradiative Losses in Metal Halide Perovskites." In: *ACS Energy Letters* 2.7 (July 2017), pp. 1515–1525 (cit. on p. 86).

[243] Yue Xing et al. "New fullerene design enables efficient passivation of surface traps in high performance p-i-n heterojunction perovskite solar cells." In: *Nano Energy* 26 (Aug. 2016), pp. 7–15 (cit. on p. 87).

[244] Yen Chen Shih et al. "Effect of Fullerene Passivation on the Charging and Discharging Behavior of Perovskite Solar Cells: Reduction of Bound Charges and Ion Accumulation." In: *ACS Applied Materials and Interfaces* 10.14 (Apr. 2018), pp. 11722–11731 (cit. on p. 87).

[245] Thomas Kirchartz, Jenny Nelson, and Uwe Rau. "Reciprocity between Charge Injection and Extraction and Its Influence on the Interpretation of Electroluminescence Spectra in Organic Solar Cells." In: *Physical Review Applied* 5.5 (May 2016), p. 054003 (cit. on pp. 87, 117).

[246] K. M. Muhammed Salim et al. "Extended Absorption Window and Improved Stability of Cesium-Based Triple-Cation Perovskite Solar Cells Passivated with Perfluorinated Organics." In: *ACS Energy Letters* 3.5 (May 2018), pp. 1068–1076 (cit. on p. 87).

[247] Silver-Hamill Turren-Cruz, Anders Hagfeldt, and Michael Saliba. "Methylammonium-free, high-performance and stable perovskite solar cells on a planar architecture." In: *Science* 362.6413 (Oct. 2018), eaat3583 (cit. on pp. 88, 129).

[248] F. Javier Ramos et al. "Versatile perovskite solar cell encapsulation by low-temperature ALD-Al2O3 with long-term stability improvement." In: *Sustainable Energy and Fuels* 2.11 (Oct. 2018), pp. 2468–2479 (cit. on p. 88).

[249] Alexander D. Jodlowski et al. "Large guanidinium cation mixed with methylammonium in lead iodide perovskites for 19% efficient solar cells." In: *Nature Energy* 2.12 (Dec. 2017), pp. 972–979 (cit. on p. 88).

[250] Aurélien M. A. Leguy et al. “Reversible Hydration of CH 3 NH 3 PbI 3 in Films, Single Crystals, and Solar Cells.” In: *Chemistry of Materials* 27.9 (May 2015), pp. 3397–3407 (cit. on p. 89).

[251] H. Ishida, R. Ikeda, and D. Nakamura. “Pre-melting state of methylammonium iodide as revealed by proton magnetic resonance.” In: *physica status solidi (a)* 70.2 (Apr. 1982), K151–K154 (cit. on p. 89).

[252] Zhaoning Song et al. “Impact of Processing Temperature and Composition on the Formation of Methylammonium Lead Iodide Perovskites.” In: *Chemistry of Materials* 27.13 (July 2015), pp. 4612–4619 (cit. on p. 89).

[253] Fan Fu et al. “High-efficiency inverted semi-transparent planar perovskite solar cells in substrate configuration.” In: *Nature Energy* 2.1 (Jan. 2017), p. 16190 (cit. on p. 89).

[254] Konrad Domanski et al. “Systematic investigation of the impact of operation conditions on the degradation behaviour of perovskite solar cells.” In: *Nature Energy* 3.1 (Jan. 2018), pp. 61–67 (cit. on p. 89).

[255] Zonglong Zhu et al. “Enhanced Efficiency and Stability of Inverted Perovskite Solar Cells Using Highly Crystalline SnO2 Nanocrystals as the Robust Electron-Transporting Layer.” In: *Advanced Materials* 28.30 (Aug. 2016), pp. 6478–6484 (cit. on p. 89).

[256] Hsinhan Tsai et al. “Light-induced lattice expansion leads to high-efficiency perovskite solar cells.” In: *Science (New York, N.Y.)* 360.6384 (Apr. 2018), pp. 67–70 (cit. on p. 90).

[257] Camille Stavrakas et al. “Probing buried recombination pathways in perovskite structures using 3D photoluminescence tomography.” In: *Energy & Environmental Science* 11.10 (Oct. 2018), pp. 2846–2852 (cit. on p. 90).

[258] Roberto Brenes et al. “Metal Halide Perovskite Polycrystalline Films Exhibiting Properties of Single Crystals.” In: *Joule* 1.1 (Sept. 2017), pp. 155–167 (cit. on p. 90).

[259] Jérémie Werner et al. “Perovskite/Perovskite/Silicon Monolithic Triple-Junction Solar Cells with a Fully Textured Design.” In: *ACS Energy Letters* 3.9 (Sept. 2018), pp. 2052–2058 (cit. on p. 91).

[260] Amran Al-Ashouri et al. “Conformal monolayer contacts with lossless interfaces for perovskite single junction and monolithic tandem solar cells.” In: *Energy & Environmental Science* (2019) (cit. on p. 91).

[261] Marko Jošt et al. “21.6%-Efficient Monolithic Perovskite/Cu(In,Ga)Se ₂ Tandem Solar Cells with Thin Conformal Hole Transport Layers for Integration on Rough Bottom Cell Surfaces.” In: *ACS Energy Letters* 4.2 (Feb. 2019), pp. 583–590 (cit. on p. 91).

7

PHOTOPHYSICS OF HIGH-PERFORMANCE PEROVSKITE SOLAR CELLS

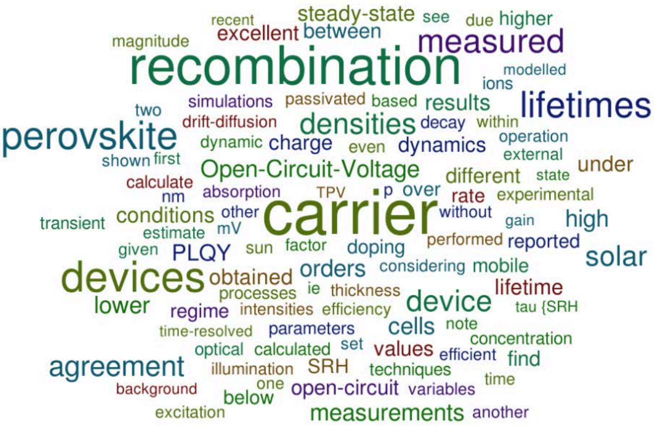

This work was motivated by the wide spread of charge carrier lifetimes and ambiguity of the dominant recombination processes in perovskite solar cells. Here it is shown, that the recombination dynamics are dominated by a first-order process, but otherwise consistent with the dynamics in perovskite-only samples. The results are corroborated with drift-diffusion simulations, reproducing the employed devices accurately.

This chapter is based on:

Photophysics of High-Performance Perovskite Solar Cells

Christian M. Wolff, Sean Bourelle, Le Phuong, Jona Kupiers, Sascha Feldmann, Pietro Caprioglio, Jose Antonio Marquez-Prieto, Jonas Diekmann, Thomas Unold, Martin Stolterfoht, Safa Shoaee, Felix Deschler, and Dieter Neher

in prepraration

7.1 ABSTRACT

Using time-resolved spectroscopic and opto-electronic techniques we probe the fate of carriers in state-of-the-art perovskite solar cells to establish a consistent picture of their decay pathways and rates under operating conditions. Ideally, all photoexcited charges deliver power externally, however, they may be lost due to recombination in the bulk of the absorber, at interfaces, or within other functional layers. We find that charge recombination in perovskite devices is fully described by a model based on mono- and bi-molecular recombination. We experimentally determine the values for the recombination constants and find that recombination at 1 sun illumination is dominated by a first-order process, which we attribute to interfacial losses. Improving carrier lifetimes to >3µs will take perovskite devices into the radiative regime, where performance will benefit from photon-recycling. We demonstrate that, using the extracted recombination constants, device operation can be fully described by drift-diffusion simulations for carriers and mobile ions. We argue that in our studied solar cells mobile ion concentrations must not exceed $3 \cdot 10^{15}\mathrm{cm}^{-3}$ to enable the measured fill-factors and low hysteresis.

7.2 INTRODUCTION & BROADER CONTEXT

Lead halide perovskites and optoelectronic devices made thereof have attracted enormous attention due to a rapid rise in efficiency, the versatility of applications, and ease of processing. Concerted efforts in the development of perovskite solar cells has led to very high photovoltaic and electroluminescence (power) conversion efficiencies of >20%[44, 262], surpassing other single junction thin-film solar cell technologies within just a decade. As for every semiconductor, the performance of perovskite-based optoelectronic devices is limited by nonradiative decay processes which compete with the radiative free carrier recombination Therefore, detailed insights into the device operation and efficiency limits require understanding of the dynamic carrier recombination processes. The dynamic properties of photogenerated charges in neat perovskite layers have been extensively studied by time-resolved optical techniques including transient absorption spectroscopy (TAS)[31, 62, 263], optical-pump-terahertz-probe (OPTP)[264], time-resolved-microwave-conductivity (TRMC)[265], time-resolved-photoluminescence (TRPL)[152], time-resolved-2D-Fourier-transformed-infrared spectroscopy (TR-2D-FTIR)[266] and many other techniques. The results from these techniques have been explained by a superposition of first-, second and third-order recombination processes. On the other hand, results from opto-electronic characterization techniques for full devices such as transient photovoltage (TPV), charge extraction(CE)[65, 66] or impedance spectroscopy (IS) have been interpreted in terms of mixed recombination orders. Also, effective carrier lifetimes deduced from these measurements differ by orders of magnitude (see Figure S1, SI). For example, in the traditional perovskite absorber methylammonium lead iodide, lifetimes ranging from µs-ms have been reported from TMRC/TPV/IMVS under comparable excitation conditions. While such differences are expected due to the larger number of layers and interfaces in the device, it has been noted that lifetimes from TPV and IS measurements are affected by capacitive contributions.[67] A second complication arises from the fact, that the external bias of an illuminated cell may not properly reflect the conditions within the perovskite absorber[267]. Precise knowledge of the recombination parameters and/or time constants is, however, required to rationalize performance in complete devices, such as the open-circuit voltage. Given this spread of reported recombination orders and carrier lifetimes in literature, a link between the dynamic processes on ultrafast timescales and the device operation in steady-state is missing. Knowledge of the detailed recombination parameters enables the description of perovskite solar cells through global drift diffusion simulations to precisely identify the limiting processes or components for further device improvements towards 30% efficiency.[268, 269] Here, we apply a combination of all-optical spectroscopy (transient absorption, steady state photoinduced absorption and steady state photoluminescence) with electro-optical charge extraction techniques (TDCF[167], time-delayed-collection-field and TPV/CE) on highly efficient perovskite devices under operating conditions to gain unprecedented insights into carrier recombination dynamics in fully operational devices. We corroborate the measurements with drift-diffusion simulations providing in-depth insight into the working principles of perovskite solar cells. Our comprehensive analysis quantifies recombination orders and velocities, carrier densities and distributions, and simulations fully reproduce the photovoltaic parameters under relevant operation conditions.

7.3 RESULTS

Transient Absorption and Carrier Extraction Measurements

We prepared efficient state-of-the-art p-i-n structured devices with a triple-cation-perovskite as the absorber layer (CsMAFA; $CsI_{0.05}[FA_{0.85}MA_{0.15}Pb(I_{0.85}Br_{0.15})_3]_{0.95}$) and organic p- and n-type charge transport layers (CTL; poly-triarylamine: PTAA and C_{60})[168]. We also employ interlayers at the perovskite|CTL interfaces for optimal performance[99, 171]. Figure 34A displays a cross-sectional SEM and corresponding schematic of a device. Devices are prepared with top electrode (Cu) thicknesses of either 100 nm for photovoltaic characterization or 20nm for optical and optoelectrical measurements in transmission. In Figure 34B,C we provide jV-scans and EQE spectra of the two device types, reaching efficiencies of ~21% with a V_{OC} of 1.165 V, a J_{SC} of 22.5 mA cm^{-2} and a FF ~80% (~15% for the semitransparent devices). The devices with thinner electrodes exhibit reduced J_{SC} due to lower reflectivity of the back electrode and lower FF because of the higher series resistance of the thin Cu. Moreover, the average V_{OC} is ~25 mV lower in the semitransparent device which we attribute to a less restricted emission angle. The is in close agreement with the expected entropic loss of $k_B T/q \cdot \ln(2) \approx 18$ mV, similar to bifacial silicon solar cells, which exhibit at least ~20mV lower V_{OC} compared to devices with well-reflecting back mirrors .

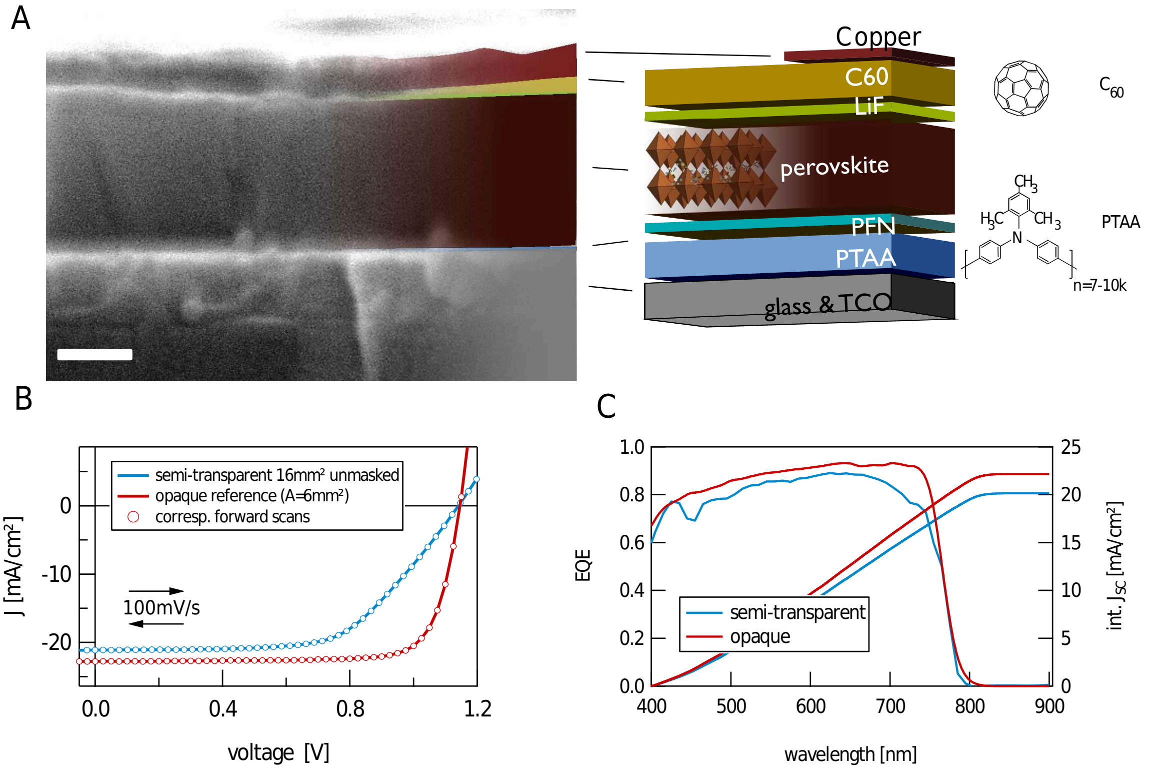

Figure 34: A) SEM cross-section and stack schematics of the p-i-n-type device architecture with the position of the individual layers, as well as the chemical structure of C_{60} and PTAA (scale is 200 nm). B) typical jV-curves of the devices used in this study. Shown are an unmasked semi-transparent device (blue) and an opaque reference device (red) in forward (open circles) and backward (lines) scan direction at a scan rate of ~100 mV/s. C) IPCE spectrum and integrated current (AM1.5G) of working devices, delivering ~22 mA/cm^2 (opaque) and ~20 mA/cm^2 (semi-transparent).

Transient Absorption and Carrier Extraction: We performed TAS and Time-Delayed-Collection-Field (TDCF) experiments on operating devices to follow the decay of charge carrier density in the devices after pulsed photoexcitation. The experiments are carried out with a background illumination ranging from 0.01 to 1 suns (see Figure S3, SI) at open-circuit to probe carrier dynamics under operational conditions, taking into account size-effects (Supplementary Note 1, SI). The experiments were performed with excitation densities ranging over five orders over magnitude to probe the recombination dynamics at high and low excitation densities[270]. The initial TAS signal at t=0 can be translated to a photogenerated charge-carrier concentration (Supplementary Note 2, Figure S1, SI), whereas in the TDCF experiments, the amount of extracted charge is directly measured and translated into carrier density by considering the volume of the perovskite. Figure 35A shows transients for both techniques under 1 sun equivalent background illumination. Despite the complexity of the multilayer device structure, the carrier decay depends only on the charge carrier density at the given time, regardless of the initial carrier concentration and delay time after photoexcitation. This is shown in Figure 35A, where transients measured under different initial carrier concentration are overlaid by shifting the transients in the time-domain. This first result is important in two aspects: 1) it shows that the devices do not change their behavior – through *e.g.* degradation – even if exposed to high irradiance over the time of measurement and 2) that there exists a single set of intrinsic recombination parameters that describes the decay of the charge carrier population in the device. Both techniques reveal consistently a mono-exponential decay at low densities and an accelerated decay from higher carrier concentrations $>10^{16}$ cm^{-3}. We extract the recombination order from the time derivative of the measured carrier density kinetics – *i. e.* dn/dt – as shown in Figure 35B. We find that the entire set of data can be well fitted by a superposition of first-, second and third-order recombination processes (solid blue line):

$$dn/dt = G - k_1 \cdot n - k_{2,ext} \cdot n \cdot (n + p_0) - k_3 \cdot n^3$$

Here, G is the generation rate (which is zero during the decay) k_1, $k_{2,ext}$ and k_3 are the coefficients for first-, second and third-order recombination processes, n is the carrier density andp_0 is a background doping concentration [271, 272]. Note that $k_{2,ext}$ is the external bimolecular recombination coefficient, which differs from the internal (local) recombination coefficient $k_{2,int}$ through the probability of photon outcoupling p_{em}: $k_{2,ext} = p_{em} \cdot k_{2,int}$.[52, 273–275]. The values from the fit are listed in Table 2. The colored regions indicate the carrier density regimes in which mono-, bi- and tri-molecular processes dominate. The value for k_3 corresponds to an upper limit, as we didn't reach a clear n^3 - dominated (Auger-) regime due to the >nanosecond time resolution of the setup. In contrast, the region of dominant second order recombination is clearly revealed, yielding an external bimolecular recombination coefficient $k_{2,ext} = 3 \cdot 10^{-11} cm^3 s^{-1}$. Using $p_{em} = 1/(2n_r^2) = 8\%$ (with n_r=2.5 the refractive index of the perovskite) yields $k_{2,int}$= $3.7 \cdot 10^{-10} cm^3 s^{-1}$, which is in excellent agreement with the value of $3.5 \cdot 10^{-10} cm^3 s^{-1}$ as calculated from the optical absorption of the perovskite absorber via the van Roosbroeck-Shockley equation[38] (see Figure 35C).

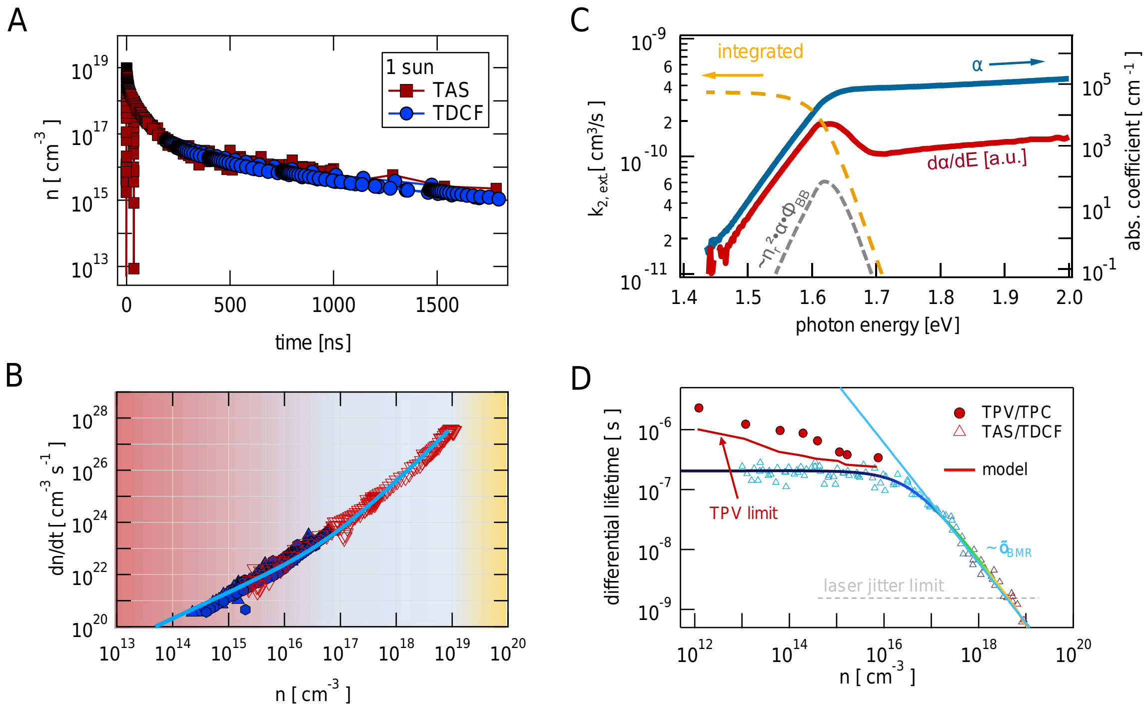

Figure 35: A) Transient charge carrier dynamics with 1 sun equivalent background illumination. TAS(red) and TDCF (blue) are performed on full devices at V_{OC}. B) temporal derivative of (A), showing three ranges with first-, second- and third-order dominated regimes. Additionally, we show the modeled recombination rate as a function of carrier density (light blue). The background color shading indicates the three regimes (SRH-red, BMR-blue, Auger-orange). C) Absorption coefficient (blue), $d\alpha/dE$ (red), spectral emission and integrated $k_{2,int}$ according to van Roosbroeck-Shockley equation. D) Differential lifetimes (TAS/TDCF, triangles) and measured lifetimes (TPV, red circles) as a function of carrier density. The red line shows the limit for TPV measurements according to Kiermasch *et. al.* [67], the solid lines show the total fit (dark blue) and the second-order/BMR contribution (light blue). The dashed gray line denotes the resolution limit.

It's common practice to express the recombination dynamics in terms of an effective carrier lifetime (Figure 35D). In the high carrier density regime ($n > 10^{16}$ cm^{-3}), the lifetimes deduces from our combined TDCF/TAS measurements decrease linear with increasing density. This regime is dominated by bimolecular (BMR) second order recombination, where $\tau = (k_{2,ext} \cdot n)^{-1}$. At densities below 10^{16}cm^{-3}, the lifetime values become independent of carrier concentration, meaning that the fate of photogenerated carriers in this regime is entirely determined by a first order recombination process ($\tau = k_1^{-1}$). As noted earlier, TPV/CE measurements are popular techniques to determine carrier recombination lifetimes in devices under operational conditions. Results from such measurements on our devices are plotted by full circles in Figure 35D. Interestingly, In contrast to our TAS/TDCF data, the lifetimes from TPV/CE increase with decreasing carrier density according to a mixed recombination order of ca. 1.7. It's only withing a small range of carrier densities (10^{15} - 10^{16} cm^{-3}) that lifetimes are similar for all techniques. Higher lifetimes and mixed recombination orders seem to be common for many electrical measurements on full devices (Figure S2, SI). Related to this, reported carrier lifetimes in devices are generally larger than in neat perovskite layers, particularly when considering low carrier densities. This can in part be attributed to an experimental limitation (solid red line) of the employed methods, *i.e.* the resistance-capacitance (RC) time of the devices, as shown by Kiermasch *et. al.* [67] Considering that we minimized the RC-time in our experiments by choosing an active area of only 0.55 mm^2, this appears to be a significant limitation for the applicability of these methods or at least has to be rigorously taken into account. In contrast to TPV/CE, our data reveal a constant lifetime $\tau = k_1^{-1}$= 250 ns ±50 ns, which we assign to Shockley-Read-Hall recombination.

Comparing Transient and Steady-State Results

Having quantified the kinetic parameters for the main recombination processes in our solar cells, we aim to establish a direct link between the dynamic processes and the steady-state device operation. Using the results from TAS and TDCF, we can calculate the charge carrier densities under steady-state conditions by numerically solving said Equation with a constant generation rate G. With $G = J_{SC}/(q \cdot d) = 2.8 \cdot 10^{21} cm^{-3}s^{-1}$ under simulated solar illumination, we find a steady-state carrier concentration of $n_{1sun} = (0.73 \pm 0.3) \cdot 10^{15} cm^{-3}$. Combined with an intrinsic carrier density $n_i = 0.8 \cdot 10^5 cm^{-3}$ (calculated fro the radiative dark recombination current $J_{0,rad} = 3 \cdot 10^{-21}$ mAcm^{-2} and $k_{2,ext} = 3 \cdot 10^{-11} cm^3 s^{-1}$) yields a quasi-Fermi level splitting (QFLS) in the perovskite bulk of ~1.21eV. This agrees very well with the measured V_{OC}. We have shown earlier that cells comprising PTAA and C_{60} CTLs exhibit a slow enough recombination at the internal interfaces to not cause a significant bending of the quasi-Fermi levels of the majority carriers near the charge extracting contact, justifying the approximation qV_{OC}=QFLS. Notably, our estimate of the carrier density under AM1.5 G illumination is almost one order of magnitude lower than in many previous reports[65, 66, 276, 277], which is not inconsistent with the $k_{2,ext}$ estimated from our experimental TAS/TDCF data. In the fact, even if the recombination was only bimolecular, *i. e.* $G = R = k_{2,ext} \cdot n^2$, the carrier density would not exceed $9 \cdot 10^{15} cm^{-3}$ and any improvement in light outcoupling (enhancing $k_{2,ext}$) will actually reduce the internal carrier density in the radiative limit[278]. Johnston and Herz predicted a maximum $n_{1sun} = 6 \cdot 10^{15} cm^{-3}$ for a 300 nm sample when SRH recombination is slow (τ_1>10 µs). Figure S4(SI) shows n_{1sun} calculated from our experimentally obtained $k_{2,ext}$, k_3 for varying non-radiative lifetimes between 1ns and 1ms. Indeed, the carrier concentration saturates for τ_1>10 µs at a value of $\approx 9 \cdot 10^{15} cm^{-3}$, for an absorber thickness of 300-500 nm (Figure S4, SI). That number poses an upper limit, since any additional recombination (*e. g.* due to Auger, interfacial or trap recombination) or extraction would reduce the carrier density even further. This is exactly the case in our devices where recombination at internal interfaces but also SRH recombination in the bulk reduces the steady state concentration.

Transient and steady state PL properties

In an alternative way, we compare the above mentioned potential V_{OC} values to the QFLS in the same samples. This reveals good agreement with 1.15eV, 1.21eV and 1.28eV on the basis of $QFLS = k_B T/q \cdot ln[PLQY \cdot J_{SC}/J_{0,rad.}]$, where J_{SC} and $J_{0,rad.}$ are calculated from the device EQE_{PV}, and the measured PLQY values where 0.35%, 1.9% and 24.8% for the device, the uncontacted and the passivated perovskite films, respectively. We calculate the PLQY on the basis of

$$PLQY = \frac{k_2 \cdot n \cdot (n + p_0)}{k_1 \cdot n + k_2 \cdot n \cdot (n + p_0) + k_3 \cdot n^3}$$

and find good agreement between measured and simulated external PLQYs (Figure S5, SI). Furthermore we can estimate that the internal PLQY of the device is on the order of 5% with $PLQY_{int} = PLQY_{ext}/p_{em} = 3.8\%$. With such high internal PLQYs, the question arises, whether the open-circuit voltage and in turn the V_{MPP}/FF is impacted by photon-recycling. We calculate, that the improvement in open-circuit voltage is very minor < 10mV, below batch-to-batch variations (Figure S6B, SI). Increasing the minority carrier lifetime ony by a threefold to ~1µs, should allow an additional gain of 20 mV, and for lifetimes exceeding 3µs this gain could then be also preserved, when reducing the carrier density, as is the case at the operating point (*i. e.* MPP), so that an actual efficiency gain is possible. Based on these considerations, we believe that recent record cells with >1% external PLQY are already benefiting from PR. Encouraged by the good agreement between measured and simulated PLQY under standard conditions, we sought to extend the analysis over multiple illumination intensities to verify, whether a singular set of recombination variables can explain the PLQY values in a device over a broader range of carrier densities. In Figure 36, our experimental values for the device PLQY are shown versus intensity along with a calculated PLQY.

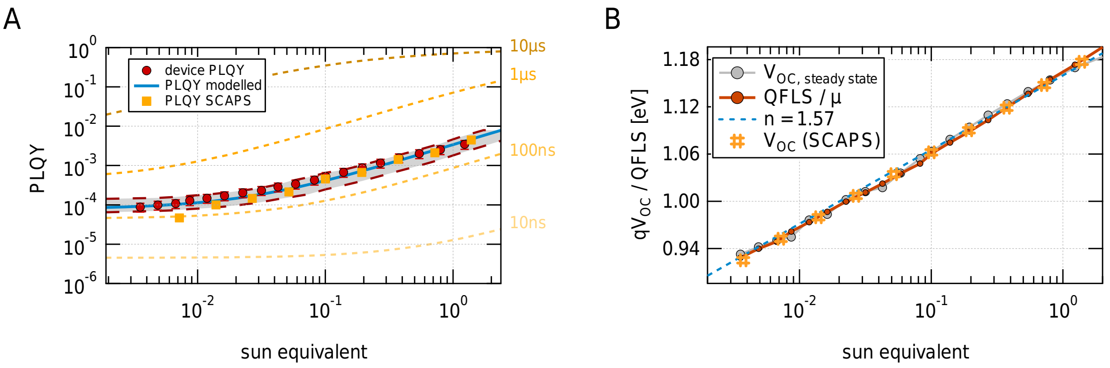

Figure 36: A) PLQY measurements (red circles) on full devices. The kinetic model (light blue) with an error band (grey) explains the measured values reasonably well. In orange shadings we show PLQY values expected for the given SRH lifetimes when keeping k_2 and p_0 constant and the orange symbols show the PLQY extracted from SCAPS at V_{OC}. B) Open circuit voltage as a function of light intensity, measured in the device (grey), extracted from PLQY (*i. e.* QFLS, red), calculated from SCAPS (orange) and additionally a line indicating an ideality factor of 1.57 (blue).

Within a small confidence interval – indicated by the grey area – the experimental and modeled values are in excellent agreement. At this point it is worth mentioning that we had to introduce a doping density of $10^{13}\mathrm{cm}^{-3}$ to explain the plateau at intensities below 0.1 suns adequately. This value is in good agreement with recent findings on mixed perovskites[271]. The actual doping density could be higher without impacting the overall recombination dynamics below a threshold of $p_0 < k_1/k_2 \approx 10^{17}\mathrm{cm}^{-3}$. This poses an upper limit, because of the comparably low TRPL lifetime in the full devices. To test, whether such high doping densities are reasonable, we return to the samples we used for the PIA measurements and the obtained lifetimes. We measured lifetimes >3µs for the passivated films, limiting the doping density to $< 4\mathrm{x}10^{15}\mathrm{cm}^{-3}$. Considering that even longer lifetimes have already been reported, even lower numbers are probable. These numbers are in perfect accord with results by Yavari and Ebadi *et. al.* [279] The authors artificially doped the perovskite (likewise triple cation perovskite) with >10ppm heterovalent Bi^{3+} atoms. With an unit cell volume of ~1nm³ this corresponds to a doping density of $10^{16}\mathrm{cm}^{-3}$, which in turn already reduces the TRPL lifetime by roughly a twofold.

Device Simulations

Finally, we sought to describe the device by emplyoing drift-diffusion simulations (SCAPS)[267]. To account for surface recombination, we translated the measured lifetimes into surface recombination velocities S, with τ_{bulk} being the bulk lifetime (800ns), d the thickness (480nm) and D the electron/hole diffusion coefficient (2.5cm²/s).

$$k_1 = 1/\tau = 1/\tau_{bulk} + ((4d^2)/(\pi^2 D) + d/S)^{-1}$$

We also estimated the impact of mobile ions and observe agreement between JV scans at different scan speeds and simulations (IonMoger)[280] for mobile ion densities $< 10^{16}\mathrm{cm}^{-3}$ in excellent agreement with the results from Futscher *et. al.* [281, 282] who identified up to three ion species with a cumulated density of $<10^{16}\mathrm{cm}^{-3}$ in devices with lower efficiency, entailing higher defect and mobile ion density. We obtain JV-curves as shown in Figure 37A, compared to a representative devices with high efficiency (>20%). The agreement is excellent, even when including mobile ions in the simulations (IonMoger).

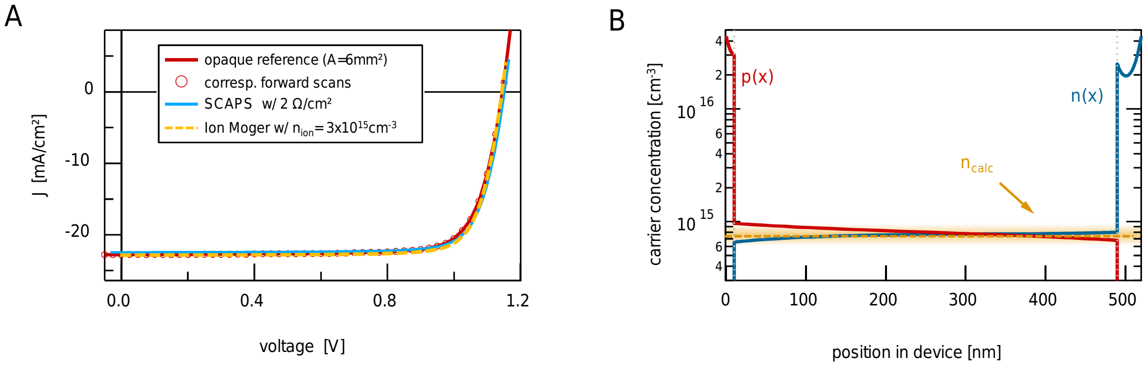

Figure 37: A) Measured (red) and simulated JV-scans with (yellow) and without (blue) mobile ions at a scan rate of 120mV/s. B) Carrier profiles (electrons – blue, holes – red) from the SCAPS simulation in panel A at 1 sun and open-circuit. Additionally we present the calculated singular carrier density of 0.7·10^{15}cm^{-3} (orange) with an error margin (orange shading).

. We finally compare the aforementioned singular carrier density calculated based on the dynamic variables with the carrier profile in the simulations in Figure 37B. At open circuit and one sun illumination, we expected slightly imbalanced carrier profiles (see V_{OC} vs. I – ideality factor), and a steady-state carrier density of ~0.7·10^{15}cm^{-3}. The simulated (SCAPS) and calculated densities are in excellent agreement. The presented results have three consequences: 1) The presented perovskite solar cells can be well described with integer recombination orders within the framework of SRH-, bimolecular- and Auger- recombination, without the need for mixed orders and using a singular carrier density. 2) State of the art devices with open-circuit voltages below 1.2V (at a bandgap of ~1.6eV) operate in the non-radiative regime, but slight improvements in non-radiative lifetime to >1µs and outcoupling efficiency – through *e.g.* roughened surfaces – will be sufficient to enter the radiative regime and benefit from photon-recycling. The latter is probably the case for recent record devices, considering *e.g.* the FF (85%) of to dates' world record cell[198]. 3) The concentration of mobile ions in efficient perovskite solar cells is likely not to exceed 3·10^{15}cm^{-3} , especially for devices with low hysteresis, when scanning at typical rates of 10-100mV/s (Figure S7, SI) in contrast to recently reported 10^{17}cm^{-3} [283, 284].

7.4 CONCLUSION

In summary, we measured charge carrier recombination dynamics in efficient p-i-n-type perovskite solar cells and find that recombination can be described in the framework of first-, second- and third-order recombination, without the necessity to introduce mixed recombination orders. We find the kinetic variables: $k_1 \approx 3 \cdot 10^6 s^{-1}$, $k_{2,ext} \approx 3 \cdot 10^{-11} cm^3 s^{-1}$, $k_3 \approx 10^{-30} cm^6 s^{-1}$ and a background doping density of $p_0 \approx 10^{13} cm^{-3}$. Numerically solving the rate equation $dn/dt = G - k_1 \cdot n - k_{2,ext} \cdot n \cdot (n + p_0) - k_3 \cdot n^3$ allows us to calculate a singular steady-state carrier density of $< 1 \cdot 10^{15} cm^{-3}$ under 1 sun conditions with relatively homogeneous carrier profiles throughout the active layer at open-circuit. The lower carrier density compared to uncontacted and passivated perovskite layers is a consequence of additional recombination. With the obtained rate constants and carrier densities we are able to accurately reproduce external luminescent efficiencies and the open-circuit voltage/ideality factor of the devices over several orders of magnitude. When employing drift-diffusion simulations, the measured and experimentally determined JV-characteristics are in excellent agreement. This is valid, even when including mobile ions; where we find that only a

	measurements	dynamic model	SCAPS
τ_{SRH}[ns]	250 ± 60	250 ± 60	800 ns (bulk) + S1/2 = 150 & 50cm/s
k_2[cm^3/s]	$2.9 \pm 0.4\text{x}10^{-11}$	$2.9 \pm 0.4\text{x}10^{-11}$	$3\text{x}10^{-11}$
k_3[cm^6/s]	$< 10^{-30}$	$< 10^{-30}$	10^{-30}
p_0[cm^{-3}]	$1.1 \pm 0.5\text{x}10^{13}$	$1.1 \pm 0.5\text{x}10^{13}$	10^{13}
$n_{steady,1sun}$[cm^{-3}]	–	$7.2 \pm 0.3\text{x}10^{14}$	slightly imbal. $5 - 7.5\text{x}10^{14}$
n_i^2[cm^{-6}]	–	$1.6 \pm 0.2\text{x}10^{10}$	–
$N_C N_V$[cm^{-6}]	–	$1.0 \pm 0.3\text{x}10^{37}$	$1\text{x}10^{37} = (3.2\text{x}10^{18})^2$
V_{OC}[V]	1.155 ± 0.018	1.159 ± 0.025	1.166
$J_{0,rad.}$[A/m^2]	$3.0 \pm 0.2\text{x}10^{-20}$	$3.0 \pm 0.2\text{x}10^{-20}$	–
PLQY[%]	0.33 ± 0.05	0.43 ± 0.06	0.38
E_G[eV]	1.60 ± 0.01	–	1.6
d[nm]	480 ± 15	–	–
m^*/m_e	–	0.25 ± 0.03	–

Table 2: Measured and Simulated Variables.

density lower than 10^{16}cm^{-3} can explain the measured small hysteresis and high fill-factors. By estimating photon emission probability, we calculate an intrinsic $k_{2,int} \approx 3.7 \cdot 10^{-10}\text{cm}^3\text{s}^{-1}$. Our work sheds light on the internal recombination in efficient perovskite solar cells and suggests that the state-of-the-art devices operate in the non-radiative regime, at the verge to the radiative regime, where photon-recycling will benefit the performance. Optical management, that will enhance the emission at the bandedge of the perovskite, will enhance luminescent outcoupling and in turn enable higher photovoltages.

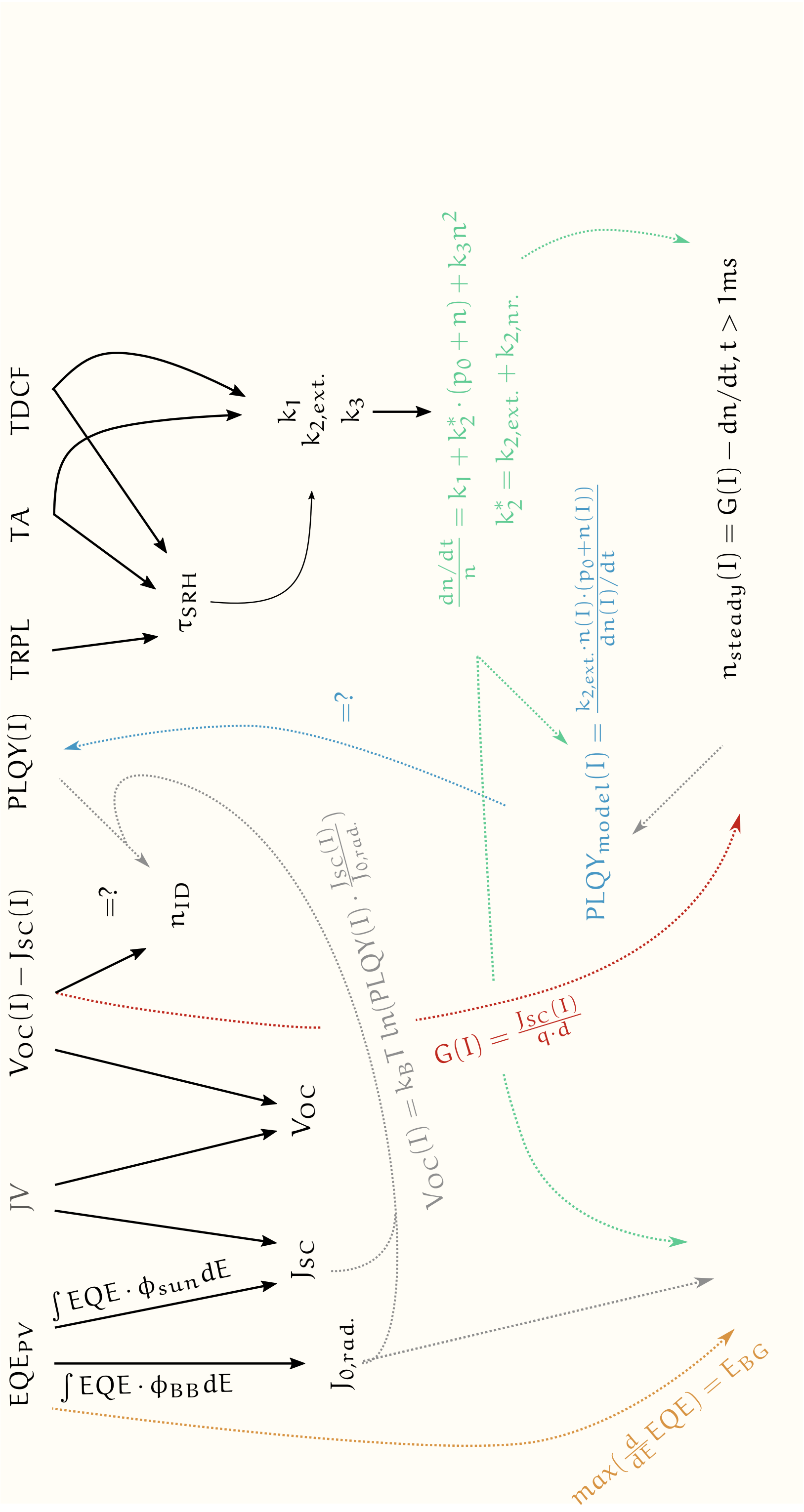

Figure 38: Flow Chart explaining the different experimental and simulated values.

[262] Yu Cao et al. “Perovskite light-emitting diodes based on spontaneously formed submicrometre-scale structures.” In: *Nature* 562.7726 (Oct. 2018), pp. 249–253 (cit. on pp. 97, 132).

[263] Guichuan Xing et al. “Long-Range Balanced Electron- and Hole-Transport Lengths in Organic-Inorganic CH3NH3PbI3.” In: 6960.2012 (2013), pp. 498–500 (cit. on p. 97).

[264] Christian Wehrenfennig et al. “High charge carrier mobilities and lifetimes in organolead trihalide perovskites.” In: *Advanced Materials* 26.10 (2014), pp. 1584–1589 (cit. on p. 97).

[265] Eline Mathilde Hutter et al. “Charge Carriers in Planar and Meso-Structured Organic-Inorganic Perovskites: Mobilities, Lifetimes and Concentrations of Trap States.” In: *The Journal of Physical Chemistry Letters* (2015), p. 150720142148008 (cit. on p. 97).

[266] Artem a. Bakulin et al. “Real-Time Observation of Organic Cation Reorientation in Methylammonium Lead Iodide Perovskites.” In: *The Journal of Physical Chemistry Letters* (2015), pp. 3663–3669 (cit. on p. 97).

[267] Pietro Caprioglio et al. “On the Relation between the Open-Circuit Voltage and Quasi-Fermi Level Splitting in Efficient Perovskite Solar Cells.” In: *Advanced Energy Materials* 9.33 (Sept. 2019), p. 1901631 (cit. on pp. 97, 103, 113, 117, 119, 129, 131).

[268] Jonas Diekmann et al. “Pathways towards 30 percent efficient perovskite solar cells.” In: (Oct. 2019) (cit. on pp. 97, 138).

[269] Martin Stolterfoht et al. “How To Quantify the Efficiency Potential of Neat Perovskite Films: Perovskite Semiconductors with an Implied Efficiency Exceeding 28%.” In: *Advanced Materials* (Mar. 2020), p. 2000080 (cit. on p. 97).

[270] Zhiping Wang et al. “High irradiance performance of metal halide perovskites for concentrator photovoltaics.” In: *Nature Energy* 3.10 (Oct. 2018), pp. 855–861 (cit. on p. 99).

[271] Sascha Feldmann et al. “Photodoping through local charge carrier accumulation in alloyed hybrid perovskites for highly efficient luminescence.” In: *Nature Photonics* 14.2 (Feb. 2020), pp. 123–128 (cit. on pp. 100, 103).

[272] Rebecca L. Milot et al. “Radiative Monomolecular Recombination Boosts Amplified Spontaneous Emission in HC(NH 2) 2 SnI 3 Perovskite Films.” In: *The Journal of Physical Chemistry Letters* 7.20 (Oct. 2016), pp. 4178–4184 (cit. on p. 100).

[273] L. M. Pazos-Outon et al. “Photon recycling in lead iodide perovskite solar cells.” In: *Science* 351.6280 (Mar. 2016), pp. 1430–1433 (cit. on pp. 100, 132).

[274] Wolf-Alexander Quitsch et al. “The Role of Excitation Energy in Photobrightening and Photodegradation of Halide Perovskite Thin Films.” In: *The Journal of Physical Chemistry Letters* 9.8 (Apr. 2018), pp. 2062–2069 (cit. on pp. 100, 116).

[275] Timothy W. Crothers et al. “Photon Reabsorption Masks Intrinsic Bimolecular Charge-Carrier Recombination in CH3NH3PbI3 Perovskite.” In: *Nano Letters* 17.9 (Sept. 2017), pp. 5782–5789 (cit. on p. 100).

[276] David Kiermasch et al. “Unravelling steady-state bulk recombination dynamics in thick efficient vacuum-deposited perovskite solar cells by transient methods.” In: *Journal of Materials Chemistry A* 7.24 (June 2019), pp. 14712–14722 (cit. on pp. 102, 114, 115).

[277] Shuyan Shao et al. “N-type polymers as electron extraction layer in hybrid perovskite solar cells with improved ambient stability.” In: *J. Mater. Chem. A* 4 (2016), pp. 2419–2426 (cit. on pp. 102, 131).

[278] Owen D. Miller, Eli Yablonovitch, and Sarah R. Kurtz. "Strong Internal and External Luminescence as Solar Cells Approach the Shockley–Queisser Limit." In: *IEEE Journal of Photovoltaics* 2.3 (July 2012), pp. 303–311 (cit. on pp. 102, 132).

[279] Mozhgan Yavari et al. "How far does the defect tolerance of lead-halide perovskites range? The example of Bi impurities introducing efficient recombination centers." In: *Journal of Materials Chemistry A* 7.41 (Oct. 2019), pp. 23838–23853 (cit. on p. 103).

[280] Nicola E. Courtier et al. "How transport layer properties affect perovskite solar cell performance: Insights from a coupled charge transport/ion migration model." In: *Energy and Environmental Science* 12.1 (2019), pp. 396–409 (cit. on p. 103).

[281] Moritz H. Futscher et al. "Quantification of ion migration in CH 3 NH 3 PbI 3 perovskite solar cells by transient capacitance measurements." In: *Materials Horizons* 6.7 (2019), pp. 1497–1503 (cit. on pp. 103, 114).

[282] Moritz H. Futscher et al. "Quantifying mobile ions and electronic defects in perovskite-based devices with temperature-dependent capacitance measurements: Frequency vs time domain." In: *Journal of Chemical Physics* 152.4 (2020) (cit. on p. 103).

[283] Luca Bertoluzzi et al. "Mobile Ion Concentration Measurement and Open-Access Band Diagram Simulation Platform for Halide Perovskite Solar Cells." In: *Joule* (2019), pp. 1–19 (cit. on p. 104).

[284] Philip Calado et al. "Evidence for ion migration in hybrid perovskite solar cells with minimal hysteresis." In: *Nature Communications* 7 (2016), pp. 1–10 (cit. on p. 104).

8

NONRADIATIVE RECOMBINATION IN PEROVSKITE SOLAR CELLS: THE ROLE OF INTERFACES

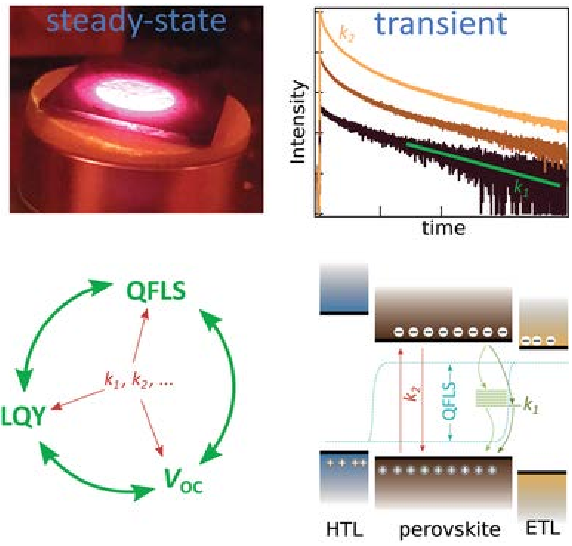

This progress report was an invited contribution on the basis of the results obtained in previous work. In particular, linking recombination in neat absorbers with and without transport layers and how these impact the device performance, is an integral part of this work, highlighting the importance of reliable tools and outlining upcoming challenges and possible next steps in future device improvements.

This chapter is a preprint of:

Nonradiative Recombination in Perovskite Solar Cells: The Role of Interfaces

Christian M. Wolff, Pietro Caprioglio, Martin Stolterfoht, and Dieter Neher

published in : *Adv. Mater. 2019, 31, 1902762*

8.1 INTRODUCTION & BROADER CONTEXT

Sustainable and efficient energy production is one of the greatest challenges of humanity in the 21st century. Due to their outstanding opto-electronic and material properties, perovskite solar cells provide a highly efficient and sustainable alternative to fossil fuels and provide an enormous potential to trigger a revolution in power generation for the coming generation. After just a few years of research, lead halide perovskite solar cells have reached certified efficiencies of 25.2%, thereby already exceeding other well established thin film solar cell technologies, such as CIGS or CdTe in small devices (<1cm^2).[18, 198] Considering their nearly ideal opto-electronic properties for a solar cell semiconductor; *i. e.* a high absorption coefficient, long carrier diffusion lengths, and highly luminescent nature, it is expected that perovskites will reach or even surpass the PCE of monolithic silicon solar cells (26.7%).[174, 285] Moreover, their comparatively wide bandgap and simple fabrication (from solution or evaporation) renders them ideal candidates for applications in silicon-based tandem devices, where the perovskite solar cell is attached as add-on to, *e. g.* industrially fabricated passivated emitter rear contact (PERC) or heterojunction with an intrinsic thin layer (HIT) silicon cells.[183, 214, 286] Today silicon/perovskite tandem solar cells have the largest potential for a rapid industrial realization in the near future and silicon/perovskite tandem solar cells with 28.0% PCE have already been demonstrated.[287] Importantly, tandem solar cells, are not bound to the thermodynamic limitations of single-junction cells and efficiencies beyond 35%[288] have been predicted for two- and four-terminal silicon/perovskite tandem cells. In order to unlock these potential PCEs for single-junction and tandem perovskite solar cells, it is essential to gain a more detailed understanding of the underlying recombination loss processes. Today, it is well established that non-radiative recombination losses are the primary reason that perovskite solar cells have not yet achieved their full thermodynamic potential.[69, 289] Non-radiative recombination losses limit not only the cells' open-circuit voltage (V_{OC}) but also the fill factor through an ideality factor larger than one.[69, 176] The source of non-radiative recombination loses in perovskite cells remains a heavily debated topic. Historically, the main focus was reducing trap-assisted recombination at defects in the perovskite bulk or at grain boundaries.[69, 173, 290] Indeed, considerable improvements were achieved through advanced perovskite fabrication schemes to increase the grain size, enhance crystallinity and the invention of multication and/or multihalide formulations. More recently, an increasing number of publications have been dedicated to addressing the issue of recombination at the perovskite surfaces[149, 178, 291] which differs from the bulk in terms of chemical composition and morphology.[173, 177, 178] For example, Beard and coworkers studied the charge carrier dynamics in single crystals and polycrystalline thin layers of methlyammonium lead iodide/bromide ($MAPbI_3$/$MAPbBr_3$) using transient reflectance spectroscopy TRS.[173, 292] In contrast to the often employed transient absorption spectroscopy (TAS), this technique is very sensitive to the photoinduced carrier concentration in the surface-near region of the semiconductor. Experiments were performed with different excitation energies, thereby varying the penetration depth of the incident light. These investigations showed that surface recombination is more important than recombination within the crystalline grains and at internal grain boundaries. A detailed analysis of the data revealed a surface recombination velocity of less than 10^3 cm/s, orders of magnitude smaller than the recombination velocity of non-passivated surfaces of traditional semiconductors which are of the order of 105 cm/s and above. Interestingly, the MAPI polycrystalline thin layer exhibited longer carrier lifetimes than the corresponding single crystal samples, which was attributed to unintentional trap passivation during thin film preparation. These findings put a strong emphasis on the understanding of the nature of surface traps and the suppression of surface recombination. This is particularly important when considering that advanced perovskites, which comprise multiple anions and/or anions of different chemical nature, are becoming increasingly used throughout the community. Molecular modifiers (*e. g.* tri-n-octylphosphine oxide, TOPO) are often applied to passivate the surface traps. As shown in Figure 39, Braly *et. al.* [51] recently demonstrated that even the most simple methlyammonium lead iodide (MAPI) perovskite absorber (with a bandgap of

1.6 eV) can show an external photoluminescence quantum yield (PLQY) of ~20%, which would in principle allow a high open-circuit voltage of ~1.28 V after passivating the top surface with TOPO. This value is very close to the absolute thermodynamic limit of 1.32V, demonstrating that bulk defects are, at least in this case of little importance. Moreover, high external PLQYs were also obtained in other perovskite absorbers (*e. g.* 66% by Abdi-Jalebi *et. al.* [85]). However, the open-circuit voltage of today's perovskite cells barely exceeds 1.2 V[83, 293, 294] which suggests that significant losses have their origin elsewhere in the multilayer assembly of the device. Recently, significant evidence emerged that main recombination losses in full operational devices originate at or across the interface between the perovskite and charge-transporting layers (CTLs).[51, 66, 99, 150, 241] This will be the major focus of this review.

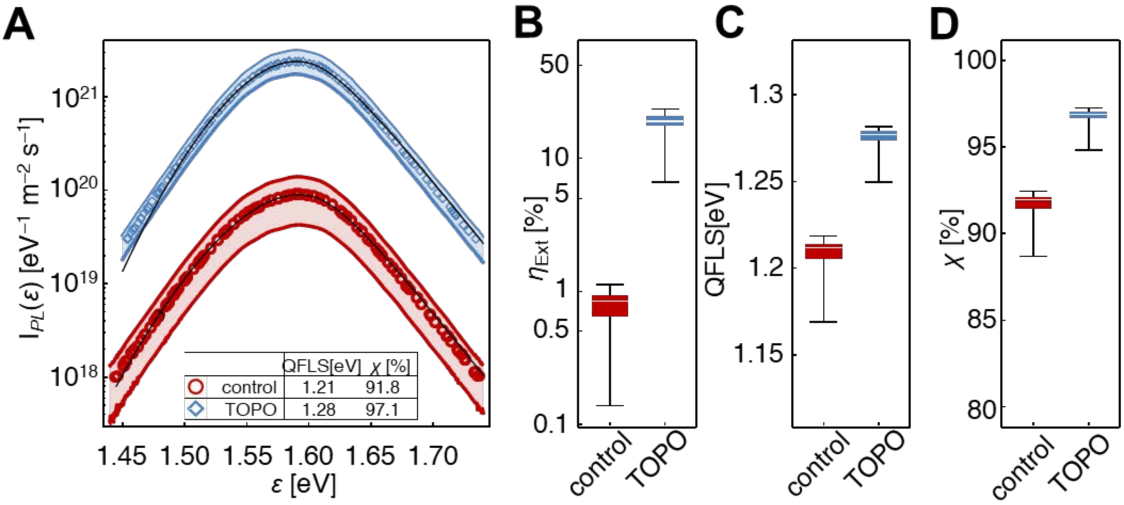

Figure 39: A) Absolute intensity photoluminescence spectra of neat $CH_3NH_3PbI_3$ (MAPI) films with and without TOPO on an Au back-reflector substrate. The black lines are fits to the experimental data (symbols) using the generalized Planck model. B) The external quantum efficiency, C) the quasi-Fermi-level splitting (QFLS), and D) the corresponding fraction of measured quasi-Fermi level splitting versus radiative limit (χ). A-D) Reproduced with permission.[51] Copyright 2018, Springer Nature.

This progress report consists of four parts: We first focus on the steady-state performance and of state-of-the-art perovskite solar cells in n-i-p and p-i-n configuration. We discuss several techniques - and their pitfalls - historically used to gain information about the recombination processes in full devices including ideality factor measurements and small-perturbation measurements such as impedance spectroscopy, TPV and CE. In the second part, we rationalize that absolute photoluminescence measurements on variable layer stacks allow disentangling different recombination pathways. We show that non-radiative recombination has its main origin at the interfaces between the perovskite and the charge-transporting layers, and how these losses depend on the details of the energetics at the hybrid interface. Thirdly, we review work dedicated to fundamentally understand the microscopic origin of interfacial recombination utilizing techniques with high time-resolution. We close by presenting successful pioneering approaches to overcome the limitations of interfacial recombination and give an outlook on concepts we believe will be the next steps in bringing perovskite solar cells even closer to their thermodynamic limit.

8.2 STUDIES OF STEADY STATE NONRADIATIVE RECOMBINATION IN COMPLETE PEROVSKITE SOLAR CELLS

Traditionally, information on the steady-state recombination is deduced from measurements on complete solar cells. One very popular approach to understand recombination processes in perovskite cells is to measure the ideality factor. Historically, ideality factors were quantified from dark current vs. voltage characteristics according to (analogous to Equation 46) :

$$J(V) = J_0 \cdot \left(e^{(qV)/(n\ k_B\ T)} - 1\right) . \tag{54}$$

with q is the elementary charge, V the externally applied voltage, kB the Boltzmann constant and T the temperature. On the other hand, it is common to write the recombination current density JR is terms of the carrier density n: $J_R \propto n^{\alpha}$. Here, α is the recombination order, which depends on the details of the recombination pathway. For example, $\alpha = 1$ is realized for ideal trap-assisted recombination through mid-gap impurities, $\alpha = 2$ for radiative band-to-band recombination of free charges and $\alpha = 3$ for nonradiative Auger[37]. Finally, in the most simple case of an intrinsic semiconductor with sharp band edges, the density of free electrons and holes, n and p, is comparable and proportional to $e^{(qV)/(2\ k_B\ T)}$. This yields the well-known relation between n and $\alpha : n = 2/\alpha$.[295] Interestingly, in perovskites solar cells, the ideality factor varies between ≈ 1 - 2,[123, 176, 289, 290] which is interpreted in terms of a competition between free carrier recombination and trap-assisted recombination (Shockley-Read Hall or SRH recombination). For example, measurements of the dark current of p-i-n perovskite devices by Wetzelaer *et. al.* [68] yielded a temperature-independent ideality factor of 1.75, though within a small voltage range (0.75-0.9V). On the other hand, plotting the electroluminescence intensity I_{EL} from radiative recombination vs. applied voltage yielded a light ideality factor of nearly one. In combination, these observations led to the conclusion that light emission stems from free carrier-band to-band recombination while the total recombination current is dominated by trap-assisted recombination. However, dark JV-measurements may be considerably influenced by the shunt resistance at low voltages and the series resistance at high voltages, rendering this method error-prone. A more elegant and already well-established approach in this regard is to cancel the influence of the series resistance by measuring the V_{OC} as a function of the light intensity I (or the generation current density J_G) according to:

$$J_{light}(V = V_{OC}) = J_0 \cdot \left(e^{(qV_{OC})/(n\ k_B\ T)} - 1\right) - J_G(I) . \tag{55}$$

Since there is no current flowing at V_{OC}, the series resistance becomes irrelevant and the obtained ideality factor is only dependent on the (internal) recombination pathways and the shunt which can be however readily identified and disregarded in the analysis. Using this approach, Tress *et. al.* obtained an ideality factor of ~1.6 in the relevant intensity regime in efficient n-i-p cells based on planar SnO_2 or mesoporous TiO_2 and concluded that this value is a result of distributed SRH recombination via bulk defects (Figure 40).).[69] Moreover, for an aged cell, an ideality factor close to 2 was interpreted to be a consequence of increased SRH recombination, due to a large increase in bulk defects. However, in samples without HTL, where the perovskite was in direct contact to the metallic Au electrode, the ideality factor was close to 1 which could be easily misinterpreted as dominant free carrier radiative recombination. Such a scenario would, however, give rise to a high photoluminescence quantum efficiency, which is a very rare case for complete perovskite device stacks (see above). Instead, a detailed analysis of the data revealed surface recombination as the major loss process. Strong surface recombination for both types of carriers would even allow for ideality factors <1, *i. e.* the V_{OC} saturates and cannot be increased with higher illumination intensity. This was shown *e. g.* by Tvingstedt *et. al.* [123] In line with this interpretation, measurements in p-i-n type solar cells with unmodified (semimetallic) PEDOT:PSS as HTL exhibited an ideality factor close to 1.[296]

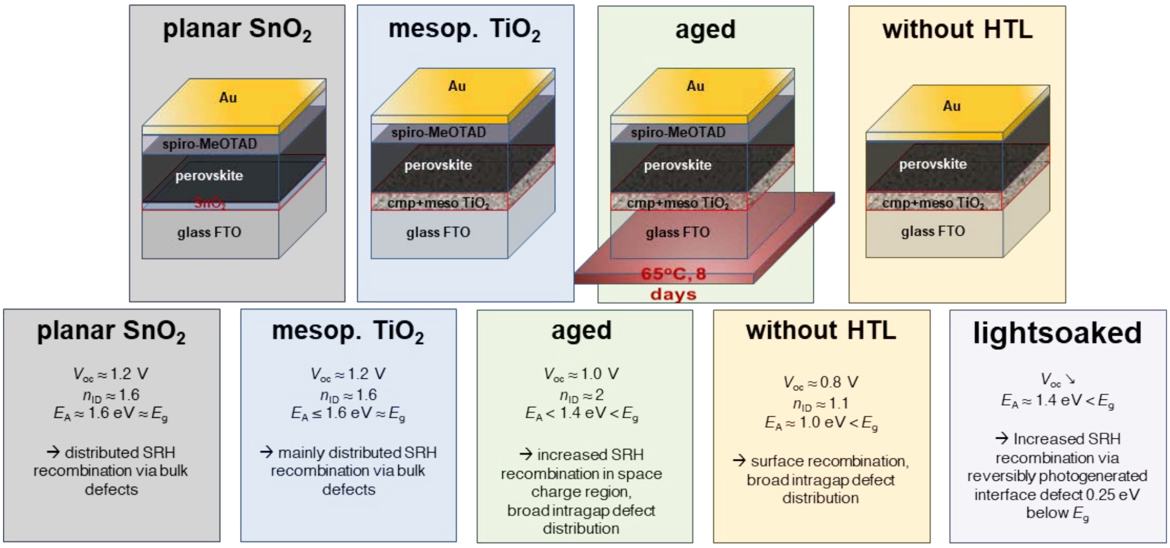

Figure 40: Ideality factors and attributed recombination mechanism in n-i-p cells with different electron transport layers (SnO_2 and TiO_2), an aged device (based on TiO_2, kept 8 d under 1 sun white-light LED illumination at 65 °C in N2), a device without HTL and a light-soaked device (1 sun equivalent illumination for 80 min at open-circuit). Adapted with permission.[290] Copyright 2018, Royal Society of Chemistry.

The above findings and interpretations point to the difficulty in assigning a measured value of to a specific recombination process. Moreover, the above relations assume that the densities of electrons and holes are comparable and homogeneous throughout the active layer. Consider for example radiative band-to-band recombination. Here, the local rate $R(x)$ depends on the local densities of electrons and holes via $R(x) = k_2 n(x) p(x)$. Charge injection from ohmic contacts, selective trapping, the attachment of charge-transporting layers and electrodes, etc., may result in a large variation of the carrier concentrations across the active layer thickness but also give rise to imbalanced electron and hole densities even at V_{OC}[32, 178, 267, 297, 298]. In such a case, the ideality factor does not necessarily reflect the order of the predominant recombination process[295]. Recently, Bongiovanni and coworkers pointed out that electrons and holes may even have different recombination orders. In this case, $n_{ID} = \left(\frac{1}{\alpha_e} + \frac{1}{\alpha_h}\right)$, where α_e and α_h is the individual recombination order ($\alpha_{e/h} =$ 1,2,3; see above) for electrons and holes, respectively.[295] These others considered a trap-assisted recombination process, where the first step is the capture of electrons by a trap, followed by the recombination of a free hole by the trapped electron. If the trap is situated such that the fraction of occupied traps are small, the rate of free electron capture is proportional to its density and $\alpha_e = 1$. Holes, on the other hand, recombine in a bimolecular fashion with trapped electrons, whose density n_T is proportional to n_h, resulting in $\alpha_h = 2$. In combination, this picture leads to $n_{ID} \approx 1.5$; a frequently reported value for perovskite solar cells. This approach, therefore, provides an elegant explanation for the observation that recombination is mostly nonradiative but that the ideality factor differs significantly from the prediction of SRH recombination, where $n_{ID} \approx 2$. In addition, will also depend on the exact shape of the density of states distribution through which recombination proceeds[299]. For example, for an exponential band tail, $n \propto e^{qV/mk_BT}$, where m is a parameter describing the width of the tail. This results in $n_{ID} m/\alpha$ for the most simple case of similar band tails for electrons and holes. The situation becomes even more complicated when considering the exact recombination pathway, *e.g.* trapped with free carriers, free with free carriers, or different shapes of the DOS of electrons and holes near the band-edge.[299] This renders it even more challenging to interpret the value of in terms of the predominant recombination mechanism without additional information on the details of the recombination pathways and the energetic and spatial distribution of carriers. This conclusion is particularly important in view of the complex multilayer architecture of perovskite solar cells, where recombination is not restricted to the bulk of the perovskite layer and carrier distributions are influenced by the dynamic equilibrium of extraction, reinjection, and recombination mediated by the CTLs. Furthermore, slow dynamic processes, that depend *e. g.* on ionic movement[281] – which itself depends on a manifold of parameters such as processing conditions, dielectric constants or doping of the CTLs, complicate the information one can draw from this "figure-of-merit". For example, Calado *et. al.* [300] nicely showed that the ideality factor can take any value between 1 and 2 in the same device, depending on pre-biasing condition and settling time of the measurement, typically not reported, but - bearing these results in mind - should be. Alternative to these "steady-state" measurements, small-perturbation techniques such as impedance spectroscopy (IS)[70, 301–303], and transient photovoltage measurements (TPV)[66, 276] in combination with differential charging (DC)[65] have been extensively applied to perovskite solar cells in order to provide a comprehensive picture of the recombination in full devices. In IS, the solar cell is held under steady-state illumination with a set intensity, while the external bias is modulated around a given DC bias. This causes a periodic variation of the current which is recorded as a function of the modulation frequency. While IS has the advantage that it can be easily performed with a commercially available impedance spectrometer, the analysis of the data requires to "simplify" the device by an equivalent circuit, which is not a trivial task[304]. For example, Zarazua *et. al.* [302] performed IS measurements on n-i-p perovskite solar cells for different illumination intensities and perovskite thicknesses. The analysis of the data with an equivalent circuit with two capacitors and three resistors revealed two regimes, a high-frequency regime assigned to processes in the bulk and a low-frequency regime associated to interfacial charge accumulation and recombination. The detailed analysis led to the conclusion that the steady-state response of these cells is mainly determined by the charge carrier kinetics at the surfaces, while processes in the bulk are of minor importance. Recombination times from this study were, however, in the range of 1 ms - 1 s, which is several orders larger than charge carrier decay times deduced from TPV or PL measurements (see below). One difficulty in analyzing IS data comes from the motion of ions in response to the alternating voltage, meaning that the low-frequency response of the cell may reveal the combined properties of ions, electrons and holes.[304] TPV records the dynamics of the V_{OC} drop of a cell after it has been exposed to a short laser pulse. In most cases, the sample is held at a given V_{OC} by illuminating the sample with a given illumination intensity and by using a large output resistor. Exposing the sample to a laser pulse of low fluence causes a small perturbation from quasi-equilibrium, expressed by a sudden increase of the V_{OC}. The transient decay of V_{OC} back to its stationary value is analyzed in terms of the charge carrier dynamics. Figure 41 summarizes the results from such a study, where TPV and DC were applied to p-i-n cells. Here, the bandgap of the perovskite was enlarged by increasing the concentration of Br in the mixed $CH_3NH_3Pb(I_{1-x}Br_x)_3$ perovskite. PEDOT:PSS served as the HTL while either PCBM or PCBM blended with 20% of the higher adduct fullerene ICBA was used as the ETL. As shown in Figure 41a, the V_{OC} was affected by both the composition of the perovskite and the choice of the ETL, going along with distinct changes of the carrier concentration at a given steady-state illumination intensity (from DC) and carrier lifetime (from TPV). Increasing the Br-content increased the V_{OC} but reduced the carrier lifetime, while the addition of the ICBA was beneficial for both properties. A detailed analysis of the data revealed the existence of an exponential tail of defect states, which serve as recombination centers. Interestingly, the ideality factor of the sample with a 20% Br content and a PCBM ETL was below one at higher light intensities, indicating failing contact selectivity, which may also diminish the carrier lifetime. Following this line of arguments, the addition of ICBA to the ETL was proposed to reduce the impact of recombination at the perovskite/PCBM interface, which was attributed to a different interface energetics as discussed in greater detail next.

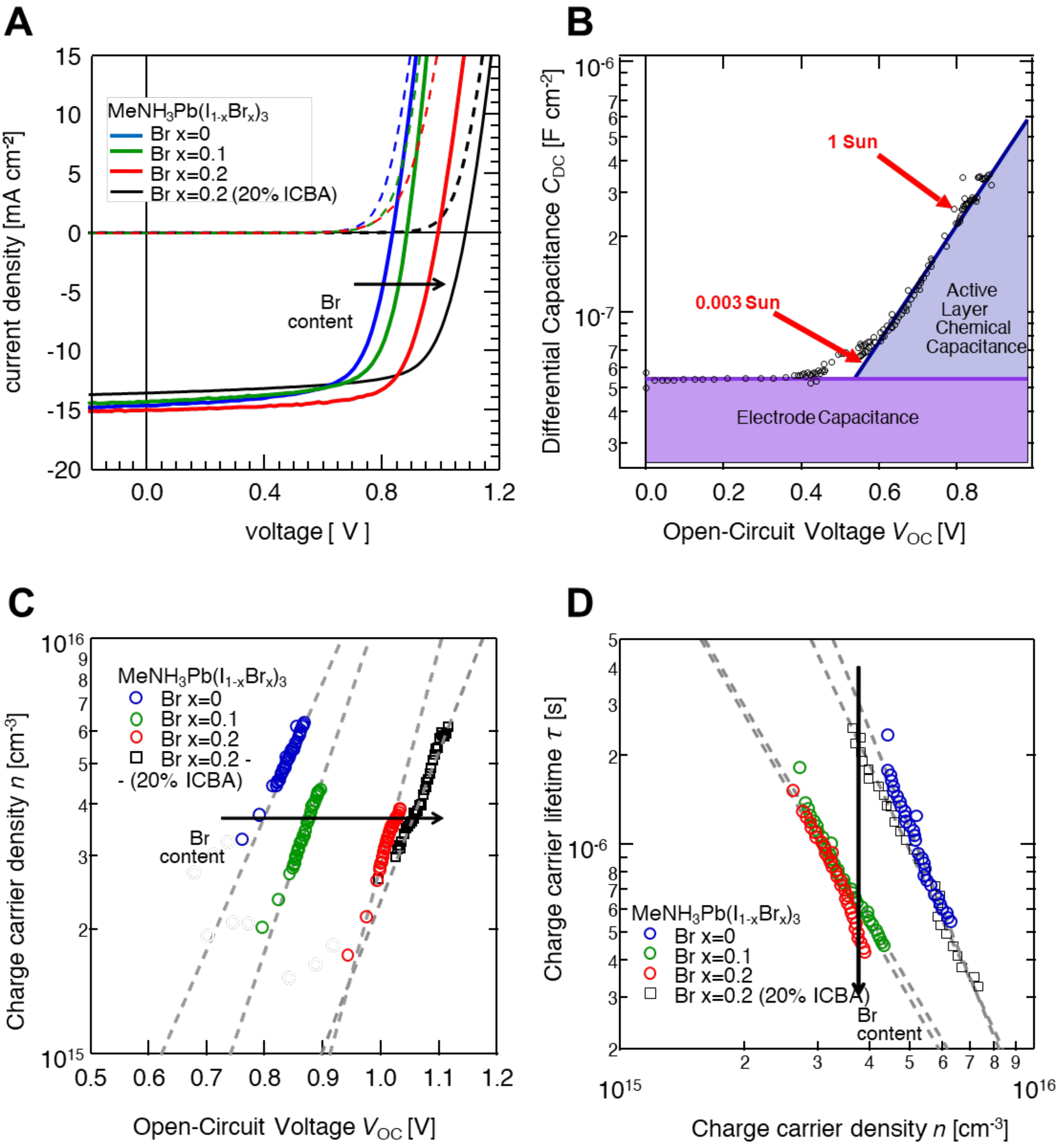

Figure 41: Results from transient optoelectronic measurements on p-i-n solar cells, comprising a mixed $CH_3NH_3Pb(I_{1-x}Br_x)_3$ perovskite sandwiched between a PEDOT:PSS hole transporting layer and a PCBM electron transporting layer to which ICBA was also added in one case. A) The addition of Br to the perovskite and of ICBA to the ETL both increase the V_{OC}. B) Differential charging indicates that most photogenerated charges reside in the active layer under application-relevant illumination conditions. C,D) Despite similar effects on the V_{OC}, the addition of Br and ICBA changes the carrier concentration and the carrier lifetime in different ways, pointing to the interplay between bulk and interface recombination. A-D) Adapted with permission.[65] Copyright 2017, American Chemical Society.

It has been pointed out that carrier lifetimes measured via TPV may be affected by capacitive effects[67]. More recently, Kiermasch *et. al.* provided further guidance under which conditions measured carrier lifetimes may not be influenced by the capacitive discharge,[276] which allows quantifying true lifetimes in perovskite solar cells. Measurements on samples with “sufficiently” thick perovskite layers and high enough carrier densities were interpreted in terms of bulk recombination with a recombination order of 1.6 - 2. Notably, the analysis of the data yielded a disorder factor m of 2.8, again indicating a significant exponential broadening of the sites involved in the recombination process. This finding seems at variance with the very sharp absorption onsets of typical perovskite absorbers, and suggest that such states are dark (they do not contribute to the optical absorption and radiative recombination). However, DC measures only the average carrier density, while the recombination properties are depending on the spatial distributions of the photogenerated excess carriers as pointed out above. Notably, the attachment of a selective CTL (which specifically extracts only one type of carrier while blocking the other) introduces very inhomogeneous carrier profiles. Charge carrier lifetimes as deduced from TPV measurements range typically between few hundreds of nanosecond to several microseconds, depending on the sample layout and the illumination intensity. Such values seem reasonable in the view of significant nonradiative V_{OC} losses in these devices. Discrepancies of “carrier lifetimes” between measurements with different techniques including electrical such as impedance or capacitance measurements, electro-optical such as OTRACE[305], TPV or TDCF[167] and finally all-optical such as TRPL, TAS, TRS or TRMC and optical pump terahertz probe (OPTP)[306] calls for comparative examination of the different techniques. Particular care should be taken regarding several parameters which may influence the result. These include the excitation condition (excitation wavelength,[274, 307] repetition rates[308], and intensities), the setup time-resolution (resistance-capacitance limitation) and the “sample-history”[189] (*e.g.* measuring from high-to-low intensity or vice versa). Moreover, it is clear that very different processes happen on different timescales, *i.e.* carrier-cooling, -trapping, -extraction on ps-timescales, carrier-motion, -detrapping, -recombination and electrode charge-up on ns- to µs-timescales, and finally ionic movement, (electro-)chemistry at the electrodes, in the bulk or at CTLs on ms-timescales.

8.3 PINPOINTING THE ORIGIN OF NONRADIATIVE RECOMBINATION IN PEROVSKITE MULTI-LAYER STACKS USING ABSOLUTE PL MEASUREMENTS

A disadvantage of the above-mentioned electrical and electro-optical methods is that they require complete solar cells. This renders it difficult to pinpoint or locate the origin of the nonradiative losses in the multilayer system as recombination through different channels occurs in parallel.[241] This problem can be circumvented when probing the density and fate of carriers with all-optical techniques, *e.g.* by studying the (temporal change in) absorption/reflectance or luminescence upon illumination. In this spirit, we and others utilized measurements of the absolute intensity of the emitted PL (ϕ_{PL}) to analyze the steady-state recombination losses in (perovskite) thin films and solar cells[185, 191, 192, 309]. The strategic advantage of these measurements is that it can be performed on any layer assembly, with and without the presence of CTLs or electrodes. Also, if PL experiments are performed in steady-state in the absence of electrodes or at V_{OC}, the emitted photon flux under illumination with a given intensity yields the absolute radiative and nonradiative recombination currents. This is a decisive advantage over other techniques when trying to assess nonradiative recombination in perovskite films. Moreover, the absolute emitted PL - or equivalently the radiative recombination current density - is a direct measure of the chemical potential per free electron-hole pair (μ) or the quasi-Fermi level splitting (QFLS) in the active material (Equation 27) :[85, 190–192, 289]

$$q\phi_{PL}(\mu) = J_{rad.} = J_{0,rad.}e^{\mu/_B T} .$$

Here, $J_{0,rad.}$ is the radiative thermal recombination current density in the dark. We note that above equation is a simplification of Würfel’s generalized Planck law which is only valid for a QFLS a few $k_B T$ smaller that the bandgap $\mu < E_G - 3k_B T$.[39] If, on the other hand, all absorbed photons generate free charges, and all photon emission stems from the recombination of free electron-hole pairs, QFLS can be related to the photoluminescence quantum efficiency of the active layer (PLQY) according to Equation 27:

$$\mu = k_B T \cdot \ln \left[\mathrm{PLQY} \cdot \frac{J_G}{J_{dark}} \right].$$

These equations are valid if the spectral dependence of $J_{rad.}$ is identical to $J_{0,rad.}$, meaning recombination goes through the same channels regardless of the QFLS. In the case of electrically injected charges, Equation 51 can be varied by exchanging QFLS with eV_{OC} and PLQY by EQE_{EL} (the electroluminescence quantum efficiency), named Rau's reciprocity relation.[43] This exchange holds true for equivalent injection and extraction efficiencies (Donolato-Theorem[245, 310]) and the high photovoltaic external quantum efficiencies (EQE_{PV}) of perovskite solar cells suggest that extraction and injection are indeed very efficient. Based on these basic considerations, Sarritzu *et. al.* [192] proposed to decouple the contributions of bulk and interfacial recombination currents in n-i-p type perovskite solar cells through the measurement of the QFLS in the individual layers of the cells, *i. e.* the perovskite on glass with and without attached transport layers. The authors found that attachment of an electron- or hole-transport layers (ETL/HTL) to the perovskite resulted in a substantial reduction of QFLS and with that the maximum achievable V_{OC} by several tens to hundreds of meV.[192] Figure 42a shows that the QFLS of the neat perovskite is larger than the QFLS of the TiO_2/perovskite film, the perovskite/Spiro-OMeTAD film and the n-i-p stack which had the lowest QFLS. The authors concluded that non-radiative recombination proceeds mostly at or across the perovskite/CTL interfaces, meaning that the interfacial recombination currents set the largest limitation on the V_{OC} and the performance of their cells, see Figure 42b. Wu *et. al.* [185] further extended this approach by measuring the intensity dependence of the QFLS[267] which allowed the authors to obtain pseudo-JV-curves of the perovskite absorber layer with and without transport layers or electrodes. This powerful approach enables to quantify the impact of non-radiative interfacial recombination not only on the V_{OC} but also on the fill factor.

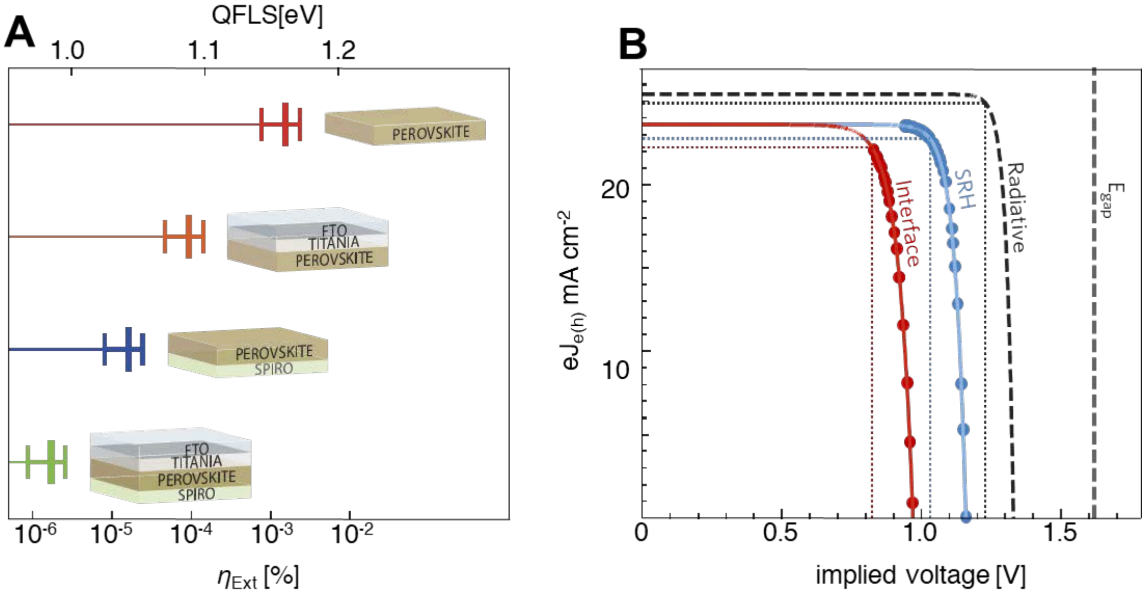

Figure 42: A) Comparison of the free electron-hole energy (top axis) and external photoluminescence quantum yield (bottom axis) in neat perovskite with and without attached transport layers under a 1 sun equivalent CW laser excitation at 532 nm (50 mW cm^{-2}). Substantial interfacial recombination losses were obtained in the presence of the interlayers. B) Predicted J-V curves, that is, external electron and hole currents that equal the generation current JG and the total recombination current $J_{e/h} = J_G - J_R = J_0 e^{\mu / n_{ID} k_B T}$ which were calculated based on the experimentally measured ideality factors (n_{ID}) on the neat perovskite layer and the n-i-p stack. A,B) Adapted under the terms of the CC-BY Creative Commons Attribution 4.0 International License (http://creativecommons.org/licenses/by/4.0/).[192] Copyright 2017, The Authors, published by Springer Nature.

More recently, we used hyperspectral PL imaging (2-dimensional maps with coordinates [x, y, $I_{PL}(\lambda)$]) to pinpoint the origin of non-radiative recombination losses in p-i-n type perovskite solar cells with the architecture ITO/PTAA/perovskite/C_{60}/BCP/Cu. Measurement of the depth-averaged absolute PL yield (I_{PL}) enabled the creation of two-dimensional QFLS maps[190, 191] (size: 10x10 m^2) on perovskite film with and without attached transport layers as shown in Figure 43.[289] On the neat perovskite an average QFLS of 1.21 eV was obtained which was significantly below the radiative limit (1.34 eV). Addition of PTAA (1.125 eV) or C_{60} (1.13 eV) lowered the QFLS considerably, however, in contrast to Sarritzu *et. al.* , the QFLS of the p-i-n stack was only slightly lower (1.12 eV) compared to the bilayers. This result would be consistent with the expectation that the recombination currents at the bottom and top interface are superimposed in the p-i-n stack, yet both recombination currents lower the QFLS only via the logarithm (see further below). Inserting ultrathin interlayers (PFN-Br and LiF) allowed a substantial reduction of interface-induced recombination losses at both interfaces which increased the V_{OC} of the optimized cells to 1.17 V. These improvements enabled p-i-n type solar cells with efficiencies of 21.6% on small areas and a stabilized certified PCE of 19.83% for a 1 cm^2 perovskite solar cell. We note that the V_{OC} of both the unoptimized and the optimized cell [ITO/PTAA/(PFN-Br)/perovskite/(LiF)/C_{60}] was identical to the QFLS of the corresponding p-i-n stacks on glass which will be discussed in more detail further below. The study also included a direct comparison between absolute PL and TRPL measurements, which revealed a concurrent increase of the TRPL decay time and the PL yield with reducing interfacial recombination. Interestingly, the mono-exponential TRPL lifetime of the neat perovskite film (~500 ns) and the optimized p-i-n stack (~200 ns) allows to analytically predict the corresponding QFLS of the neat perovskite film (1.21 eV) and the optimized p-i-n stack (1.17 eV) considering dominant first-order recombination at V_{OC}.[69] Moreover, through quantification of the interface recombination velocity S, the V_{OC} of the unoptimized and optimized cell could be accurately reproduced. These results suggested that the TRPL decays were dominated by interfacial recombination rather than the transfer of photogenerated carriers to the transport layers, although this may depend on the exact measurement conditions as we discuss further next.

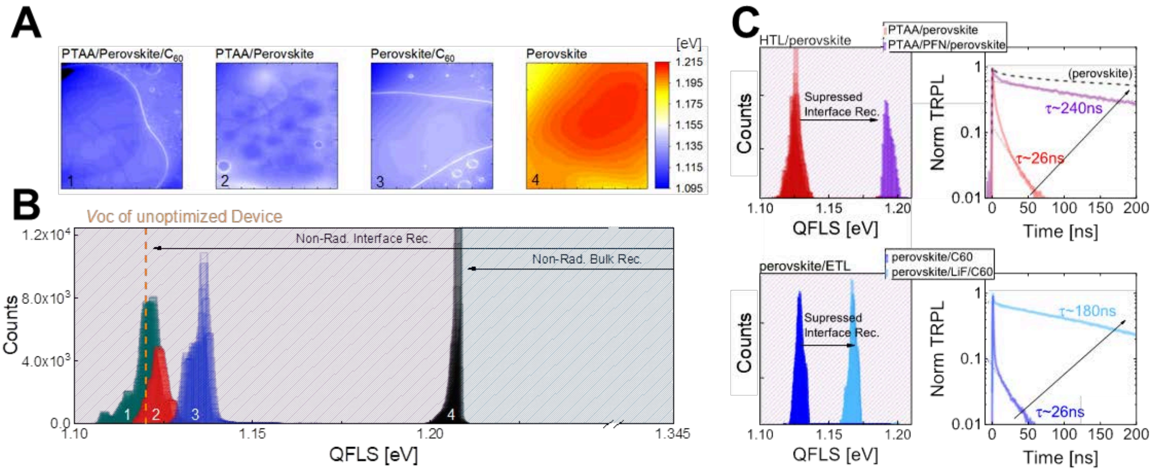

Figure 43: A) Hyperspectral QFLS maps (1 × 1 cm^2) of the neat perovskite and in conjunction with different CTLs providing information on interfacial and defect recombination in the bulk and the interfaces. B) The QFLS distribution as obtained from the maps shown in (A). Films with transport layers attached to the perovskite exhibit a significantly lower QFLS due to large nonradiative interfacial recombination losses. C) The improvement in QFLS upon inserting additional interfacial layers resulted in a substantial and concurrent increase in QFLS and TRPL lifetime. A-C) Reproduced with permission.[171] Copyright 2018, Springer Nature.

More recently, we generalized this approach to all major perovskite solar cell architectures, including 1) planar p-i-n type cells, 2) mesoporous, and 3) planar n-i-p type cells. This included the study of triple cation perovskite cells and other perovskite compositions[241] with 10 different CTLs (see Figure 44) including conjugated polymers, small molecules, fullerenes and metal oxides (SnO_2 and TiO_2). For most studied CTL it was found that the interfacial recombination current outweighs the recombination current through defects in the neat perovskite (Figure 44). The best transport layers in this study were PTAA/PFN-Br and PolyTPD/PFN-Br and SnO_2 which allowed a QFLS close to the neat perovskite. Among CTL on top of the perovskite, Spiro-OMeTAD was found to be superior to PCBM and C_{60} which might be one reason why n-i-p type cells have historically delivered higher V_{OC}'s compared to p-i-n type cells (with few recent exceptions[225, 267, 293, 311]). At this stage we want to emphasize that the myriad of explored and unexplored combinations[27] that can be obtained by alloying and mixing any of the three components (A, B, X) within the generic structure ABX_3 or even minor changes in supposedly identical compositions[155, 312] or concentrations[313] will render it difficult to compare and assess achievements unless the community moves towards reliable metrics that allow for comparability. We believe that radiative efficiencies, both PLQY and EQE_{EL}, are the most promising candidates for such metrics and would very much appreciate these numbers to be reported alongside photovoltaic efficiencies.[198] In fact, other semiconductors such as kesterites[314–316] or III-V, have similar bandgap tunability, entailing the same problem. In this regard, in a recent report, Green and Ho-Baillie[44] collected the highest reported radiative efficiencies for a broad number of photovoltaic systems, thereby highlighting the importance of the external radiative efficiency (PLQY) in limiting the V_{OC} and overall performance of such state of the art devices.

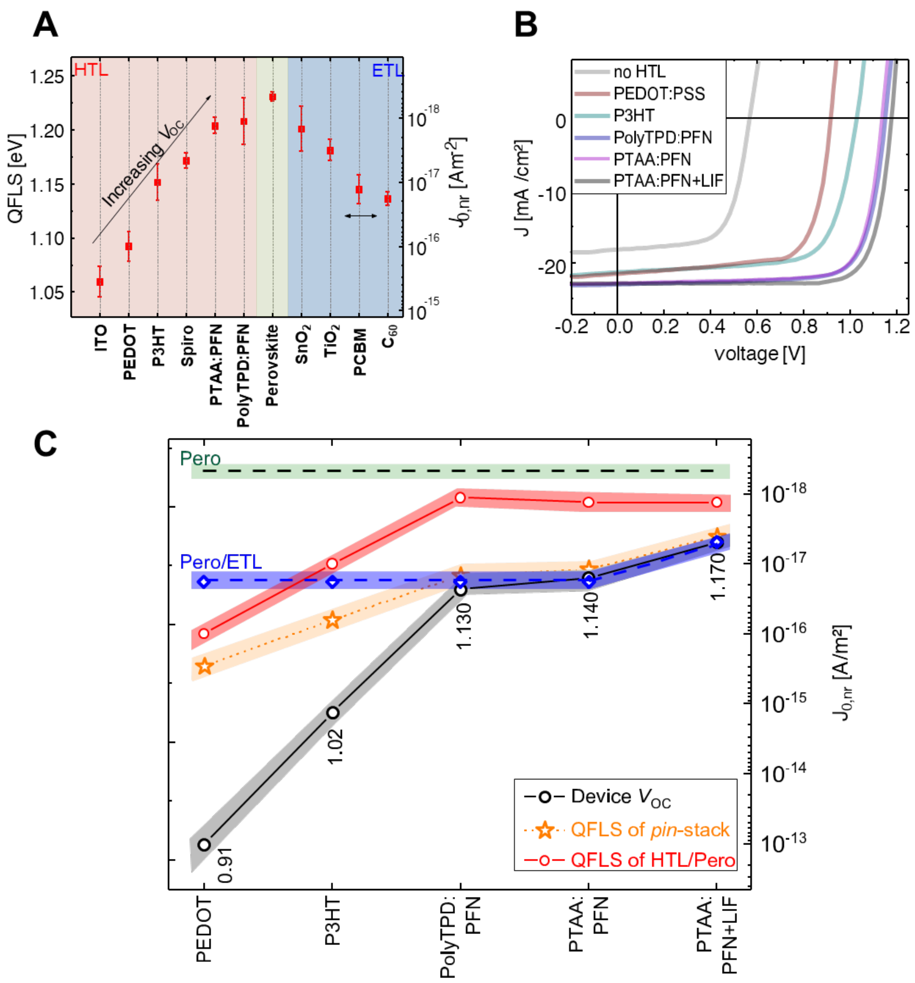

Figure 44: A) The quasi-Fermi level splitting as deduced from absolute photoluminescence measurements in the perovskite absorber without and various transport layers being present (hole CTLs are shown in red, electron CTL in blue). The corresponding thermal nonradiative recombination current ($J_{0,nr} = J_0 - J_{0,rad}$) is plotted on the right. B) The current density versus voltage (J-V) characteristics of the p-i-n type cells with different conjugated polymers serving as a hole-transporting layer and with C_{60} as the ETL. In the "PTAA:PFN+LiF" device, a thin layer of LiF had been added between the perovskite and the C_{60} to reduce interfacial recombination. C) The average V_{OC} (black line) of cells shown in (B) as compared to the average QFLS of the corresponding HTL/perovskite and perovskite/C_{60} bilayers, as well as the QFLS of the p-i-n stacks, is shown in red, blue, and orange, respectively. The brown line represents the QFLS of the neat bulk material on fused silica, which also separates the interface (shaded purple area) and bulk limited regime (shaded orange area). A-C) Reproduced with permission.[289] Copyright 2019, Royal Society of Chemistry.

In Figure 44c, the QFLS of 4 different HTL/perovskite films were compared to the QFLS of perovskite/(LIF)/C_{60} films, the corresponding p-i-n stacks, and the final device V_{OC}.[241] It was found that for efficient cells (>18% PCE), the V_{OC} of the cells (columns) approaches the QFLS of the corresponding p-i-n stacks (black stars) within a small error (< 20 meV). This was also confirmed for n-i-p type cells based on SnO_2 and TiO_2. The QFLS-V_{OC} match implies that (a) the dominant free energy losses occur at the perovskite/transport layer interfaces, (b) the inferior interface dominates the energy loss and (c) completion of the device by the addition of contact metals does not introduce significant losses. It was further found that the perovskite top surface and its interface with organic CTLs - fullerenes for p-i-n devices and spiro-OMeTAD for n-i-p devices - appears to be the critical interface in the efficient devices. This may be an intrinsic property of interfaces involving organic semiconductors - in particular fullerenes[317] – but can potentially be overcome by addressing this very limiting interface properly, as we will discuss below. The results were corroborated by drift-diffusion simulations which confirmed the QFLS-V_{OC} match only in case of an energy alignment between the perovskite and the transport layers.[241] The simulations also highlighted the importance of energy level alignment between the perovskite and the CTLs, and also suggest that a high built-in voltage of at least 1.0 V is required in order to reproduce the experimental current-density vs. voltage (JV)-curves. However, in devices with energetically misaligned CTLs, a QFLS-V_{OC} mismatch exists (Figure 44c) due to additional recombination losses at the interfaces or contacts. These energy offsets were further confirmed with ultraviolet photoelectron spectroscopy (UPS) and DC capacitance measurements.[241] Such internal voltage drops were also proposed by Wu *et. al.* [185] who observed an identical PL yield of cells with different external V_{OC}s where TiO_2 was annealed in different gas environments. This potentially impacted its work function and electron affinity and thereby the energy alignment with respect to the perovskite layer. Moreover, this may also rationalize the mismatch obtained by Guo *et. al.* [318] when comparing V_{OC} in devices and QFLS calculated from rate constants, albeit the authors come in part to a different conclusion, namely that in some cases bulk recombination is predominant, which would be only possible if interfacial recombination is practically overcome in these cells.

8.4 QUANTIFICATION OF RECOMBINATION CURRENTS AT V_{OC}

In order to quantify the actual parallel recombination currents at V_{OC}, we consider that the PLQY is a measure of the ratio of emitted ($\phi_{emission}$) to absorbed photons ($\phi_{absorption}$), which equals - at V_{OC} - the radiative recombination current density divided by the total recombination current ($J_{R,tot.}$). The latter is a sum of radiative recombination and all non-radiative recombination losses in the bulk ($J_{nr,B}$), and the interfaces ($J_{nr,p-i}$ & $J_{nr,i-n}$) and potentially other recombination currents at the metal contacts.[241, 319]

$$\text{PLQY} = \frac{\phi_{emission}}{\phi_{absorbtion}} = \frac{J_{rad.}}{J_{tot.}} = \frac{J_{rad.}}{J_{rad.} + J_{nonrad.}} = \frac{J_{rad.}}{J_{rad.} + J_{nr,B} + J_{nr,p-i} + J_{nr,i-n} + \dots} \tag{56}$$

Using the last expression of the PLQY allows writing the QFLS/μ as a function of all non-radiative recombination currents. Equation 6 highlights the impact of parallel recombination currents on the QFLS. The situation of the cell at V_{OC} is perhaps best compared to a bucket[320] that represents the cell with the water level representing the cells' V_{OC}. A constant water stream fills the bucket which corresponds to the generation current density from the sun.[304] The holes in the buck represent the recombination losses at V_{OC} in the bulk, interfaces, etc. Depending on the exact size of the holes, the water level will change, and so will the V_{OC} of the device. The absolute PL approach allows estimating the recombination currents, including $J_{0,rad}$. The latter can be quantified from the overlap of the cells' EQE and black body spectrum at 300°K.[122, 145, 146] Measurement of the PLQY of the different stack layers allows then quantification of the non-radiative recombination currents in the bulk and at the interfaces according to Equation 27. We note that the recombination currents need to be known at the QFLS of the final cell which requires the knowledge of the ideality factor of the QFLS of the individual layers. The obtained recombination currents at V_{OC} for a standard p-i-n type cell with PTAA:PFN as HTL and C_{60} as ETL are shown in Figure 45.

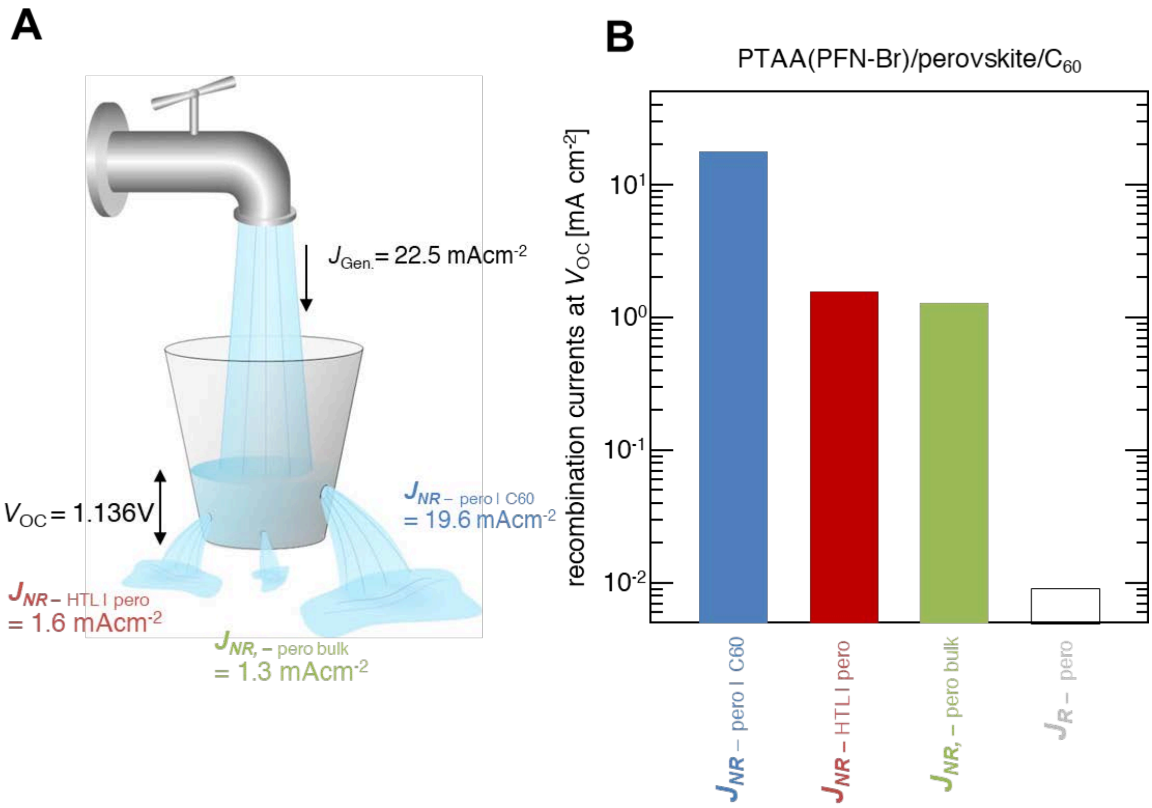

Figure 45: A) A ITO/PTAA/PFN-Br/perovskite/C_{60}/BCP/Cu solar cell under AM1.5G illumination at V_{OC}, illustrated by a bucket with holes. The holes in the bucket depict the recombination currents at V_{OC} (radiative bulk recombination is negligible and not shown). B) The recombination at the perovskite/C_{60} interface greatly outweighs the recombination in the perovskite bulk and at the HTL/perovskite interfaces. Adapted with permission.[241] Copyright 2019, Royal Society of Chemistry.

We want to emphasize that Figure 45a & b represent the recombination currents in the situation of an already well-performing perovskite cell. Should the perovskite layer be processed such that the defect density is much higher, recombination within the perovskite may dominate and even excellent contact layers could not improve the radiative efficiency (we note, that worse perovskite systems have been shown in Supplementary Information of ref.[241]). To state this in the bucket frame, the biggest hole will dominate the losses. It is therefore imperative to identify the predominant loss channel and reduce this first. In this sense, we believe that some of the reported improvements with respect to open-circuit-voltage - stated to stem from an improved bulk through additives or different (post-) processing - may be in fact improvements at the interfaces to the adjacent layers. As a side note, considering the (often) significant impact of interfacial recombination on the overall recombination current at V_{OC}, the ideality factor must be strongly influenced by interfacial recombination as well. Efficient p-i-n type cells exhibit ideality factors of ~1.4-1.5[99, 176, 241], which may be interpreted as the competition between radiative bulk and non-radiative SRH recombination. However, given the fact that n_{ID} stays constant over a broad range of intensities and that the non-radiative interfacial recombination is roughly ~15x stronger at the perovskite/C_{60} interface compared to the radiative recombination in the bulk, it becomes apparent that some earlier interpretations of n_{ID} in terms of the dominant recombination pathway need to be revisited.

8.5 RECOMBINATION KINETICS REVEALED BY TRANSIENT MEASUREMENTS

While steady-state PL allows quantifying the recombination losses in the bulk, interfaces and/or metal contacts, little is known how and at which rates recombination proceeds exactly at the interfaces. In particular, the steady-state PL measurements cannot disclose whether the addition of a transport layer worsens the performance because of an increased rate of recombination at the perovskite surface, across the perovskite/CTL interface or even by introducing recombination within the transport layers. In order to resolve the kinetics of bulk and interfacial recombination in perovskite films and solar cells, transient techniques with high time resolution are required. The most popular technique in the community is arguably transient photoluminescence (TRPL).[99, 151, 152, 321] Other transient techniques that have been applied less frequently to perovskite thin films include microwave conductivity (TRMC),[150] transient absorption or reflection spectroscopy (TAS[322, 323] or TRS[173]) and transient terahertz spectroscopy (THz).[324] These techniques allow to track the fate of charges from below picoseconds to milliseconds, which provided deep insights into the fundamental recombination processes in the bulk and interfaces, however, the accurate implementation of these measurements is more challenging as well as a solid interpretation of the results. In contrast to the steady-state PL emission at V_{OC}, the TRPL decay is influenced by numerous processes. This is because the PL intensity is proportional to the product of the free electron and hole density on the perovskite layer (while TAS, TRMC or THz yield a weighted sum of the two densities). It is, therefore, often difficult to disentangle the actual recombination loss in the TRPL signal from processes which depopulate only one of the two carrier reservoirs (electrons or holes). As such, the PL decay of a perovskite/CTL stack may be dominated by the transfer of charges to the transport layers, while the recombination of the remaining charges contribute only little to the transient.[69, 151] TRPL: Transient PL is an all-optical technique and a very popular tool in the community. As pointed out above, PL is a sensitive measure of the product of electron and hole densities in the perovskite absorber. In case of a neat perovskite film, at sufficiently low fluences, a mono-exponential decay is usually observed, which has been assigned to different first-order processes, *e.g.* , trapping and trap-assisted recombination, or radiative recombination with doping-induced background charge. If CTLs are attached to the perovskite an accelerated (sometimes multi-exponential) decay is observed, which has been explained by the extraction of majority charges[304], fast interfacial recombination or a combination of both. A comprehensive description of charge transfer and recombination processes at the perovskite/transport layer interfaces based on TRPL has been recently presented by Krogmeier *et. al.* [151] who corroborated their experimental study on perovskite/PCBM bilayers with transient drift-diffusion simulations. The authors predicted that the TRPL decay at low fluences is determined by the rapid extraction of photogenerated electrons to the PCBM layer at early times while interfacial recombination dominates the decay at latter times, as shown in Figure 46. While these two regimes might be experimentally difficult to disentangle, application of the transient simulation allowed the authors to quantify the velocity of charge transfer and recombination at the perovskite interface. The authors concluded that the interfacial transfer and recombination velocities could be readily obtained at low fluences (≈ 1 nJcm^{-2}) although they noted that this condition might be difficult to realize experimentally. In contrast, at higher intensities, the obtained differential lifetime $\tau_{PL}(t) = -\left(\frac{d\ \ln(\phi_{PL}(t))}{dt}\right)^{-1}$ can be substantially influenced by the accumulation of charges at the interfaces and the concurrent built-up of a space charge field, which would lead to erroneous (underestimated) lifetimes. For a perovskite/PCBM film, the authors quantified a charge transfer and recombination velocity to be $S_T = 5300$ cm/s and $S_R = 200$ cm/s, respectively. Nevertheless, there are multiple processes that could potentially lead to a multi-exponential TRPL decay, such as a graded generation profile or trap-filling and in many experimental studies only a single exponential decay is observed. Typical surface recombination velocities induced by the transport layers range from ~10 cm/s to 10^4 cm/s, where - for the case of $CH_3NH_3PbI_3$ - the former puts the potentially obtainable V_{OC} close to 1.3V and the efficiency to >27% if high current densities can be preserved (>23mA cm^{-2}) and the FF would approach the radiative limit (~90%).[53, 304]

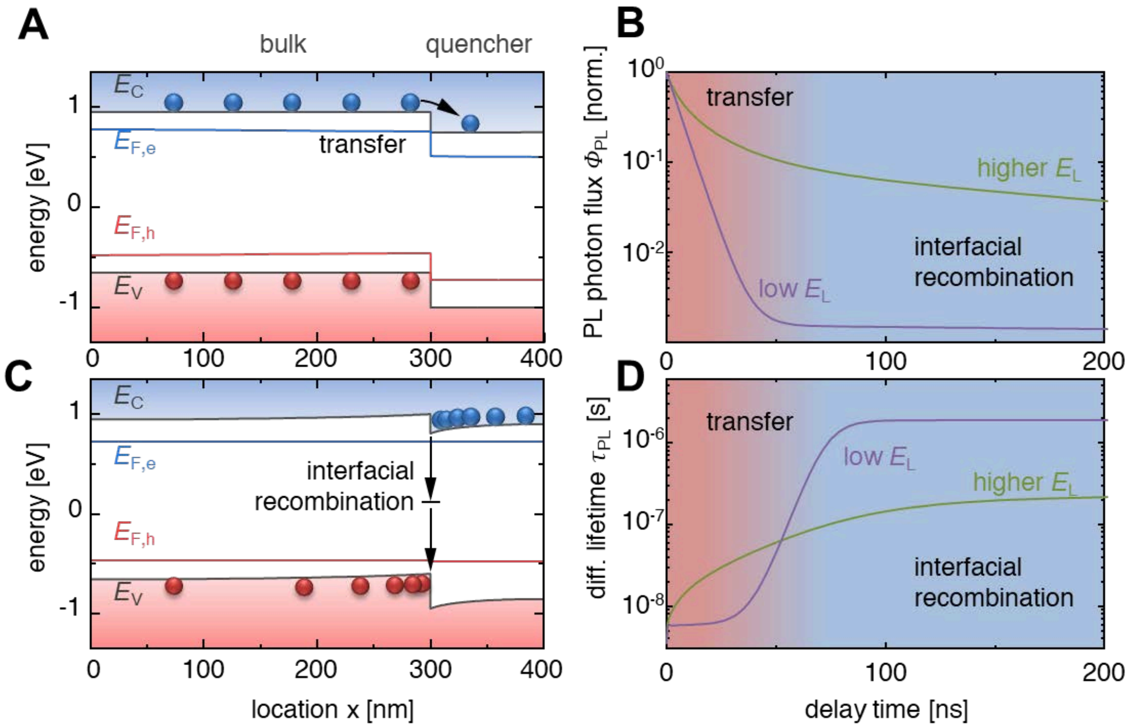

Figure 46: Results from 1D drift-diffusion simulations of TRPL on a perovskite/PCBM bilayer. A) Band diagram shortly after the laser pulse. Charge carriers are generated in the bulk and electrons transfer to the quencher. B) Band diagram for longer delay times. Charge carriers accumulate at the interface due to their mutual Coulomb attraction, leading to increased interfacial recombination. C) TRPL signal for two laser fluences (EL), both displaying two slopes, assigned to electron transfer and interfacial recombination. D) Differential lifetime showing two constant, clearly distinguishable regions for low laser fluences and a less distinguishable case for higher light intensities, where the latter case is affected by due to an accumulation of charge carriers. An interface recombination velocity of S_R = 10 cm s^{-1} was assumed and E_L is 1 nJ cm^{-2} for the low fluence case and 100 nJ cm^{-2} for the high fluence case. A-D) Adapted with permission.[151] Copyright 2018, Royal Society of Chemistry.

TRMC is an optical pump microwave-probe technique that measures the photoconductivity of charge carriers (σ) from absorbed microwave power ($\Delta P/P$) with a GHz frequency as a function of delay time ($\Delta P/P = c\sigma$), where c is a cavity dependent prefactor.[325] The photoconductivity is given by the mobility-weighted sum of the densities of free electron and hole density, n_e and n_h : $\sigma = e\Sigma(n_e\mu_e + n_h\mu_h)$, with μ_e and μ_h being the respective mobilities. Considering that right after photogeneration, the photogenerated charge carrier density is equal for electrons and holes, and given by the number of absorbed photons, the sum of the charge carrier mobilities can be readily quantified at early times. Assuming further that the free carrier mobilities remain at their initial values, the decay of the photoconductivity allows obtaining quantitative information on the kinetics of bulk recombination, interfacial charge transfer, and interfacial recombination. For example, Hutter *et. al.* [150] analyzed the TRMC decay dynamics of neat MAPI films on glass and MAPI/CTL junctions using a global kinetic model based on the continuity equations for electrons and holes. They proposed that CTL-assisted recombination is a multi-step process where the majority charge is first transferred to the CTL, followed by recombination with the photogenerated minority carrier on the perovskite (see Figure 47). For common CTLs - such as PCBM and C_{60} - the rate of electron transfer, ke, is more than one order of magnitude faster than the rate of subsequent interfacial capture of the electron on the CTL, kh, (see the Table in Figure 47), meaning that the rate-limiting process is the interfacial charge recombination. Importantly, both rates were reduced by approximately one order of magnitude when exchanging the C_{60} by higher-adduct fullerenes such as ICBA. ICBA has a ca. 0.2 eV higher-lying LUMO than PCBM, which may explain the reduction in the electron transfer rate. The picture of fast electron-transfer to PCBM followed by slow interfacial hole recombination is also in line with findings from transient lateral conductivity studies by Leijtens *et. al.* [149].

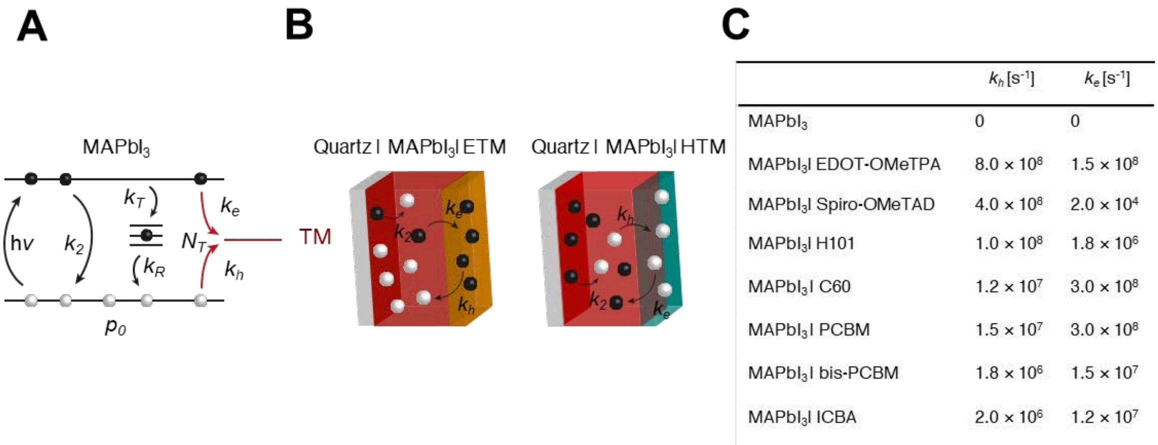

	k_h [s^{-1}]	k_e [s^{-1}]
$MAPbI_3$	0	0
$MAPbI_3$| EDOT-OMeTPA	8.0×10^8	1.5×10^8
$MAPbI_3$| Spiro-OMeTAD	4.0×10^8	2.0×10^4
$MAPbI_3$| H101	1.0×10^8	1.8×10^6
$MAPbI_3$| C60	1.2×10^7	3.0×10^8
$MAPbI_3$| PCBM	1.5×10^7	3.0×10^8
$MAPbI_3$| bis-PCBM	1.8×10^6	1.5×10^7
$MAPbI_3$| ICBA	2.0×10^6	1.2×10^7

Figure 47: The kinetic model developed by Hutter *et. al.* [150] for charge recombination across the interface between $MAPbI_3$ and an adjacent CTL. Interfacial recombination involves the extraction of a majority carrier (*e. g.* , k_h to the HTM) followed by its recombination with the remaining minority carrier in the perovskite (*e. g.* , k_e to the HTM). The table shows the obtained charge transfer and recombination rate constants in different bilayers. A-C) Adapted with permission.[150] Copyright 2017, Wiley-VCH.

Transient absorption spectroscopy (TAS) (either in transmission or reflection mode) relies on the sensitive measurement of the photoinduced change in absorption/reflection (ΔOD) as a function of the delay between a pump and a probe pulse. State of the art laser equipment allows performing measurements with high sub-ps time-resolution. The absorption spectra comprise different features associated to ground state bleaching (GSB), stimulated emission and/or photoinduced absorption (PIA) of photogenerated charges, but may also comprise associated changes of the refractive index[326] and thus reflectivity of the stack according to the Kramers-Kronig relation.[326] Pioneering works using TAS on perovskite/CTL heterojunctions suggested ultra-fast injection (<200 fs) of photogenerated charges into PEDOT:PSS and PCBM,[323] and other transport layers,[93,101] much faster than the time scales of interfacial charge transfer and recombination as recorded by TRPL and TRMC as noted above. Considering that the absorption features of polarons on the CTLs are generally distinct from the photoinduced signals in the perovskite layer,[93, 327] the transfer of charge can be readily visualized. Figure 48 shows the PIA and GSB as measured on a perovskite film on glass, while the presence of a PEDOT:PSS underneath the perovskite layer demonstrated a sub-ps charge transfer of charges to the HTL layer. The impact of the high fluence (25 μJcm^{-2}, corresponding to carrier densities at ~1000 suns) in these results needs to be carefully considered. Moreover, the decay of the polaron signal in the PEDOT:PSS containing film is remarkably fast (0.7 ps). This time constant is at least 3 orders of magnitude faster than typical interfacial recombination lifetimes on timescales above nanoseconds. This discrepancy suggests that transient measurements at high excitation conditions may be dominated by processes which are not visible under application-relevant conditions.

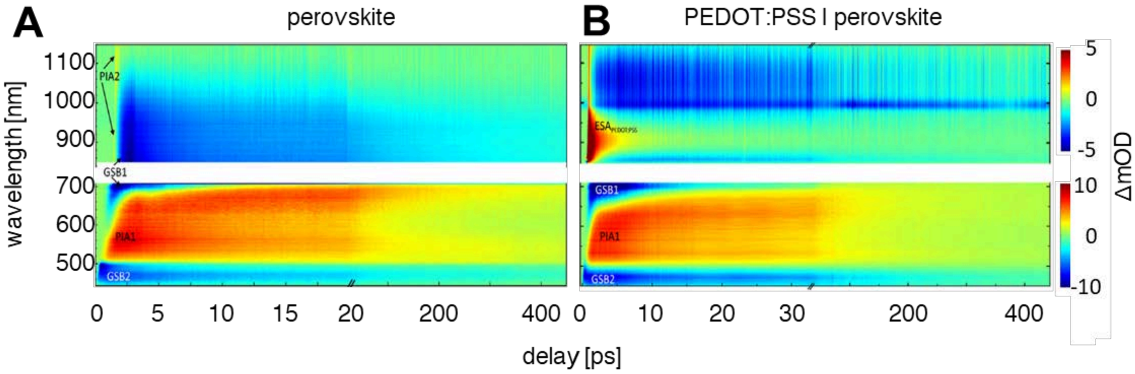

Figure 48: A,B) 2D color plots showing the change in absorption (ΔmOD) across a large spectral range versus delay time measured on a neat perovskite ($CH_3NH_3PbI_{3-x}Cl_x$) film and a perovskite/PEDOT:PSS bilayer. The TAS of the neat perovskite film shows fairly long-lived ground state bleaches at 480 nm (GSB2) and 775 nm (GSB1) and a photoinduced absorption signal at 600 nm (PIA1), in addition to a rapidly decaying transient absorption signal in the near-infrared (PIA2). In the sample with the PEDOT:PSS present, the immediate appearance (<200 fs) of the signal at 900 nm ($ESA_{PEDOT:PSS}$) was assigned to holes being injected into PEDOT:PSS. We note that this signal decays rapidly with a time constant of 0.7 ps. A pump wavelength of 388 nm with a fluence of 25 µJ cm^{-2} was used. A,B) Adapted with permission.[323] Copyright 2018, Wiley.

8.6 SUPPRESSION OF RECOMBINATION

Having demonstrated the importance of interfacial recombination through steady-state and transient measurement techniques, the last part of this progress report aims at highlighting several selected, promising optimization strategies in order to suppress non-radiative recombination with particular focus on interfacial recombination. The general outline of the presented optimization strategies is as follows: 1) Energy alignment, 2) suppression of non-radiative defect recombination at the interfaces and the perovskite surface, and finally overcoming interfacial recombination.

Energy Level Alignment

One of the most debated topics in the community is the importance of energy level alignment between the perovskite and the transport layers. Although the topic is far from being fully understood, from a theoretical point-of-view, it is expected that having aligned perovskite/CTL energy levels is highly beneficial to maximize the V_{OC} of the cells. The reason is that in order to yield the maximum achievable V_{OC} the electron and hole quasi-Fermi levels within the illuminated perovskite absorber layer need to perfectly align with the Fermi-levels of the respective contacts. In other words, the electron (hole) quasi-Fermi levels must not exhibit any tilt within the perovskite semiconductor or with the electron (hole) transporting layers. Ideally, this case is realized if the electron (hole) current density is zero at any point in the device, meaning that recombination at internal interfaces or at the electrodes is negligible compared to bulk recombination in the perovskite layer.[37, 328] Now, any energy level offset would exponentially increase the charge carrier density within the CTL, causing a drastic increase of the interfacial recombination currents and concurrently introducing a bending of the quasi-Fermi levels of the majority charge carrier.[185, 241] These basic considerations are readily confirmed from drift-diffusion simulations on n-i-p and p-i-n type perovskite solar cells.[185] An energy level offset of 0.3eV between the perovskite and the C_{60} would thereby lead to a similar voltage loss due to the downward bending of the electron quasi-Fermi level (in case this interface is determining the recombination loss). Indeed, as a rule of thumb, we find that any majority carrier band offset leads to an equal loss in V_{OC}. [241] As pointed out above, such offsets are only irrelevant in the case that the surface recombination velocity is negligible ($S_R < 1$ cm/s), or if the interface (with the offset) is not limiting the overall recombination.

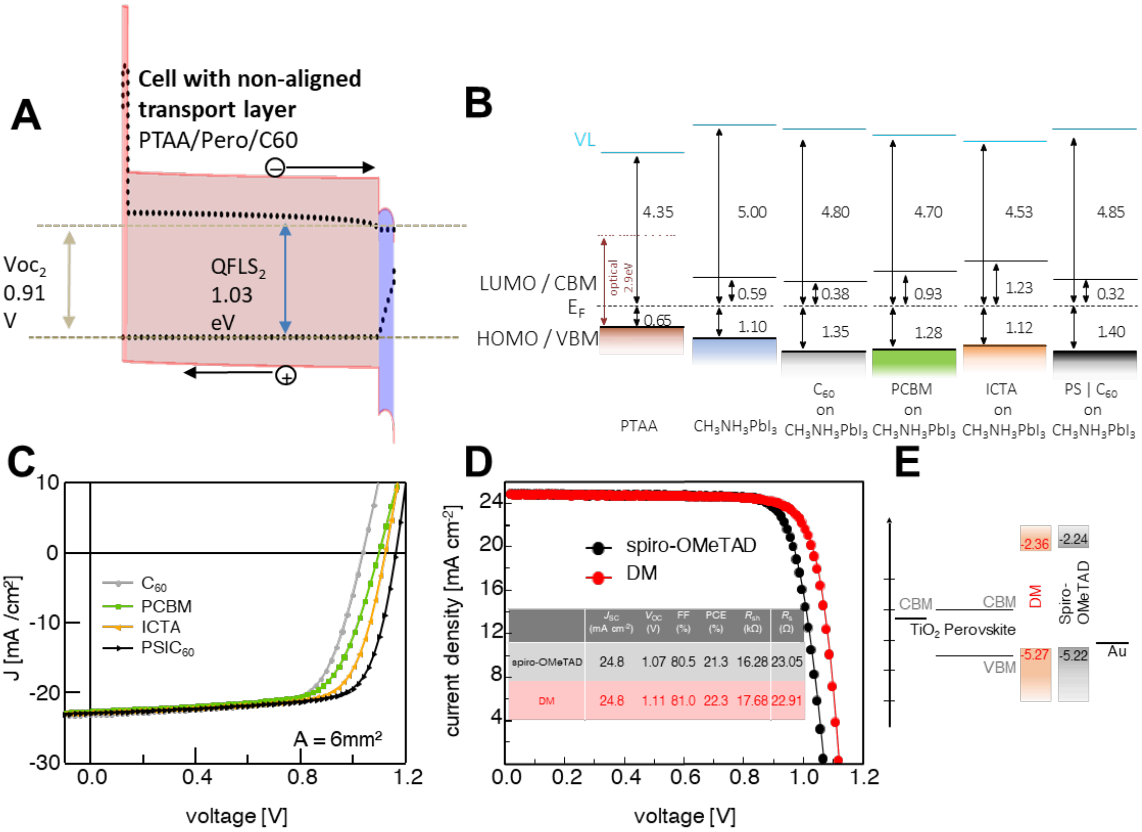

	J_{SC} (mA cm^{-2})	V_{OC} (V)	FF (%)	PCE (%)	R_{sh} (kΩ)	R_s (Ω)
spiro-OMeTAD	24.8	1.07	80.5	21.3	16.28	23.05
DM	24.8	1.11	81.0	22.3	17.68	22.91

Figure 49: A) Device simulations of perovskite cells (ITO/PTAA/perovskite/C_{60}/BCP/Cu) with and an energy offset of 0.3 eV at the perovskite/C_{60} interface which leads to considerable V_{OC} loss of 0.27 V (from 1.18 to 0.91 V) due to a built-up of charge carriers a the electron selective contact, which increases the interfacial recombination. B) Energy levels of MAPI and of different ETLs on top of the perovskite (C_{60}, PCBM, ICTA, and PS/C_{60}) as obtained from ultraviolet photoelectron spectroscopy (UPS) and inverse photoelectron spectroscopy (IPES). A (detrimental) downhill energy level offset was obtained between the perovskite and the C_{60} layer, while PCBM and ICTA show an uphill energy level offset. C) The J-V curves of the corresponding p-i-n devices demonstrating the improved V_{OC} from C_{60} to PCBM to ICTA to PS/C_{60}. D) J-V characteristics of n-i-p devices with the hole-transporting layer formed either by the traditional spiro-OMeTAD or from the fluorene-terminated spiro-based molecule DM. Devices with DM exhibit a significantly larger V_{OC}, resulting in record efficiencies of above 22%. E) The improvement was assigned to the better-aligned ionization potential of DM with respect to the perovskite valence band. A) Adapted with permission.[241] Copyright 2019, Royal Society of Chemistry. B,C) Adapted with permission.[99] Copyright 2017, Wiley-VCH. C,D) Adapted with permission.[212] Copyright 2018, Springer Nature.

From an experimental perspective, it has been shown that the energetic offset at the interface between the perovskite and the hole or electron transport layer has a large influence on the device V_{OC} (*e.g.* Schulz *et. al.* [329], Polander *et. al.* [74], us[99] and others[125, 330, 331]). Figure 49b and c show the case where MAPI was combined with different fullerene derivatives in a p-i-n type architecture. Employing C_{60} led to a poor V_{OC} of only 1.03 V, indicating an unfavorable energy alignment. Indeed, inverse photoelectron spectroscopy (IPES) showed that the lowest unoccupied molecular orbital (LUMO) level of C_{60} lies below the conduction band minimum (CBM) of the MAPI, causing accumulation of electrons on the ETL. The energetic situation changes drastically when replacing C_{60} with the higher adduct fullerenes, where the LUMO now lies 0.6 eV above the CBM in case of ICTA. This inversion of the energy offset at the hybrid interface goes along with a significant improvement of the V_{OC}. Note that the LUMO positions were obtained by linear fits to the IPES spectra. These spectra also display a significant density of states below the specified LUMO position which may enable the efficient extraction of electrons even in case of PCBM, ICBA or ICTA. However, in contrast to the expectation from the interface energetics, the highest V_{OC} was realized by inserting an ultrathin polystyrene (PS) interlayer between MAPI and C_{60}. The reasons for this will be discussed below. More recently, higher adduct fullerenes have been used as ETLs in low bandgap mixed Pb-Sn-based perovskite solar cells, reaching an impressive V_{OC} of 0.89 V (at a radiative limit of 0.97V).[332] This was attributed to a better energy alignment and reduced non-radiative losses. Lastly, we note that one of the major recent efficiency advancements of n-i-p perovskite solar cells was achieved by introducing a novel, fluorene terminated hole transport material (which the authors called "DM"), with a higher ionization potential compared to the prototypical spiro-OMeTAD. The improved V_{OC} was attributed to the better alignment of the IP of the HTM and the valence band of the perovskite. This enabled a steady-state power conversion efficiency of 22.85% for small area cells and a certified PCE of 20.9% of a 1 cm^2 device (Figure 48d and e).[212] Despite these successes, several other experimental studies showed little to no correlation between the energy levels of the transport layers and the device V_{OC}[75, 333, 334]. For example, Belisle *et. al.* studied the correlation between the V_{OC} and the ionization potential (IP) of several hole transport layers in p-i-n cells. Despite the significant increase of the IP from 5.1 eV to 5.35 V, the V_{OC} remained at around 1 V (with one exception). This indicates that more research is necessary to understand the role of energy level alignment. We also note that the determination of the energy level alignment is an experimentally difficult task and the energetic at the hidden perovskite/CTL interface in the complete stack is generally not accessible by UPS and IPES. Recent experimental work also highlighted the role of band dispersion on the UPS spectra of polycrystalline perovskite samples.[335] Finally, the IP, electron affinity (EA) and work function of the perovskite has been shown to depend sensibly on the level of exposure to oxygen, water, and even light; this also includes the magnitude of surface band bending within the perovskites, induced by gap (defect) states. The key consideration in this regard is that the energy levels of the layers need to be measured in the actual cell stacks, as values of IP, EA, and work function determined for each individual material do not allow accurate estimation of the interfacial energy level alignment based on the Schottky-Mott limit. For example, several possible interfacial phenomena lead to a charge rearrangement - and therefore to modified energy levels - upon contact of two materials, ranging from the "push-back" effect in the physisorption regime, to Fermi level pinning at valence and conduction band edges, covalent interactions with polar character or band bending due to surface states[335]. In this regard, it is interesting to note that cross-sectional Kelvin probe measurements have been performed to quantify the local contact potential difference (LCPD, *i. e.* the difference in surface potential) across the whole cross-section of the devices, which was polished using a focused ion beam.[336, 337] If the sample is in the dark at SC, the Fermi-level is flat, meaning that under these conditions, KP measures the local work function long the sample cross-section. Illuminating the sample and/or increasing the bias causes a redistribution of charge (ions, electrons and holes) which becomes visible through changes in the local KP potential. The authors observed remarkably different LCPD distribution under short- and open-circuit conditions in cells with TiO_2 and C_{60} as ETLs. However, the question remains how the surface energetics (as created with the ion beam) compares to bulk properties of the film. Nevertheless, samples which are prepared in the same way can be compared which has provided useful insights that are difficult to assess otherwise.

Interfacial Optimizations: Interlayers, Graded Junctions and Doping

Other optimization strategies were often targeted at passivating traps at the perovskite surface[51, 85, 240, 338] or grain boundaries, or through the insertion of high bandgap interlayers between the perovskite and the CTL.[99, 177, 179, 289, 339] Examples of successfully applied interlayers to improve the V_{OC} include polystyrene (PS),[99, 339] Ga2O3,[179] choline chloride,[177] LiF[289], and Poly(methyl methacrylate) (PMMA),[240, 247] or most recently phenethylammonium iodide (PEAI)[340]. While qualitative explanations were suggested to explain the observed performance improvements, little is known how these interlayers work on a fundamental level. For example, a wide-gap interlayer may passivate defects, reduced across-interface recombination, or suppress the transfer of the minority carrier to the CTL, thereby suppressing recombination. In an ideal scenario, such strategies passivate surface traps and suppress the across-interface recombination by blocking the minority carriers from the interface while still allowing the majority carriers to efficiently tunnel through the barrier.[339] However, the addition of interlayers often comes at the price of charge extraction losses due to the series resistance of the interlayer. Another possibility to suppress recombination which is inspired by silicon solar cells, although much less exploited in the perovskite field, is to chemically dope the CTL or the perovskite in order to create a backfield which expels the minority carriers from the critical interface. For example, we have shown that adding SrI_2 into the perovskite precursor solution resulted in an n-doped perovskite surface which leads to a substantial improvement of the open-circuit voltage to 1.18 V in mixed quadruple cation perovskite cells (Figure 50d-f).[267] The V_{OC} could be further raised to 1.23 V by inserting an ultrathin layer of PS, however, at the price of FF losses as often the case with (wide-gap) interfacial layers. An attractive alternative approach is to engineer the perovskite bandgap at the interface to the CTL. For example, reduced recombination was attained by spin-coating a formamidinium bromide (FABr) precursor on an as-prepared mixed Br-poor perovskite, thereby forming a graded composition perovskite with a Br-enriched layer at the top surface. It was proposed that this higher bandgap top layer suppresses the transfer of electrons to the HTM, with the result of a substantial increase of the V_{OC} from 1.1 V to 1.16 V.[154] More recently, Luo *et. al.* [293] employed a similar secondary growth technique to create a perovskite surface layer with a wider bandgap and a more n-type character. Optimized p-i-n-type cells had a V_{OC} of 1.21 V, only 0.41 V lower than the bandgap of 1.62 V (Figure 50a-c).

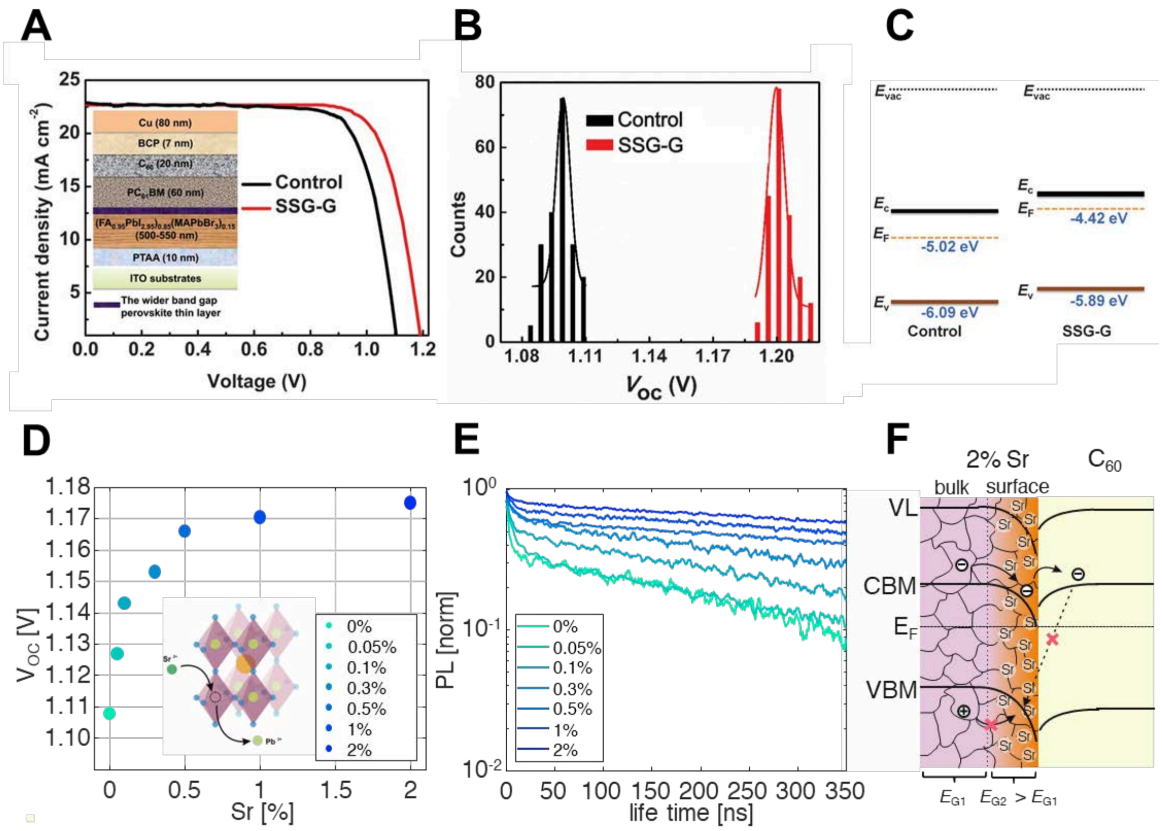

Figure 50: A-C) J-V characteristics of p-i-n solar cells fabricated based on a "secondary perovskite growth approach (SSG-G)" which creates a perovskite surface with a larger bandgap and a more n-type character, both resulting in large V_{OC} gains (B). D-F) Addition of SrI_2 into the precursor solution led to a significant increase in V_{OC} (D) and TRPL lifetime (E) of quadruple cation perovskite cells. F) Energy levels as obtained from UPS measurements which demonstrated the formation of a back-surface field which reduces interfacial recombination by repelling photogenerated minority carriers from the interface. A-C) Adapted with permission.[293] Copyright 2018, AAAS. D-F) Adapted with permission.[169] Copyright 2019, the Royal Society of Chemistry.

8.7 OVERCOMING INTERFACIAL RECOMBINATION

Although more complicated perovskite including multiple cation/and or halide are becoming more and more popular across the community, the standard MAPI perovskite remains subject of substantial research, particularly for (co-) evaporated solar cells.[182] Today, record MAPI cells have allowed efficiencies above 21% PCE.[341] Moreover, as discussed above, MAPI exhibits potentially the largest QFLS close to the thermodynamic efficiency limit if the top surface is properly passivated as shown in Figure 39.[51] In this regard, Liu *et. al.* [225] could recently add an extraordinary result. A special MAPI recipe based on lead acetate enabled perovskite cells with record open-circuit voltages of 1.26 V (with a bandgap of 1.6 eV) after a light soaking for 10 minutes. The JV-scans of the corresponding solar cells are shown in Figure 51a. Notably, an external PLQY of ~8% was demonstrated in perovskite films passivated with TOPO, in the full p-i-n stack (PTAA/MAPI/PCBM) and the final device, leaving the devices with only 60 mV loss in V_{OC} compared to the radiative limit. This result stands out not only because of its extraordinary low voltage loss, but also because such performance was realized by optimizing the preparation scheme for the active absorber and the PCBM transport layer, leaving the chemical composition of the constituents unaffected. PCBM is generally considered to induce significant non-radiative losses (see above). For example, our comparison of MAPI devices with different fullerene-based ETLs[99] suggested that the inferior V_{OC} of PCBM-containing cells is intrinsic to the system and related to its fairly high electron affinity (and possibly too low ionization potential). The very high V_{OC} in the work by Liu *et. al.* , where the PCBM was coated directly onto an as-prepared perovskite, questions this simple picture and asks for a detailed analysis of the chemical and energetic structure at the interface. For example, Huang and coworkers[277] showed that post-deposition solvent annealing of the electron transport layer (PCBM) caused a significant increase in the V_{OC}. By combining results from X-ray and IS, the authors proposed that solvent annealing improves the structural order in the fullerene-based ETL, thereby reducing the energetic disorder and the density of low energy states in the ETL. In an alternative approach Jiang *et. al.* [340] reduced losses at the perovskite/Spiro-OMeTAD interface in n-i-p cells by spin-coating a thin phenethylammonium iodide layer (PEAI). It was proposed that this procedure passivates the perovskite and thereby reduces non-radiative recombination at the top surface. Consequently, they realized an $\mathrm{EQE}_{\mathrm{EL}}$ of 7% (at $J_{\mathrm{inj.}}$=24mA cm^{-2} injection, shown in Figure 51d), corresponding to a voltage deficit of only ~70 mV.[340] Other examples include secondary phases at the top and or bottom surface[154, 267, 293], polymeric[99, 240, 339], salt[85, 339, 342] or molecular[311, 343] passivation. These are only a few demonstrations where interfacial recombination was significantly reduced.

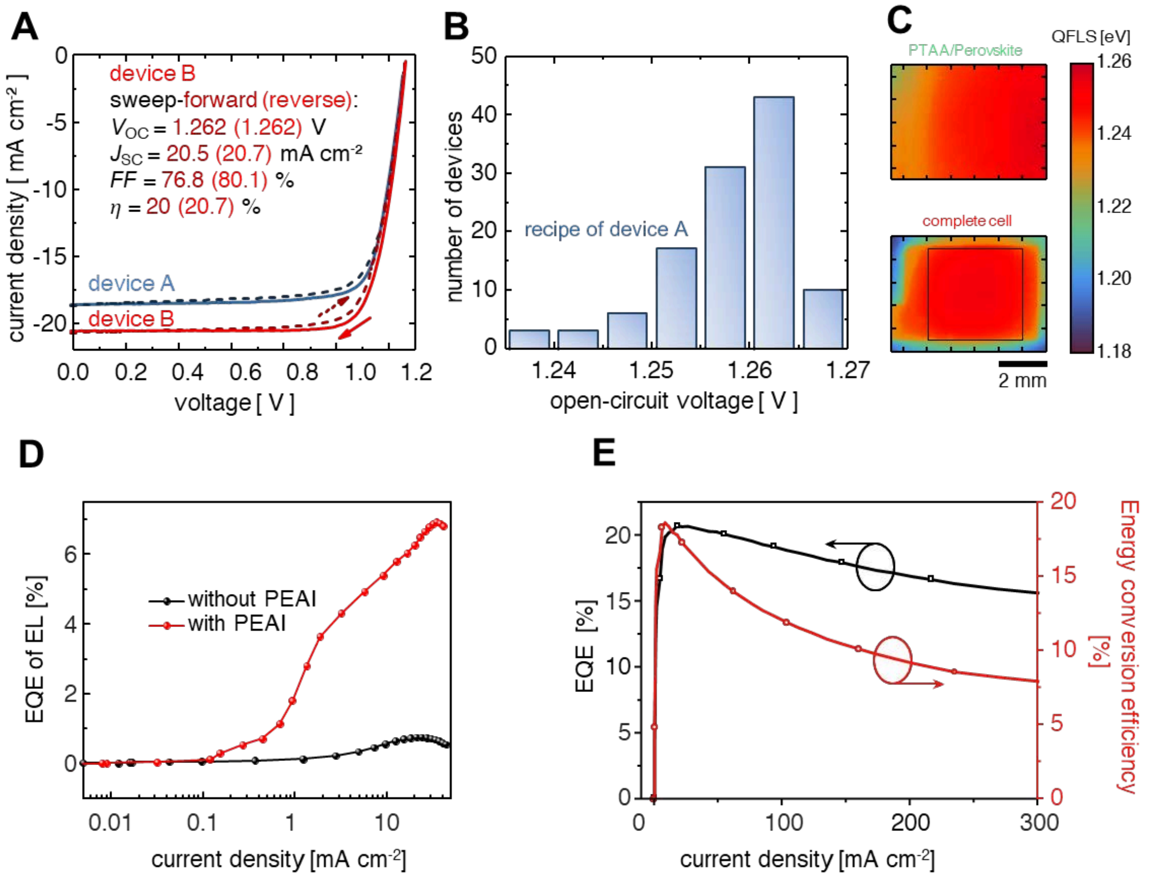

Figure 51: A,B) Liu *et. al.* [225] recently showed very high open-circuit voltages of 1.26 V for methylammonium lead iodide perovskite cells. C) The PL quantum efficiency (PLQY) of the complete solar cell was quantified to be 8%, which was equal to the PLQY of the perovskite absorber layer, thus enabling a quasi-Fermi level splitting of 1.26 eV in the cells. D) n-i-p structured perovskite solar cell passivated with PEAI that exhibits an $\mathrm{EQE}_{\mathrm{EL}}$ of 6% at 20 mA cm^{-2}. E) Perovskite LED based on micrometer-structured perovskite layers with LED efficiencies up to 20.7%. A-C) Adapted with permission.[225] Copyright 2018, American Chemical Society. D) Adapted with permission.[340] Copyright 2018, Springer Nature. E) Adapted with permission.[262] Copyright 2019, Springer Nature.

Overall, we conclude that the V_{OC} will be primarily limited by 1) unfavorable energy alignment, which can cause large V_{OC} losses through a mismatch between the internal QFLS and the external V_{OC}. 2) defect recombination at the interfaces or 3) in the perovskite or 4) by a low probability of photons to leave the cell. This is because the externally measurable luminescence efficiency and in turn the open-circuit voltage is reduced through a reduced emission probability. We consequently expect four main strategies that will allow further improvements: 1) Proper energy level matching between the perovskite and the transport layers; 2) reduction of interfacial recombination efficient contact layer passivation or design thereby; 3) optimization of the perovskite layer *e. g.* with secondary interfacial phases that passivate the bulk and the surfaces; and finally 4) optical management strategies facilitating light trapping and enhancing light-outcoupling. We predict, that in the near future, optical management[62, 273, 344] will play a significant role and could push external PLQYs in full devices to values of GaAs solar cells (22.5%) and beyond.[345] Exemplary, by optimizing light outcoupling [62, 278, 346, 347] and reducing non-radiative recombination, red-emitting perovskite LEDs - with transport layers feasible for solar cells - have now surpassed 20% emission efficiency at low injection levels comparable to 1 sun illumination ($J_{inj.}$= 18 mA cm^{-2}, Figure 51e)[262]. We believe that solar cells with even higher external luminescent efficiencies - and therefor V_{OC} and PCE - are well within reach. Although the exact mechanism behind the high V_{OC}s in these devices remains to be fully understood and transferred into highly stable devices, it underlines the great potential of perovskite solar cells when essentially overcoming interfacial/surface recombination.

CONCLUSIONS After 10 years of research, the perovskite solar cell community has experienced incredible efficiency improvements from 3.9% to 24% in single-junction cells and 28% in tandem solar cells with a Si bottom cell. Alongside this rapid improvement, the community has reached a considerable understanding of the photophysical properties of the perovskite and the device operation. This progress report demonstrates recent advances in pinpointing the origin of non-radiative recombination losses in the perovskite bulk, the perovskite/CTL interfaces and/or metal contacts through measurement of the absolute PL emitted from perovskite films with and without transport layers. These measurements reveal that the perovskite bulk would allow a QFLS that is very close to the thermodynamic limits and demonstrate that non-radiative recombination at the perovskite/CTL interfaces can consistently explain the open-circuit voltage losses of perovskite cells in n-i-p and p-i-n configurations and for a wide range of transport layers. Intriguingly, improving the perovskite bulk will not result in further efficiency improvements if the interfaces do not improve concurrently. In fact, both interfaces need to be simultaneously optimized, though it has also been shown that the majority of recombination losses in highly-efficient devices happen at the top surface/interface (*i. e.* perovskite/fullerene or perovskite/spiro-OMeTAD in case of p-i-n of n-i-p devices, respectively). These conclusions are solid, as the intensity of the emitted PL is ultimately only reduced by non-radiative recombination losses. Therefore, the quality of each interface in the perovskite solar cell stack can be readily checked by comparing the QFLS of perovskite films with and without the transport layers. Measurements on several efficient solar cells in p-i-n and n-i-p configuration further reveal a match between the internal and the external QFLS (*i. e.* the V_{OC}) which indicates an alignment between the energy levels of the perovskite absorber and the CTLs. However, in less efficient cells with PEDOT:PSS and P3HT HTLs at the bottom, the QFLS can be larger than the V_{OC} due to energy level offsets across the interfaces. Although the absolute QFLS-PL approach allows quantifying the recombination currents in the bulk, interfaces or metal contacts, the precise recombination pathway at the interfaces remains poorly understood today. Sophisticated all-optical transient and electro-optical measurement techniques such as TRPL, TRMC, THz, and TAS have enabled the community insights into the ultrafast processes of charge recombination within the perovskite bulk and interfaces and charge transfer to the transport layers. This allowed quantification of transfer rates and recombination rate constants which can consistently describe the V_{OC} of the final cells. Although much less employed today, TAS allows to asses even faster timescales and suggest ultrafast charge transport (<1 ps) into standard CTL such as PEDOT:PSS or PCBM which would be invisible to transient PL measurements that are based on the concept of time-correlated single-photon counting. However, further research is required to cross-check results obtained from different transient methodologies. Lastly, among the most debated topics in the field remain the impact of energy level alignment at the interfaces and its impact on cell performance. Although aligned perovskite/CTL energy levels are expected to be highly beneficial from basic considerations of charge accumulation and interfacial recombination, experimental evidence does not fully support these conclusions which we believe that is related to difficulties in assessing the true energy levels in the operational solar cells. Going forward, multiple promising optimization strategies have been recently proposed to further suppress non-radiative recombination. As such, it was recently demonstrated how to overcome interfacial recombination in MAPI and $MAFAPbI_3$ based perovskite cells. In the coming years, an improved understanding of the mechanisms that enable suppressed interfacial recombination will allow designing passivation strategies and new transport layers ideally suited for perovskite solar cells. Combining these strategies with elaborate light-management will pave the way to surpass the efficiencies of monocrystalline silicon cells in the near future.

[285] Kenji Yamamoto et al. "High-efficiency heterojunction crystalline Si solar cells." In: *Japanese Journal of Applied Physics* 57.8S3 (Aug. 2018), 08RB20 (cit. on p. 110).

[286] Steve Albrecht et al. "Towards optical optimization of planar monolithic perovskite / silicon-heterojunction tandem solar cells." In: *Journal of Optics* 18.6 (2016), pp. 1–10 (cit. on p. 110).

[287] Oxford PV. *Oxford PV sets world record for perovskite solar cell*. 2018 (cit. on p. 110).

[288] Moritz H Futscher and Bruno Ehrler. "Modeling the Performance Limitations and Prospects of Perovskite/Si Tandem Solar Cells under Realistic Operating Conditions." In: *ACS Energy Letters* 2.9 (2017), pp. 2089–2095 (cit. on p. 110).

[289] Martin Stolterfoht et al. "The perovskite/transport layer interfaces dominate non-radiative recombination in efficient perovskite solar cells." In: *arXiv.org* (Oct. 2018) (cit. on pp. 110, 112, 116, 118, 120, 129).

[290] Wolfgang Tress et al. "Interpretation and evolution of open-circuit voltage, recombination, ideality factor and subgap defect states during reversible light-soaking and irreversible degradation of perovskite solar cells." In: *Energy and Environmental Science* 11.1 (2018), pp. 151–165 (cit. on pp. 110, 112, 113).

[291] Dongqin Bi et al. "High-Performance Perovskite Solar Cells with Enhanced Environmental Stability Based on Amphiphile-Modified CH 3 NH 3 PbI 3." In: *Advanced Materials* (2016), n/a–n/a (cit. on p. 110).

[292] Minyu Xiao et al. "Understanding Molecular Structures of Buried Interfaces in Halide Perovskite Photovoltaic Devices Nondestructively with Sub-Monolayer Sensitivity Using Sum Frequency Generation Vibrational Spectroscopy." In: *Advanced Energy Materials* (Nov. 2019), p. 1903053 (cit. on pp. 110, 138).

[293] Deying Luo et al. "Enhanced photovoltage for inverted planar heterojunction perovskite solar cells." In: *Science* 360.6396 (June 2018), pp. 1442–1446 (cit. on pp. 111, 119, 129–131).

[294] Lukas Kegelmann et al. "Mixtures of Dopant-Free Spiro-OMeTAD and Water-Free PEDOT as a Passivating Hole Contact in Perovskite Solar Cells." In: *ACS Applied Materials & Interfaces* 11.9 (Mar. 2019), pp. 9172–9181 (cit. on p. 111).

[295] Thomas Kirchartz et al. "Sensitivity of the Mott-Schottky analysis in organic solar cells." In: *The Journal of Physical Chemistry C* 116.14 (2012), pp. 7672–7680 (cit. on pp. 112, 113).

[296] Bo Wu et al. "Charge Accumulation and Hysteresis in Perovskite-Based Solar Cells: An Electro-Optical Analysis." In: *Advanced Energy Materials* (2015), n/a–n/a (cit. on p. 112).

[297] Carsten Deibel, Thomas Strobel, and Vladimir Dyakonov. "Origin of the Efficient Polaron-Pair Dissociation in Polymer-Fullerene Blends." In: *Phys. Rev. Lett.* 103.3 (July 2009), p. 36402 (cit. on p. 113).

[298] Uli Würfel et al. "Recombination between Photogenerated and Electrode-Induced Charges Dominates the Fill Factor Losses in Optimized Organic Solar Cells." In: *The Journal of Physical Chemistry Letters* 10.12 (June 2019), pp. 3473–3480 (cit. on p. 113).

[299] Andreas Hofacker and Dieter Neher. "Dispersive and steady-state recombination in organic disordered semiconductors." In: *Physical Review B* 96.24 (Dec. 2017), p. 245204 (cit. on p. 113).

[300] Phil Calado et al. "Identifying Dominant Recombination Mechanisms in Perovskite Solar Cells by Measuring the Transient Ideality Factor." In: *Physical Review Applied* 11.4 (Apr. 2019), p. 044005 (cit. on p. 114).

[301] Adam Pockett et al. “Characterization of Planar Lead Halide Perovskite Solar Cells by Impedance Spectroscopy, Open-Circuit Photovoltage Decay, and Intensity-Modulated Photovoltage/Photocurrent Spectroscopy.” In: *The Journal of Physical Chemistry C* 119 (2015), pp. 3456–3465 (cit. on p. 114).

[302] Isaac Zarazua et al. “Surface Recombination and Collection Efficiency in Perovskite Solar Cells from Impedance Analysis.” In: *The Journal of Physical Chemistry Letters* 7.24 (Dec. 2016), pp. 5105–5113 (cit. on p. 114).

[303] Victoria Gonzalez-Pedro et al. “General working principles of CH3NH3PbX3 perovskite solar cells.” In: *Nano Letters* 14.2 (2014), pp. 888–893 (cit. on p. 114).

[304] Qiong Wang et al. “Rationalizing the Molecular Design of Hole-Selective Contacts to Improve Charge Extraction in Perovskite Solar Cells.” In: *Advanced Energy Materials* 9.28 (July 2019), p. 1900990 (cit. on pp. 114, 121, 123, 124).

[305] a. Baumann et al. “Persistent photovoltage in methylammonium lead iodide perovskite solar cells.” In: *APL Materials* 2.8 (2014), p. 081501 (cit. on p. 116).

[306] Christian Wehrenfennig et al. “Charge-Carrier Dynamics in Vapour-Deposited Films of the Organolead Halide Perovskite CH3NH3PbI3- xClx.” In: *Energy & Environmental Science* 7 (2014), p. 2269 (cit. on p. 116).

[307] Aboma Merdasa et al. “Impact of Excess Lead Iodide on the Recombination Kinetics in Metal Halide Perovskites.” In: *ACS Energy Letters* 4.6 (June 2019), pp. 1370–1378 (cit. on p. 116).

[308] Liudmila G. Kudriashova et al. “Impact of Interfaces and Laser Repetition Rate on Photocarrier Dynamics in Lead Halide Perovskites.” In: *The Journal of Physical Chemistry Letters* 8.19 (Oct. 2017), pp. 4698–4703 (cit. on p. 116).

[309] Thomas Unold and Levent Gütay. “Photoluminescence Analysis of Thin-Film Solar Cells.” In: *Advanced Characterization Techniques for Thin Film Solar Cells*. Weinheim, Germany: Wiley-VCH Verlag GmbH & Co. KGaA, Apr. 2011, pp. 151–175 (cit. on p. 116).

[310] C. Donolato. “A reciprocity theorem for charge collection.” In: *Applied Physics Letters* 46.3 (Feb. 1985), pp. 270–272 (cit. on p. 117).

[311] Shuang Yang et al. “Tailoring Passivation Molecular Structures for Extremely Small Open-Circuit Voltage Loss in Perovskite Solar Cells.” In: *Journal of the American Chemical Society* 141.14 (Apr. 2019), pp. 5781–5787 (cit. on pp. 119, 131).

[312] Pascal Becker et al. “Low Temperature Synthesis of Stable γ-CsPbI ₃ Perovskite Layers for Solar Cells Obtained by High Throughput Experimentation.” In: *Advanced Energy Materials* 9.22 (June 2019), p. 1900555 (cit. on p. 119).

[313] Steffen Braunger et al. “Cs x FA 1- x Pb(I 1- y Br y) 3 Perovskite Compositions: the Appearance of Wrinkled Morphology and its Impact on Solar Cell Performance.” In: *The Journal of Physical Chemistry C* 122.30 (Aug. 2018), pp. 17123–17135 (cit. on p. 119).

[314] Antonio Cabas-Vidani et al. “High-Efficiency (Li x Cu 1-x) 2 ZnSn(S,Se) 4 Kesterite Solar Cells with Lithium Alloying.” In: *Advanced Energy Materials* 8.34 (Dec. 2018), p. 1801191 (cit. on p. 119).

[315] José Márquez et al. “Chemistry and Dynamics of Ge in Kesterite: Toward Band-Gap-Graded Absorbers.” In: *Chemistry of Materials* 29.21 (Nov. 2017), pp. 9399–9406 (cit. on p. 119).

[316] S. Levcenko et al. “Deep Defects in Cu2ZnSn (S,Se)4 Solar Cells with Varying Se Content.” In: *Physical Review Applied* 5.2 (Feb. 2016), p. 024004 (cit. on p. 119).

[317] Johannes Benduhn et al. “Intrinsic non-radiative voltage losses in fullerene-based organic solar cells.” In: *Nature Energy* 2.6 (June 2017), p. 17053 (cit. on p. 121).

[318] Dengyang Guo et al. “Comparing the Calculated Fermi Level Splitting with the Open-Circuit Voltage in Various Perovskite Cells.” In: *ACS Energy Letters* 4.4 (Apr. 2019), pp. 855–860 (cit. on p. 121).

[319] Shanshan Zhang et al. “The Role of Bulk and Interface Recombination in High-Efficiency Low-Dimensional Perovskite Solar Cells.” In: *Advanced Materials* 31.30 (June 2019), p. 1901090 (cit. on p. 121).

[320] Eli Yablonovitch. *Science of Solar Cells*. 2013 (cit. on p. 121).

[321] Lukas Kegelmann et al. “It Takes Two to Tango—Double-Layer Selective Contacts in Perovskite Solar Cells for Improved Device Performance and Reduced Hysteresis.” In: *ACS Applied Materials & Interfaces* 9.20 (May 2017), pp. 17245–17255 (cit. on p. 123).

[322] Giulia Grancini et al. “Femtosecond Charge-Injection Dynamics at Hybrid Perovskite Interfaces.” In: *ChemPhysChem* 18.17 (2017), pp. 2381–2389 (cit. on p. 123).

[323] Jonas Horn et al. “Direct Observation of Charge Injection From CH 3 NH 3 PbI 3-x Cl x to Organic Semiconductors Monitored With sub-ps Transient Absorption Spectroscopy.” In: *Physica Status Solidi (B) Basic Research* 256.3 (2019), pp. 1–7 (cit. on pp. 123, 125, 126).

[324] C. S. Ponseca Jr. and V. Sundström. “Revealing the ultrafast charge carrier dynamics in organo metal halide perovskite solar cell materials using time resolved THz spectroscopy.” In: *Nanoscale* 8.12 (2016), pp. 6249–6257 (cit. on p. 123).

[325] Tom J Savenije et al. “Revealing the Dynamics of Charge Carriers in Polymer:Fullerene Blends Using Photoinduced Time-Resolved Microwave Conductivity.” In: *J Phys Chem C* 117.46 (2013), pp. 24085–24103 (cit. on p. 124).

[326] Michael B. Price et al. “Hot-carrier cooling and photoinduced refractive index changes in organic–inorganic lead halide perovskites.” In: *Nature Communications* 6.1 (Sept. 2015), p. 8420 (cit. on p. 125).

[327] Piotr Piatkowski et al. “Direct Monitoring of Ultrafast Electron and Hole Dynamics in Perovskite Solar Cells.” In: *Phys. Chem. Chem. Phys.* (2015) (cit. on p. 125).

[328] Annika Spies et al. “On the Impact of Contact Selectivity and Charge Transport on the Open-Circuit Voltage of Organic Solar Cells.” In: *Advanced Energy Materials* 7.5 (Mar. 2017) (cit. on p. 126).

[329] Philip Schulz et al. “Interface energetics in organo-metal halide perovskite-based photovoltaic cells.” In: *Energy & Environmental Science* 7.4 (2014), p. 1377 (cit. on p. 127).

[330] Qi Wang et al. “Large fill-factor bilayer iodine perovskite solar cells fabricated by a low-temperature solution-process.” In: *Energy & Environmental Science* 7.7 (2014), p. 2359 (cit. on p. 127).

[331] Qianqian Lin et al. “Electro-optics of perovskite solar cells.” In: *Nature Photonics* 9.December (2014), pp. 106–112 (cit. on p. 127).

[332] Adharsh Rajagopal et al. “Defect Passivation via a Graded Fullerene Heterojunction in Low-Bandgap Pb–Sn Binary Perovskite Photovoltaics.” In: *ACS Energy Letters* 2.11 (Nov. 2017), pp. 2531–2539 (cit. on p. 128).

[333] Zhurong Liang et al. “Large grain size perovskite thin film with dense structure for planar heterojunction solar cells via spray deposition under ambient condition.” In: *RSC Advances* 5 (2015), pp. 60562–60569 (cit. on p. 128).

[334] Cheng Bi et al. “Non-wetting surface-driven high-aspect-ratio crystalline grain growth for efficient hybrid perovskite solar cells.” In: *Nature Communications* 6.1 (Nov. 2015), pp. 1–7 (cit. on p. 128).

[335] Fengshuo Zu et al. “Constructing the Electronic Structure of CH 3 NH 3 PbI 3 and CH 3 NH 3 PbBr 3 Perovskite Thin Films from Single-Crystal Band Structure Measurements.” In: *Journal of Physical Chemistry Letters* 10.3 (Feb. 2019), pp. 601–609 (cit. on p. 128).

[336] Ilka M. Hermes et al. “The Interplay of Contact Layers: How the Electron Transport Layer Influences Interfacial Recombination and Hole Extraction in Perovskite Solar Cells.” In: *Journal of Physical Chemistry Letters* 9.21 (2018), pp. 6249–6256 (cit. on p. 128).

[337] Stefan A.L. Weber et al. “How the formation of interfacial charge causes hysteresis in perovskite solar cells.” In: *Energy and Environmental Science* 11.9 (2018), pp. 2404–2413 (cit. on p. 128).

[338] Adharsh Rajagopal et al. “Overcoming the Photovoltage Plateau in Large Bandgap Perovskite Photovoltaics.” In: *Nano Letters* 18.6 (2018), pp. 3985–3993 (cit. on p. 129).

[339] Mingchao Wang and Shangchao Lin. “Anisotropic and Ultralow Phonon Thermal Transport in Organic-Inorganic Hybrid Perovskites: Atomistic Insights into Solar Cell Thermal Management and Thermoelectric Energy Conversion Efficiency.” In: *Advanced Functional Materials* (May 2016) (cit. on pp. 129, 131).

[340] Qi Jiang et al. “Surface passivation of perovskite film for efficient solar cells.” In: *Nature Photonics* (2019) (cit. on pp. 129, 131, 132).

[341] Seong Sik Shin et al. “Colloidally prepared La-doped BaSnO 3 electrodes for efficient, photostable perovskite solar cells.” In: *Science* 356.6334 (Apr. 2017), pp. 167–171 (cit. on p. 130).

[342] Dongbing Zhao et al. “Hexaazatrinaphthylene Derivatives: Efficient Electron-Transporting Materials with Tunable Energy Levels for Inverted Perovskite Solar Cells.” In: *Angewandte Chemie International Edition* (June 2016) (cit. on p. 131).

[343] Dongqin Bi et al. “Multifunctional molecular modulators for perovskite solar cells with over 20% efficiency and high operational stability.” In: *Nature Communications* 9.1 (Dec. 2018), p. 4482 (cit. on p. 131).

[344] Marko Jošt et al. “Efficient Light Management by Textured Nanoimprinted Layers for Perovskite Solar Cells.” In: *ACS Photonics* (Apr. 2017), acsphotonics.7b00138 (cit. on p. 132).

[345] Martin A. Green. “Radiative efficiency of state-of-the-art photovoltaic cells.” In: *Progress in Photovoltaics: Research and Applications* 20.4 (June 2012), pp. 472–476 (cit. on p. 132).

[346] Emily D Kosten et al. “Highly efficient GaAs solar cells by limiting light emission angle.” In: *Light: Science & Applications* 2.1 (Jan. 2013), e45–e45 (cit. on p. 132).

[347] Florian Staub et al. “Manipulating the Net Radiative Recombination Rate in Lead Halide Perovskite Films by Modification of Light Outcoupling.” In: *Journal of Physical Chemistry Letters* 8.20 (Oct. 2017), pp. 5084–5090 (cit. on p. 132).

CONCLUSION

This thesis focuses on the identification and suppression of efficiency and stability losses in inverted (p-i-n) perovskite solar cells. At the heart of all investigations lies the critical role of interfacial phenomena, responsible for recombination losses and instability. Different interlayers have been introduced to address these interfaces, enabling highly efficient and stable devices above the state-of-the-art. The impact of energy level alignment in comparison to charge-blocking layers has been thoroughly studied in Chapter 3. Through a detailed analysis of energetics (photoemission studies), optoelectronic characteristics such as JV, $\mathrm{EQE}_{\mathrm{PV}}$, $\mathrm{EQE}_{\mathrm{EL}}$ and intensity dependent $\mathrm{EQE}_{\mathrm{EL}}$ & V_{OC}/J_{SC} a comprehensive picture of the dominant recombination at the ETL/perovskite interface was derived. Firstly, it was clearly shown that luminescence under current injection (EL) or open-circuit (PL) is a highly desirable quantity in contrast to many reports at the time (and to date). Secondly, simple energy level alignment is not sufficient to explain the difference observed primarily in V_{OC}. This is in part due to the comparably broad DOS distribution of fullerene acceptor states (*i. e.* LUMO or HOMO DOS), reaching far into the bandgap of the perovskite. The LUMO distribution is highly relevant as lower lying states will enable a higher density of electrons at the interface, accelerating recombination, so that a larger offset w.r.t. the conduction band minimum of the perovskite, the faster the recombination. Likewise a small offset (comparing VBM (perovskite) and HOMO (fullerene)) and again DOS - tailing into the bandgap of the perovskite facilitate also hole extraction into the fullerene, where a low dielectric constant and a high density of vibrational relaxation pathways facilitate nonradiative recombination. To overcome this limitation a thin layer of polystyrene was interjected between the perovskite and C_{60}, which in turn reduced the electron and hole extraction and the subsequent recombination enhancing the V_{OC} from ~1.05V up to 1.16V, which also manifested in high electroluminescent efficiencies ~0.3%, overall allowing >19% efficient devices. In essence, C_{60} and PCBM are found not to be ideal transport layers by themselves, as they facilitate nonradiative recombination at the perovskite/ETL interface. This conclusion was challenged by recent findings by Liu *et. al.* [225], where a V_{OC} of 1.26V is achieved. The contradicting findings can however be explained when looking into details of the mentioned study by Liu *et. al.* : The high performance and V_{OC} is only obtained upon extensive light-soaking for a very specific perovskite composition including lead chloride and lead acetate. Since the fullerene interface is the limiting one in these devices[99, 171, 216], doping the electron transport layer would allow to repel holes from that interface, improving charge separation[268]. Iodine and chlorine are well-known to dope fullerenes, which is likely the reason for these findings, especially considering the likewise rapid degradation of the cells upon illumination. The question, to which extend energy level alignment is important is still a debated topic, complicated by the fact the interfaces are usually not accessible – or hidden – in completed cells and therefore reliable energy level alignment diagrams are inherently hidden, too. New techniques such as *e. g.* sum-frequency generation[292] approach this difficult question. Nevertheless, identifying the inferior interface in the sense of a higher recombination current eventually is able to explain the ambiguity in the relevance of transport layer energetics. In fact, a study similar to the one in Chapter 3 was carrier out using PEDOT:PSS as a HTL[76], where the V_{OC} was practically unchanged, when looking at the same four fullerenes: C_{60}, PCBM, ICBA and ICTA. This can be then understood, as in this case the HTL interface was limiting the V_{OC}, so that recombination at the ETL interface is not the bottleneck, masking the effects the energetics have.

The flexibility of fabricating perovskite layers from various routes including thermal evaporation, multiple solution-processes, redox-driven lead transformation, mechanical grinding and many more is considered a big asset of halide perovskites. Without a doubt, easy and cheap fabrication is a key prerequisite, when aiming at commercialization, especially considering the development of *e. g.* silicon photovoltaics fabrication prices over the last four decades. At the same time this opens the possibility of extreme lab-to-lab variations, inducing possibly contradicting results, despite having seemingly the "same" perovskite at the center of studied devices. The ambiguity is further amplified, when considering the myriad of (organic) transport layers and fabrication routes thereof. Unarguably, fundamental properties may be studied without having the highest efficiency devices, but several critical aspects must be taken into account. These include *e. g.* electronically or electrochemically active defects that may accelerate degradation or ionic movement. To improve reproducibility detailed protocols of the fabrication methods are imperative and Chapter 4 describes the methods we developed at University Potsdam in great detail, including critical details and pitfalls during the fabrication steps of highly efficient (>20%) p-i-n type solar cells. These include the use of fresh precursor materials, high control over environmental factors such as glovebox temperature (<28°C) and atmosphere (low H_2 and O_2 levels ~1ppm), control over solution aging (< 1 week), atmospheric contamination with solvent vapors (predominantly DMF & DMSO), but also the importance of practical experience and a *trained eye* to spot small differences along a typically long learning curve. We present detailed statistics of all device parameters over the course of years, which allow to identify systemic problems that are likely to occur in complex precursor solutions, where the perovskite precursor alone already contains five salts, dissolved in two solvents. Even when taking all these factors into account underperforming batches may still occur, although obvious mistakes are often easily spotted, which emphasizes the importance of experience. Currently an important debate is revolving around reliable test protocols, where a big group of researchers has reached a certain consensus to follow ISOS protocols when reporting solar cell stability data in future. This development should expand towards methods that enable to assess the quality of *e. g.* the perovskite only, when aiming to perform fundamental research but is currently missing. At the core of all these considerations are the fabrication protocols, which – in future – need to be made even more robust and described in even greater detail and novel media formats such as videos of critical steps are likely to improve reproducibility and further efficiency gains in the coming years.

When seeking to commercialize any solar technology scaling the device area from typically mm^2 on lab-scale to at least cm^2 is imperative. The produced current scales linearly with area and so resistive losses become increasingly important. In this sense it is important to eliminate parasitic resistances by limiting the distance current has to traverse through the constituent with the highest resistivity. In [176], we identified that the low mobility PTAA represents the lowest conductivity and reduced the imposed resistance to a bare minimum by thinning the undoped layer down to <10nm, where then the TCO (ITO) became the obstacle. In Chapter 5, the limitation of ITO was addressed, focusing in particular on devices with an active area of $1cm^2$, albeit the results can be generalized to bigger active areas (not including scribing losses). By varying the aspect ratio of the fixed area and calculating the resulting series resistances, we found that a low aspect ratio, *i. e.* short distances through the ITO is crucial and more important than decreasing the resistivity, *e. g.* through a thicker TCO. Consequently, scaling the active area from $6mm^2$ to $1cm^2$ was possible without appreciable transport losses, *i. e.* maintaining high fill factors ~80%. Irrespective of the device area, after the fabrication of either a neat absorber or a (half-finished) solar cell stack a remaining obstacle is then to identify where in a device losses occur. Much in the same way as above, a reliable technique is a prerequisite to then aim at reducing any given losses. In this context a popular technique in the field of perovskite research is TRPL, but the information gained is often obstructed by technical limitations and dynamical processes upon pulsed laser excitation may not be representative of the electrostatics within the solar cell under operation, irrespective of the working point (*e. g.* at V_{OC} or V_{MPP}). To remove this ambiguity we introduced a previously overseen technique that allows to deduce the maximum obtainable QFLS by definition in steady-state: absolute PL. Here in particular in an imaging mode that enables to obtain hyperspectral maps of the perovskite with and without transport layers or electrodes. In relating the PLQY to the QFLS, we identified 1. the perovskite layer allows for a QFLS~1.22eV and 2. that the transport layers, in particular C_{60}, impose a voltage loss in the device, limiting the V_{OC} to ~1.1V. The reduction of PLQY was in accord with faster TRPL decays, especially when exciting ~10^{15}cm^{-3}. Importantly, the losses in the device V_{OC} are not a superposition of the individual losses, but impact the V_{OC} through the logarithm of the sum of the nonradiative currents they induce. This is important, since in the case of equally "bad" interfaces on both sides addressing only one interface or the bulk of the perovskite will not result in appreciable gains. Consequently, we introduced interlayers at both interfaces (PFN-P2 at the HTL-side and LiF at the ETL-side) and thereby increased the QFLS and with the the V_{OC} by ~70 m(e)V. This came with prolonged TRPL decays and increasing PLQYs by ~one order of magnitude. With the improved interfaces and the lessons learned to scale the active area, we fabricated 20% 1cm^2 devices, which were certified to 19.83% by Fraunhofer ISE, which was the highest reported value at the time.

Apart from efficiency and fabrication cost a third cornerstone for commercial relevance of any photovoltaic technology is its operational stability. Perovskite layers have been shown to degrade under several relevant conditions including heat, illumination, moisture, electrical load or a combination thereof. In particular the volatile nature of the organic cations in the perovskite have been identified as the weakest link in the devices. Ideally an interlayer would be able to block the escape of the volatile species and repel harming molecules – especially at elevated temperatures or in moist conditions – while maintaining or even improving device performance. In Chapter 6 we introduce a family of self-assembled monolayers (SAMs) that are deposited atop of the perovskite and act as an interlayer between the perovskite and C_{60}. The SAMs are based on a perfluorinated backbone and a halogenated binding moiety ($CF_3(CF_2)_{n-1}X$, where X is I/Br and n=7-12). Similarly to PS in Chapter 3 and LiF in Chapter 5 the interlayers reduce the nonradiative losses at the perovskite/C_{60} interface, with increasing length of the backbone, thereby allowing higher V_{OC}s that are rigorously confirmed by higher PLQYs, ELQYs and prolonged TRPL decays. Up to a threshold of n=10 the fill-factor is not impacted (with iodine as binding moiety), so that the overall efficiency is improved by ~1% absolute, reaching 21.3% for $CF_3(CF_2)_9 - I$, $IPFC_{10}$. When characterizing the perovskite surface, we find that the molecules mildly bind to the surface via halogen-bonding and increase the contact-angle of isopropanol to ~90°. Repelling the ingress of polar solvents that may dissolve parts of the perovskite is likely a consequence of the perfluorinated backbone and manifests in a drastically improved shelf-stability (>95%, when stored in the dark in ambient, ISOS-D1), where water molecules are less likely to penetrate through the SAM layer. We further detected that a mixture of $IPFC_{10}$ and MAI showed a higher resistance to heat, evident from a ~15°C increase in dissociation temperature as measured from DSC. This encouraged us to perform a harsh heat-light-load stress test on one of the most efficient devices, where the solar cells are MPP-tracked under white-light illumination at 85°C (ISOS-L2). The reference device quickly degrade to <5% within 30h, while the $IPFC_{10}$-modified device maintain there efficiency over the course of 250h without appreciable loss. The versatile and simple deposition method is likewise encouraging, as it is not limited to flat surfaces but can be adapted to textured perovskites, deposited *e.g.* from thermal evaporation.

The optoelectronic analyses outlined in chapters 3,5 and 6 rely on the fundamental assumption, that the solar cells, behave in essence very similar to an idealized device where the semiconductor is predominantly described by the photo-physics of the "main" semiconductor – that is the perovskite. This prerequisite can be disregarded on the basis of the argument that the description of the devices, in particular the open-circuit voltage, works very well, as outlined above. On the other side the complex multilayer architecture of *e.g.* a p-i-n device, with organic transport layers poses the question, whether this is true. Factors to be considered are *e.g.* the differences in dielectric constants (~3 in organics vs. >20 in perovskite) or the nature of charge transport (hopping in organics vs. band-like transport in perovskite), but also charge accumulation effects due to vastly different carrier mobilities. In Chapter 7, we measured charge carrier recombination dynamics in efficient p-i-n-type perovskite solar cells and find that recombination can be described in the framework of first-, second- and third-order recombination, without the necessity to introduce mixed recombination orders, which is still often reported in literature, when measuring with *e.g.* TPV/TPC. We find the kinetic variables: k_1 ~$3 \cdot 10^6$ s^{-1}, $k_{2,ext.}$ ~$3 \cdot 10^{-11} cm^3 s^{-1}$, k_3 ~$10^{-30} cm^6 s^{-1}$ and a background doping density of p_0 ~$10^{13} cm^{-3}$. Numerically solving the rate equation $dn/dt = G - k_1\ n - k_2\ n \cdot (n + p_0) - k_3\ n^3$ allows us to calculate a singular steady-state carrier density of $\leqslant 10^{15} cm^{-3}$ under 1 sun conditions suggesting relatively homogeneous carrier profiles throughout the active layer at open-circuit. The lower carrier density compared to uncontacted and more so a passivated perovskite layers is a consequence of additional recombination. With the obtained rate constants and carrier densities we are able to accurately reproduce external luminescent efficiencies, the open-circuit voltage and ideality factor of the devices over several orders of magnitude. When employing drift-diffusion simulations, the measured and experimentally determined JV-characteristics are in excellent agreement. This is valid, even when including mobile ions, where we find that only a density lower than $10^{16} cm^{-3}$ can reproduce the JV curves with measured small hysteresis and high fill-factors. By estimating photon emission probability, we calculate an intrinsic $k_2 \approx 3.7 \cdot 10^{-10} cm^3/s$, which excellently fits the values obtained from van Roosbroeck-Shockley calculation. Our work sheds light on the internal recombination in efficient perovskite solar cells and suggests that state-of-the-art devices operate in the nonradiative regime, at the verge to the radiative regime, where photon-recycling will benefit the performance. Optical management, that will enhance the emission at the bandedge of the perovskite, will enhance luminescent outcoupling and in turn enable higher photovoltages.

Finally, Chapter 8 highlights the progress we and others made over the course of this thesis, particularly focusing on the critical role interfaces play in dictating the device performance through interfacial recombination losses. Advantages and disadvantages/pitfalls of several experimental techniques such as Impedance Spectroscopy, Charge Extraction, Transient (Terahertz or Microwave) Absorption or Reflection (TAS/TRS) and Transient Photoluminescence are discussed, where we conclude that the safest methodology to assess nonradiative losses is absolute PL, in particular as is allows to determine the origin of nonradiative losses under relevant illumination conditions (*i.e.* 0.01 - 1 sun equivalent) without finalizing the devices, a significant strategic advantage over most other techniques. The technique has been used in several studies such as chapters 5, 6 and 7, but is growing more popular among the research community in it's own right. We advertise the use of a metaphor/analogy, where a solar cell is represented by a bucket, neatly illustrating that recombination current (represented as leakages in the bucket) flow in parallel and that reduction of the largest recombination current is imperative when seeking to increase the V_{OC}, which in this analogy would be the water level. Different strategies that allow to reduce nonradiative recombination losses are discussed, highlighting the importance of energy level alignment (between the perovskite and the respective CTL) and interface optimization, including interlayers, doped transport layers or graded junctions. Implementing such strategies, recent record solar cells are already approaching or even operating in the radiative regime. Recognizing this fact is highly important as it shifts the focus of future endeavors to improve perovskite solar cells then not through interface/bulk optimization, but also considering light management, particularly focusing on improved light trapping, but also light emission.

The goal of this work was to identify and reduce the mechanisms that induce losses in perovskite solar cells. To this end different luminescence measurements – *i.e.* TRPL, absolute PL and EL – were found as the most reliable means to identify the origin of nonradiative losses in highly efficient p-i-n devices. The interfaces, in particular the interface between perovskite and C_{60}, were identified as limitation for further improvements and different interlayers were introduced mitigating these losses. Specifically, insulating PS, LiF and a family of SAMs were interjected, all of which reduced the surface recombination velocity at the perovskite/C_{60} interface, enhancing the V_{OC} and reaching efficiencies >21%. The SAMs have the additional advantage that they drastically improve the stability of the solar cells both when stored in the ambient but also when subjected to heat-light-bias stress such as MPP-tracking under 85°C. The developed, reasonably robust protocols that enable highly efficient p-i-n- perovskite solar cells are discussed in great detail, specifically pointing towards pitfalls. Probing the recombination dynamics directly in working devices was achieved through a combined approach of multiple spectroscopic tools, allowing to describe the solar cell under multiple illumination conditions. The conclusions drawn are in concert with the overall picture laid out, namely that perovskite solar cells are at the verge of operating in the radiative regime and further progress towards 30% efficiency can be expected.

Part III

APPENDIX

SCIENTIFIC CONTRIBUTIONS

FULL LIST OF PUBLICATIONS

1. M. J. Berr, F. F. Schweinberger, M. Döblinger, K. E. Sanwald, C. Wolff, J. Breimeier. A. S. Crampton. C. J. Ridge. M. Tschurl. U. Heiz, F. Jäckel, J. Feldmann. *Nano Lett.* **2012**, 12, 5903.
2. F. F. Schweinberger. M. J. Berr, M. Döblinger, C. Wolff, K. E. Sanwald, A. S. Crampton, C. J. Ridge, F. Jäckel, J. Feldmann, M. Tschurl, U. Heiz. *J. Am. Chem. Soc.* **2013**, 135, 13262.
3. A. Paulke, S. D. Stranks, J. Kniepert, J. Kurpiers, C. M. Wolff, N. Schön, H. J. Snaith, T. J. K. Brenner, D. Neher. *Appl. Phys. Lett.* **2016**, 108, 113505.
4. C. M. Wolff, F. Zu, A. Paulke, L. P. Toro, N. Koch, D. Neher. *Adv. Mater.* **2017**, 29, 1700159.
5. J. A. Love, M. Feuerstein, C. M. Wolff, A. Facchetti, D. Neher. *ACS Appl. Mater. Interfaces* **2017**, 9, 42011.
6. Z. Chen, A. Savateev, S. Pronkin, V. Papaefthimiou, C. Wolff, M. G. Willinger, E. Willinger, D. Neher, M. Antonietti, D. Dontsova. *Adv. Mater.* **2017**, 29, 1700555.
7. A. Savateev, S. Pronkin, J. D. Epping, M. G. Willinger, C. Wolff, D. Neher, M. Antonietti, D. Dontsova. *ChemCatChem* **2017**, 9, 167.
8. L. Kegelmann, C. M. Wolff, C. Awino, F. Lang, E. L. Unger, L. Korte, T. Dittrich, D. Neher, B. Rech, S. Albrecht. *ACS Appl. Mater. Interfaces* **2017**, 9, 17245.
9. M. Jošt, S. Albrecht, L. Kegelmann, C. M. Wolff, F. Lang, B. Lipovšek, J. Krč, L. Korte, D. Neher, B. Rech, M. Topič. *ACS Photonics* **2017**, acsphotonics.7b00138.
10. M. Stolterfoht, C. M. Wolff, Y. Amir, A. Paulke, L. Perdigón-Toro, P. Caprioglio, D. Neher. *Energy Environ. Sci.* **2017**, 10, 1530.
11. M. Saliba, M. Stolterfoht, C. M. Wolff, D. Neher, A. Abate. *Joule* **2018**, 2, 1019.
12. C. M. Wolff, P. D. Frischmann, M. Schulze, B. J. Bohn, R. Wein, P. Livadas, M. T. Carlson, F. Jäckel, J. Feldmann, F. Würthner, J. K. Stolarczyk. *Nat. Energy* **2018**, 3, 862.
13. S. Braunger, L. E. Mundt, C. M. Wolff, M. Mews, C. Rehermann, M. Jošt, A. Tejada, D. Eisenhauer, C. Becker, J. A. Guerra, E. Unger, L. Korte, D. Neher, M. C. Schubert, B. Rech, S. Albrecht. *J. Phys. Chem. C* **2018**, 122, 17123.
14. M. Saliba, J.-P. Correa-Baena, C. M. Wolff, M. Stolterfoht, N. Phung, S. Albrecht, D. Neher, A. Abate. *Chem. Mater.* **2018**, 30, 4193.
15. M. Stolterfoht, C. M. Wolff, J. A. Márquez, S. Zhang, C. J. Hages, D. Rothhardt, S. Albrecht, P. L. Burn, P. Meredith, T. Unold, D. Neher. *Nat. Energy* **2018**, 3, 847.
16. Q. Wang, E. Mosconi, C. M. Wolff, J. Li, D. Neher, F. De Angelis, G. P. Suranna, R. Grisorio, A. Abate. *Adv. Energy Mater.* **2019**, 9, 1900990.
17. P. Caprioglio, F. Zu, C. M. Wolff, J. A. Márquez Prieto, M. Stolterfoht, P. Becker, N. Koch, T. Unold, B. Rech, S. Albrecht, D. Neher. *Sustain. Energy Fuels* **2019**, 3, 550.

18. V. M. Le Corre, M. Stolterfoht, L. Perdigón Toro, M. Feuerstein, C. Wolff, L. Gil-Escrig, H. J. Bolink, D. Neher, L. J. A. Koster. *ACS Appl. Energy Mater.* **2019**, 2, 6280.
19. F. Zu, C. M. Wolff, M. Ralaiarisoa, P. Amsalem, D. Neher, N. Koch. *ACS Appl. Mater. Interfaces* **2019**, 11, 21578.
20. M. Stolterfoht, P. Caprioglio, C. M. Wolff, J. A. Márquez Prieto, J. Nordmann, S. Zhang, D. Rothhardt, U. Hörmann, Y. Amir, A. Redinger, L. Kegelmann, F. Zu, S. Albrecht, N. Koch, T. Kirchartz, M. Saliba, T. Unold, D. Neher. *Energy Environ. Sci.* **2019**, 12, 2778.
21. P. Caprioglio, M. Stolterfoht, C. M. Wolff, T. Unold, B. Rech, S. Albrecht, D. Neher. *Adv. Energy Mater*, **2019**, 9, 1901631.
22. C. M. Wolff, P. Caprioglio, M. Stolterfoht, D. Neher. *Adv. Mater.* **2019**, 1902762.
23. U. Würfel, L. Perdigón-Toro, J. Kurpiers, C. M. Wolff, P. Caprioglio, J. J. Rech, J. Zhu, X. Zhan, W. You, S. Shoaee, D. Neher, M. Stolterfoht. *J. Phys. Chem. Lett.* **2019**, 10, 3473.
24. L. Kegelmann, P. Tockhorn, C. M. Wolff, J. A. Márquez, S. Caicedo-Dávila, L. Korte, T. Unold, W. Lövenich, D. Neher, B. Rech, S. Albrecht. *ACS Appl. Mater. Interfaces* **2019**, 11, 9172.
25. S. Zhang, S. M. Hosseini, R. Gunder, A. Petsiuk, P. Caprioglio, C. M. Wolff, S. Shoaee, P. Meredith, S. Schorr, T. Unold, P. L. Burn, D. Neher, M. Stolterfoht. *Adv. Mater.* **2019**, 31, 1901090.
26. F. Zu, P. Amsalem, D. A. Egger, R. Wang, C. M. Wolff, H. Fang, M. A. Loi, D. Neher, L. Kronik, S. Duhm, N. Koch. *J. Phys. Chem. Lett.* **2019**, 10, 601.
27. C. M. Wolff, L. Canil, C. Rehermann, N. Ngoc Linh, F. Zu, M. Ralaiarisoa, P. Caprioglio, L. Fiedler, M. Stolterfoht, S. Kogikoski, I. Bald, N. Koch, E. L. Unger, T. Dittrich, A. Abate, D. Neher. *ACS Nano* **2020**, 14, 1445.
28. L. Perdigón-Toro, H. Zhang, A. Markina, J. Yuan, S. M. Hosseini, C. M. Wolff, G. Zuo, M. Stolterfoht, Y. Zou, F. Gao, D. Andrienko, S. Shoaee, D. Neher. *Adv. Mater.* **2020**, 32, 1906763.
29. M. Stolterfoht, M. Grischek, P. Caprioglio, C. M. Wolff, E. Gutierrez-Partida, F. Peña-Camargo, D. Rothhardt, S. Zhang, M. Raoufi, J. Wolansky, M. Abdi-Jalebi, S. D. Stranks, S. Albrecht, T. Kirchartz, D. Neher. *Adv. Mater.* **2020**, 2000080.
30. F. Zu, T. Schultz, C. M. Wolff, D. Shin, L. Frohloff, D. Neher, P. Amsalem , N. Koch. *RSC Adv.*, **2020**,10, 17534-17542

SELECTED CONFERENCE CONTRIBUTIONS

1. HOPV 2015 Symposium. Berlin. Germany : Charge Extraction in Organometallic Perovskite Solar Cells (Poster)
2. DPG Spring Meeting 2016. Regensburg. Germany: Charge Extraction in Organometallic Perovskite Solar Cells (Poster)
3. PSCO 2016. Genova. Italy: Recombination in $CH_3NH_3PbI_3$ Solar Cells with Varying All-Organic Transport Layers (Poster. **NATURE's Best Multi-Disciplinary Poster Prize**)
4. DPG Spring Meeting 2017. Dresden. Germany: Reduced Recombination for High-Open-Circuit Voltages in $CH_3NH_3PbI_3$ Solar Cells (Contributed Talk)
5. ABXPV 2017. Valencia. Spain: Reduced Recombination for High-Open-Circuit Voltages in Perovskite Solar Cells (Contributed Talk)
6. PSCO 2017. Oxford. UK: Reduced Recombination for High Open-Circuit Voltages in Perovskite Solar Cells and Tandem-Applications (Contributed Talk)
7. DPG Spring Meeting 2018. Berlin. Germany: Self-assembled Monolayers Enhance the Stability and Efficiency of p-i-n Perovskite Solar Cells (Contributed Talk)
8. PSCO 2018. Lausanne. Switzerland: Suppressed Interfacial Recombination enables High Efficiency p-i-n-Perovskite Solar Cells (Contributed Talk)
9. DPG Spring Meeting 2019. Regensburg. Germany : Probing Charge Carrier Dynamics in Perovskite Solar Cells (Contributed Talk)
10. E-MRS Spring Meeting 2019. Nice. France: Multilayer Design for Efficient and Stable p-i-n Perovskite Solar Cells (Invited Talk)

DECLARATION OF ORIGINALITY

I declare that this thesis is my own original work and that I have not sought or used inadmissible help of third parties to produce this work and that I have clearly referenced all sources used in the work. I have fully referenced all text directly or indirectly quoted from a source. This work has not been submitted to another examination institution – neither in Germany nor outside Germany – neither in the same nor in a similar way and has not yet been published. Permission for reproduction of chapters, figures and text fragments has been granted by the respective journals.

Potsdam, Mai 2020

Christian Michael Wolff

ADDITIONAL DATA

SUBSTRATE CLEANING

- brush– without scratching/damaging the ITO surface – using a 3% Hellmanex cleaning solution diluted with deionized water
- rinse with copious amounts of deionized water
- ultrasonic bath in acetone for about 15 min
- ultrasonic bath in a 3% Hellmanex cleaning solution
- rinse with copious amounts of deionized water
- ultrasonic bath in deionized water for about 15 min
- ultrasonic bath in isopropanol for about 15 min
- dry the isopropanol quickly under nitrogen flow
- microwave plasma cleaning for 4 min at 200W

CHEMICALS FOR INVERTED PEROVSKITE SOLAR CELL FABRICATION

chemical	**producer**	**CAS**	**product number**
PbI_2	TCI	10101-63-0	L0279
$PbBr_2$	TCI	10031-22-8	L0288
CsI	Sigma-Aldrich	7789-17-5	203033
MABr	Dyesol	6876-37-5	MS301000
FAI	Dyesol	879643-71-7	MS150000
MAI	Dyesol	14965-49-2	MS101000
dimethylformamide	Alfa-Alesar	68-12-2	41859.AK
dimethyl sulfoxide	Sigma-Aldrich	67-68-5	276855
ethyl acetate	Sigma-Aldrich	141-78-6	270989
PTAA	Sigma-Aldrich	1333317-99-9	702471
methanol	Sigma-Aldrich	67-56-1	34860
PFN-P2	1-Material	889672-99-5	OS0995
C_{60}	creaphys	99685-96-8	V0502010
BCP	Sigma-Aldrich	4733-39-5	699152
copper	Sigma-Aldrich	7440-50-8	254177
polystyrene	Sigma-Aldrich	9003-53-6	331651
dichlorobenzene	Sigma-Aldrich	95-50-1	240664

Table 3: Chemicals used in the Fabrication of samples in this thesis.

STANDARD TRIPLE CATION RECIPE

composition	**concentration**	**material**	**solvent**
$FAPbI_3$ (FA)	1.32M	PbI_2	1mL DMF/DMSO; 4:1(v/v)
	1.2M	FAI	
$MAPbBr_3$ (MA)	1.32M	$PbBr_2$	1mL DMF/DMSO; 4:1(v/v)
	1.2M	MABr	
CsI	1.5M	CsI	1mL DMSO
PTAA	1.5mg/mL	PTAA	1mL toluene
PFN-P2	0.5mg/mL	PFN-P2	1mL methanol
CsMAFA		170µL MA + 830µL FA + 40µL CsI	

Table 4: Standard recipe for triple cation perovskite used in the fabrication of samples in this thesis. The FA/MA ratio may be modified to vary the bandgap slightly.

Supporting Information to Chapter 7:

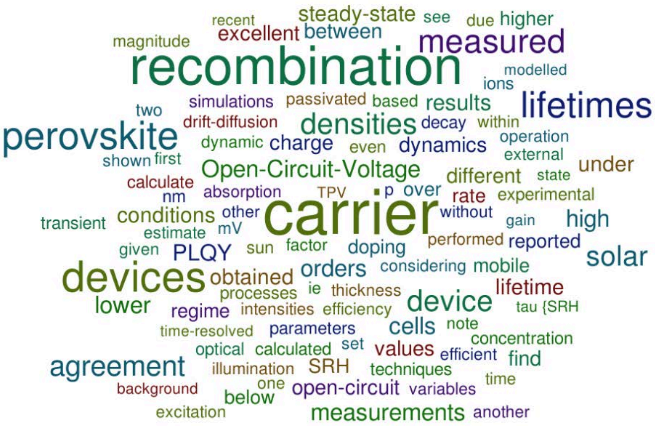

SI: Photophysics of High-Performance Perovskite Solar Cells

Christian M. Wolff, Sean Bourelle, Phoung Le, Jona Kupiers, Sascha Feldmann, Pietro Caprioglio, Jose Antonio Marquez-Prieto, Jonas Diekmann, Thomas Unold, Martin Stolterfoht, Safa Shoaee, Felix Deschler, and Dieter Neher

in prepraration

Solar Cell Preparation

Pre-patterned *ITO* (Automatic Research, 15Ω/□) was washed by sonication for 15 min. with acetone, Hellmanex III (3% in DI water), DI-water and isopropanol, respectively. After 4 min of microwave plasma (200W), the samples were taken to a N_2-filled glovebox and *PTAA* (Sigma-Aldrich, 1.5mg/mL in toluene, dissolved over night by stirring) was spin-coated at 6000 rpm for 30 sec after spreading around 70 μL on the substrate before starting. The *PTAA* coated substrate is subsequently annealed at 100 °C for 10 minutes and left to cool for 5 minutes. Before perovskite deposition, 50 μL of a 0.5 mg/mL *PFN* solution (1-Material in MeOH) is dynamically spin-coated at 6000rpm, which ensures full coverage of the perovskite on *PTAA*. The perovskite solution *CsMAFA* is prepared by dissolving (stirring overnight) *MABr* (0.2 M, dyesol), *FAI* (1.03 M, dyesol), PbI_2 (1.13 M, Alfa-Aesar) and $PbBr_2$ (0.2 M TCI) in anhydrous *DMF*/*DMSO* = 4:1 (v/v, Alfa-Aesar and Sigma-Aldrich, respectively). In parallel *CsI* (1.5 M, Sigma-Aldrich) is dissolved in DMSO. Before deposition, the solutions are mixed as follows MAFA:CsI: = 960:40 μL/μL to produce a composition with the stoichiometry $Cs_{0.05}[MA_{0.15}FA_{0.85}PbI_{0.85}Br_{0.15}]_{0.95}$ where the initial PbI_2 excess (10%) is partially compensated by the addition of CsI. The mixtures are vigorously shaken for a minute (vortexer) right before use. Typically 100 μL of perovskite solution is drop-casted on the 2.5x2.5cm² substrate and spin-coated at 3500 prm with 3 seconds acceleration (i.e. 1160 rpm/s) for a total of 41 seconds (3 sec. acceleration +35 sec. spinning + 3 sec. deceleration). 13 seconds after the start of the spin-coating 500μL of ethyl acetate (Sigma-Aldrich) are dispersed on the spinning substrate inducing a color change to dark reddish-brown. 0.8nm LiF(Lasker), 30 nm C_{60} (creaphys) and 8nm BCP (Sigma-Aldrich) are evaporated at 0.1-0.2 A/s under high vacuum < 10^{-6} mbar on the full area before 30 or 100nm Cu are evaporated at 0.2-0.8 A/s through a shadow-mask defining the active area. Devices have typical active area sizes of 0.055mm² for the TDCF measurements. For the semi-transparent devices we evaporated 6mm² devices. For simultaneous Voc-PLQY-Jsc measurements, we developed an electrode pattern that closely follows the PLQY spot size.

jV and IPCE

The *JV* scans were performed under N_2 with a Keithley 2400, while the substrates were Peltier cooled to 25°C. The illumination source was a filtered Oriel class AAA

Xenon lamp and the intensity has been monitored simultaneously with a Si reference cell. The calibration was done with a KG5 filtered reference silicon solar cell (calibrated by Fraunhofer ISE). EQE_{PV} spectra were recorded with a halogen lamp (Philips Projection Lamp Type7724 12 V 100 W) in front of a monochromotor (Oriel Cornerstone 74100) and the light was mechanically chopped at 40 Hz. The photogenerated current is measured with a lock-in-amplifier (EG&G Princeton Applied Research Model 5302, integration times 300ms-10s) and evaluated after calibrating the lamp spectrum with an UV-enhanced Si photodetector (Newport).

Transient Absorption Spectroscopy

A Ti:Sapphire amplifier system (Coherent Libra) operating at 1 kHz generated ~100-fs pulses was used to generate and the probe beam pulses. The broad band probe beam was generated in a home-built noncollinear optical parametric amplifier with a 3mm thick YAG crystal. For pump 532nm ns-pulses are generated by frequency doubling (AOT innolas) triggered and electronically delayed relative to the probe pulse. The transmitted probe light was collected with a CMOS line array detector driven and read out by a custom-built board from **Stresing Entwicklungsbüro.**

Absolute PL

The setup consists of a 445nm excitation laser, an integrating sphere, whose output is directed onto a spectrometer (Andor iStar DH740 CCI-010) and a sample holder with electrical contacts. The setup was calibrated spectrally for absolute measurements using a calibrated lamp (spectral response) and three molecular standards.

Supplementary Note 1:

The electrodes of the devices – ITO and Cu – have high conductivities, so carriers reaching the electrodes might quickly diffuse away from the excitation spot. This would reduce the carrier density detected by the probe pulse and mask recombination dynamics. To overcome this obstacle, we performed all measurements on samples, with an active area and a spot-size of roughly the same size.

Supplementary Note 2:

The initial TAS signal at *t*=0 can be translated to a photogenerated charge-carrier concentration, considering the laser fluence, the absorption coefficient of the perovskite at the excitation wavelength and the thickness of the absorbing layer[5], if the signal scales linearly with intensity, as shown in Figure S1.

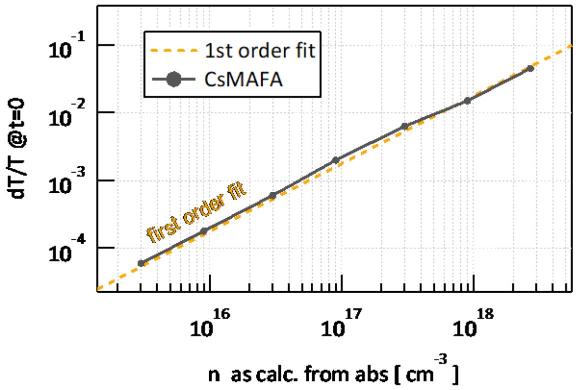

Figure S1. Intensity calibration of TA signal versus calculated carrier density at t=0. The linearity assures that we are able to capture all dynamics within the time-resolution.

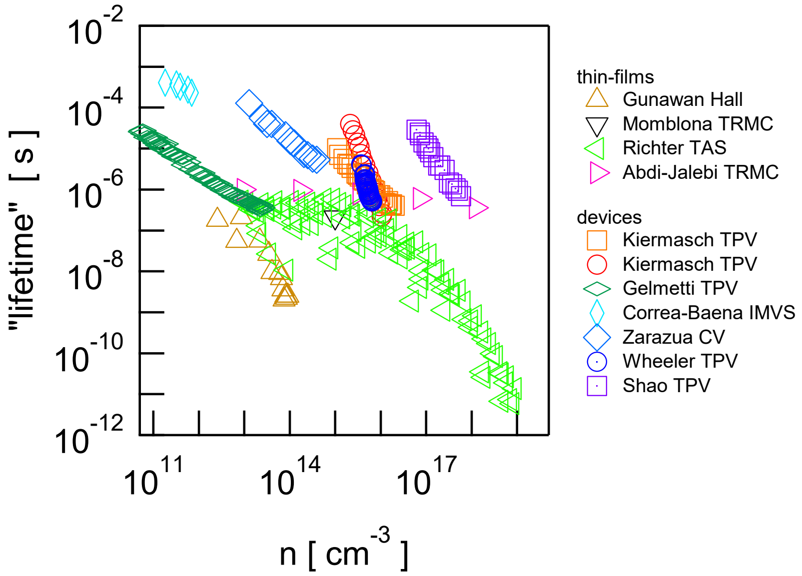

Figure S2. Reported “lifetimes” versus carrier densities for thin film (green) and devices (blue).

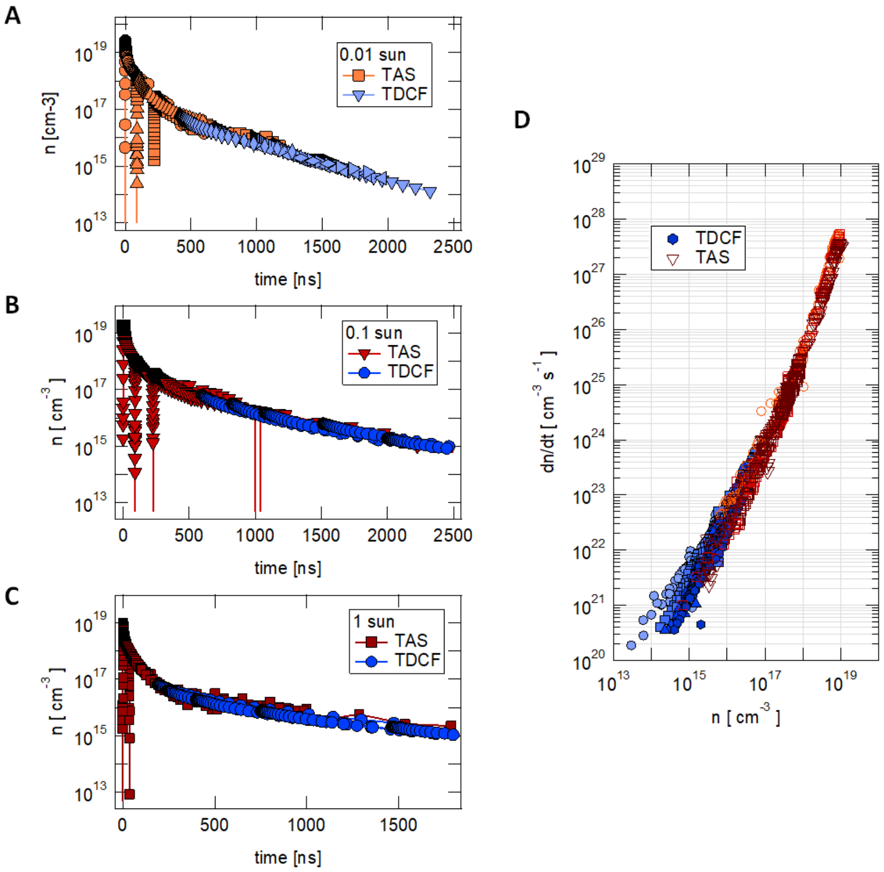

Figure S3. (A,B,C) temporally shifted TAS and TDCF transients under 0.01, 0.1 and 1 sun equivalent background illumination and corresponding *dn/dt vs. n* for all measurements (D).

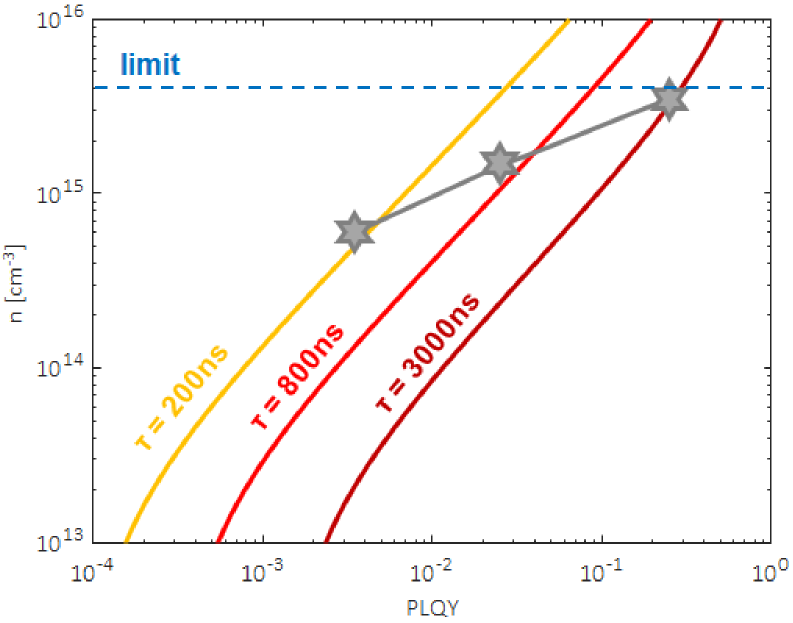

Figure S4. Carrier density and corresponding PLQY values for the measured devices (grey stars) and for different samples based on the denoted SRH lifetimes.

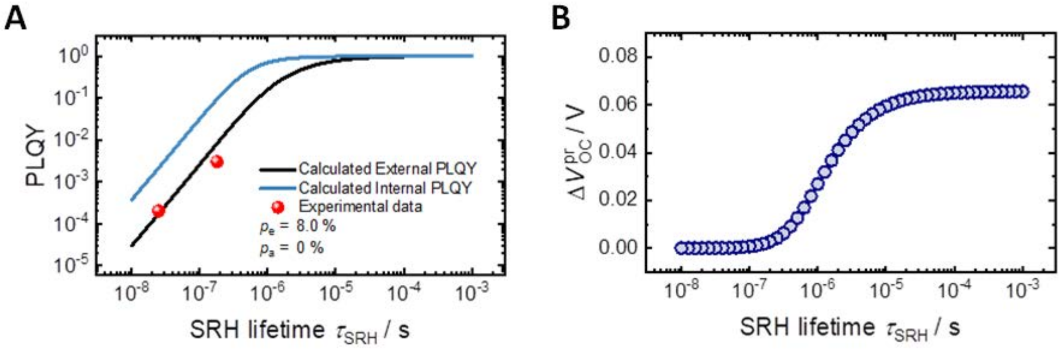

Figure S5. (A) Calculated external (black) and internal (blue) PLQY as a function of SRH lifetime, based on the kinetic variables obtained, assuming a perfect back mirror and no parasitic absorption. The experimentally observed external PLQYs of two devices – one with and one without interlayers – (red dots) fit nicely to the calculated curve. (B) Expected V_{OC} gain due to photon-recycling under the same assumptions.

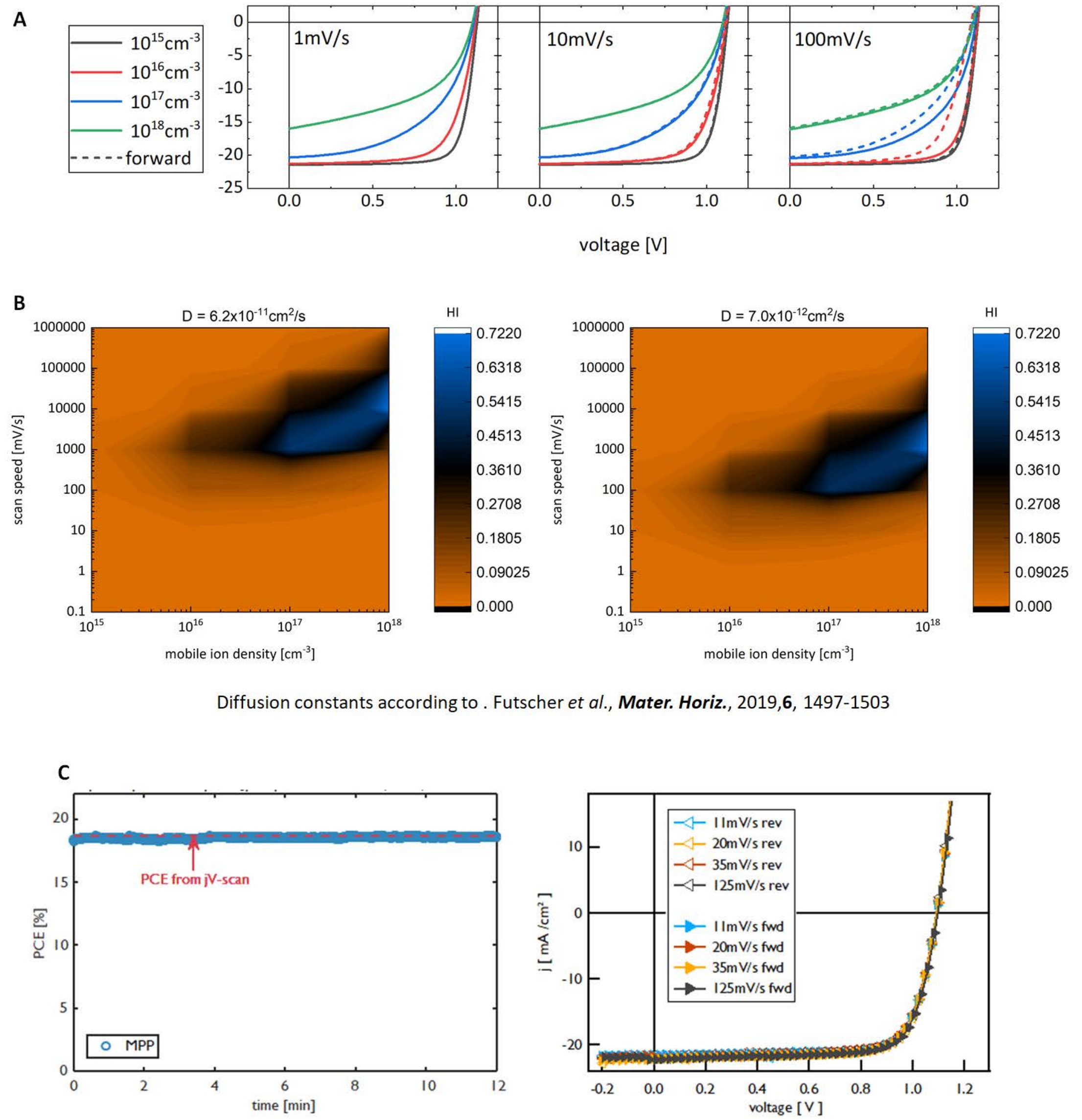

Diffusion constants according to . Futscher *et al.*, ***Mater. Horiz.***, 2019,**6**, 1497-1503

Figure S6 (A) Simulated *JV*-scans with varying scan direction (full lines = reverse and dashed lines forward) for varying mobile ion concentrations (black to green = 10^{15}-10^{18}cm^{-3}) under different scan rates (1,10,100mV/s, $D_{ion} = 6.2\text{x}10^{-11}$cm^2/s).(B) 2D plots of a calculated hysteresis index $HI = \int J_{rev}(V) - J_{fwd}(V)dV / \int J_{rev}(V)dV$ for different mobile ionic concentrations (x axis), and scan speeds (y-axis) as well as two different diffusion constants (left *vs.* right.).

(C) Experimentally obtained MPP and *JV*-scans suggesting low mobile ion concentration <10^{16}cm^{-3} in the measured devices, when comparing to simulations.

ACKNOWLEDGMENTS

First, I want to thank my supervisor *Prof. Dr. Dieter Neher* for the opportunity to conduct the research presented in this work:

Dear Dieter, without your enthusiasm, your trust in my abilities and me as a person, none of this work would have been possible. You taught me things that go well beyond science and I cannot describe my gratitude in adequate words. I am still amazed how you manage all your responsibilities and still find time to discuss and dive deep into scientific questions on an almost daily basis – *touché*. You enabled me to attend conferences that turned out to expand my horizon and develop me as a person and scientist. I am ever grateful for the time we had during the last years and I hope we manage to keep in touch in and out of academia. To *Dr. Thomas Unold*: you were always a great inspiration and I am grateful that you were my "scientific mentor". This rather inappropriate description doesn’t reflect my gratitude for the insight you provided throughout the years. I am humbled to have worked with you on many subjects and your broad knowledge about physics and beyond have led to much of what is presented here. I wish you all the best in the years to come and am looking forward to future encounters. I want to express my gratitude to *Prof. Dr. Steve Albrecht* (special thanks!!), *Prof. Dr. Bernd Rech, Prof. Dr. Norbert Koch, Prof. Dr. Ilko Bald, Prof. Dr. Michael Saliba, Prof. Dr. Antonio Abate, Prof. Dr. Eva Unger* and *Dr. Thomas Dittrich* for the great collaborations we have had and hope to continue working together in future. Special thanks also go to *Dr. Felix Deschler*, who hosted me during my stay in Cambridge along with the rest of his group: *Sean, Sascha, Greg, Haralds, Lissa* and *Tim*.

At this point I want to thank the people that enable and foster that we can explore the realms of science because of their relentless work that keeps the labs running. Foremost *Dr. Frank Jaiser*, who is the go-to-person whenever questions about setups and things that can or cannot be done arise. I am amazed by your calmness when facing obvious – well – human failures, both by myself and others. You keep the labs running and one of the things that lured me to Potsdam in the first place was the excellent setups and facilities in general, which clearly have your handwriting on them; thank you so much! Not to forget *Andreas Horka*, whom I constantly kept busy with ordering new materials for my and others’ – sometimes crazy– ideas. *Andreas Pucher* and *Burkhard Stiller* always had an open ear for my needs and were the heart of every group excursion and/or BBQ party! Dear *Florian Dornack*, we shared funny stories about our love/hate relationship with soccer and quite a few cigarettes. You were a great office companion and a technician anyone could wish for. I mean common: "Do you need this today or is it fine tomorrow morning?". How can you not love this guy? Not to be forgotten *Elke Derlig*, whom I loved to visit in the mornings for a short chat and cheerful laughter and who always had an open ear and helping advice when facing UP or Brandenburg buro*CRAZY*. Without all of you people the PwM group in Potsdam would be at least half as much fun and probably 1/10 as productive, so I want to thank you deeply. In our group there were many great minds over the years, but *Dr. Martin Stolterfoht, Dr. John Love, Dr. Steffen Roland, Dr. Jona Kurpiers, Lorena Perdigon-Toro, Pietro Caprioglio, Prof. Dr. Safa Shoaee, Mehrdad Hosseini, Meysam Raoufi, Dr. Lee Phung, Dr. Juliane Kniepert, Malavika Arvind* and *Andreas Paulke*; you were especially important for me, both in and out of academia; it was a blast, thanks! Not to be forgotten are the students I got to work with over the years, namely *Yohai Amir, Mathis Manzel, Jakob Wolansky* and *Lukas Fiedler*; greets to *Pacho* and *Emilio* keep it up! I really enjoyed the last couple of years and had a great time during workshops within our graduate school HyPerCells and more so after the workshops ;). In particular I want to thank *Dr. Lukas Kegelmann, Dr. Fengshuo Zu, Dr. Ula Yasin, Carolin Rehermann, Philipp Tockhorn, Dr. Paul Sonntag, Laura Canil, Dr. Marko Jost, Dr. Aboma Merdasa, Dr. Jose Marquez, Amran Al-Ashouri, Eike Köhnen, Dr. Steffen Braunger, Dr. Sergiu Levcenco, Dr. Charles Hages, Hannah Funk, SeCaDa, Dr. Qiong Wang, Nga Phung, Dr. Maryline Ralaiarisoa, Dr. Felix Lang, Marion Flatken and*

Dr. Oleksandra Shargaieva and all the others, what an amazing journey! I want to greet and thank *Dr. Kristoffer Tvingstedt*, *Philipp Rieder*, *David Kiermasch*, *Dr. Andreas Baumann* and the others from Würzburg, *Dr. Ardalan Armin*, *Prof. Dr. Paul Meredith*, *Prof. Dr. Thomas Kirchartz* and *Dr. Julian Steele* for great discussions. Special thanks to *Lukas*, *Ula* and *Caro* for proof reading this thesis! Sending love to my friends back home, in Munich, Berlin and around the world: *Benni Schulz, Fred Gössele, Christoph Sattler, Simon Lechler, Simon Blaich, Sören Brüstle, Stefan Zimmermann, Janji Lederer, Svenja Urban, (Anne-) Marie Summer, Anna Elsässer, Conni Lechler, Dina Falk, Sophie Kurz, Sina Müller, Sevi Zeviley, Simon Dirmeier, Nils Aldag, Friederike Krüger, Julia Kamml, Susi Scherr, Aurora Manzi, Jonathan Roland, Jakob Lenz, Christian Gruber, Valentin Feneberg, Roberta Saponaro, Stephan Liegmann, Martha Lippich* and my beloved Berlin-roomies *Savanna Bonfig* and *Maria Kochs* - <3!!! Speical thanks go to my teacher *Michael Krist* for encouraging my interest in physics in the first place. Finally, I want to thank my parents *Renate* and *Michael* for sparking this love to science and my brother *Sebastian* for being a brother to wish for both in realizing dreams and dreaming about things to realize! Likewise, I want to thank the rest of our family for encouraging and nagging me throughout this journey that started sometime in 2009 (probably before in all honesty...) with me moving to Munich (also thanks to my cousins *Mark* and *Bernd*) to follow my urge to understand this world a bit better through equations - crazy after all!
Dear *Philine*, thank you for being at my side during the most challenging parts of this. Your company, love, patience and encouragement have made my life so much more joyful and I am looking forward to what comes next for us. *#micdrop*

COLOPHON

This document was typeset using the typographical look-and-feel `classicthesis` developed by André Miede and Ivo Pletikosić with a few changes. Plots were done in WaveMetrics Igor Pro 6.37 and MathWorks MatLAB R2019a and editted in Inkscape 0.92 for compatibility.